UNIVERSITAT
POLITÈCNICA
DE VALÈNCIA

Implementation of new algorithms for an accurate gamma-ray impact determination in scintillation monolithic blocks for PET applications

Doctoral Thesis

Marta Freire López-Fando
Instituto de Instrumentación para Imagen Molecular
(i3M, CSIC-UPV)

Under the supervision of
Antonio J. González
Andrea González-Montoro
Valencia, May 2023

For the development of this thesis, the PhD candidate Marta Freire López-Fando was partially supported by the Program for Researchers in Predoctoral Phase of the Ministry of Labor and Social Economy (Generalitat Valenciana) and the EU Social Fund: ACIF/2019/112.

Contents

Acknowledgements

Esta tesis es fruto de mucho esfuerzo pero sobre todo mucha ilusión por superar desafíos que permitan avances científicos en el ámbito de la Imagen Médica. Ha sido un recorrido largo, y muchas veces complicado pero, cuando te apasiona tanto lo que haces, las dificultades sólo son un impulso para seguir avanzando y alcanzando retos. Sin embargo, debo admitir que todo lo logrado ha sido posible gracias al apoyo y ayuda de todas las personas con las que he compartido esta etapa.

Quiero agradecer, en primer lugar, a Marcin Balcerzyk, quien me enseñó los primeros conocimientos sobre Imagen Médica y me puso en contacto con José María Benlloch, director del Instituto del Instrumentación para Imagen Molecular (i3M), a quien le doy sumamente las gracias por haberme abierto las puertas del i3M y haberme presentado cada uno de los departamentos que conforman el centro.

Quiero dar las gracias especialmente a mis directores de tesis, Antonio J. González y Andrea González-Montoro, por haber confiado en mí desde el principio, por vuestro apoyo en todo momento y por haberme enseñado tantísimas cosas, sobre todo, las bases del conocimiento necesarias para llevar a cabo investigación científica de calidad. Gracias también por brindarme grandes oportunidades que han permitido importantes avances en mi carrera investigadora. Quiero además mostrar mi profunda admiración por vosotros, por vuestra dedicación, constancia, perseverancia y humildad. Creo que sois los mejores directores de tesis que un estudiante puede tener. Me gustaría agradecer también a Filomeno Sánchez porque su ayuda y apoyo han hecho que sea como un director de tesis más.

Quiero agradecer por supuesto a todo el equipo PET del i3M, a los que lo conforman actualmente y a los que han pasado por él, porque todos habéis aportado un trocito a esta tesis: Koldo, Celia, Eff, Gabi, David, Riccardo, John, Liczandro, Neus, Sara, Alex, Santi, Alejandro, Andrew, Daniel, Noriel. Muchas gracias también a Amadeo Iborra por haber compartido conmigo sus conocimientos sobre Redes Neuronales. Por supuestísimo, millones de gracias a Carlos de Alfonso por su predisposición, ayuda y asistencia en todos los temas informáticos. Trabajar con personas como él es todo un lujo.

Me gustaría mostrar mi agradecimiento a todo el equipo de Bruker y Oncovision, por su ayuda durante todo el recorrido de mi tesis. Especialmente a Julio Barberá, Constan Morera, Jorge Álamo, Ramiro Polo, Carlos Correcher y Vicente Carrilero. I would also like to thank Peter Bruyndonckx because many of the results achieved during this thesis have been thanks to his guidance.

I would especially like to thank Dimitris Visvikis for giving me the opportunity to stay at the Laboratory of Medical Information Processing in Brest (France) for three months. Moreover, thanks to Stuart Berr and Mark Williams for their trust and help in the scientific projects in which we collaborate.

Quiero dar las gracias infinitas a mi familia al completo por los valores que me han inculcado y por haber apoyado siempre todas mis decisiones. Quiero agradecer también a Celia, quien ha sido mi familia en Valencia durante todo el desarrollo de la tesis y quien ha estado presente en los buenos y los no tan buenos momentos estos últimos años. Muchísimas gracias también a Rafa por haber aparecido en mi vida; sé que estarás a mi lado para siempre. Además me gustaría mostrar mi gratitud hacia mi familia senegalesa, especialmente hacia Wolly, quien me ha enseñado las lecciones de vida más importantes.

Por último, quiero dar las gracias infinitas a mis amigos, a los de siempre y a los más recientes, porque han conseguido sacar siempre lo mejor de mí. Creo que no son conscientes de lo feliz que me hacen y de lo mucho que me ayudan. Gracias de corazón a Macarena, Sara, Reyes, Luis (y Pepito), Martín, Mica, Valle, Delia, Alegría, Julia, Marta, Cristina, Marina, Ángela, Chusi, Amalia, Laura, Alfonso, Cata, Bibi, Carmen. Imposible nombraros a todos...

List of Publications

This doctoral thesis includes a compendium of the following peer-reviewed articles:

1. **M. Freire**, et al., “Calibration of gamma ray impacts in monolithic-based detectors using Voronoi diagrams,” IEEE Trans. Radiat. Plasma Med. Sci. **4**, 350-360, 2019.
2. **M. Freire**, et al., “Reducing Calibration Time in PET Systems Based on Monolithic Crystals,” Front. Med. **8**, 734476, 2021.
3. **M. Freire**, et al., “Experimental validation of a rodent PET scanner prototype based on a single LYSO crystal tube,” IEEE Trans. Radiat. Plasma Med. Sci. **6**, 697-706, 2021.
4. **M. Freire**, et al., “Performance evaluation of side-by-side optically coupled monolithic LYSO crystals,” Med. Phys. **49**, 5616-5626, 2022.

List of Abbreviations

AdaGrad	Adaptative Gradient Descent
Adam	Adaptative Moment Estimation
ADC	Analog to Digital Converter
AI	Artificial Intelligence
APD	Avalanche Photodiode
ASIC	Application Specific Integrated Circuit
ANN	Artificial Neural Network
BGO	Bismuth Germanate Oxid
BPF	Back Projection Filtering
CoG	Center of Gravity
CTR	Coincidence Time Resolution
CT	Computed Tomography
CNN	Convolutional Neural Network
CNR	Contrast to Noise Ratio
CPU	Central Processing Unit
DAQ	Data Acquisition System
dSiPM	Digital Silicon Photomultiplier
DOI	Depth of Interaction
ESR	Enhanced Specular Reflector
FBP	Filtered Back Projection
FC	Fully Connected
FCNN	Fully Connected Neural Network
FOV	Field of View
FPGA	Field Programmable Gate Arrays
FUS	Focused Ultrasound
FWHM	Full Width Half Maximum
GPU	Graphics Processing Unit
GTB	Gradient Tree Boosting
LD	Light Distribution
LM	List Mode

LOR	Line of Response
LSO	Lutetium Orthosilicate
LS	Least Squares
LUT	Look-up Table
LY	Light Yield
LYSO	Lutetium–Yttrium Oxyorthosilicate
MAE	Mean Absolute Error
MI	Molecular Imaging
MLE	Maximum Likelihood Estimator
MLP	Multilayer Perceptron
ML	Machine Learning
MLEM	Maximum Likelihood Expectation Maximization
MNN	Mean Nearest Neighbor
MRI	Magnetic Resonance Imaging
NAG	Nesterov Accelerated Gradient
NEMA	National Electrical Manufacturers Association
NMI	Nuclear Molecular Imaging
NMR	Nuclear Magnetic Resonance
NN	Neural Network
OSEM	Ordered Subsets Expectation Maximization
PET	Positron Emission Tomography
PCB	Printed Circuit Board
PDE	Photon Detection Efficiency
PDF	Probability Density Function
PMT	Photomultiplier Tube
QE	Quantum Efficiency
RELU	Rectified Linear Activation Function
RF	Radio frequency
RMSprop	Root Mean Squared Propagation
RMSE	Root Mean Squared Error
RR	Retroreflector
RTP	Raise to the Power
SGD	Stochastic Gradient Descent
SiPM	Silicon Photomultiplier

SPAD	Single Photon Avalanche Diode
SPECT	Single Photon Emission Computed Tomography
SNR	Signal to Noise Ratio
SOM-NN	Self Organizing Method Neural Network-based Nearest Neighbor
SVM	Support Vector Machine
TB	Total Body
TDC	Time to Digital Converter
TOF	Time of Flight
TIFF	Tagged Image Files Format
WB	Whole Body
WLS	Weighted Least Squares

Summary

Positron Emission Tomography (PET) is a powerful imaging technique that provides quantitative measurements of biological and physiological processes occurring within the body at the molecular level by using specific radiopharmaceuticals. PET imaging returns functional information that allows for early diagnosis and personalized therapy treatment follow up. It has applications in several research and clinical areas, such as oncology, neurology or cardiology, among others. Efforts to improve PET systems performance are focused on increasing their sensitivity and image quality, allowing for more accurate clinical assessments.

In PET imaging, a radiotracer labeled with a positron-emitting radionuclide is injected to the patient and consequently, distributed throughout the body. During the radiotracer decay, the isotope emits a positron that annihilates with an electron of the surrounding tissues, generating two 511 keV gamma-rays emitted at ~180°. The PET technique is based therefore on the simultaneous detection of these two gamma-rays, called annihilation photons, by usually employing a ring of detectors around the patient. Improving the design and performance of these detectors, increases the diagnostic capabilities of PET imaging.

To boost PET performance, it has been suggested to use detectors based on monolithic crystals designs, due to their advantages compared to pixelated detectors. However, their implementation in commercial scanners requires overcoming some challenges mostly related to photon impact positioning methods and calibration procedures to provide the impact coordinates and time of arrival of the annihilation photons. This PhD thesis focuses on the development and experimental validation of methodologies for an accurate determination of this information in monolithic detectors, emphasizing in their practical application to full PET systems.

During this thesis, the main principles of monolithic-based PET detectors have been studied to understand their behavior and limitations. Typical monolithic detector configurations based on continuous scintillation blocks coupled to flat SiPM arrays have been first considered; additionally, other novel approaches have been also validated. Two main methodologies for 3D photon interaction positioning, one based on analytical methods and another based on Deep Learning algorithms, have been developed to increase the overall detector performance. The proposed methods have been validated at the detector level but also in different PET scanners developed by our group.

The present thesis is based on a compendium of the most relevant papers published in peer-reviewed journals by the PhD candidate and is organized as follows. Chapter I presents an introduction to the thesis work, composed by three sections: Medical Imaging, principles of Positron Emission Tomography and, Position estimation and calibration in monolithic-based detectors. Chapter II contains the specific objectives of this thesis and the main contributions of the candidate to the field. This chapter also includes some recent methodologies and results that have not yet been published. Chapter III collects an author copy of the four published articles selected for the compendium, in which the candidate is the first author [1]-[4]. In Chapter IV the main results and conclusion achieved during the thesis are discussed. Finally, Chapter V presents the discussion of this thesis, summarizing the main contributions and highlighting the scientific achievements.

Resumen

La Tomografía por Emisión de Positrones (PET) es una potente técnica de imagen que proporciona mediante el uso de radiofármacos específicos medidas cuantitativas de los procesos biológicos y fisiológicos que tienen lugar en el organismo a nivel molecular. Las imágenes PET proporcionan información funcional que permite el diagnóstico precoz y el seguimiento personalizado del tratamiento terapéutico. La PET tiene aplicaciones en diversas áreas clínicas y de investigación, como la oncología, la neurología o la cardiología, entre otras. Los esfuerzos por mejorar las prestaciones de los sistemas PET se centran en aumentar su sensibilidad y calidad de imagen, lo que permite una evaluación clínica más precisa.

En las imágenes PET, se inyecta al paciente un radiotrazador marcado con un radionúclido emisor de positrones que se distribuye por todo el cuerpo. Durante la desintegración radiactiva del trazador, el isótopo emite un positrón que se aniquila con un electrón del tejido circundante, generando dos rayos gamma de 511 keV emitidos a ∼180º. La técnica PET se basa por tanto en la detección simultánea de estos dos rayos gamma, denominados fotones de aniquilación, empleando habitualmente un anillo de detectores alrededor del paciente. Mejorando el diseño y el rendimiento de estos detectores, se mejoran las capacidades diagnósticas que ofrece la imagen PET.

Para aumentar el rendimiento, se ha sugerido utilizar detectores basados en diseños de cristales monolíticos, debido a sus ventajas en comparación con los detectores pixelados. Sin embargo, su implementación en escáneres comerciales requiere superar algunos retos relacionados principalmente con los métodos de posicionamiento y los procedimientos de calibración necesarios para proporcionar las coordenadas de impacto del fotón de aniquilación y el tiempo de llegada de los fotones. Esta tesis doctoral se centra en el desarrollo y validación experimental de metodologías para la determinación precisa de esta

información en detectores monolíticos, haciendo hincapié en su aplicación práctica también a sistemas PET completos.

Durante esta tesis se han estudiado los principios fundamentales de los detectores PET monolíticos para comprender su comportamiento y limitaciones. En primer lugar, se han considerado las configuraciones típicas de detectores monolíticos basadas en bloques de centelleo continuo acoplados a matrices de SiPMs planas; además, también se han evaluado y validado otros enfoques novedosos. Se han desarrollado dos metodologías principales, una basada en técnicas analíticas y otra en algoritmos de Aprendizaje Profundo, para el posicionamiento 3D de la interacción del fotón con el fin de aumentar el rendimiento global del detector. Finalmente, los métodos propuestos han sido validados a nivel de detector, pero también en diferentes escáneres PET desarrollados en i3M.

La presente tesis se basa en un compendio de los artículos más relevantes publicados en revistas revisadas por pares por el doctorando y está organizada de la siguiente manera. El Capítulo I presenta una introducción al trabajo de la tesis, compuesto por tres secciones: Imagen Médica, principios de la Tomografía por Emisión de Positrones y, Estimación de posición y calibración en detectores monolíticos. El Capítulo II contiene los objetivos específicos de esta tesis y las principales contribuciones del candidato a este campo. Este capítulo también incluye algunas metodologías y resultados recientes que aún no han sido publicados. El Capítulo III colecciona una copia de los cuatro artículos publicados seleccionados para el compendio, en los que el candidato es el primer autor [1]-[4]. En el Capítulo IV se discuten los principales resultados y conclusiones alcanzados durante la tesis. Por último, el Capítulo V presenta la discusión de esta tesis, resumiendo las principales contribuciones y destacando los logros científicos.

Resum

La Tomografia per Emissió de Positrons (PET) és una potent tècnica d'imatge que proporciona mitjançant l'ús de radiofàrmacs específics mesures quantitatives dels processos biològics i fisiològics que tenen lloc en l'organisme a nivell molecular. Les imatges PET proporcionen informació funcional que permet el diagnòstic precoç i el seguiment personalitzat del tractament terapèutic. La PET té aplicacions en diverses àrees cliniques y d´investigació, com l'oncologia, la neurologia o la cardiologia, entre altres. Els esforços per millorar les prestacions dels sistemes PET se centren en millorar la seua sensibilitat i qualitat d'imatge, la qual cosa permet una avaluació clínica més precisa més precís.

En les imatges PET, s'injecta al pacient un radiotraçador marcat amb un radionúclid emissor de positrons que es distribueix per tot el cos. Durant la desintegració radioactiva del traçador, l'isòtop emet un positró que s'aniquila amb un electró del teixit circumdant, generant dos raigs gamma de 511 keV emesos a ~180^{o}. La tècnica PET es basa per tant en la detecció simultània d'aquests dos raigs gamma, denominats fotons d'anihilació, emprant habitualment un anell de detectors al voltant del pacient. Millorant el disseny i el rendiment d'aquests detectors, es millora les capacitats diagnòstiques que ofereix la imatge PET.

Per a augmentar el rendiment, s'ha suggerit utilitzar detectors basats en dissenys de cristalls monolítics, a causa dels seus avantatges en comparació amb els detectors pixelats. No obstant això, la seua implementació en escàners comercials requereix superar alguns reptes relacionats principalment amb els mètodes de posicionament i els procediments de calibració necessaris per a proporcionar les coordenades d'impacte del fotó d'anihilació i el temps d’arribada dels fotons. Aquesta tesi doctoral se centra en el desenvolupament i validació experimental de metodologies per a la determinació precisa d´aquesta informació en detectors monolítics, posant l'accent en la seua aplicació pràctica també a sistemes PET complets.

Durant aquesta tesi s'han estudiat els principis fonamentals dels detectors PET monolítics per a comprendre el seu comportament i limitacions. En primer lloc, s'han considerat les configuracions típiques de detectors monolítics basats en blocs de centellege continu acoblats a matrius SiPM planes; a més, també s'han evaluat i validat altres enfocaments nous. S'han desenvolupat dues metodologies principals, una basada en tècniques analítiques i una altra en algoritmes d'Aprenentatge Profund, pel posicionament 3D de la interacció del fotó amb la finalitat d'augmentar el rendiment global del detector. Finalment, els mètodes proposats han sigut validats a nivell de detector però també en diferents escàners PET desenvolupats en i3M.

La present tesi es basa en un compendi dels articles més rellevants publicats en revistes revisades per parells pel doctorand i està organitzada de la següent manera. El Capítol I presenta una introducció al treball de tesi, compost per tres seccions: Imatge Mèdica, principis de la Tomografia per Emissió de Positrons i, Estimació de posició i calibració en detectors monolítics. El Capítol II conté els objectius específics d'aquesta tesi i les principals contribucions del candidat a aquest camp. Aquest capítol també inclou algunes metodologies i resultats recents que encara no han sigut publicats. El Capítol III col·lecciona una còpia dels quatre articles publicats seleccionats pel compendi, en els quals el candidat és el primer autor [1]-[4]. En el Capítol IV es discuteixen els principals resultats i conclusions aconseguits durant la tesi. Finalment, el Capítol V presenta la discussió d'aquesta tesi, resumint les principals contribucions i destacant els assoliments científics.

I Introduction

Chapter I is composed of three sections. In Section 1 the most important Medical Imaging techniques are outlined, focusing on anatomical and functional imaging systems, as well as on multimodality ones. PET technique is introduced in Section 2, including a description of its principle, operational characteristics and the main aspects of PET detectors. Finally, the position estimation methods and impact calibration procedures used in monolithic-based PET detectors are described in Section 3.

1 Medical Imaging

1.1 Medical Imaging history

Invasive medical procedures such as surgery or endoscopy allow to observe inside the body by accessing it directly (see Figure 1 left) [5]. These methods might cause patient discomfort, high costs, and a small risk of potentially life-threatening complications [6]. In contrast to this, Medical Imaging techniques generate visual representations of the human body, allowing the clinicians to "see inside the patient" and observe all the relevant structures and processes. The basic principle of Medical Imaging techniques consists of using a source of energy that can penetrate the human body and interact with the different tissues of the body, creating signals (see Figure 1 right). These signals are measured using detectors compatible with the source of energy and then, mathematically manipulated to create an image (see Figure 1 right) [7].

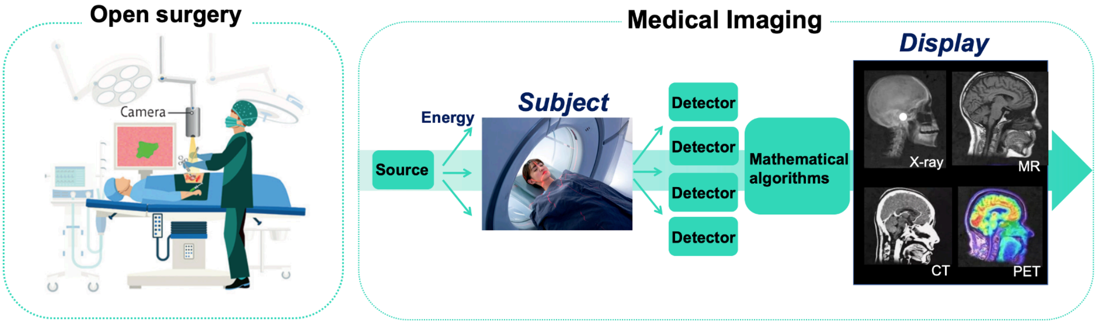

Figure 1.- Left, open surgery picture. Right, basic principle of Medical Imaging techniques.

Medical Imaging systems are typically classified as anatomical (morphological, structural) or functional [8]. Figure 2 shows the main techniques of each modality. While, anatomical techniques generate detailed representations of the anatomy of the patient, functional techniques provide information about the behavior of different organs at cellular and molecular levels (see Figure 3) [7][9][10].

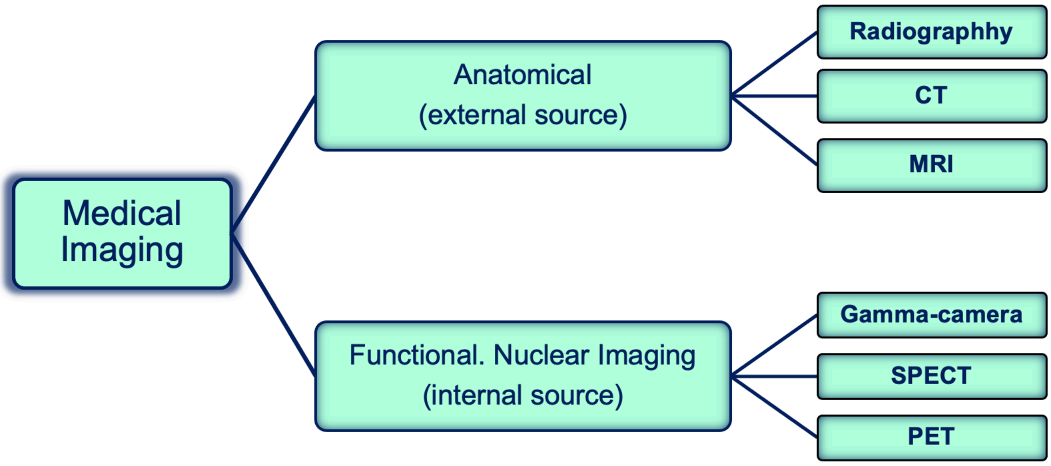

Figure 2.- Most relevant Medical Imaging techniques and type of emission sources used.

The first published medical image was a radiograph of the hand of Roetgen´s wife in December 1895 [11]. Roentgen discovered *x*-rays while he was investigating with a Crooke's tube, that is the predecessor of today's *x*-ray tube [5]. Several decades later, in 1972, Hounsfield presented the first Medical Imaging system named Computed Tomography (CT), based on a *x*-rays tube that irradiates the subject from many different angles providing 3- dimensional (3D) images of the internal structures of the body [12]. Following CT, the 1980s witnessed the appearance of clinical Magnetic Resonance Imaging (MRI), which is of particular relevance for imaging patients because it does not require the use of ionizing radiation. CT and MRI techniques are typically located at the radiology departments and they are the principal imaging techniques of human anatomy. However, in diagnosing and staging of diseases or monitoring the response to therapy, anatomical imaging does not always provide complete information since functional or metabolic changes can and occur even in the absence of a corresponding anatomical correlate.

Nuclear Medicine techniques initiated in the late 1940s to image functional processes by using radioactive tracers (radionuclides) and gamma-ray (γ-ray) detectors [13][14]. The first human tomographic images with positron-emitting isotopes were presented in 1972 [15][16], and then Single Photon Emission Computed Tomography (SPECT) and PET were widely established in the field of medical imaging [14]. Recently, Medical Imaging has also become a crucial tool in the early detection and risk stratification of the COVID-19 disease [17].

1.2 Anatomical imaging

Anatomical imaging encloses all techniques that allow to visualize internal structures of the body, such as bones, organs or tissues. The main anatomical imaging techniques are summarized in the following paragraphs.

1.2.1 Radiography

Radiography is a diagnostic technique that uses ionizing electromagnetic radiation, such as *x*-rays, to image the structure of objects. *X*-rays are high energy electromagnetic radiation with wavelengths in the range of 0.01 to 10 nanometers (123 to 0.123 keV, respectively), thus can penetrate solids and ionize gases. In Medical Imaging, the generated *x*-rays pass through the body where they are attenuated accordingly to the density and atomic number of the different tissues thus, creating a transmission intensity profile. This intensity distribution is revealed using a scintillation material, which converts the *x*-rays into visible light. Finally, the scintillation light is detected either on a sheet of photographic film, a camera, or by solid-state detectors to generate a 2D projection image of the 3D subject [5].

1.2.2 Computed Tomography

CT is an *x*-ray imaging modality in which an *x*-ray source rotates around the object. The *x*-rays that pass through the object are detected on the opposite side. The detected projection data at different angles are sent to an acquisition system returning 3D tomographic images (see Figure 3 left) [18].

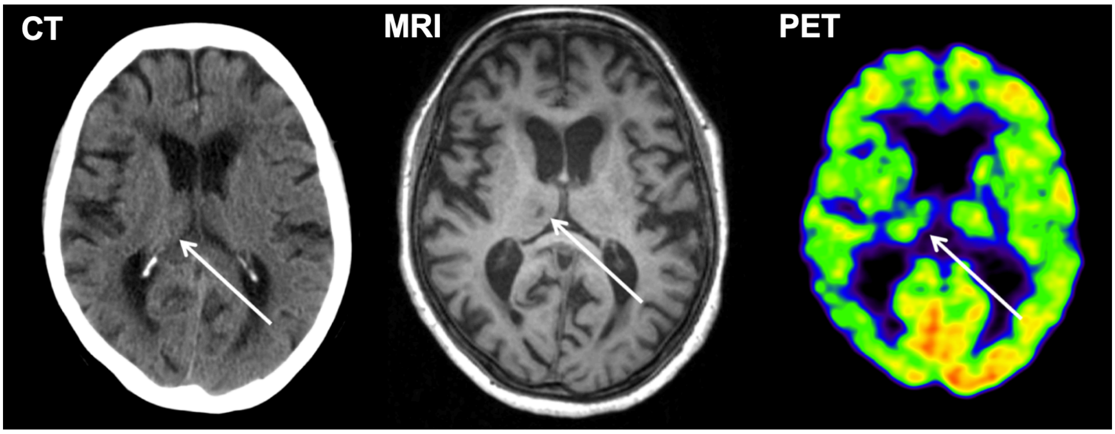

Figure 3.- Brain imaging using different Medical Imaging techniques. From left to right, CT, MRI and PET images. Extracted from [9].

1.2.3 Magnetic Resonance Imaging

MRI is a non-invasive imaging modality which produces 3D tomographic images of physical and chemical characteristics of internal organs of the human body from externally measured Nuclear Magnetic Resonance (NMR) signals (see Figure 3 center) [19]. Atoms with an odd number of protons and/or of neutrons, such as hydrogen, infer a nuclear spin angular momentum and therefore exhibit the NMR phenomenon. Hydrogen with a single proton is the element most abundant in biological specimens, and, for that reason, MRI primarily images the NMR signal coming from the hydrogen nuclei [20].

If no external magnetic field is applied, the spins are randomly oriented due to thermal motion and the net macroscopic magnetic moment is zero as shown in Figure 4. When the subject is exposed to the main magnet field of MRI system named B_0, the magnetic moment vectors tend to align in the direction of B_0 (referred to as the *z*- direction) to create a net magnetic moment *M* (see Figure

4). Also, the spins exhibit a resonance at a well-defined frequency, named the Larmor frequency. At equilibrium, the transverse component of *M* (i.e., the projection of *M* in the *xy*- plane, namely, M_{xy}) is zero (see Figure 4) [19]. However, when a radio-frequency (RF) field, called B_1, is applied, the spins are excited and tilt *M* away from the *z*- axis (the direction of B_0), creating a measurable (non-zero) transverse component M_{xy} as shown in Figure 4. When turning the excitation off, the relaxation backs to its equilibrium with the length of the magnetization vector not remaining constant over time. The time constant characterizing the return of the magnetization vector along the *z*- axis (longitudinal axis) is called T_1, while the time constant characterizing the decay of the transverse component is called T_2. Localizing the MR signal spatially to a region of interest requires the use of gradients, that is, additional spatially linear variations in the static field strength B_0. Faster or slower precession is detected as higher or lower MR signal, respectively. Thus, the frequency measurements can be used to distinguish MR signals at different positions in space and enable image reconstruction in 3D [19].

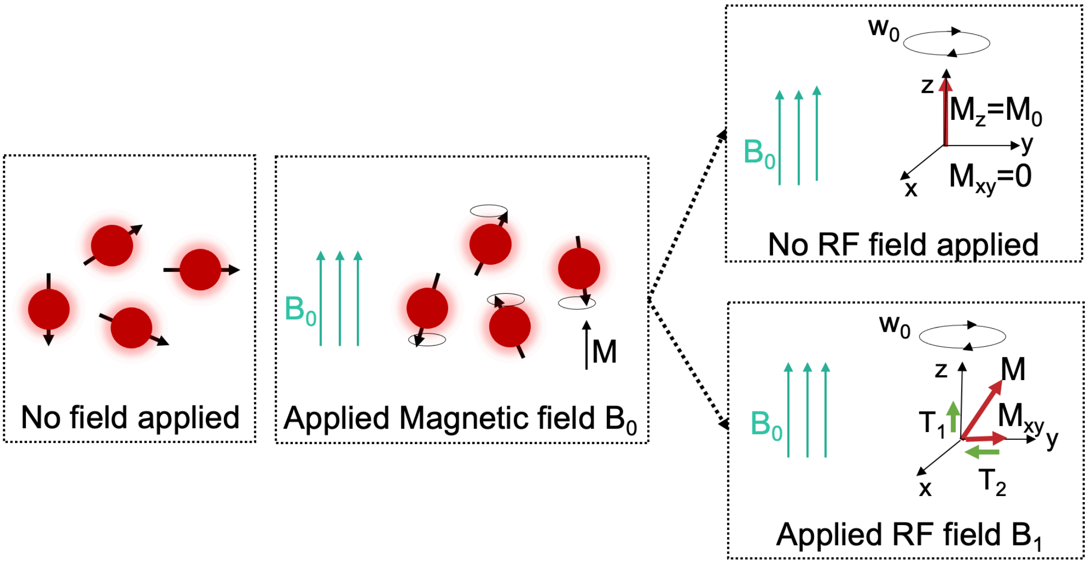

Figure 4.- Sketch of the MRI principle. From left to right, proton spins are randomly oriented; the spins aligned parallel or antiparallel with the field if the main field is applied (B_0); when RF field is applied the spins direction changes and when the RF field stops, the detected signal is modulated by the fundamental relaxation process, T_1 and T_2 decays. *M* is the net moment and the projection of *M* in the *xy*- and *z*- directions are named, M_{xy} and M_z, respectively.

MRI has revolutionized the diagnostic imaging field because provides unique soft tissues contrast and high spatial resolution without using ionizing radiation [21][22].

1.3 Molecular Imaging

Functional or Molecular Imaging (MI) is defined as the measurement, characterization and visualization of biological processes in vivo at molecular and cellular levels [23]. This modality enables to study processes while cells reside in their native environment with all molecular processes intact, therefore maintaining optimal and relevant biological context for MI measurements [24][25]. Herein, this functional information allows doctors to efficiently monitor and follow-up each treatment strategy. Furthermore, since diseases begin with microscopic cellular changes, MI have the potential to identify diseases at a very early stage, when treatment is most effective, and often before conventional morphological imaging techniques and other tests are able to reveal anomalies [26].

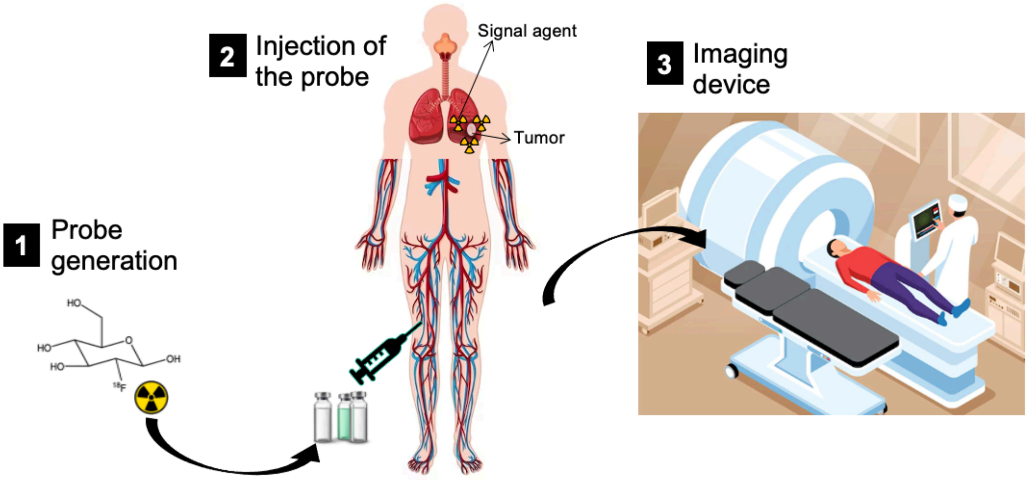

Figure 5.- Nuclear Medicine Imaging process.

MI involves signal producing/imaging agent (probe) that is introduced into the body, usually by injection or inhalation, and an imaging device that detects and uses the signal agent to generate images (see Figure 5). Probes, which are designed to accumulate in a specific organ or attach to certain cells, enable cell activity and biological processes to be measured and visualized [26]. Non-radioactive probes such as light or sound are also used in non-nuclear MI modalities, such as optical imaging and Focused Ultrasound (FUS) [26]. In Nuclear MI (NMI), the imaging agent is a radiotracer, also named radiopharmaceutical, that is, a substance in which one or more atoms are replaced by a small amount of radioactive material called radioisotope (see Figure 5) [26].


Gamma camera **SPECT/CT** **PET/CT**

Figure 6.- Most relevant Nuclear Medicine Imaging devices. From left to right, Gamma camera, SPECT/CT and PET/CT.

Radiotracers are introduced into the patient body producing a signal that can be detected by a gamma camera, a SPECT or a PET scanner (see Figure 6). They allow one to study physiological processes, the functionality of certain organs or the presence of tissues with altered metabolism and then, non-invasively diagnose and stage diseases (see Figure 3) [14][27]. The radiotracers employed in NMI applications are pharmaceuticals developed to follow specific metabolic pathways or for binding to precise receptor systems or molecules. They contain gamma- or positron-emitting isotopes. Even though there are many isotopes that could possibly be used in NMI applications, due to practical reasons only few of them are routinely employed in clinical practice [28]. A brief description of the three most relevant NMI systems is presented below.

1.3.1 Gamma camera

The Gamma camera is based on the detection of gamma radiation emitted from the single-photon-emitting radioisotopes injected to the patient. This technique is used to obtain planar images of radionuclides distribution.

Standard Gamma cameras have been used for decades in NM. These detectors are composed by a single scintillation crystal, an array of photodetectors and a collimator (see Figure 7 left) [24][29]. The collimator typically consists of a single plate made of lead or tungsten with drilled holes to allow only photons traveling parallel to the collimator holes to reach the crystal located behind the collimator. In the last decade, solid state detectors, such as Cadmium Zinc Telluride (CZT), have been also employed in these systems, due to their higher stopping power and, energy and spatial resolution compared to scintillator-based detectors [30].

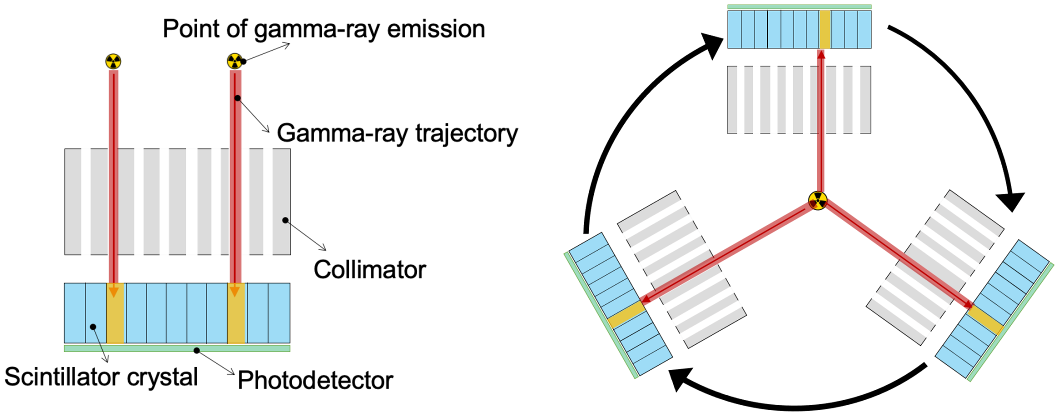

Figure 7.- Left, working principle of a standard Gamma camera; a gamma-ray reach the detectors passing through a collimator. Right, scheme of a rotating gamma camera-based SPECT system; the gamma cameras rotate around the subject acquiring cross-sectional images.

1.3.2 Single Photon Emission Computed Tomography

The SPECT technique is also based on the detection of gamma radiation emitted from single-photon-emitting radiotracers. However, in this technique, data is acquired at different angular orientations around the subject in order to provide 3D tomographic images. They require correction of the acquired data for non-uniform scanner responses and other signal-degrading effects, as well as mathematical reconstructions of thin transverse tissue-section images [31]. Although there are many possible scanner combinations, rotating gamma camera-based SPECT systems are by far the most common (see Figure 7 right).

Table 1 shows the most typical single-photon-emitting radionuclides used in Gamma camera and SPECT techniques.

SPECT images can in principle be quantitative, with voxel values representing the local activity concentration. However, in contrast to PET, this is often not the case because the corrections or effects such as scatter and attenuation more challenging in SPECT than in PET.

Isotope	Half-life	Mode of decay	Energy gamma (keV)
^{67}**Ga**	3.26 days	EC (100)	93; 185; 300
^{99m}**Tc**	6.0 h	EC (100)	141
^{111}**In**	2.8 days	EC (100)	171; 247
^{123}**I**	13.2 h	EC (100)	159

Table 1.- Most relevant characteristics of isotopes of interest used in Gamma camera and SPECT.

1.3.3 Positron Emission Tomography

PET is a quantitative tomographic imaging technique based on the administration of a positron-emitting radionuclide that, after beta plus (β^+) decay, emits a positron that subsequently annihilates with an electron generating two co-linear (approximately 180º) 511 keV gamma-rays (annihilation photons), that are detected in coincidence [31]. PET scanners consist of many detectors that surround the subject to be imaged and are designed to convert the annihilation photons into electrical signals that are fed to the electronic chain (see Figure 8). After a data reconstruction processes, PET images allow one to visualize the 3D spatial distribution of radiotracers to be quantitatively mapped in the body. Since this thesis is mainly focused on the PET technique, a detailed description about their physic and working principles are explained in Section 2.

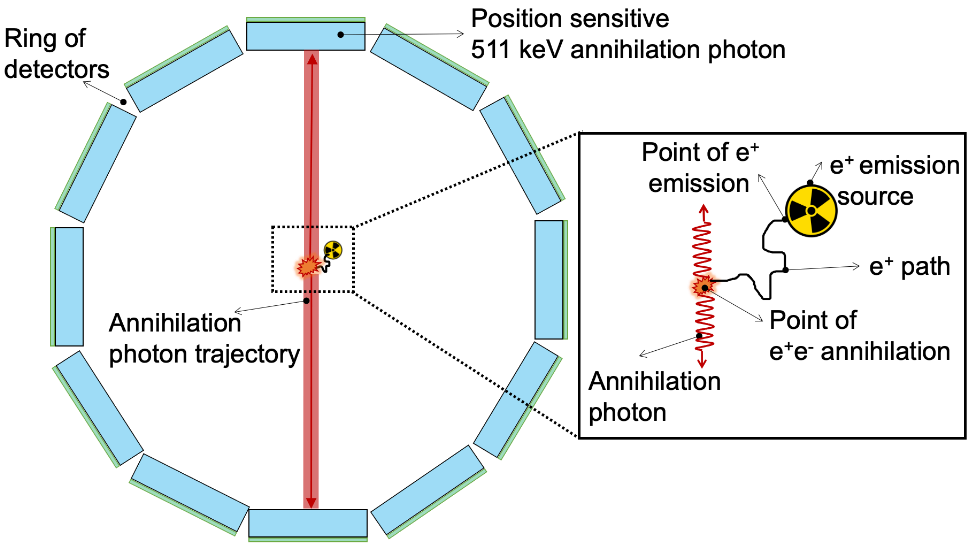

Figure 8.- Working principle of PET. After β^+ decay, the isotope emits a positron and, it annihilates with an electron, generating two annihilation photons that are emitted in opposite directions.

1.4 Multimodality imaging techniques

Multimodality imaging is defined as the image of a subject provided by the combination of two or more imaging modalities with the images being co-registered (see Figure 9). In the case of merging morphological and functional information, they allow for a better understanding of physiological mechanisms at molecular and cellular levels and, thus, improving diagnosis and therapeutic planning of a disease [31]-[36].

Prior to the advent of multimodality such as PET/CT or SPECT/CT scanners, co-registering images from two separate imaging devices was almost exclusively carried out through retrospective software registration of the volumetric datasets. However, this is challenging due to changes in patient pose or temporal changes between the two scans, leading to attenuation artifacts and diagnostic inaccuracies [33].

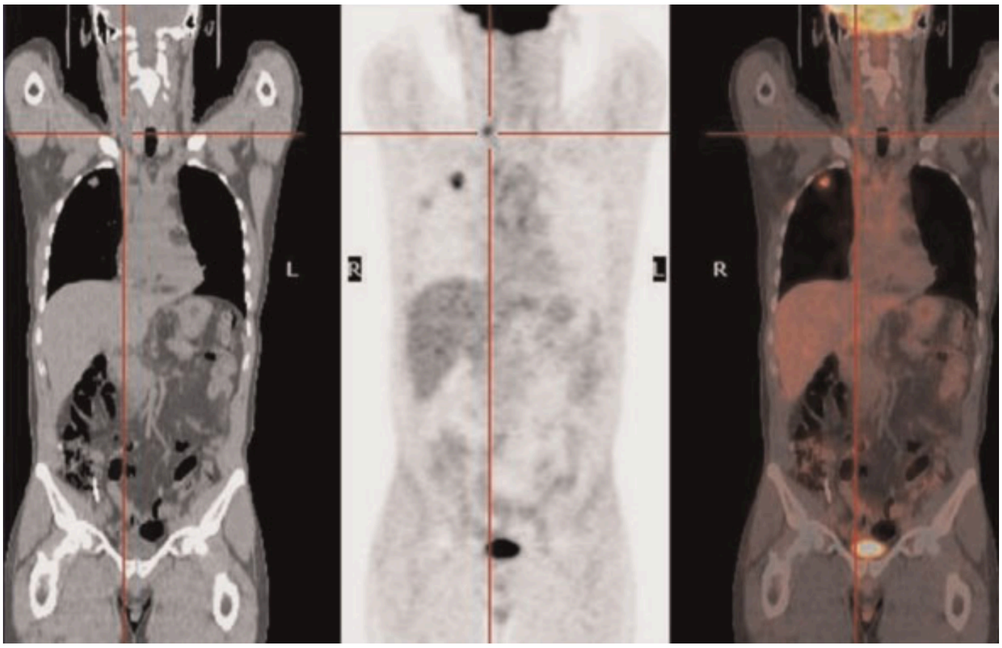

Figure 9.- Left, CT. Center, PET. Right, PET/CT images. Extracted from [37].

SPECT/CT and PET/CT acquisitions cannot be performed simultaneously due to technical challenges [33]. The approach followed by current hybrid PET/CT and SPECT/CT systems is based on a tandem configuration (see Figure 6), which enables sequential functional and anatomic imaging, without moving the patient off the bed. One of the main drawbacks occurring in the tandem configuration is that most human organs and tissues are in continuous motion leading to possible mismatches in the different images. Gating techniques have been developed to correct for cardiac or respiratory movements in sequential imaging acquisitions [38].

Another possibility is to simultaneously acquire PET and MRI data sets [39][40][41]. One of the main barriers for simultaneous PET/MRI systems is the technical operation challenges produced because the photosensors used in PET systems are influenced by the magnetic fields and the electronics for processing PET signals may generate interferences in the MR signal. Traditional PET detectors were based on Photomultiplier Tubes (PMTs) that are susceptible to even small magnetic fields and, therefore they are incompatible with the large magnetic fields associated to MRI. For this reason, the first PET/MR systems were installed also following a tandem (sequential) approach. However, the development of solid-state photosensors that are MR compatible made it possible to build simultaneous PET/MRI systems. These systems provide important benefits in the clinical practice [40].

2 Positron Emission Tomography

This section briefly describes the history of PET, followed by an exhaustive explanation on the principles of PET imaging. Finally, an overview of state-of-the-art PET scanners is presented.

2.1 PET history

The development of the PET technique demonstrates how advances in basic sciences can translate into benefits for human health. The timeline of its historical advances is shown in Figure 10 and summarized in the following paragraphs. For further information see references [42][43].

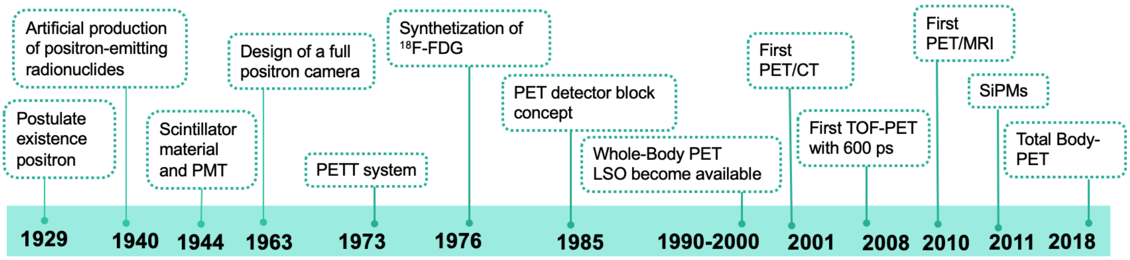

Figure 10.- Timeline showing some of the most historical breakthroughs during PET technique development.

The historical breakthroughs related to PET started in 1929 with the postulation of the existence of the positron by P. Dirac [44] and its experimental discovery by C. D. Anderson in 1933 [45]. After a year, M. Curie and F. Joliot discovered artificial radioactivity and later, investigators at the University of California made use of a cyclotron to produce positron-emitting radionuclides for the first time [12][46][47]. Lastly, two more important milestones were achieved, the production of scintillation materials for the detection of high energy photons [48] and the development of the PMTs [49]. These advances allowed F. R. Wren, M. L. Good and P. Handler from Duke University to employ positron-emitting radioisotopes and a coincidence detection approach for the localization of tumors [50]. Two years later, G. L. Brownell and W. Sweet built the first positron imaging device for imaging brain tumors at the Physics Research Laboratory of the Massachusetts General Hospital (MGH). The system was based on a pair of NaI detectors placed on either side of the head and operating in coincidence [51]. In the following years, S. Rankowitz and his team designed the first operative positron scanner based on NaI(Tl) cylindrical scintillation detectors assembled in a ring geometry [52] and, in 1963, the design of a positron camera device was published by H. O. Anger and A. Gottschalk [53][54].

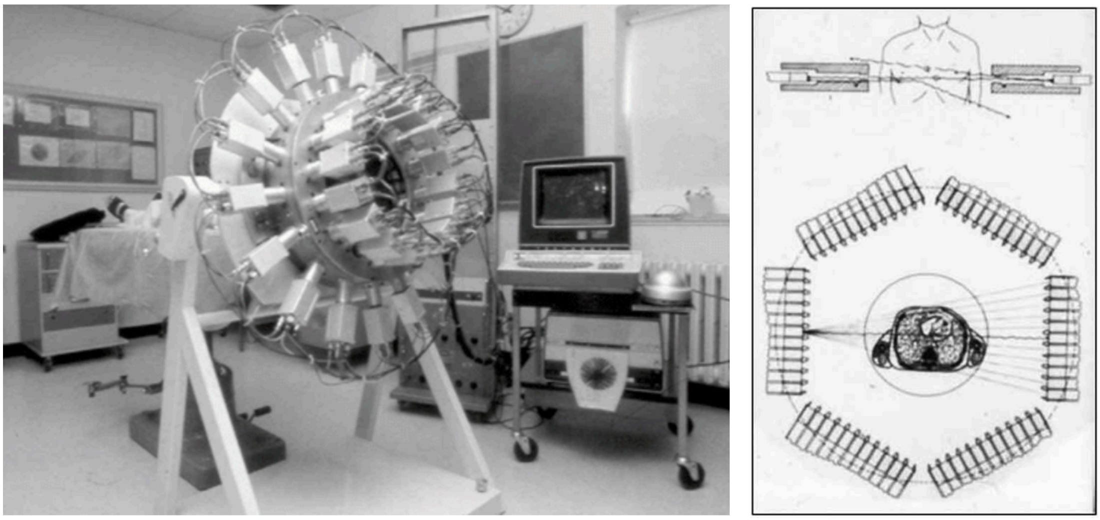

Figure 11.- Left, photo of the Positome system developed by Thompson and collaborators at Montreal Neurological Institute; original figure extracted from [55]. Right, first commercial PET, the ECATII, developed by EG & G ORTEC in Oak Ridge, Tennessee. Original figure extracted from [43].

In the early ‘70, great advances in PET instrumentation allowed launching the first PET scanners in the form of current devices [56]. C. J. Thompson from the Brookhaven National Laboratory built the so-called Positome. The system was designed for the measurement of regional cerebral blood flow and was based on a ring of 32 detectors (see Figure 11 left) [57]. Moreover, M. E. Phelps, E. J. Hoffman, N. A. Mullani and M. M. Ter-Pogossian from the University of Washington built the so-called Positron Emission Transaxial Tomography (PETT) [15][16]. Shortly after this development, M. E. Phelps and E. J. Hoffman started a collaboration with EG & G ORTEC. In 1973, Phelps and Hoffman proposed the PETT II based on a ring of 24 hexagonal detector arrays of NaI(Tl). Later, they refined the design in the PETT III increasing the number of detectors to 48 allowing to show the potentiality of PET in functional brain imaging [55][56]. With the experience from PET III, in collaboration with EG & G ORTEC, they build the first commercial PET scanner called Emission Computed Axial Tomography, ECAT (see Figure 11 right), also based on NaI(Tl) crystals conforming a ring [58][59]. In 1974 the Lawrence Berkeley Laboratory group suggested for the first time that Bismuth Germanate Oxide (BGO) could be an excellent crystal for PET.

Soon, BGO replaced NaI(Tl) and became the crystal of election for PET for the following 20 years, until Lutetium Ortho-silicate (LSO) became available in the late 1990s [55]. Between 1976 and 1980, advancements of PET cameras resulted on the construction of several scanners such as a single ring of NaI(Tl) [60] and its expansion to multiple rings using BGO crystals [61]. Development of Lutetium-based scintillators in the late 1990 and early 2000s leads to LSO and Lutetium–Yttrium Oxyorthosilicate (LYSO) crystals which report high stopping power and very good Coincidence Time Resolution (CTR) [62]. In parallel to the advancements in PET instrumentation, many efforts were dedicated to the improvement of radiotracers, such as the synthetization of ^{18}F-FDG in 1976 [63]. Currently, the ^{18}F-FDG is the most common radiotracer used in PET scans.

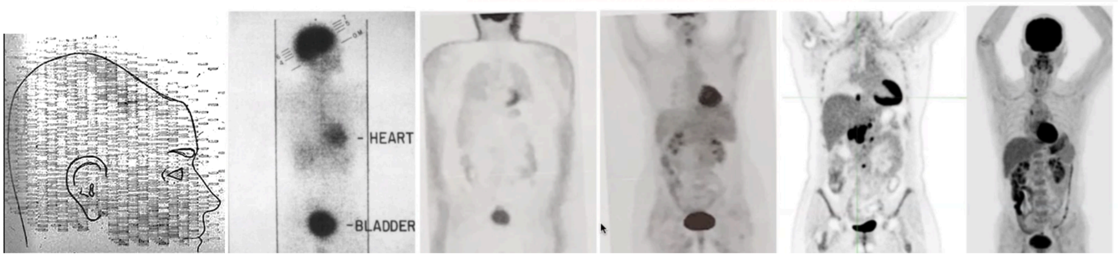

1st PET image 1953

1st FDG scan 1976

ECAT 931 1992

ECAT HR+ 2001

Vision PET 2018

Explorer PET 2018

Figure 12.- Evolution of PET imaging from 1976 to 2018.

In 2001, the introduction of multimodal imaging, in particular, the hybrid approach of PET/CT, resulted in the wide establishment and spread of the PET technique. Most commercial PET/CT systems have an axial length of 25 cm and are named Whole Body PET/CT (WB-PET/CT). They are based on pixelated scintillation crystals coupled to PMTs. The development of SiPMs allowed for more compact, lower cost, and higher performance detectors for PET/CT [66].

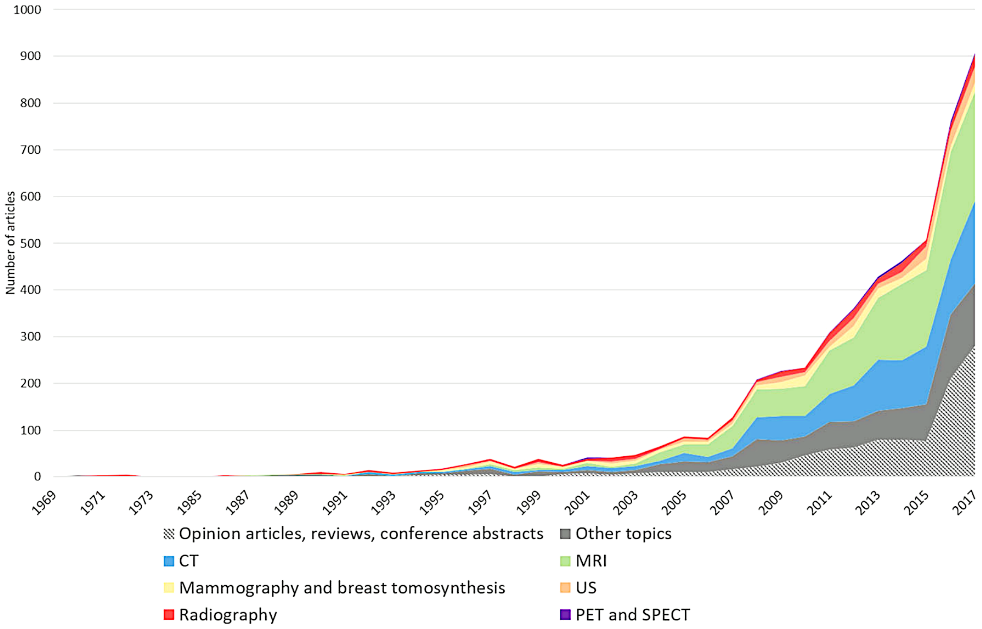

Figure 13.- Number of articles related to AI indexed on EMBASE obtained on April 24, 2018. Extracted from [73].

During the last years, PET systems based on faster scintillation crystals and electronic readout platforms have been developed [64][65], improving the timing capabilities and allowing the use of Time of Flight (TOF) information during the image reconstruction process. Moreover, Total Body-PET (TB-PET) systems that tend to cover the whole patient body by extending the axial Field of View (FOV) of typical WB-PET scanners have been proposed aiming to boost the sensitivity to maximize the acquired counts per unit of radiation dose injected to the patient. The first TB-PET system with 2 m axial length was announced in 2018 [69] and two commercial long axial FOV PET systems are nowadays available [68]. Figure 12 shows PET images acquired by different PET systems from 1976 to 2018, showing the significant progress that PET has undergone over the years.

Finally, while Artificial Intelligence (AI) has been investigated over decades for the interpretation of medical images [70], the interest in developing AI techniques for Medical Imaging applications is demonstrated by the increased number of publications on this topic (see Figure 13). There is an illustrative number of clinical applications both at scanner technology and, in the reconstruction process or post-processing step [71][72].

2.2 PET basics

2.2.1 Positron emission and annihilation

In PET imaging, the radiotracer injected to the patient contains a positron-emitting radionuclide, that is, an unstable isotope (parent isotope) that contains more protons than neutrons in their nucleus and decays following a β^+ process:

$$ {}_{Z}^{A}X \rightarrow {}_{Z-1}^{A}X' + e^{+} + \nu_e \tag{1}$$

In β^+ decays, a proton is transformed to a neutron, ejecting a positron -the antimatter conjugate of an electron with the same mass but positive charge- and an electronic neutrino (ν_e) (see Figure 14). These positrons are emitted from the nucleus with different energies generating a continuous spectrum with a specific maximum value (E_{max}) and mean value (E_{mean}) that is characteristic of the parent isotope (see Table 2). Once emitted from the nucleus, the positron propagates through the surrounding material undergoing scattering interactions, changing its direction and losing kinetic energy [74]. Within a short distance, the positron comes to rest and combines with an electron from the surroundings. This distance, named as positron annihilation range, is dependent on the energy of the positron and is typically ~1 millimeter (see Table 2). The combination of a positron and an electron results in the annihilation of both particles and the generation of two 511 keV γ-rays, called annihilation photons, in opposite directions (~180°) because the net momentum when the annihilation occurs is close to zero since the positron and electron are almost at rest. This process is shown schematically in Figure 14. Higher order annihilation, in which more than 2 photons are emitted, is also possible, but only occurs in about 0.003% of the cases [75][76].

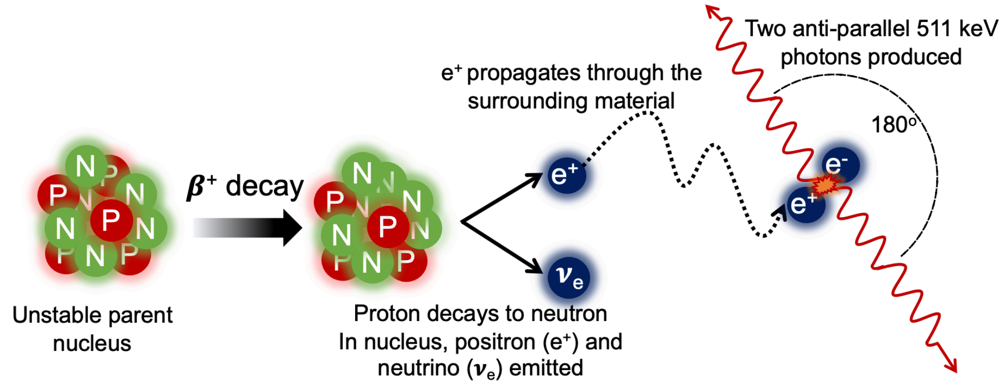

Figure 14.- Sketch of the β^+ decay scheme. A proton decays to a neutron in the nucleus emitting an electron neutrino and a positron that annihilates with an electron of the surrounding generating two back-to-back γ-rays of 511 keV each.

The most used positron-emitting radionuclides in academic and clinical PET are described in Table 2, including their more relevant applications.

Isotope	**Half-life**	**E_{max} (MeV)**	**E_{mean} (MeV)**	**Mean e^+ range in H_2O (mm)**	**Tracer compound**	**Application**
^{11}C	1222 s	0.96	0.39	1.1	Methionine	Protein synthesis
^{18}F	110 min	0.64	0.25	0.6	Fluordeoxyglucose (FDG)	Glucose metabolism
					Dluoromisonidazole (FMISO)	Hypoxia
^{13}N	10 min	1.20	0.49	1.8	Ammonia	Blood perfusion
^{68}Ga	68 min	1.89	0.89	2.9	Prostate-specific membrane antigen (PSMA)	Prostate cancer

Table 2.- Most relevant characteristics of positron-emitting radionuclides of interest used in PET.

2.2.2 Coincidence detection

The two back-to-back 511 keV annihilation photons are measured by PET detectors placed around the subject (see Figure 15). The typical role of a PET detector is to efficiently stop the incoming 511 keV annihilation photons and accurately measure their interaction position, energy and timestamp (time information of the arrival event).

Coincidence detection involves the association of two detected annihilation photons in two opposite PET detectors within a defined time coincidence window, usually in the nanosecond order. Moreover, if the measured energy of some of the detected photons is not within a 20-30% energy window around the 511 keV peak, the coincidence event is typically discarded. Coincidences that pass both the energy and time coincidence windows are used to define a Line of Response (LOR) joining the coordinates of the two events involved in the coincidence. The

LOR is assumed to intersect the unknown location of the annihilation event (see Figure 15).

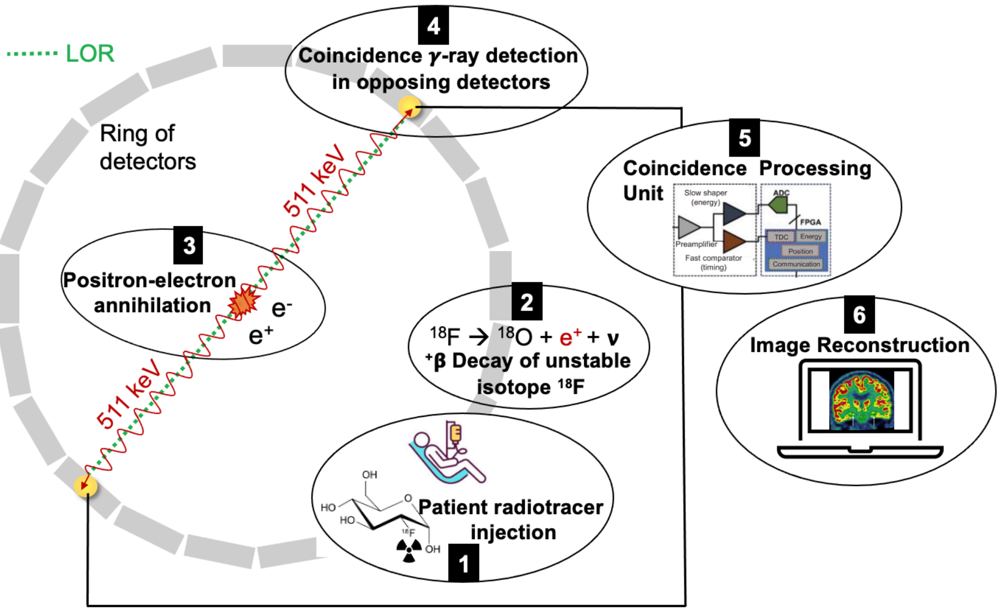

Figure 15.- Sketch of the operation principle of PET imaging.

In a typical PET exploration, millions of these annihilation photons pairs are emitted and the more efficient approach for detecting them consists of building a complete ring of detectors around the patient (see Figure 16). Many projections are acquired at the same time. The maximum angle between detectors (with respect to their perpendicular direction) for which coincidences are allowed defines the useful FOV of an annular scanner (see Figure 16).

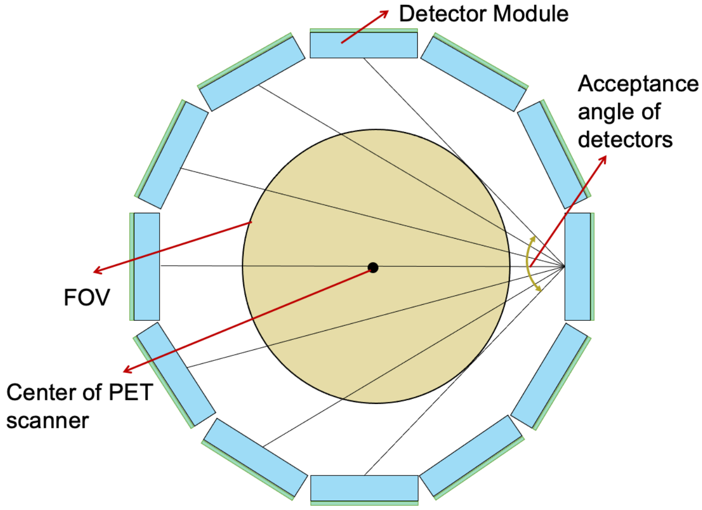

Figure 16.- Sketch of a PET system composed of a ring of detector modules. The FOV of the scanner is defined by the acceptance angle of the detectors.

By collecting all possible LORs around the object (full angular coverage) and assuming a uniform emission probability along the full length of the LORs (and within the object boundary), reconstruction algorithms are employed to generate an image showing the 3D radiotracer distribution in the subject (see Figure 15).

As described below, there are several effects in PET systems related to physical processes or to the detection coincidence method, that might result in a degradation of the reconstructed image quality.

2.2.2.1 Physical effects limiting image performance

i) *Positron range*. The positron range is defined as the distance travelled by the ejected positron before annihilating (see Figure 14). This distance depends on the initial energy of the positron (see Table 2). From the perspective of PET imaging, the positron range is the quantity that directly degrades the spatial resolution, and can be measured as the perpendicular distance from the positron emission site to the line defined by the two generated annihilation photons [77][78].

ii) *Non-collinearity*. The two back-to-back annihilation photons will not be exactly emitted at 180° and will instead be emitted with a distribution of angles around 180° [79]. This is because positrons annihilate before losing all their momentum which translates into a small deviation of about ±0.25° from the expected back-to-back emissions [80]. After detecting the annihilation photons, PET assumes that the emission of the two annihilation photons was exactly back-to-back, resulting in a small error in assigning the true LOR. This phenomenon tends to degrade spatial resolution as detector separation increases [79].

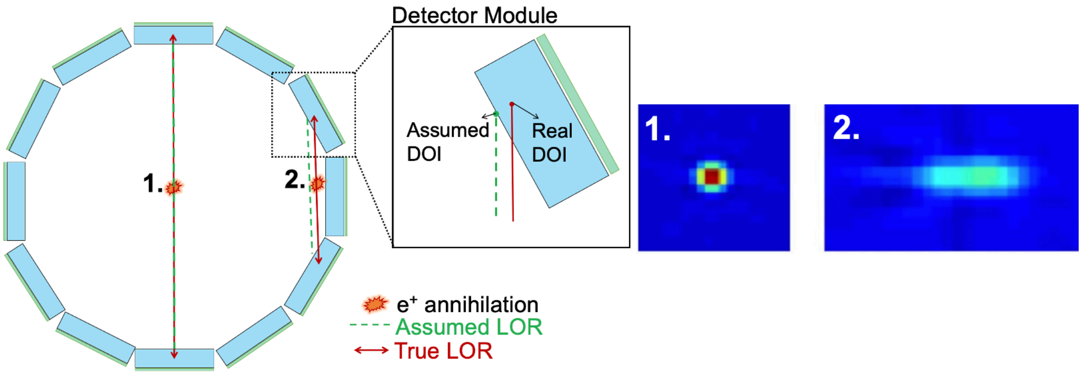

Figure 17.- Left, illustration of parallax error. The continuous red line represents the true LOR, while the dash green line shows the LOR that would be assigned in the absence of DOI information. Right, reconstructed point source at the center and at the edge of a PET scanner. The spatial resolution is degraded when moving radially form the center to the edge. Adapted from [86].

iii) *Parallax error*. This effect is related to the uncertainty of the annihilation photon interaction depth coordinate in the scintillation crystal. When the annihilation photons enter at an oblique angle, the photon interaction position will be different from the point of entry in the crystal (see Figure 17) [81][82]. If the Depth of Interaction (DOI) is not considered an incorrect LOR will be assigned causing parallax error, thus degrading the system spatial resolution when moving radially away from the center of the system (see Figure 17) [82]-[85]. The parallax error increases for LORs placed closer to the edge of the FOV, thus, this effect tends to increase for small diameter PET systems. Commercial clinical PET scanners do not estimate the DOI, and therefore it is assigned as a constant value for all events based on the attenuation coefficient of the detector crystal, or simply defined as the position on the face of the crystal [81]. If the PET detector provides DOI information, this can be included to address the parallax error and provide homogeneous spatial resolution across the entire FOV [87].

iv) *Detector intrinsic resolution*. The detector intrinsic resolution refers to the uncertainty in obtaining precise impact position and energy; and is independent of the previous effects. This quantity is limited by several factors, such as the scintillation material, the crystal thickness, the surface crystal treatment or, the photodetector type and size, to name but a few.

2.2.2.2 Image degradation caused by coincidence detection method

A coincidence is generated when two annihilation photons are detected within the same time coincidence window and, is considered as a true coincidence if they have not interacted before being detected. In ideal PET systems, only true coincidences would be encountered. In real systems, due to different factors, true coincidence data are contaminated with undesirable events, which includes scatter, random and multiple coincidences (see Figure 18).

i) *Scatter coincidence.* It refers to a coincidence detection in which one or both annihilation photons have been scattered and thus their trajectory is modified generating an incorrect LOR. This phenomenon increases in areas with higher radiotracer concentration, producing inhomogeneous noise that degrades locally the image contrast.

ii) *Random coincidence.* It refers to a coincidence detection in which both gamma-rays are detected within the defined time coincidence windows and with the appropriated energy but, each of them comes from different annihilation process. This effect introduces homogenous noise to the image background.

iii) *Multiple coincidence.* It refers to a coincidence detection of more than two annihilation photons in different detectors, making it impossible to generate a LOR and causing event mispositioning.

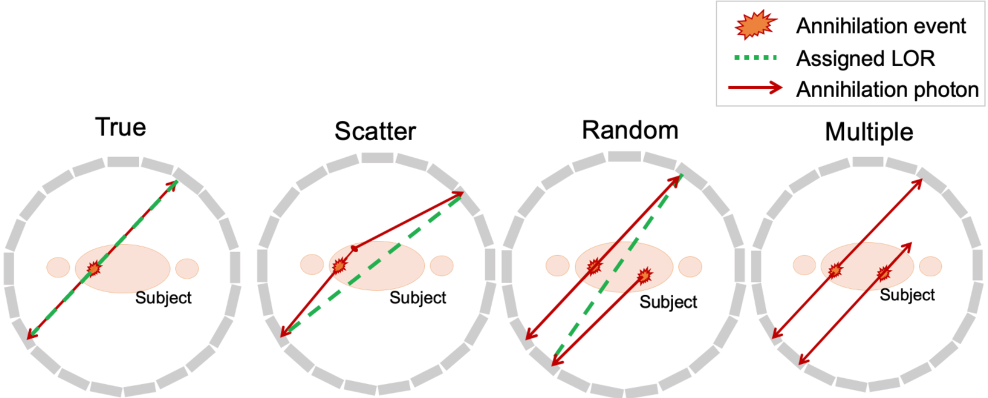

Figure 18.- Sketch of the types of coincidences detected in PET. From left to right: true, scattered, random and multiple coincidences.

2.2.2.3 Role of Time of Flight (TOF)

In PET systems without TOF information, all points (voxels) along the LOR are equally probable to allocate the annihilation event, see Figure 19 left. However, in TOF-PET scanners, the difference in the arrival time of the two annihilation photons is measured, and thus, a probability function along the LOR is used during the reconstruction process, which helps in better localizing the true annihilation point along the LOR (see Figure 19 left) [88][89][90]. This function follows a Gaussian distribution centered on the position provided by the arrival time differences of the detected annihilation photons with a width corresponding to the system Coincidence Time Resolution (CTR), see Figure 19 left. Thus, only a segment of the LOR constrains the probable annihilation point.

The main benefit resulting from accurate TOF information is the boosting of the image Signal to Noise Ratio (SNR), see Figure 19 right. Moreover, TOF information makes it possible generating images less affected by statistical noise and with higher Contrast to Noise Ratio (CNR). Therefore, a TOF-PET image is equivalent to a non-TOF PET image obtained with a large number of counts [90]. Herein, the measured sensibility in TOF-PET is amplified and often defined as effective sensitivity. This virtual increase in the effective sensitivity improves the PET diagnostic [90][91][92].

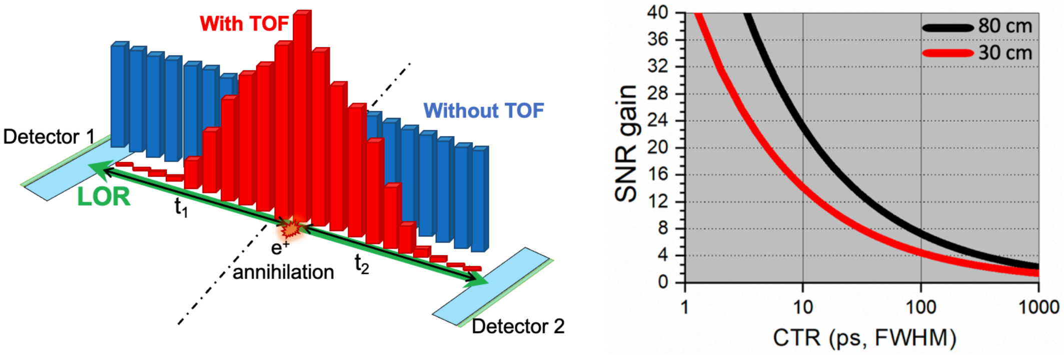

Figure 19.- Left, annihilation event location within the LOR with and without TOF information. Right, improvement in the SNR compared to non-TOF scanner as a function of the CTR, for 80 and 30 cm scanner diameter.

2.3 Physical principles

The main goal of the detection process is stopping the incoming 511 keV annihilation photons and provide electrical signals for the determination of the time, energy and 3D position of the photon interaction. Standard PET detectors use a scintillation crystal, that efficiently stop and convert the annihilation photons into low energy scintillation photons (i.e., optical photons), coupled to a photosensor, that converts those optical photons to an electrical signal and, connected to an electronics chain for signal processing (see Figure 20). The main process involved in the detection process are described below.

2.3.1 Scintillator

When the annihilation photons enter the scintillation material, they can be either transmitted or attenuated. The number of γ-rays that pass-through matter is given by a Lambert's law:

$$N(x) = N_0 e^{-\mu x} \tag{2}$$

where $N(x)$ is the number of photons that travel through the scintillation material without interacting, N_0 the initial number of photons, x the scintillator thickness and μ the linear attenuation coefficient. The linear attenuation coefficient may be described as the probability per unit path length that a photon has an interaction with the absorber and it depends on the energy of the photon and the atomic number of the absorber. The attenuation coefficients μ for each element or material are determined experimentally.

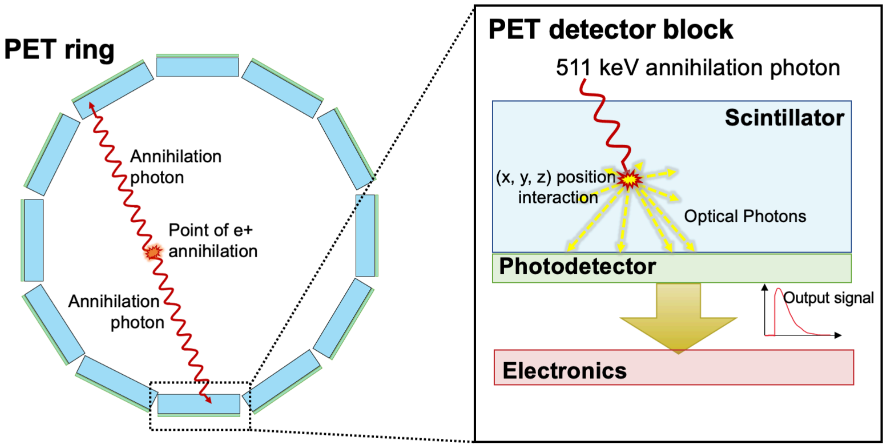

Figure 20.- Sketch of the operating principle of PET detector blocks conforming the PET system. The 511 keV annihilation photos are stopped and converted into optical photons and then to a detectable electrical signal.

Photons mainly interact with the atoms of the scintillation material by Photoelectric or Compton effects, and less likely pair production, depending on the effective atomic number (Z_{eff}) of the absorber and the incoming photon energy (see Figure 21). For PET applications, the scintillator is used to stop the 511 keV annihilation photons (see green arrow in Figure 21) [93].

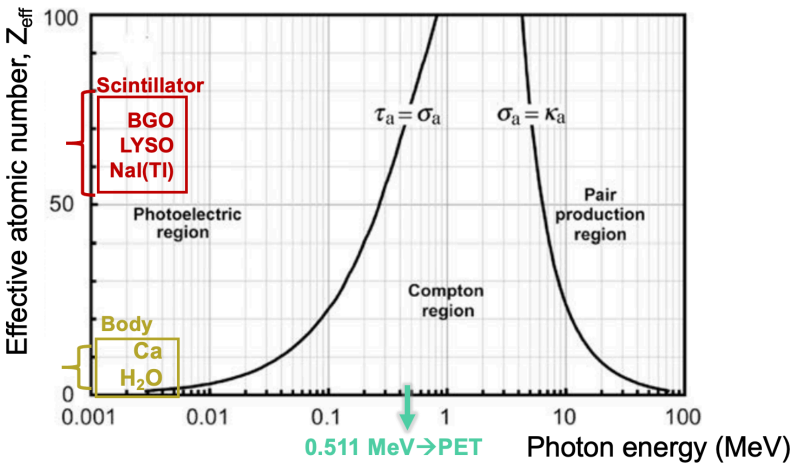

Figure 21.- Relative predominance of the three main interaction processes as a function of the photon energy and the effective atomic number of the material: Photoelectric effect, Compton effect and pair production. The black lines indicate when these interactions are equally probable. τ_a σ_a,κ_a are the Photoelectric, Compton and pair production attenuation coefficients, respectively. Adapted from [74].

In Photoelectric processes, the full energy of the γ-ray is transferred to an electron of the scintillation material and, thus, can be used to determine the photon energy (see Figure 22). However, γ-rays can also suffer Compton scattering, that is scatter by an electron losing some of its energy depending on the scattering angle [94]. In PET, the photoelectric effect should be favored, since this enables the detection of the whole amount of energy of the incident γ-ray in a single interaction and, therefore, scintillation materials with high atomic number are preferred.

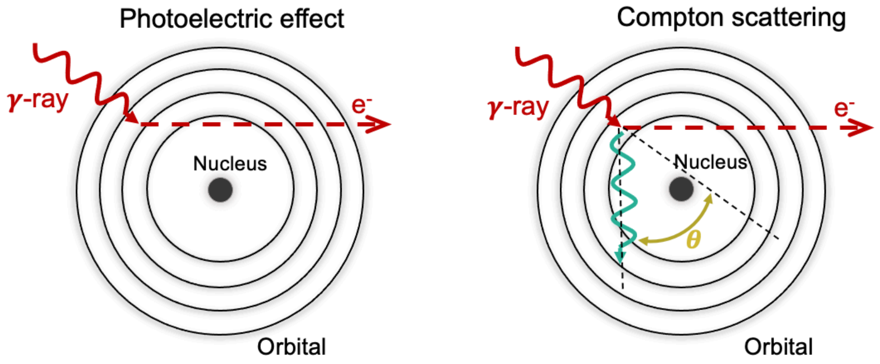

Figure 22.- Interaction of a 511 keV gamma-ray within an atom via Photoelectric interaction or Compton scattering.

Scintillation crystals have a discrete structure of bands, called valence and conduction, being the energy between them the gap (see Figure 23). When a γ-ray interacts within the crystal, via Photoelectric effect or Compton scattering, it deposits its energy exciting electrons from the occupied valence to the conduction band thus. Each of these interactions result in an electron-hole (e-h) pair formation. Such electrons return to the valence band emitting photons with an energy equal to the energy needed to generate the e-h pair. However, the emission of a photon is an inefficient process and furthermore, band gap widths in pure crystals are such that the resulting energy of the emitted photon is too high (ultraviolet range, UV) to lie within the visible range. For this reason, small amounts of impurities, called activators, are added to the crystal [95]. The energy structure of the overall crystal is not changed, just the energy structure at the activator sites. As a result of this process, the electron can de-energize, emitting less energetic photons that lie in the visible or near ultraviolet (NUV) range.

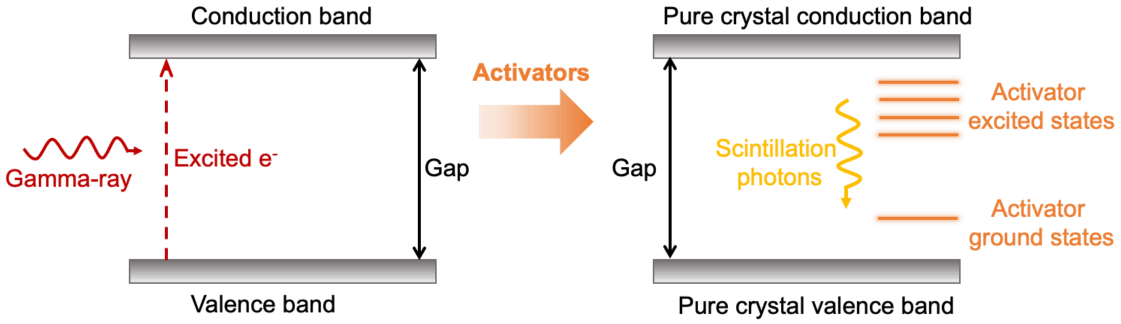

Figure 23.- Energy band structure for inorganic scintillation crystals. Left, pure crystal. Right, doped crystal.

The scintillation light is isotropically emitted and is proportional to the amount of energy deposited by the annihilation photons. The conversion of the incident 511 keV annihilation photon into optical photons has a certain efficiency and therefore, only part of the energy deposited in the crystal by the incident γ-ray is converted into low energy optical photons (the rest is converted into thermal energy via phonons) [95].

Scintillators can be solids, liquids or gases, with the solid ones being the most used in PET [93][96]. Moreover, scintillation materials can be divided into two main groups: organic and inorganic. Organic scintillators present a low effective Z_{eff} and are mainly used to track charged particles. However, inorganic scintillators, upon other properties, are more suitable to stop the 511 keV annihilation photons due to their higher Z_{eff} and therefore, are the most used in PET scanners. Regarding the choice of the scintillator, this strongly depends on the system configuration, however, some important requirements should be considered. The ideal scintillation material for PET applications should meet the following requirements [97]:

i) High *stopping power*, the attenuation coefficient of the absorbed radiation, for a given material thickness. It should be as high as possible to enhance the sensitivity of PET scanners.

ii) High Z_{eff}. For a fixed energy of the incident gamma-rays, its probability of interacting via Photoelectric instead of Compton scattering increases with Z_{eff}. As in the photoelectric interaction all the energy is deposited in a single interaction, the LOR connecting two opposite detectors is determined more accurately.

iii) High *Light Yield (LY).* The light yield is the number of scintillation photons (in the visible spectra) generated per unit of deposited energy. The higher the *LY*, the better the determination of the gamma-ray impact position and the better the energy resolution.

iv) *Proportionality of response.* The produced amount of scintillation photons should be proportional to the energy deposited by the incident radiation.

v) *Spectrum emission range* compatible with available photodetectors

vi) *Transparency.* The scintillator should be transparent to the wavelength of its own emission spectra. If not, the energy of the scintillation photon will be the same that the one needed to activate the e-h pair (UV emission). This is accomplished by adding impurities to the scintillator, as already described.

vii) *Short rise and decay times.* They are the timing characteristics of scintillation crystals and correspond to the time needed for a crystal to emit all optical photons for a given gamma-ray interaction. Should be as short as possible to improve the timing resolution and avoid pile-up events, hence minimizing dead time. Scintillation crystals with excellent timing characteristics are preferred for TOF-PET detectors.

viii) *Practical aspects,* such as, cost and accessibility, among others.

Despite the numerous scintillator types available, only some of them account for the specifications demanded by PET. The most commonly inorganic scintillators used in PET are presented in Table 3, including their main characteristics.

Scintillator material	Activator	Z_{eff}	Refractive index	ρ (g/cm^3)	LY (ph/MeV)	Decay time (ns)	μ @511keV (cm^{-1})	λ (nm)
NaI(Tl)	Talium	51	1.85	3.7	41000	230	0.35	410
BGO	-	74	2.15	7.13	9000	300	0.95	480
GSO	Cerium	59	1.89	6.7	9000	56	0.698	440
LaBr$_3$	Cerium	46.9	1.9	5.06	42500	16	0.476	380
LSO	Cerium	66	1.81	7.4	29000	40	0.866	420
LYSO	Cerium	63	1.82	7.1	32000	41	0.83	420

Table 3.- Main properties of inorganic scintillation crystals used in PET applications. Data extracted from [97].

Different scintillator geometries have been also investigated but, the two main configurations used in PET detectors are arrays of pixels and monolithic crystals, see Figure 24 left and center, respectively.

Pixelated crystals comprise a matrix of individual small scintillation elements optically isolated, while monolithic scintillators consist of a large single piece of scintillation material and therefore, there are no inter-element gaps [98][99]. A hybrid approach between the pixelated and monolithic arrangements, the so-called semi-monolithic detector, has gained interest during the last years [100]-[105]. They are also named slabs and have one dimension like a crystal pixel, and the other longer one following the monolithic scintillator approach (see Figure 24 right). Advantages and disadvantages of each configuration are described below.

2.3.1.1 Pixelated scintillators

Commercial clinical and most preclinical PET systems are based on pixelated crystals [107][108]. The most traditional way of obtaining these pixelated blocks is mechanically cutting a big block of scintillation material from an ingot into smaller pieces (pixels), treating the individual pixel surfaces to influence the reflection properties and light extraction and lately, assembling them in a matrix. An alternative production procedure is using lasers that modify the optical properties of the scintillator, the so-called Laser Induced Optical Barriers (LIOB) [109].

Pixelated detectors have shown to provide excellent timing resolution and it is expected to obtain sub-100 ps timing resolution at the system level within the next years [110][111]. However, in crystals with high aspect ratio the photons reflect on the pixel walls many times before reaching the photodetector (see Figure 24 left) and thus the light collection efficiency reduces, deteriorating their performance. Furthermore, long and thin crystals lead to larger variance of the photon transit times resulting in a worsening of the timing capabilities [112].

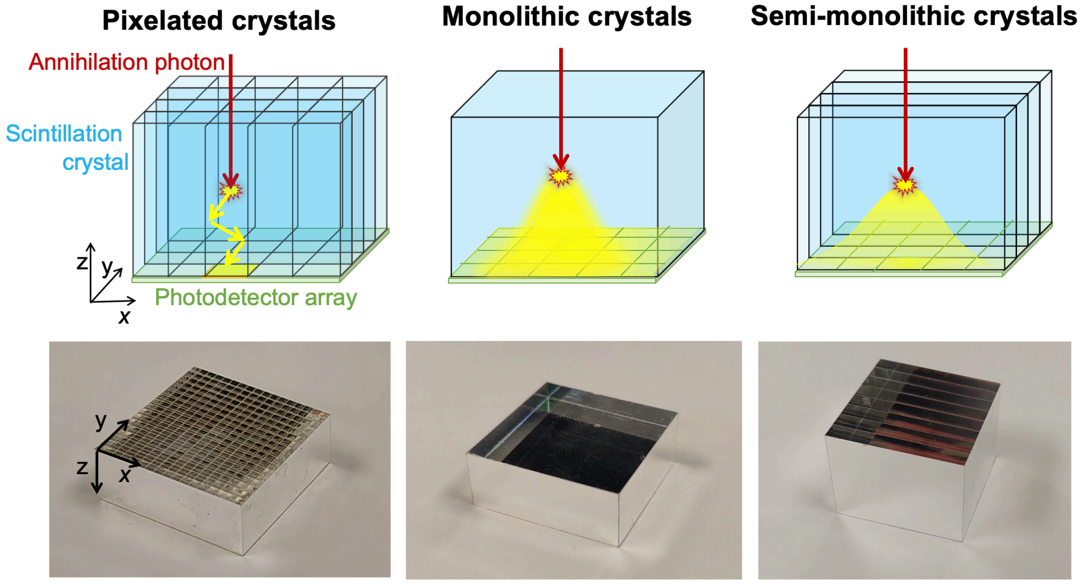

Figure 24.- Top, drawing of a pixelated (left), monolithic (center) and semi-monolithic (right) detector. Bottom, photograph of each scintillation crystal design. In all cases, the lateral and top sides were coated with Enhanced Specular Reflector (ESR).

The pixelated scintillator is coupled to a photodetector matrix either on a one-to-one or many-to-one arrangement [110]. Regardless of the configuration, the spatial resolution is limited by the pixel size. In the one-to-one configuration, the *x*- and *y*- photon impact coordinates, can simply be assigned to one of the discrete pixels in which the interaction occurred. However, mathematical algorithms are required in the many-to-one configuration which introduce pixel decoding errors that reduces spatial resolution [113].

Pixelated crystals do not inherently exhibit DOI decoding. Different methods have been proposed to retrieve DOI information in pixelated-based PET detectors, such us multi-layer detector, side-readout or poswich approaches but most of them usually require increasing production costs since extra hardware materials or more expensive crystal cutting and assembling processes are needed [114]-[116].

Regarding sensitivity, the refractive material usually included between pixels reduces the detector packing fraction and create dead areas. The smallest the pixel size, the deader areas are created, thus decreasing the detector sensitivity.

Regarding cost, decreasing the pixel size to improve spatial resolution increase the cost of detectors. Pixels as thin as 0.5 mm have been already manufactured [117]. In general, prices for crystal arrays with pixel sizes below 1.5 mm are about three times more expensive than monolithic-based detectors of similar volume.

2.3.1.2 Monolithic scintillators

In monolithic-based PET detectors, the scintillation light spreads inside the crystal volume and is tipically measured at one crystal side by a matrix of photodetectors (see Figure 24 center). This configuration provides higher detection sensitivity compared to pixelated crystals. Furthermore, the scintillation light transport is generally more efficient than in pixelated crystals due to the reflections that the scintillation photons undergo before reaching the photodetector.

Regarding timing capabilities, monolithic-based detectors could theoretically provide better timing performance than pixelated ones, since the generated optical photons might not suffer internal reflections inside the crystal pixel thus avoiding time delays. However, the spreading of scintillation light reduces the number of those photons collected at each single photodetector element. Several methods have been already implemented to estimate the photon interaction time using the multiple timestamps of each annihilation photon impact, such as a deterministic method that does not need calibration measurements [118], or statistical [119] and Machine Learning based methods [105][120] that make use of calibration data to derive the photon interaction time.

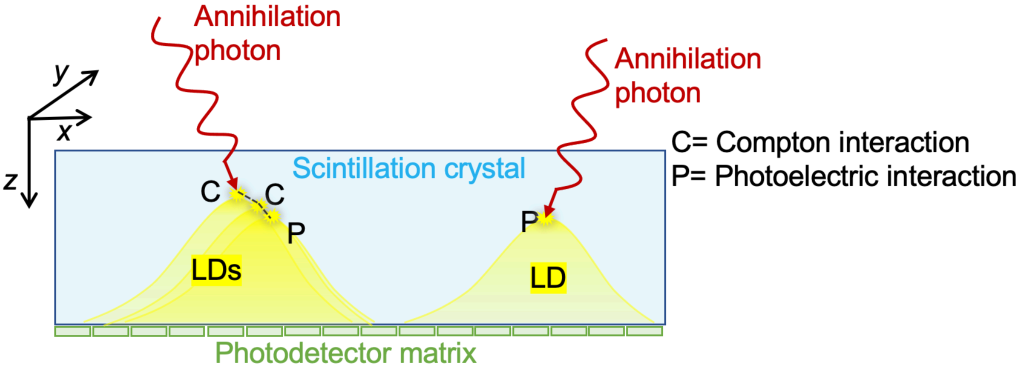

Figure 25.- Sketch of the light distributions generated in a monolithic crystal for an annihilation photon impact in which all its energy is deposed by Photoelectric interaction and for an annihilation photon impact in which its energy is deposed with two preceding Compton interactions.

Regarding spatial capabilities, the intrinsic resolution reported by monolithic crystals, is no longer limited as in the case of crystal arrays. The *x*-, *y*- and *z*-annihilation photon interaction coordinates can be estimated from the collected Light Distribution (LD) [98], that is, the intensity of the light signals acquired by each pixel of the photosensor. It should be emphasized that annihilation photons interact with the scintillation material depositing their total energy after undergoing few interactions (Compton scatter) followed by a photoelectric one. The occurrence probability of the photoelectric interaction is in the range of ~60-70% depending on the crystal used. These processes challenge to accurately determine the position of interaction since their LD overlap (see Figure 25). Moreover, LDs are strongly influenced by the so-called edge effect produced by the absorption and/or reflection of many scintillation photons in the crystal walls of the monolithic block (see Section 2.3.2) [1][98]. Although this effect produces a degradation of the spatial resolution in these regions, it can be compensated by using sophisticated position estimation algorithms and calibration procedures. These calibration procedures eventually employ timing consumption and complex mathematical algorithms, as well as hardware setups, resulting in one of the main challenges of using monolithic-based PET detectors. A detailed description of different methodologies published in the literature to accurately determine and calibrate the 3D impact position without significantly increasing processing time, will be reported in Section 3 of Chapter I. During this PhD thesis new strategies for positioning and calibration methods have been proposed, implemented and validated (see Section 4 of Chapter II)

PET scanners are typically built using a modular configuration, that is using multiple detector modules arranged in a cylindrical configuration to maximize detection area and geometrical sensitivity (see Figure 26 left). In this configuration, there are always unavoidable physical gaps between detectors in both axial and transaxial planes. These gaps cause losses in the system ability to detect annihilation events, thus reducing the system sensitivity. Moreover, modular detectors have edges, and as we have previous explained, they suffer from edge effects, although sophisticated positioning methods and calibration procedures are applied. Therefore, alternative desings to monolithic block crystal approaches have been proposed trying to improve the sensitivity and reduce edge effects [98]. One approach is constructing PET scanners following an edge-less geometry in which the detector is made of a single continuous piece of scintillation material instead of modular blocks placed nearby (see Figure 26 right). This configuration was first suggested in 1988, and then, different approaches and simulation studies have been proposed supporting this initiative [121]-[126]. During this PhD work, a proof-of-concept PET insert for small animals based on a LYSO scintillator tube with an inner circular face, but ten facetted outer faces (*ScintoTube*) was constructed (see Section 5.2 in Chapter II). One of the papers enclosed in this thesis presents the system performance in terms of 3D spatial and energy resolutions, system sensitivity, count rate capabilities and reconstructed image quality [3].

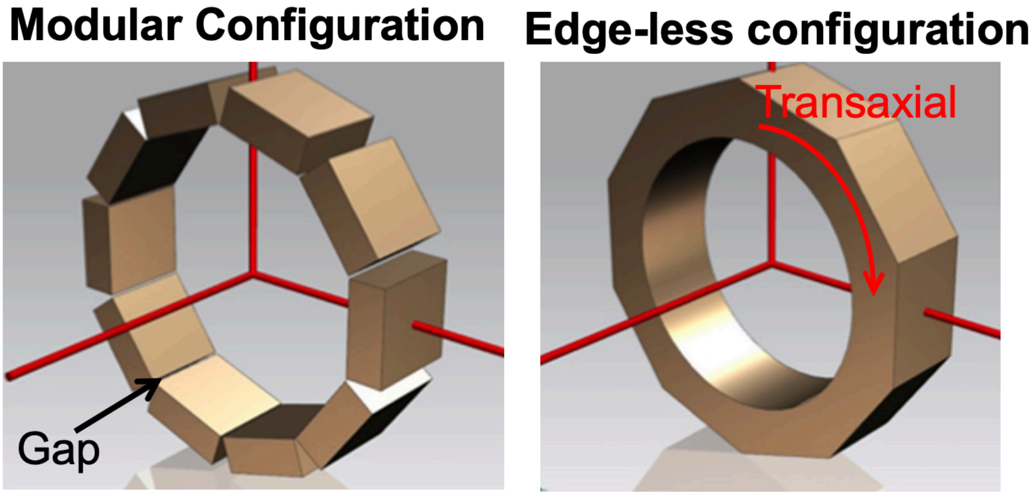

Figure 26.- Left, sketches of a PET system with the modular configuration. Right, alternative design following an edge-less approach. Extracted from [121].

For PET scanners with large dimensions, the previous edge-less design exhibits some restrictions due to the limits in crystal grown size. An alternative approach is for instance to optically couple side-by-side monolithic crystals using optical coupling compounds with a refractive index equal to the scintillation material allowing the optical photons to spread through the crystal junctions. This case cannot be achieved because this type of coupling material is not yet available. However, one interesting solution is to use a compound with a refractive index as close as possible to that of the scintillator. In this case, although some optical photons might still suffer internal reflections, the shape of the LD is almost preserved, and then, edge artifacts are substantially mitigated. This has been demonstrated by different research groups at the detector level using simulations and experimental data [127][128]. One of the papers enclosed in this thesis experimentally exhibits the potential of this approach [4]. During this thesis, a dedicated PET system for breast imaging (*DeepBreast*) based on gluing curved monolithic crystals using Meltmount material (*n*=1.7) has been constructed and it is currently under evaluation (see Section 5.3 of Chapter II).

2.3.1.3 Semi-monolithic scintillators

In semi-monolithic blocks multiple slabs are usually optically isolated from each other using reflective materials, so the optical photons generated in a slab cannot transfer to adjacent slabs (see Figure 24 right). This approach increases the number of optical photons per photodetector unit and, therefore, improves the timing and energy capabilities of the detector. Since the light can propagate in the monolithic direction, DOI information can still be retrieved from the collected LD, while preserving the high sensitivity and good 3D spatial resolution of monolithic crystals. Therefore, semi-monolithic based design takes advantage of both pixelated and monolithic approaches [100]-[105].

During this doctorate work, semi-monolithic crystals with different dimensions and surface treatments have been investigated for its use in two PET prototypes (see Section 4 of Chapter II) [106].

2.3.2 Surface treatment of the scintillator

Light transport inside the scintillation crystal depends on its geometry, the properties of the material and the surface treatment of the crystal sides, among others. The roughness of the crystal surface plays an important role since it is very dependent on the cutting process and of the effects of any additional coating or treatment. These coatings are usually coupled to the cyrstal surface by means of optical coupling material.

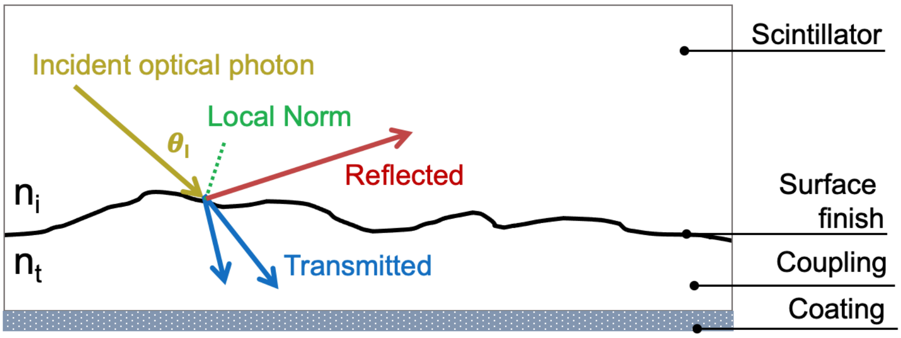

Figure 27.- Sketch showing the behavior of the optical photons when reaching the surfaces of the scintillator.

Regarding surface finish, the incident optical photon reaches the crystal surface and undergoes transmission or reflection with a probability defined by the Fresnel equations (see Figure 27) [129]-[132]. The angle θ_{crit} sets the limit above which the photon undergoes total internal reflection. Below that angle θ_{crit}, the photon may be transmitted or reflected.

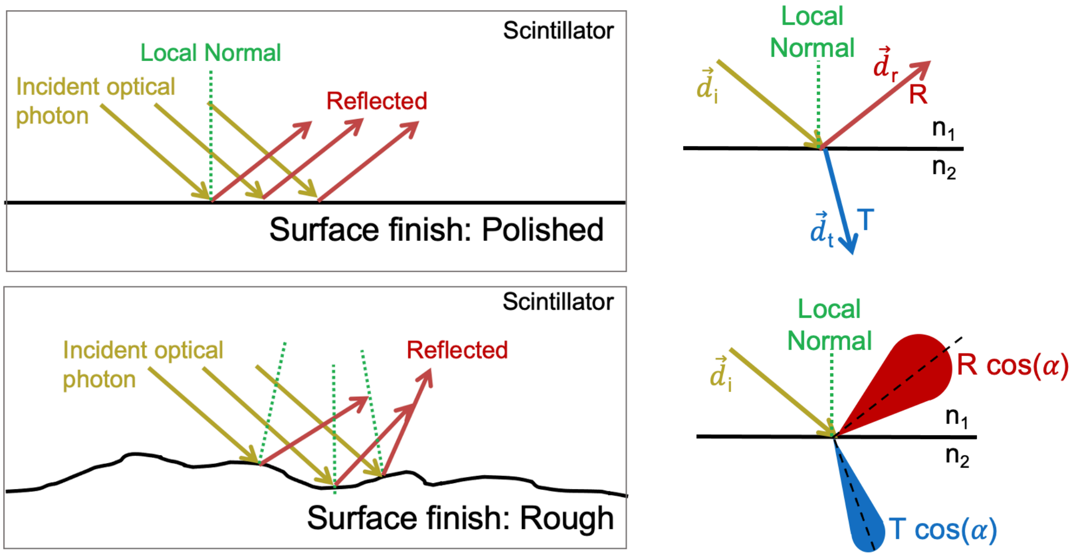

Figure 28.- Top, sketch showing specular reflection. Bottom, sketch showing the Lambertian reflection.

If transmission occurs, the optical photon is transmitted through the coating and assumed to follow Snell's Law of refraction. The angle of reflection and transmission follows different distributions depending on whether the surface finish is polished or roughened (see Figure 28). For polished surfaces, the incident optical photon emerges from the reflecting surface at the same angle as the incident ray, but with a direction opposite to the normal in the plane formed by the incident and reflected rays, i.e., specular reflection. However, for unpolished surfaces, the reflection follows a Lambertian distribution as shown in the bottom sketch of Figure 28.

Concerning crystal surface treatment, it plays an important role on 3D spatial accuracy, CTR and energy performance, thus, it must be optimized and carefully tested to improve the detector capabilities. Many different treatments have been proposed in the literature being the most important ones described below and illustrated in Figure 29:

i) *Absorbent black paint*. The optical photons are absorbed by the black paint, see Figure 29. The advantage of this treatment is that although the absorption of the optical photon causes the truncation of the LD profiles, the shape of the LD can still be well characterized and therefore, the edge effects are reduced when using analytical methods for the impact position estimation. However, high amounts of scintillation photons are not collected negatively impacting the energy and time capabilities.

ii) *Enhanced Specular Reflector (ESR)*. It is a specular reflector film. The lateral and entrance sides of the crystal are usually covered with ESR by means of some optical coupling or keeping air between the reflector and the crystal, thus, the optical photons are reflected at specular directions until reaching the photosensor (see Figure 29). The advantage of this treatment is that the amount of collected light is higher than in the previous case improving therefore both energy and timing resolutions. However, at the edges of the scintillator, the LD is not preserved and thus, spatial resolution at the edges of the crystal worsens and the E/I_{max} estimator is no longer accurate for DOI determination [99].

iii) *Teflon or white paints*. It is a Lambertian reflector, thus the optical photons are diffusely reflected (see Figure 29). The effect of this treatment is similar to the previous one, thus, the amount of collected light is increased but the LD is not preserved.

iv) *Retroreflector (RR)*. The RR is a film composed by several corner-cubes structures that are made of three-sided prisms (mutually perpendicular) reflecting the optical photons back directly towards the source but displaced a small distance (0.1 mm-6 mm) [133]. The incoming optical photon is reflected three times, once by each surface, so that its direction is exactly reversed (see Figure 29). Most of these structures are aluminized to achieve specular reflection. Following this principle, since the light is produced isotropically, adding a RR layer at the entrance detector face increases the scintillation light transferred to the photosensor, with respect to using a black absorbent. It has been proved that both spatial and energy resolutions improve when including the RR layer [133].

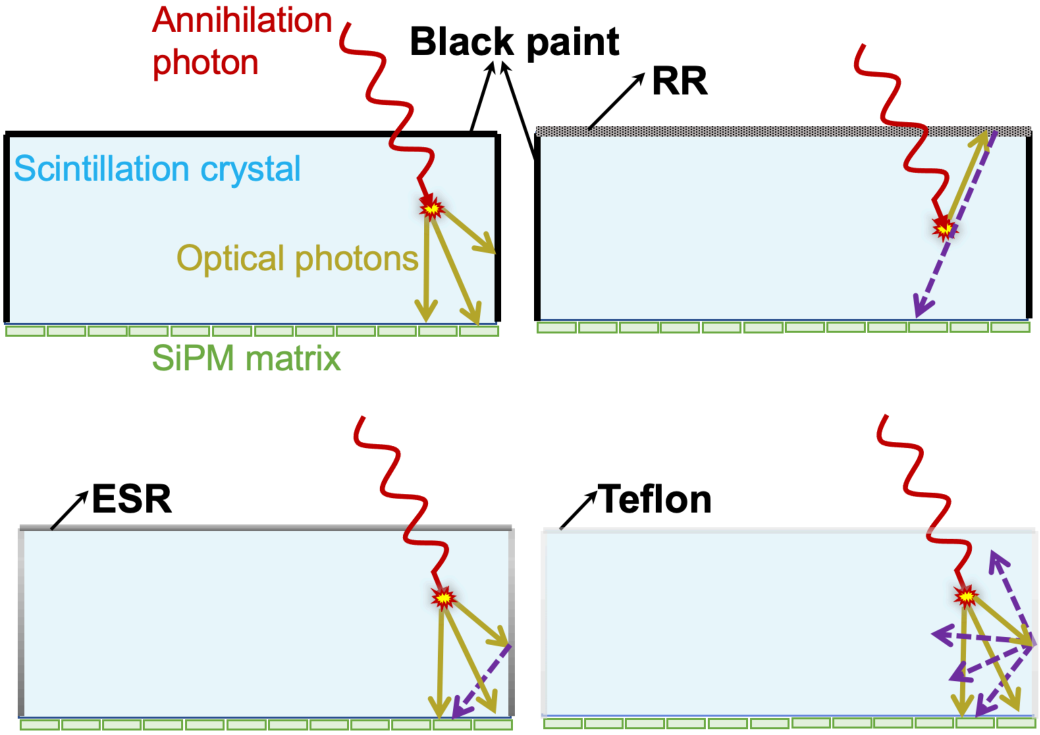

Figure 29.- Sketch of the most used surfaces treatment of scintillation crystals in PET detectors.

2.3.3 Photodetector

The scintillation photons generated within the crystal volume, typically possess an energy of few electron-volts. These photons are converted into usable electrical signals (electronic pulse) through photon-sensitive devices that are optically coupled to the scintillators [94]. The main goal of the photodetector is to convert the scintillation photons into detectable electrical signals with an amplitude proportional to the number of incident optical photons [134][135]. Photodetectors are usually optically coupled to the scintillator blocks in a way that allows the maximum light transmission. The optical coupling of scintillators and photodetectors must be implemented using optically clear compounds (grease, silicone, cement, etc.). In PET detector blocks, photosensors must optimize the following parameters [134]:

i) *Photon Detection Efficiency (PDE).* The photosensor has to efficiently convert the low energy scintillation photons into an electrical signal that is in the emission wavelength of the scintillator. This property is defined as the number of photon-discharged microcells in the photosensor divided by the number of incident photons. It is dependent on the photon wavelength and over-voltage.
ii) *Quantum Efficiency (QE)* strongly depends on the wavelength of the photons and represents the probability that an absorbed photon in the photosensor will produce a signal. Photosensor should present high PDE and QE.
iii) *Gain*. This is a multiplicative factor related to the ratio of the photodetector current output and the current directly produced by the incident photons. Gain should be high and stable.
iv) *Temperature coefficient*. This coefficient directly affects the applied overvoltage and the gain. The gain dependency on the temperature decreases with increasing overvoltage.
v) *Proportionality of response*. The response of the photodetector should be proportional to the incident radiation for a wide energy range.
vi) *Time jitter*. This is the time elapsed between the arrival of the scintillation photon and the generation of the output signal. The timing capabilities of the system is affected by the jitter.
vii) *Compactness*. It is important to use small size photosensors in PET to develop compact systems.

2.3.3.1 Photomultiplier tube

PMTs were the main photodetectors used in PET scanners until the solid-state photodetectors appeared in the market. In PMTs, the optical photons reach and excite the photocathode, which is placed closest to the scintillation crystal, resulting in the emission of photoelectrons in the vacuum (see Figure 30). These photoelectrons are accelerated due to the electric field provided by the focusing grid towards a chain of dynodes connected to a sequentially increased voltage. As soon as the photoelectrons strike the dynode, secondary low energy photoelectrons are produced and accelerated towards the next dynode. This process is repeated at each of the successive dynodes, leading to the generation of a photoelectron cascade. After a few nanoseconds, the first photoelectron results in the generation of about 10^6 electrons and, thus, into an amplified electrical signal easily detectable by the electronic chain [136].

The main advantages of PMTs are stability, high gain that results in a good SNR and fast signal response (rise time). However, mainly due to their bulkiness and sensitivity to magnetic fields, alternative photodetector devices were proposed.

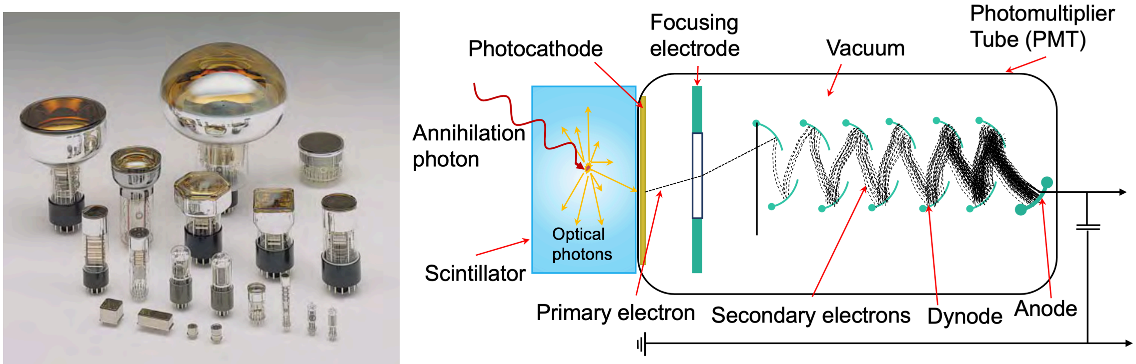

Figure 30.- Left, photograph of different models of PMTs. Extracted from [136]. Right, schematic of a PMT, showing the amplification process in the dynodes.

2.3.3.2 Solid-state photodetectors

Solid-state photodetectors were introduced due to their compatibility with MRI systems, high gain, accurate timing and compactness.

Avalanche Photodiodes (APDs) are solid-state sensors, structurally similar to PN or PIN photodiodes (see Figure 31) [137]. APDs use impact ionization (avalanche effect) to create an internal gain in the structure (see Figure 31). APDs require high reverse bias operation, near reverse breakdown voltage, such that when an incident photon generates a carrier within the depletion region, it is accelerated due to the high electric field present. This operation configuration (above the breakdown voltage) is named Geiger mode. Each photo-generated carrier creates more pairs and thus, it is multiplied by an avalanche breakdown. The electron and hole population grow exponentially with time until a stable current level is reached, which is determined by the system impedance [138]. To make the system ready again for the detection of a new photon, a process known as quenching is implemented. When the APD configuration operates in Geiger mode and a quenching circuit, it is called Single Photon Avalanche Diode (SPAD). Therefore, a SPAD acts as a logical gate that determines whether an interaction with a photon has occurred or not.

SiPMs, are solid-state photodetectors composed of thousands of micron-size SPADs cells connected in parallel while each one contains its own quenching resistor (see Figure 32) [139][140]. Typically, SPADs and SiPMs follows and array configuration. Depending on the device, the size of microcells varies from 10 μm to 100 μm and the number of microcells per SiPM array ranges from several hundreds to several tens of thousands. The most typical SiPM shapes are squares with sizes varying from 1 mm^2 to 6 mm^2 (see Figure 32). The SiPM size is referred as their active area. Each SPAD microcell, is a PN junction, biased in reverse direction above the breakdown voltage [141]. Once the bias is sufficiently high, a high field across the diode is created, which results in the generation of a large avalanche current, after the first photon is detected. Each SPAD is independent, and capable of detecting one photon. The estimation of the magnitude of the generated photon flux can be extrapolated with a certain precision, by the sum of all photocurrents of all SPADs, in a quasi-analog output [141]. The following details reported in this Section are related to analog SiPMs.

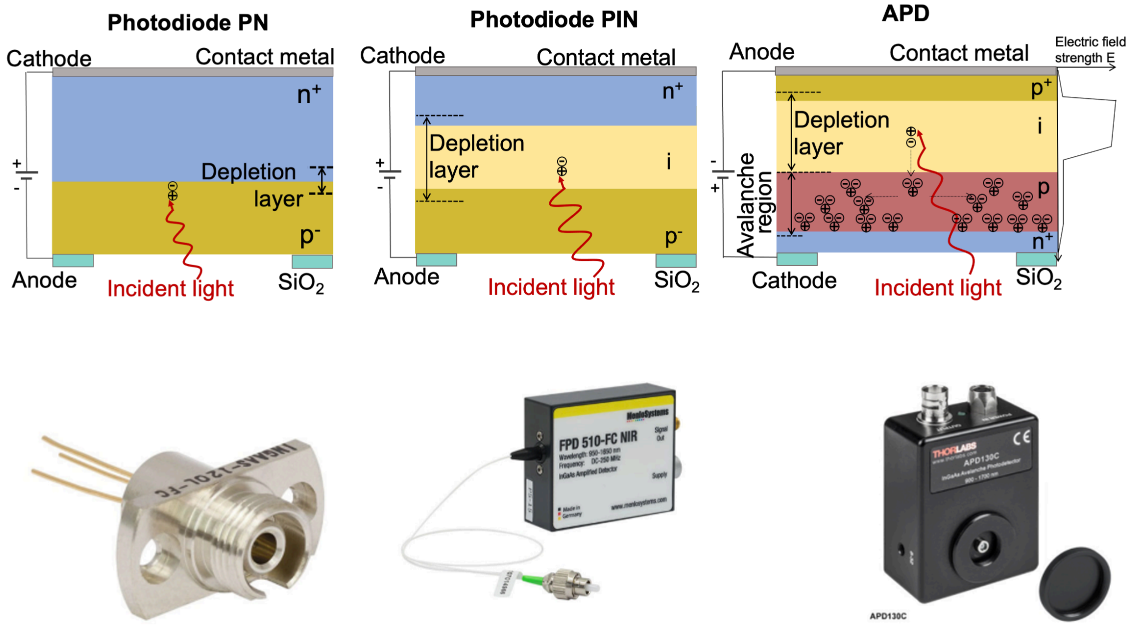

Figure 31.- Top, cross-section of PN, PIN and APD. Bottom, photograph of different solid-state photodetectors.

The SiPM output signals are typically analog with a duration in the order of few hundreds of nanoseconds (depending on the coupled scintillator type) [134]. Figure 33 shows an example of one of these analog pulses. As it can be observed, the avalanche begins at t_0 and quenches at t_{max}. The leading edge of the pulse starts at t_0 and then there is a relatively sharp rise time (t_r) until the pulse reaches the maximum value and exponentially decay (t_d). Integrating the current pulse with respect to time gives the total charge (Q) that has transferred between the terminals of the SiPM.

SiPMs present several advantages, such us compact size, low bias voltage (25-100 V), compatibility with magnetic fields, fast response of the internal avalanche amplification and large availability of providers [141]. However, they also show some disadvantages such as: fluctuations in amplitude and gain, crosstalk between individual cells and correlated noise, which might limit their performance. In addition to these, SiPMs are sensitive to dark counts, due to the generation of thermal electrons which may initiate an avalanche photocurrent, leading to false triggering of electronics. Table 4 shows the main properties of the PMT, APD and SiPM photodetectors used in PET. In this doctorate assertion, PET detectors based on analog SiPM matrix with different dimensions and from different manufacturers have been employed [1]-[4].

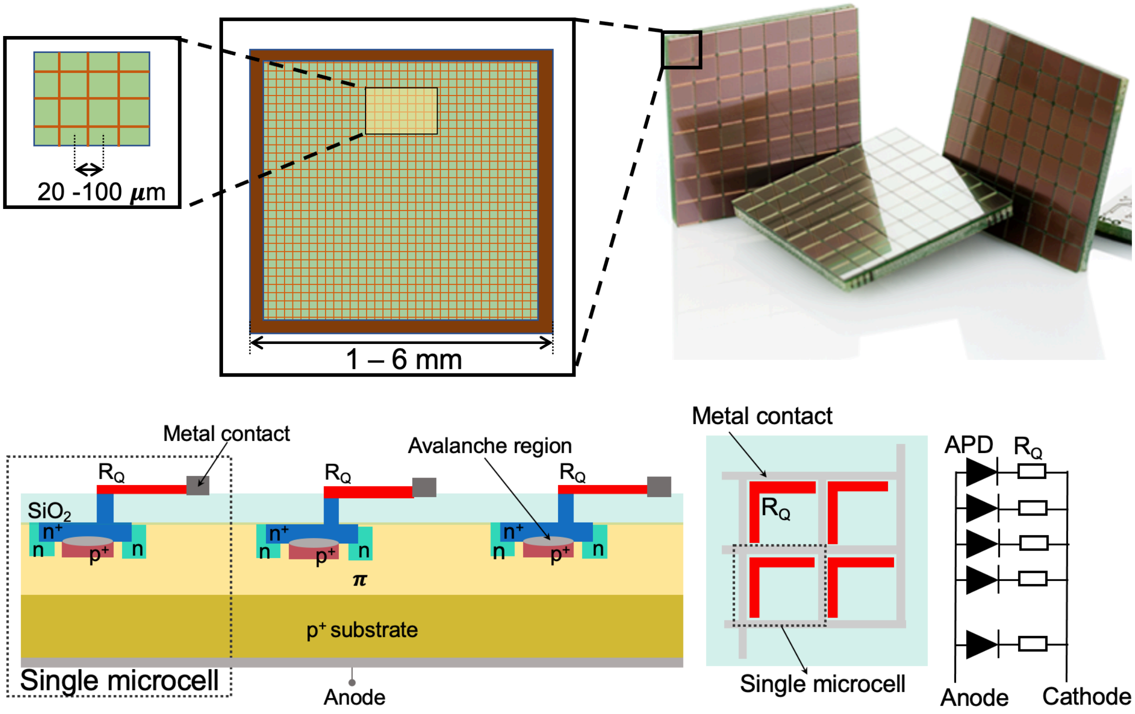

Figure 32.- Top, Photograph of SiPM arrays of 8×8 elements of 3×3 mm^2 (KETEK, PA3325) and sketch of an SiPM element with its basic components, the SPADs. Bottom, typical structure of a SiPM.

One of the main drawbacks of analog SiPMs is that all individual SPADs are read out by a common circuit, which this might result in electronic noise, degrading the timing performance. To achieve the 10 ps goal in TOF-PET, improved SiPM technology is required [92]. To overcome the limitation related to analog technology, digital SiPM (dSiPM) devices have also been suggested [142]. In this case, the interconnected SPADs are integrated with a CMOS circuit on the same substrate and the output signal is purely digital.

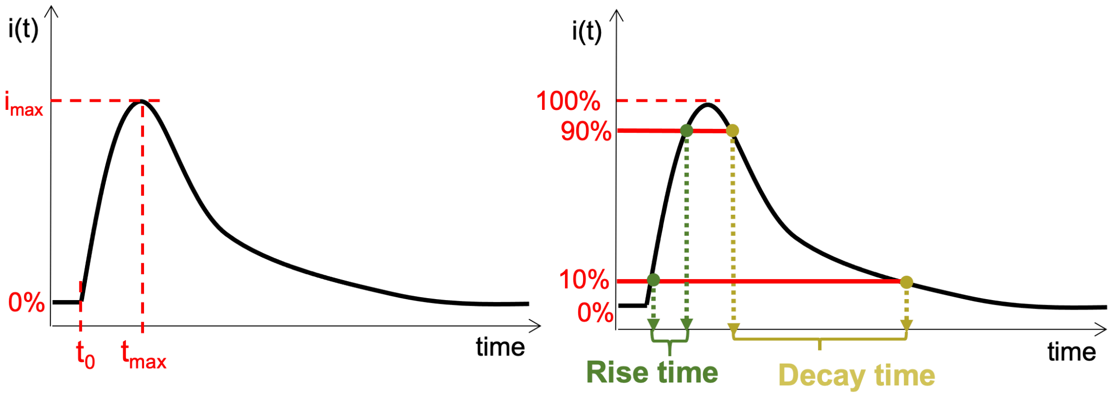

Figure 33.- Illustration of typical response profiles of the acquired waveforms, indicating the ranges considered for the estimation of the rise and decay times, respectively.

Photodetector	Amplification	Magnetic field sensitive	Bias voltage (V)	SNR	Dynamic range	Timing properties
PMT	1×10^6	Yes	1000	High	High	< 1ns
APD	1×10^2	No	350-2000	Low	High	2-4 ns
SiPM	1×10^6	No	20-70	High	Medium	< 1 ns

Table 4.- Main properties of the different photodetector types [135].

2.3.4 Front-end electronic system

The last component of a PET detector is the electronics chain. These electronics take care of shaping the photosensor output signals and of their conversion to a digital format in the Data Acquisition System (DAQ). PET readout circuits should be capable of estimating:

i) The total charge produced by each photosensor element, proportional to the total amount of optical photons detected.
ii) The fraction of time in which the photodetection took place.

The previous information should be digitized using Analog or Time to Digital Converters (ADCs or TDCs, respectively). Several types of electronic systems have been implemented over the years in PET instrumentation.

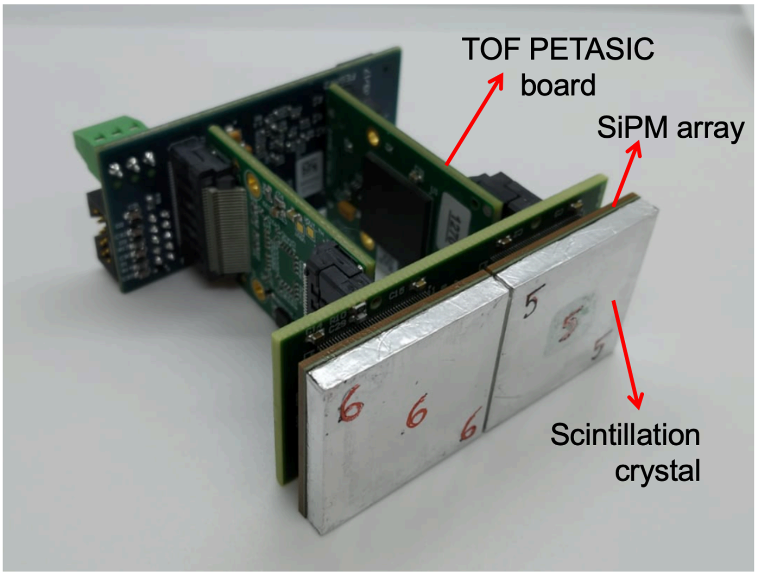

Figure 34.- Example of ASIC (TOFPET2, PETsys Electronics) boards connected to SiPM photosensors and scintillators.

The suitability of an electronic design is mainly related to three factors: performance, cost and complexity. A compromise between these factors is required for the design and implementation of PET detector blocks. Currently, Application Specific Integrated Circuits (ASICs) constitute a promising electronic system candidate in which the front-end electronics and ADCs/TDCs can be integrated without losing performance capabilities to minimize noise from the digital circuitry to the analog front-end readout, achieving compact designs [143]. This technology constitutes allows for reading and processing a high number of signal channels without significantly increasing cost and complexity. Today, numerous ASICs, suitable for PET have been developed, such as the TOF-PET ASIC from PETsys Electronics (Oeiras, Portugal) (see Figure 34) [118], the VATA240 and its improved version VATA241 [144], the PETIROC ASIC from Weeroc company (Paris, France) [145], the HRFlexToT or the FAST IC from University of Barcelona [146][147], among others.

2.3.4.1 Projection readout circuit

The most direct way to read out the signal from a photosensor matrix is to obtain information of every single photosensor element. However, this results in a significant number of signals to be processed, inferring a high implementation cost. A common solution to solve this problem is based on the reduction of this number of signals [148]. One approach is the so-called projection readout circuitry that sums the signals for every row and column of the photosensor array (see Figure 35). For this, a resistor network connects the photosensors of a row (or column) and, thus the number of output signals is reduced to the sum of the number of columns and rows. For example, with the projection readout shown in Figure 35, the number of output signals is reduced from 144 (12×12) to only 24 (12+12). The projection readout still allows one to characterize the LD profiles of an event for both the *x*- and *y*- projections, and it has shown good results when working with monolithic blocks [149]. The projection readout approach has been employed in all the PET detector modules evaluated in the articles included in this thesis [1]-[4].

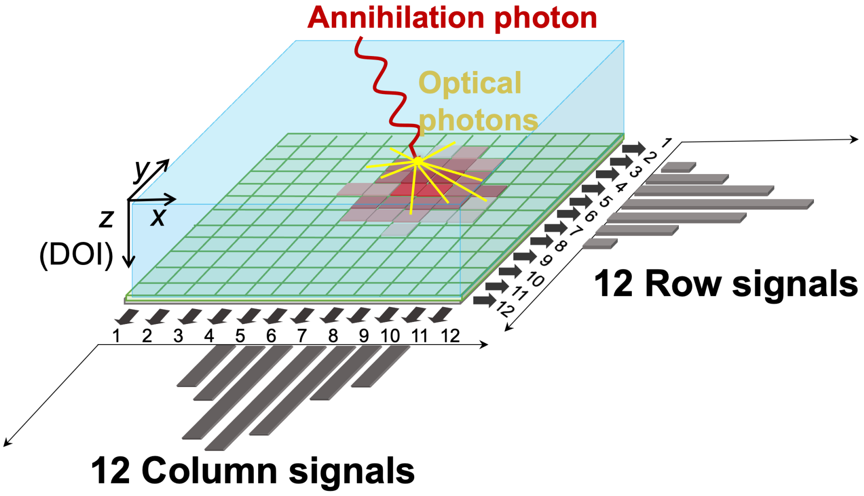

Figure 35.-Projection readout scheme reducing from 12×12 signals to 12+12 signals.

One of the drawbacks of this projection readout is that exhibits challenges when it comes to an accurate timing determination of the signals. However, the significant reduction of the channels to be digitized and processed makes them an efficient method for PET systems that do not require very high timing capabilities.

2.3.5 Performance of PET detectors

The most relevant parameters related to PET detectors performance are discussed in the following paragraphs:

i) *Sensitivity*. Sensitivity or detector efficiency is defined as the ratio between the amount of emitted and detected radiation. This parameter relies on the scintillator type and crystal thickness. Higher efficiency is accomplished using scintillator materials with higher Z_{eff}.

ii) *Energy resolution*. The energy resolution (ΔE) is defined as the detector ability to distinguih the deposition of the energy deposited directly from the generated annihilation photon. On the one hand, the photopeak ($E_{photopeak}$) in the spectrum of a 511 keV emitter become broadened by a large range of effects. Even if the same energy is deposited in the scintillation crystal there is a statistical variation of generated scintilaltion photons per keV (see Figure 36). Morever, the amount of scintillation photons that exit the crystal depend on the scintillation position and the crystal surface treatment. Due to this statistical effect the photopeak follows a Gaussian distribution (see Figure 36). The energy resolution improves with the number of collected scintillation photons, and therefore, it is convenient using scintillators with high *LY*, coupling methods reducing optical losses and photosensors with high *PDE* [150]. On the other hand, the annihilation photons can suffer scatter interactions in the patients or in the scintillator and, thefore, these events are detected at lower energy, observed as a distribution at energies below the 511 keV photopeak (see Figure 36).

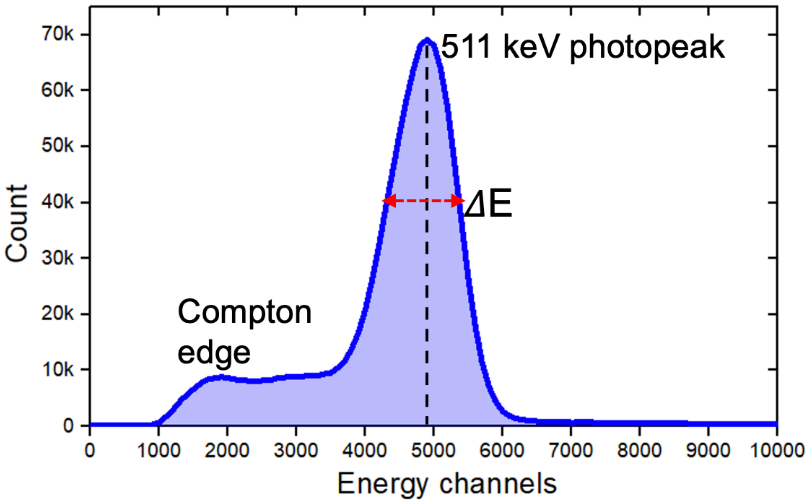

Figure 36.- Actual energy spectrum of a 511 keV emitter detected by a gamma-ray detector. The spectrum is usually fitted with a Gaussian distribution. The photopeak position and the width of the distribution define the energy resolution of the detector.

iii) *Intrinsic detector spatial resolution.* The spatial resolution can be defined as the minimum distance between two sources of radiation (approximately point-like) at which they are discernible. The intrinsic spatial resolution of a PET detector depends on many factors such as the scintillator, the SiPM pixel size and *PDE*, and the scintillator thickness. High Z_{eff} scintillation materials lead to a higher probability of photoelectric interaction (see Figure 21), that is less Compton events, reducing the uncertainty in the impact position estimation, and thus increasing the SNR.

iv) *Detector time resolution*. Timing resolution is the capability of the detector to accurately measure the time when the annihilation photon interacts within the scintillation crystal. Detectors with high timing resolution allow one to reduce the coincidence window and thus, reduce the number of random events. For detectors with good time resolution, the TOF difference measurement can be used to constrain the range of the possible annihilation position along LOR and therefore increase the SNR of the reconstructed images [88] (see Section 2.2.2.3).

2.4 PET image reconstruction and corrections

The reconstruction process in PET, consists of providing a discrete representation of the continuous unknown radiotracer distribution in a subject *f*, using a set of observation (projections), defined with the vector *p* [151][152]. The set of observations obtained from the detected coincidence events are mainly stored in two ways depending on the reconstruction algorithm, namely sinograms or List Mode (LM). A sinogram is a 2D representation of projection space data where one dimension is the distance between the LOR to the center of the FOV, and the second dimension is related to projection angle respect to the axial axis [153]. In the LM storing, the coincidence events are listed, typically sorted with their timestamp. Sinograms are the most popular data format, but as more attributes for each PET event are recorded (i.e., not only the coordinates of the two detected photons but also energy and timing measurements), LM data can become more practical for data storage without loss of information [154]. PET images can be reconstructed using analytical or iterative methods [152].

When using analytic reconstruction algorithms, PET data is considered deterministic, containing no statistical noise. Analytical methods are based on the followed formulation [151]:

$$p = Hf \tag{3}$$

where, *H* is the imaging system described by a matrix, called the imaging matrix. These methods provide a direct solution of *f* from *p*, and this simplified imaging model leads to relatively fast reconstruction techniques. Typically, these methods result in low quality images, but serve to provide the true system image spatial resolution. The most commonly analytical methods currently used are the Back Projection-Filtering (BPF) and Filtered-Back Projection (FBP) [151].

PET data has an inherent stochastic nature. In iterative reconstruction methods, uncertainties associated with several aspects of PET physics are modeled, such as the positron decay process, the attenuation effects, scatter and random events, among others [152]. These uncertainties can be considered in the process to yield more precise reconstructed images. Iterative methods model only the average behavior of the imaging system, and the statistical formulation is:

$$E[p] = Hf \tag{4}$$

where *E[p]* denotes the mathematical expectation. Therefore, through realistic models and consecutive iterations, they provide an optimum possible solution. Iterative algorithms demand higher computing resources compared to analytical approaches. Yet, due to improvements in computational processes such as the usage of multiple CPU (Central Processor Units) or GPU (Graphical Processor Units), iterative methods are still the most extended at the clinical level. The iterative methods most frequently used are the Maximum Likelihood Expectation Maximization (MLEM) [155] and the Ordered Subsets Expectation Maximization (OSEM) [156].

It should be noted that, one of the advantages of PET is its capability to quantify physiological processes. For quantification, it is needed to produce a volume image in which each voxel represents the true activity concentration. To accomplish this, several corrections must be applied to the data during the reconstruction process of the tomographic image [94]. These corrections are described below:

i) *Attenuation correction.* The two 511 keV annihilation photons might interact in the subject before exiting the body. The probability of attenuation for a given pair of annihilation photons is independent of the position of the annihilation along the LOR, making it possible to correct for this effect. Attenuation correction factors can be determined with direct measurements of the attenuation map, which usually is derived through an external transmission scanning apparatus (e.g., *X*-ray, CT) integrated into the PET system design [94]. The introduction of combined PET/CT scanners in the clinic has facilitated the attenuation correction process. When using the CT for this task, attenuation correction factors are obtained with much lower noise, and also the scan time is much faster, compared with conventional transmission scans, thus minimizing the patient dose. Currently, CT-based attenuation correction is used with most of the clinical PET/CT scanners.

ii) *Scatter correction.* Although scatter events produce a uniform error signal across the whole image, their contribution needs to be corrected for proper quantification. Most systems use some form of energy thresholding to discriminate heavily scattered photons from their 511 keV counterparts. Even with thresholding, additional correction techniques, such as simulated scatter models, are required [157][158].

iii) *Random correction.* Random events reduce the image contrast and produce image artifacts. There are two main methods for random event estimation [94]. The first is to use a delayed time window, which contains purely random events and is an estimate of the random events in the prompt window. The second method is to estimate the random event rate from the singles rate for a given detector pair and coincidence time window [151]. While these two methods can correct the mean of the data, the corrected data still present degraded variance due to the noise added by random coincidences.

iv) *Normalization.* In PET systems, the coincidence detection efficiency varies between different pairs of detector elements, due to minor variations in detector material, electronics and geometry [94]. The detector efficiency correction, named normalization correction, uses a multiplication factor to correct for these non-uniformities [159]. These correction factors can be determined by collecting data from a uniform plane source or rotating rod sources of activity [94], or by factorizing the efficiency of the detector pair as the product of individual detector efficiencies and geometrical factors, known as the component-based method [94]. These methods can provide low-variance estimates of normalization factors [159].

v) *Dead time.* Dead time is the time period in which the system is "dead" and cannot detect new events. That means that new event cannot be detected because the acquisition system is busy processing previous events and may depend on many components such as detectors, electronics, hard disk or software [160]. At high counting rates, dead time can significantly limit the detection efficiency and the true system count rate will not increase linearly with activity in the FOV. Correction for dead time typically involves a model for the system dead time behavior at different count rate levels [94].

2.5 PET system performance

A manner to determine the performance of PET scanners (at system level) is characterizing certain physical properties of the system and images that can be quantitatively measured. These properties are correlated to the quality of the images used for diagnostic purposes. For more than 20 years, some efforts have been made to standardize the evaluation of PET system performance. A series of measurements and calculations have been proposed to specifically compare different PET scanners, such as the tests developed by the (American) National Electrical Manufacturers Association (NEMA) [161]. NEMA published the first document of performance standards for WB-PET scanners in the NU 2-1994 [162]. More recently, this protocol has been actualized to the NEMA NU 2-2018 [163]. Moreover, NEMA published a document in 2008 proposing a standardized methodology for evaluating the performance of PET systems designed for animal imaging [164]. The main parameters proposed by the NEMA protocol require measurements of the spatial resolution of reconstructed images; the scatter fraction, count losses (dead time) and random coincidence; system sensitivity and image quality [163][164].

2.6 State-of-the-art PET systems

State-of-the-art clinical PET systems manufactured by commercial vendors consist of WB-PET scanners, most likely with TOF capabilities, and combined with a CT (TOF-PET/CT). These WB-PET scanners have an axial length ranging from 15 to 30 cm [165]. In the recent years, the efforts in the field of WB-PET scanners are directed towards building clinical systems with extended axial length (>1 m), named TB-PET scanners [166]. Besides high-resolution and high-sensitivity, many research efforts are currently committed to develop new instrumentation and scanner architectures for clinical systems dedicated to specific organs imaging (organ-dedicated PET), such as brain or breast, among others [67].

Finally, preclinical imaging systems are also available and are used to study living animals, such as mice, rats, or small primates, for research purposes. These animal-based studies can help translate new diagnostics and therapies to the clinical practice. Figure 37 shows the different configurations previously mentioned.

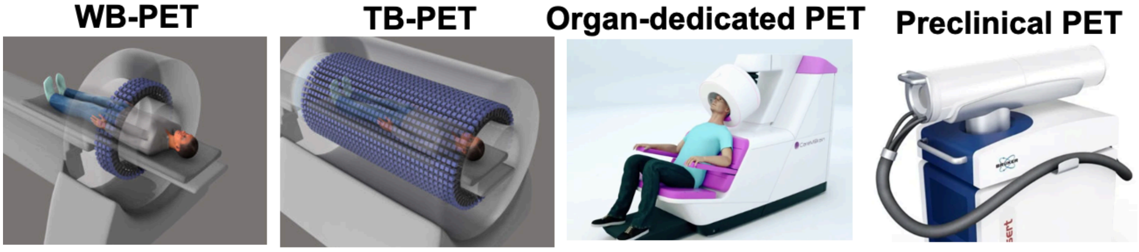
WB-PET
TB-PET
Organ-dedicated PET
Preclinical PET

Figure 37.- Different PET scanner configurations. Extracted from [166], [167] and [168].

2.6.1 Whole Body PET systems

When PET/CT was introduced in the 2000's [32], the advantages of combining metabolic information from PET with anatomical information from CT soon established the PET/CT multimodality as a new standard. Nowadays, the majority of PET scanners installed in hospitals are hybrid systems where a WB-PET scanner with a typical axial length of 15-30 cm is combined with a CT capable of performing whole body imaging of the patients [165]. Some commercial WB-PET/CT systems are described in Table 5. Currently, over 5000 WB-PET/CT systems are in clinical operation worldwide.

System	Geometry	Detector	Spatial Res.	DOI	TOF	Ref.
Siemens **Vision PET/CT**	Ring	LSO pixelated Analog SiPM	3.7 mm	No	210 ps	[169]
GE **Discovery MI PET /CT**	Ring	LYSO pixelated Analog SiPM	4.3 mm	No	382 ps	[170]
Philips **Vereos PET/CT**	Ring	LYSO pixelated Digital SiPMs	4.24 mm	No	310 ps	[171]
Canon **Cartesion PET/CT**	Ring	LYSO pixelated Analog SiPM	-	No	255 ps	[165]
United Imaging **uMI550 PET/CT**	Ring	LYSO pixelated Digital SiPM	2.98 mm	No	372 ps	[172]

Table 5.- Commercial WB-PET/CT scanners.

Even after more than 16 years of commercial PET/CT, new designs are still being introduced, particularly with the appearance of SiPMs. The research among companies focuses more on software improvements and faster electronics that allow TOF acquisition [173]-[176]. In 2015, a Philips prototype scanner based on dSiPMs was developed, reaching a time resolution of 345 picoseconds [177]; and later, the same company commercialized the so-called Vereos PET scanner with a TOF of 310 ps using such technology [170]. GE also presented a PET, capable of reaching 375 ps using analog SiPMs [178]. In 2018, Siemens announced their latest PET, the Biograph Vision PET/CT, which exhibits a timing resolution of 214 ps FWHM, the commercial system with the best timing capabilities currently available [179][180]. Nevertheless, concurrently to these developments, in the research field, several steps have been made proving an achievable roadmap towards even a better timing performance [181].

Another significant development in WB-PET is the simultaneous acquisition of PET and MRI data. This was made commercially possible by using APD-based radiation detectors in 2010. Siemens installed the first APD-based WB-PET/MRI with simultaneous imaging capability, the Biograph mMR from Siemens, at the Technical University in Munich (TUM-MED) [182]. The design generated significant interest, especially as a research instrument, and nowadays other commercial scanners have been developed, such as the Signa PET/MR from GE [183] or the Ingenuity PET/MRI from Philips [184]. Notice that as more as 80 PET/MRI systems are installed worldwide [43].

In the last decade, further research has focused on increasing the overall system sensitivity with the subsequent improvement in the image quality. This will allow users for shorter examination times with similar tracer concentrations or lower tracer concentrations and therefore radiation exposure if the total examination time is kept constant.

2.6.2 Total-Body PET systems

As aforementioned, the vast majority of commercial PET scanners account for an axial FOV of only 15-30 cm, which allows approximately one-eighth of the human patient body to be within the FOV of the scanner in one shot [165][185]. The reduced axial coverage implies low detection sensitivity since about only 1% of the events are detected. Increasing PET sensitivity has clinical benefits [185][186].

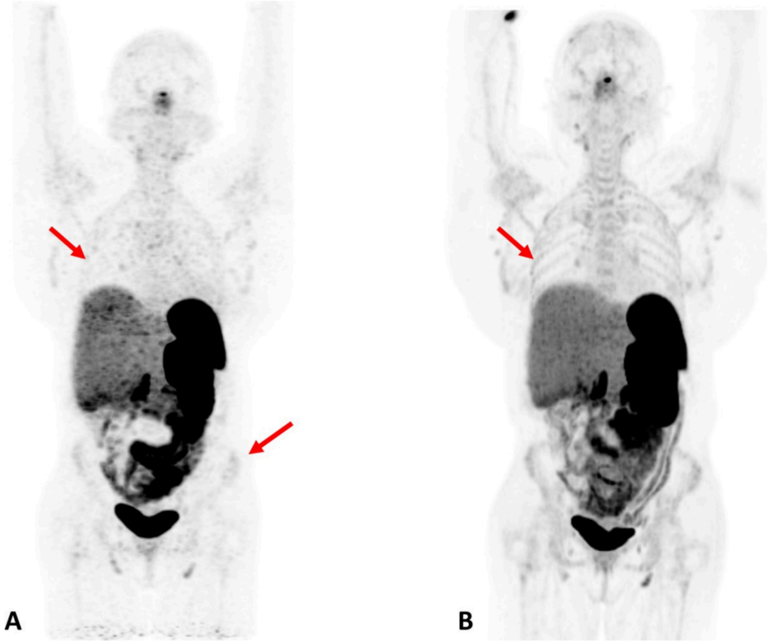

Figure 38.- Left, PET image of a patient obtained with a conventional WB-PET scanner (Siemens Biograph mCT). Right, 6 month follow up PET scan of the same patient obtained with a TB-PET scanner (uExplorer) . Note the millimetric metastases in the lung cancer (red arrows) are observed with higher level of detail using the uExplorer scanner. Extracted from [187].

One option to increase sensitivity, is extending the axial length of the scanner [185]. This approach was already introduced 30 years ago [186][188] and, since then, several simulation studies have demonstrated the benefits provided by this concept [189]. Recently, thanks to the advances in PET instrumentation, three TB-PET systems have been implemented [190], the uExplorer from the UC Davis and United Imaging Healthcare [68], the Biograph Vision Quadra from Siemens [192] and the PennPET developed at the University of Pennsylvania [191]. These systems have experimentally demonstrated to provide reduction in acquisition times, reduction in administrated activity to the patient, improvement in image quality and simultaneous total-body dynamic imaging [190]. For example, Figure 38 shows a comparison of the quality images using the uExplorer TB-PET and a conventional WB-PET system and the higher level of detail in the image acquired with the TB-PET is noticeable [187].

2.6.3 Organ-dedicated PET systems

Typical WB-PET, that are based on multiple rings of detectors, have been widely used for cancer diagnosis and treatment. However, their limited spatial resolution restricts the management of cancers in specific organs or regions. An alternative to promote the clinical research and to improve the diagnosis accuracy and treatment outcomes, is to use non-conventional PET geometries for specific applications in specific organs. Different organ-dedicated PET, SPECT or Gamma camera systems have been proposed and built [66]. These geometrical configurations optimize the positioning of the detectors to maximize spatial resolution and sensitivity in the region of interest, thus increasing the detection ability and accuracy of the resulting image. During the last decades, the different developed dedicated brain, breast, prostate and heart systems have demonstrated an improvement of the image quality and clinical sensitivity [66]. Table 6 summarize the system performance of some dedicated PET systems. Moreover, their selling price is smaller than WB-PET, typically allow for higher patient throughput and have reduced footprints. The main drawback of these systems is that they mainly focus on the examination of a single organ reducing their usage by different specialists.

System	**Organ**	**Detector**	**Spat. Res.* mm**	**DOI Res. mm**	**Energy Res. %**	**Sensitivity***
PEM/PET	Breast	Pixelated	< 2	-	25	6.88%
MAMMI	Breast	Monolithic	1.8	4.0	18	1.6%
Helmet-type	Brain	Pixelated	2.8	1.9	12.6	13.4 kcps/MBq
CareMiBrain	Brain	Monolithic	1.87	< 3	17	11.05 cps/kBq

Table 6.- Characteristics of dedicated PET systems. Extracted from [193], [194], [195], [196].*Spatial resolution and sensitivity values at the center FOV.

2.6.4 Preclinical PET systems

Small animals have high anatophysiological similarities with human body and therefore, the use of small-animal models in PET provides a unique opportunity for studying biological process or diseases at the molecular level [108]. WB-PET scanners have limited performance for scanning small animals, and therefore, dedicated PET systems have been developed, to overcome these limitations and challenges. A variety of small-animal PET prototypes, as well as commercial scanners with different configurations, architectural designs, and diversified types of software were characterized and evaluated during the last years, providing higher spatial resolution, higher detection capabilities, and easy accessibility compared to WB-PET scanners. [108].

At the beginning of the century, several studies indicated that employing monolithic-based detectors in PET scanners could significantly improve the system performance compared to the pixelated-based ones [197]. Monolithic-based PET detectors in commercial preclinical scanners have been motivated by their reduced cost and their intrinsic ability to provide DOI information without the use of additional hardware material, as described in Section 2.3.5. Table 7 summarizes the performance of some preclinical PET systems based on monolithic crystal blocks.

System	Application	Spatial Res.* mm	DOI Res. mm	Energy Res. %	Sensitivity*
Albira	Preclinical	<0.7	2.5	12	9%
DigiPET	Preclinical	0.7	2	~18	6.0 cps/kBq
β-cubes	Preclinical	0.84	1.6	12	12.4%

Table 7.- Characteristics of preclinical PET systems based on monolithic detectors. Extracted from [98]. *Spatial resolution and sensitivity values at the center FOV.

2.7 Artificial Intelligence in PET

AI can be defined as the science and engineering of making intelligent machines, especially intelligent computer programs. AI is a broad field that includes Machine Learning (ML) and Deep Learning (DL) techniques (see Figure 39) [198]. ML provides the ability to learn automatically without being explicitly programmed and improve from experience. DL is a subfield of ML that uses complex algorithms and deep neural nets to train a model. Typically, when people use the term DL, they refer to deep Artificial Neural Networks (ANN) [199].

ML techniques, including DL approaches, can be supervised or unsupervised [199]. The main difference between these two, is the need for labeled training data. Supervised Machine Learning relies on labelled input training data, whereas unsupervised learning algorithms use unlabeled data. Figure 40 show some of the most relevant ML and DL algorithms.

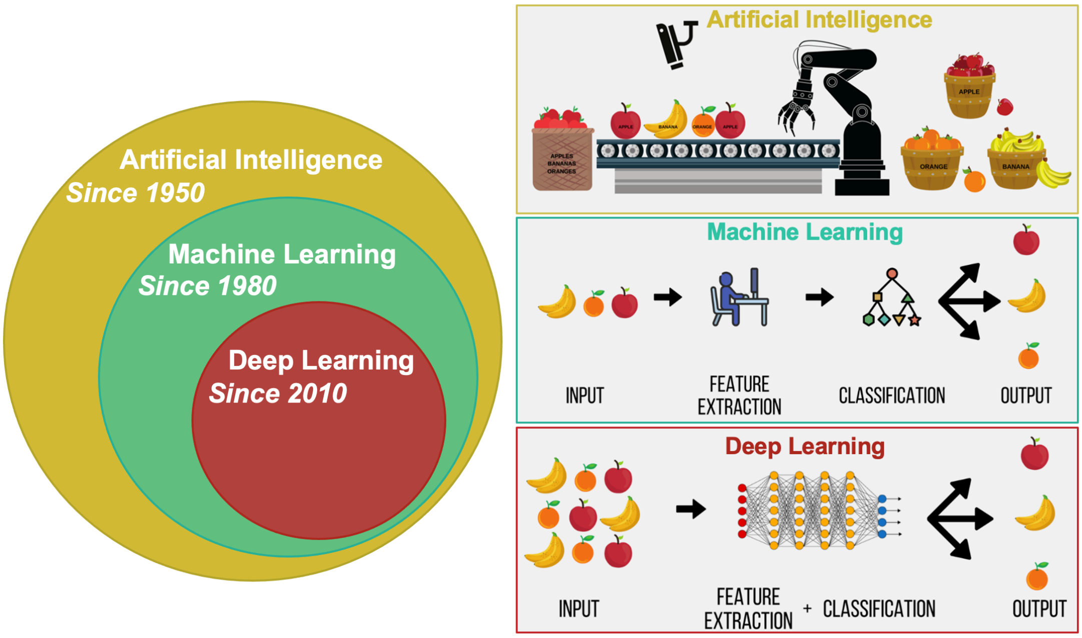

Figure 39.- Left, Relation of AI, ML and DL. Right, examples of these techniques.

AI based algorithms show tremendous promise across multiple technical aspects owing to their remarkable success in offering novel solutions to solve complex problems [198]. AI is gaining momentum in Medical Imaging as well. Recently, several AI techniques have been investigated in Medical Imaging, and their potential applications range from data acquisition and image reconstruction, to image analysis and interpretation. [200]. In fact, a large number of publications in the literature have shown the promising of the application of AI (see Figure 13) [73]. Notice that more efforts are needed to make this technology mature enough for wide real-world clinical applications [206].

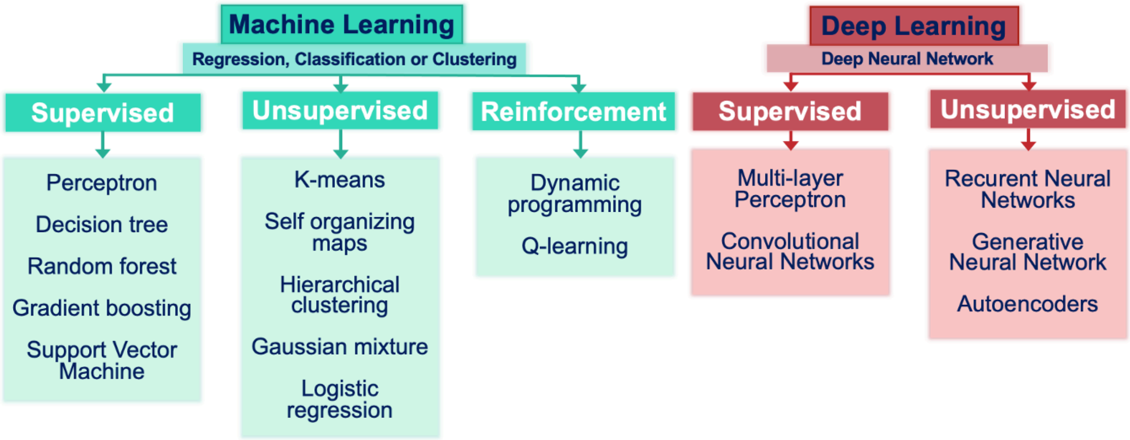

Figure 40.- Diagram showing the most important Machine Learning (left) and Deep Learning (right) techniques.

In PET and SPECT techniques, the AI algorithms range from low-level electronic signal formation/processing to high-level internal dosimetry and diagnostic/prognostic modeling (see Figure 41) [202]. At the detector level, ML and DL approaches have been employed to improve spatial resolution (see Section 3.1.4 for more details) [203] and timing resolution [204][205], aiming to upgraded the overall detector performance. During this thesis a DL technique based on ANN has been implemented to estimate the annihilation 3D photon interaction in monolithic-based PET detectors (see Section 4).

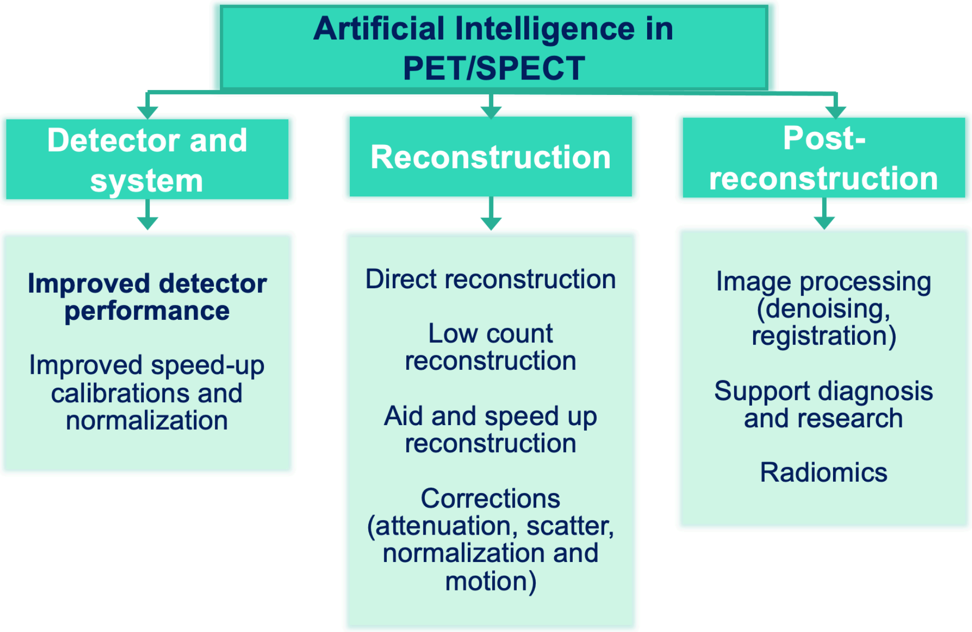

Figure 41.- Diagram showing the most important applications on AI in PET and SPECT techniques.

3 Position estimation and calibration in monolithic-based PET detectors

In monolithic-based PET detectors, the 3D photon interaction position inside the crystal is determined from the measured scintillation LD provided by the photosensors. Note that due to various physical phenomena such as, Compton scattering or the behavior of optical photons, complex positioning algorithms and calibration procedures are usually required to provide an accurate impact position determination. Therefore, successful implementation of monolithic-based PET systems deals with some technical challenges that need to be overcome. This Section presents the main position estimation methods and calibration procedures that have been proposed and implemented for monolithic-based PET detectors.

3.1 Position estimation methods

As we have described, the annihilation photon impact position in monolithic scintillators can be obtained from the measured LD (see Secion 2.3.1.2). A simplified illustration of this principle is shown in Figure 42. If the annihilation photon impact moves laterally from one side of the crystal to the other side in the *x*- axis, the maximum value of the LD moves according to the interaction point. Similarly, if the annihilation photon impact changes in depth, that is along the *z*-axis, the width of the LD is expected to change, resulting in a wider LD when the interaction is further from the photosensor and a narrower LD when the interaction is closer to the photosensor.

Using this information, different position estimation methods has been proposed for monolithic-based detectors, as shown in Figure 43. These algorithms can be divided into two main categories:

i) *Positioning algorithms that do not need reference data.* They model the relation between the 3D interaction position of the annihilation photon inside the crystal and the LD measured by the photosensors and, therefore, they extract all the necessary information immediately from the LDs themselves [98]. The main advantage of these methods is that they need minor or no calibration data, since they are based on geometrical and physical considerations. However, these methods usually misposition impacts close to the edges of the crystals, due to the difficulty of modelling the absorption and/or reflection of the scintillation light and, thus, they might not be accurate in case of a non-ideal response of the detectors. Also, some of them require quite intensive computational processing, since for each unknown event a function with several fitting parameters must be minimized or maximized. This category includes both analytical and fitting methods.

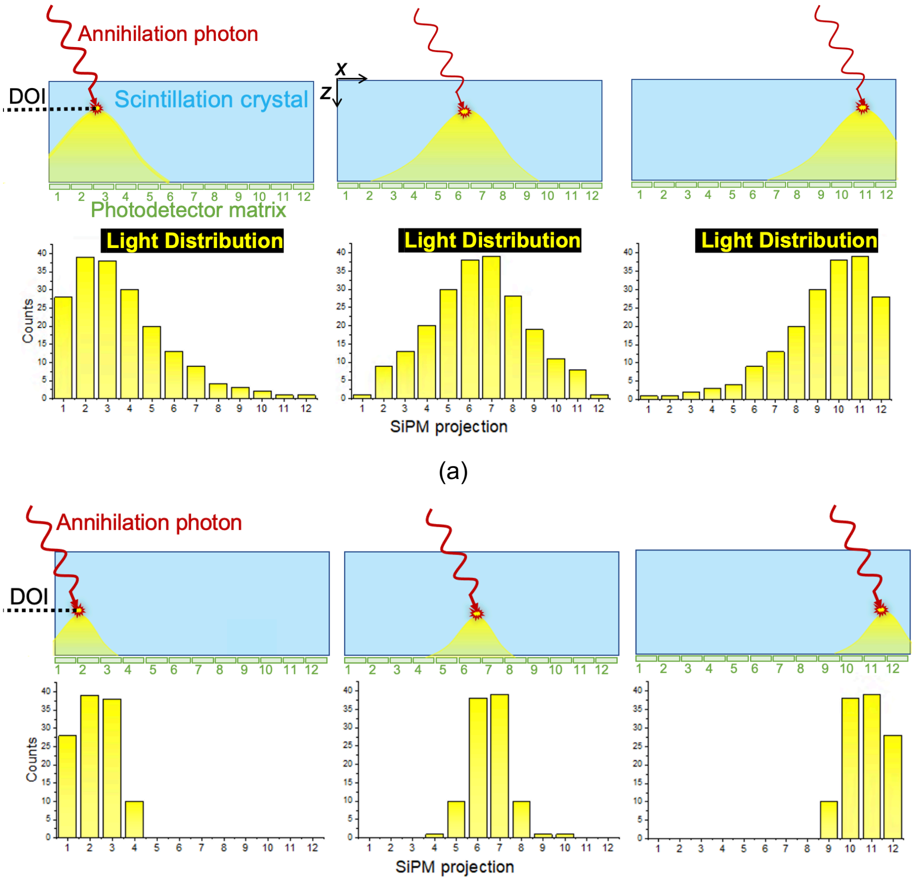

(a)

(b)

Figure 42.- Top, sketch of a monolithic crystal coupled to a matrix of 12×12 SiPMs showing the LDs generated for the interaction of the annihilation photon at the center and at the two edges of the monolithic crystal. (a) For an impact at the entrance of the crystal and (b) for an impact close to the photosensors.

ii) *Positioning algorithms that need prior reference data.* They require an experimental characterization of the detector light response as a function of the impact position [98]. The 2D detector light response is usually obtained by irradiating the detectors at a normal incidence at x_i- and y_i- precise positions, named calibration positions. Then, a collimated pencil beam of 511 keV gamma-rays is used to control the interaction location and record the LDs of *n* reference events at each position (see Figure 44 left). For thick monolithic crystals a 2D detector response is not adequate and thus, the detector response is obtained as a function of 3D position of interaction by scanning the pencil beam at other than normal incidence (see Figure 44 right). This category includes statistical methods and Machine Learning techniques.

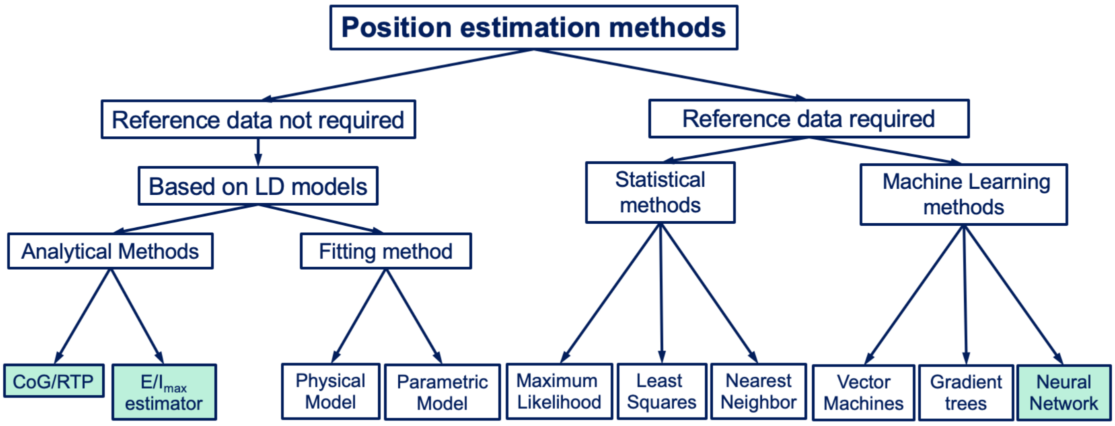

Figure 43.- Schematic diagram showing the different algorithms to estimate the position of an impinging annihilation photon using the embedded information from LDs.

The research carried out during this PhD thesis focused on the development of algorithms to accurately determine the impact positions in the detector block using, on the one hand, analytical methods since its implementation is easier and they provide good performance when using projection readout circuits. On the other hand, ML methods based on Neural Networks were also implemented since they have demonstrated to improve spatial resolution and to be computationally more efficient. The colored boxes in Figure 43 highlight these two approaches.

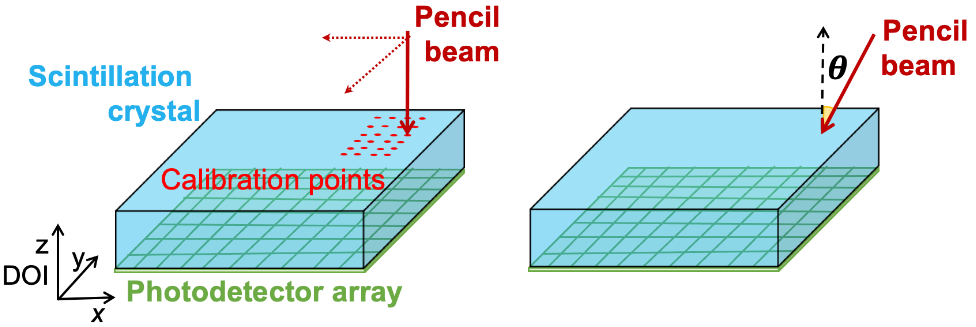

Figure 44.- Acquisition of reference data to obtain the detector response as a function of 3D position of interaction. Left, the 2D detector response is typically obtained by acquiring data moving a pencil beam on a 2D array. Right, 3D detector response can be obtained by acquiring reference data by scanning the pencil beam at other than normal incidence.

Table 8 shows a summary of the spatial resolution reported using different positioning estimations methods and detector configurations. Notice that, all positioning methods present advantages and disadvantages and therefore, their selection depends on different factors. A direct comparison of their performance is difficult since it also depends on the size, type, treatment of scintillation crystal and on the photodetector granularity, among others. In the literature, the described algorithms are usually applied to one specific combination of crystal size and photodetector arrangement.

Method	Crystal (mm^3)	Treatment	Photosensor	2D resolution (mm)	DOI resolution (mm)	Notes
Center of Gravity	50×50×10 $LaBr_3$	Black paint	MA-PMT, 8×8, 6×6 mm^2	2.4 FWHM (center)	-	[207]
Raise to the Power	50×50×10 $LaBr_3$	Black paint	MA-PMT 8×8, 6×6 mm^2	2.2 FWHM (center)	-	[207]
DOI estimator	50×50×15 LYSO	Black paint+RR	SiPM 12×12, 3×3 mm^2	-	3.7 FWHM	[208]
Parametric	50×50×8 LYSO	Rough and black paint	MA-PMT 64 channels	1.16 FWHM	3.24 FWHM	[209]
Physical model	20×20×10 LSO	Polished, teflon	APD, 8×4,1.6×1.6 mm^2	1.15 FWHM	1.8 FWHM	[210]
Maximum Likelihood	50×50×8 LYSO	Black paint	MA-PMT 64 channels	1.28 FWHM (center)	2 mm	[211]
Least Squares	26×26×10 LYSO	Black paint	MA-PMT 4×4	2.03 FWHM	-	[128]
Nearest Neighbor	20×20×12 LYSO	PTFE	MA-PMT 4×4	~3.0 FWHM	<4.5 FWHM	[212]
Support Vector Machines	20×10×10 LSO	Teflon	APD, 8×4, 1.6×1.6 mm^2	1.69 FWHM	-	[213]
Gradient Tree Boosting	32×32×12 LSO	Teflon	dSiPM 4×4	1.55 FWHM	<2.5 FWHM	[214]
Multilayer Perceptron	25.5×25.5×10 LYSO	Rough and black paint	MA-PMT 64 channels	1.86 FWHM	2.01 FWHM	[215]
Convolutional Neural Networks	50.8×50.8×30 $LaBr_3$		MA-PMT 8×8	0.96 FWHM	-	[216]

Table 8.- Characteristics of some position estimation methods used in monolithic-based PET detectors.

3.1.1 Analytical methods

3.1.1.1 Center of Gravity (CoG) method

A widely used positioning method in monolithic crystals is the CoG method [217]. This method estimates the *x*- and *y*- annihilation photon interaction coordinates, $\hat{x}$ and $\hat{y}$, by computing a weighted CoG of the measured LD. Moreover, this method is also applicable when using projection readout approaches [217]:

$$\hat{x} = \frac{\sum_{m=1}^{m=s} c_m x_m}{\sum_{m=1}^{m=s} c_m} \tag{5}$$

$$\hat{y} = \frac{\sum_{m=1}^{m=s} r_m y_m}{\sum_{m=1}^{m=s} r_m} \tag{6}$$

Here, c_m and r_m are digitized signals projected on the *x*- and *y*- directions; *m* is the number of elements in the row and column; x_m and y_m are the coordinates of the photodetector element position on the detection surface, respectively.

The CoG algorithm works well when the LD profile is fully measured, as it happens for events interacting in the central area of the scintillator (see Figure 45). However, for impacts close to the edges the LD profile is truncated. This produces a deviation of the estimated impact coordinates respect to the real interaction position. This effect is known as edge effect or compression effect (see green cross in Figure 45).

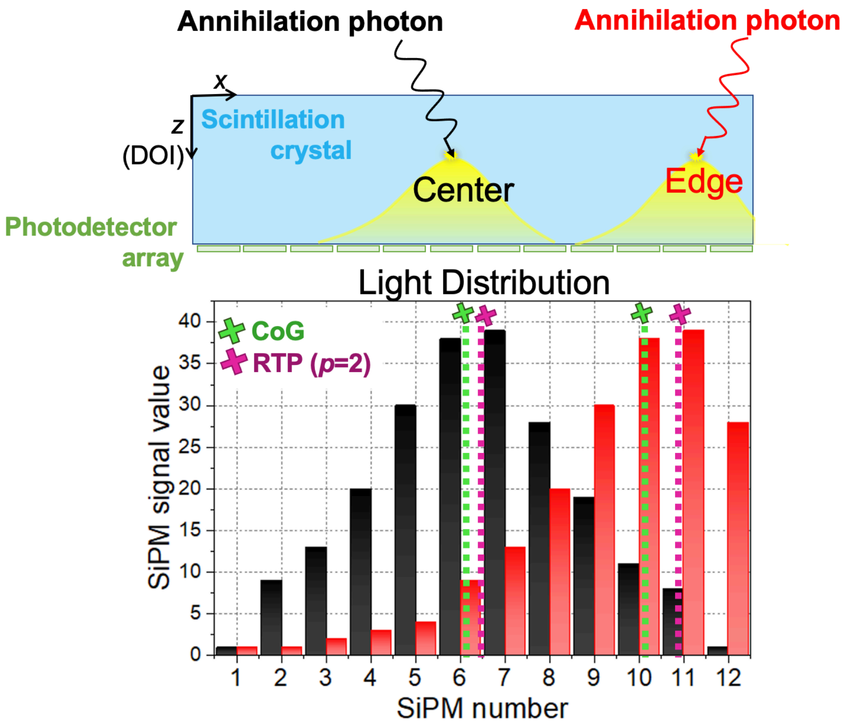

Figure 45.- Top, sketch of a monolithic crystal coupled to a matrix of 12×12 SiPMs showing two LDs for a photon interaction at the center and at the edge of the crystal, respectively. Bottom, measured LD profiles for the impact at the center and at the edge when applying CoG or RTP. The green and pink crosses represent the estimated coordinate when applying CoG or RTP methods, respectively.

3.1.1.2 Raise to the Power (RTP)

The estimation of the *x*- and *y*- annihilation photon interaction coordinates can be improved by applying a modified version of the CoG algorithm, named Raise to the Power (RTP) [218]. This method consists of rising to a power the digitized signal values, as follows:

$$\hat{x} = \frac{\sum_{m=1}^{m=s} c_m^p x_m}{\sum_{m=1}^{m=s} c_m^p} \tag{7}$$

$$\hat{y} = \frac{\sum_{m=1}^{m=s} r_m^p y_m}{\sum_{m=1}^{m=s} r_m^p} \tag{8}$$

where, w_m the digitized signals from the m^{th} photodetector element, x_m and y_m are the coordinates of the m^{th} photodetector element position on the detection surface and *p* is the power value. While increasing the *p* value, the compression effect is reduced. However, it should be noticed that, when increasing the *p* value, the estimated position is attracted to the maximum value of the LD. Therefore, the selection of the power (*p*) is a compromise between the positioning linearity and the attraction effect to the maximum [219]. Note that for $p = 1$ these equations are those shown for the standard CoG algorithm. Figure 45 illustrates the measured interaction coordinates of the impinging photon at the center and edge of the monolithic crystal when applying CoG (with p=1) and RTP (with p=2). The RTP method provides a more precise position of the annihilation photon impact (see pink cross in Figure 45).

3.1.1.3 DOI estimators

Monolithic scintillation crystals allow one for continuous DOI determination due to the expected variations of LD width generated at each different impact depth (see Figure 42). Unfortunately, the LD inside the crystals is affected from light scattering and reflections that challenges the expected width differences. Moreover, the light spread of an event might be affected by statistical variations depending on the light yield of the scintillation crystal. In [218], it was suggested modelling the LD detected for each scintillation event as a Gaussian distribution. They calculate the E/I_{max} estimator, which is the ratio of the energy (*E*) obtained as the sum of the row (or column) signals, and the maximum signal value (I_{max}) of the row (or column) of the distribution from the LD profiles along *x*- and *y*-directions, respectively. The E/I_{max} estimator values are in arbitrary units and, if the crystal sides are painted with absorbent black paint, they can be calibrated into mm using an analytical expression of the DOI distribution [133], as follows:

$$DOI = A \cdot exp^{-\alpha z} \left[erf\left(\frac{b-z}{\sqrt{2}\sigma_{int}}\right)\right] - erf\left(\frac{a-z}{\sqrt{2}\sigma_{int}}\right) \tag{9}$$

where α is the attenuation coefficient of the material, *A* is the amplitude, σ_{int} is related to the FWHM of the distribution as $2.35 \cdot \sigma_{int}$, *erf* is the Gaussian error function, and *a* and *b* are the lower and upper limits of the distribution. These two last parameters can be used to calibrate the measured E/I_{max} values to mm. In all the articles included in this PhD thesis, the so-called *E/I$_{max}$* estimator has been used for the estimation of the $\hat{z}$- coordinate.

3.1.2 Fitting methods based on physical or parametric LD models

These methods estimate the photon interaction position following three steps:

i) *LD model.* Definition of a general function $y(x_m|\theta)$, that models the number of photons reaching the m^{th} photodetector elements (dependent variable), where θ is the parameter set of the model that correspond to the 3D (or only 2D) annihilation photon interaction coordinates and x_m is the independent variable that corresponds to the 2D photodetector element position [209][210].

ii) *Model parameter fitting.* The interaction coordinates are estimated directly from the measured signals using a numerical searching method [209][210]. Three searching estimator methods have been used and are described below:

- Least Squares (LS), minimizes the sum of the squared distances between the detected signal in the m^{th} photodetector elements (y_m, dependent values) and the values of the model at the corresponding independent variable values $y(x_m|\theta)$ as follows:

$$\hat{\theta} = \underset{\theta}{\operatorname{argmin}} \sum_{m=1}^{M} (y_m - y(x_m|\theta))^2 \tag{10}$$

  where, M is the total number of photodetector elements.

- Weighted-Least Squares (WLS), adds an appropriate weight w_m to the different error terms in the sum-of-squares as:

$$\hat{\theta} = \underset{\theta}{\operatorname{argmin}} \sum_{m=1}^{M} w_m (y_m - y(x_m|\theta))^2 \tag{11}$$

  It is not always easy to choose the weights. If the noise variance σ_m^2 at each measurement m is known, and all measurements are independent, then it is common to use $w_m = \frac{1}{\sigma_m^2}$.

- Maximum Likelihood Estimator (MLE), determined using the joined probability density function for the data ($y_1, \dots, y_M$) given the parameter set θ: $Pr(y_1, \dots, y_M | \theta)$. The parameters were estimated using the Bayes rule as follows:

$$\hat{\theta} = \underset{\theta}{\operatorname{argmax}} \mathcal{L}(\theta \mid y_1, \dots, y_M) = \underset{\theta}{\operatorname{argmax}} Pr\,(y_1, \dots, y_M \mid \theta) \tag{12}$$

iii) *Optimization methods.* The parameters (i.e., the annihilation photon interaction position) are estimated using minimization or maximization methods.

Two main methods that follows the previous methodology have been proposed and are described below.

3.1.2.1 Parametric model of the LD

This method is based on an empirical parametric model of the LD where the number of the light photons reaching the m^{th} photodetector is a function of the *x*-, *y*- and *z*- photon interaction positions [209]. The $\hat{x}$- and $\hat{y}$- interaction positions are estimated by fitting the model using MLE or WLS [209]. For the MLE assumptions, the number N_m of optical photons generating signal in the m^{th} photodetector follows the Poisson distribution, and statistical analysis, are required. For the WLS, although the choice of the weight of the square errors used in Equation (11) is based on that previous analysis of MLE, no assumption is needed for the validity of the method.

Once the $\hat{x}$- and $\hat{y}$- estimated positions are obtained, the DOI is estimated by acquiring reference data because it was not directly included in the parametric model. In general, the parameters included in the LD model are a function of the DOI. For this, experimental reference data should be acquired by irradiating the monolithic block at a 45° angle [209].

3.1.2.2 Physical model of the LD

A LD model based on the relation between the scintillation light source and the solid-angle covered by the LD profiles has also been proposed [210]. The expression describing this relationship has three components:

1) A constant C_{est} that is mainly due to reflections of the optical photons on a diffuse reflector surrounding the scintillator block.
2) A term *f* corresponding to the optical photons directly impinging on the photodetector element.
3) Additional virtual light sources mirrored around the surfaces to take internal reflection into account.

For each detected event, the $\hat{x}$-, $\hat{y}$- and $\hat{z}$- annihilation photon interaction positions were estimated by fitting the model using both LS and WLS methods and an optimization method [210][226]. This method has shown a good overall performance without acquiring reference data [210]. Moreover, this approach was also applied when using projection readouts electronics [224].

3.1.3 Statistical methods

This section describes the positioning methods that apply common statistical-based techniques such as MLE, LS and k-Nearest Neighbor (k-NN) using the experimental characterization of the detector optical response obtained from the acquisition of reference data. The *mean* and *standard deviation* of the detector response for each photodetector element versus x_i-, y_i- and z_i- calibration positions are calculated from each individual light collection histograms. This information is stored in the so-called Look-up Tables (LUT), representing the detector response at different interaction positions. The interaction position of an annihilation photon is then estimated based on the comparison of the LD collected in the elements of the photodetector with the LUT. The identification of the data in the LUTs closer to the detected event is performed by means of LS, ML or *k*-NN algorithms. The main drawback for their application is the complex and time demanding calibration procedures needed to acquire a set of reference events. Moreover, ML positioning and k-NN algorithms also require intense computational power. In the following a detailed description of common statistics-based techniques is provided.

3.1.3.1 Maximum Likelihood Estimator

MLE methods estimate the parameters of a statistical model developed from a reference data set [211][220]-[231]. The MLE method is determined using the probability density function (PDF) of the measured signal output of the photodetector elements. The PDF of measured signal outputs $m = \{y_1, y_2, \dots, y_M\}$ is a function of the *x*-, *y*- and *z*- annihilation photon interaction position inside the scintillator. This PDF can be considered to follow a multivariate Poisson or a Gaussian distribution, and therefore, the *mean* number of photoelectrons produced by the m^{th} photodetector element, $\bar{N}_m(x, y, z)$ and the *standard deviation* of photoelectrons produced by the m^{th} photodetector element $\sigma_m(x, y, z)$ are included in the distributions [231]. In this method, the 2D or 3D annihilation photon interaction position is estimated using the Bayes rule as follows:

$$(\hat{x},\hat{y}) = \underset{x,y}{\operatorname{argmax}} \; = \; \mathcal{L}\left(Pr\left(y_1, \dots, y_M \,|x, y, z\right)\right) \tag{13}$$

where, $Pr\left(y_1, \dots, y_M \,|x, y\right)$ can be written following different equations depending if Poisson or Gaussian distribution of the observed signals is considered [231].

For the *x*- and *y*- position estimation, the method requires the characterization of the 2D detector light response by acquiring a set of reference data moving a collimation beam in a 2D array as shown in Figure 44 left. The values of *mean* and *standard deviation* were obtained for each photosensor element *m*, for each x_i- and y_i- calibration position and are stored in two different LUTs and they correspond to the $\bar{N}_m$ and $\sigma_m(x, y, z)$ variables that appear in the PDF [231]. The *mean* and *standard deviation response* of each photodetector pixel for gamma impact positions that were not included in the calibration set can be generated by interpolation of the LUT. Hence the LUT should be populated with enough calibration positions covering the whole crystal to report good accuracy of interpolation [220]. Note that, calculating the likelihood for every position recorded in the LUT in addition to some interpolated positions, and finding the maximum value among those likelihoods, is time consuming. To avoid this computational exhaustive search procedure, a method called contracting-grid search is sometimes used to find the MLE estimate [220].

Finally, several methods shown the possibility to extend the ML estimation method for the DOI (*z*- coordinate) calculation by adding an extra set of reference events acquired with an oblique irradiation beam (see Figure 44 right) [211][221][225][227][230]. Moreover, when including the *z*- coordinate in the process, the LUT(x, y) can be obtained for different DOI regions, increasing the detector spatial resolution, especially at the edges of the crystal, as explained in [211].

3.1.3.2 Least Squares

The methods enclosed in this section use the LS search method but obtaining the *mean* number of the light photons reaching the m^{th} photodetector from reference data, instead of a LD model (such as the methods explained in Section 3.1.2) [128][231][232]. In this case, the reference data sets are also collected by irradiating the detector with 511 keV photons at a series of x_i- and y_i- known positions as shown in Figure 44 and it is used to obtain the calibration of the *mean* response of the detector on a grid, named *mean* LUT(x,y). Then, the position of the actual events is estimated by searching the LUTs for the position that minimizes the LS difference between observation and mean response, that is the distance between the value of the position in the LUT and the collected signals on the photodetector array:

$$\hat{x}, \hat{y} = \underset{x,y,z}{\operatorname{argmin}} \sum_{m=1}^{M} (y_m - \mu_m(x,y)))^2 \tag{14}$$

where μ_m is the value recorded in the *mean* LUT corresponding to the m^{th} photodetector element and y_m are the measured signal value in the m^{th} photodetector element, and the sum runs over the M channels of the photodetector array.

Different works using 2D LUTs for different DOI layers have been already published [128][231]. In [128] the DOI separation was performed by fitting the LD collected for each event using the method described in [211] and also, by sorting the events as a function of the width of the measured distribution. The *mean* values for the LUT(x, y) generation were obtained for each channel, for each calibration position and for each DOI. Moreover, the authors propose a method to speed up the process based on a hierarchical search. No evidence of loss in resolution using the hierarchical search was found with respect to using an exhaustive search. No difference in the LS search was implemented for the three different sets of LUTs. In another approach, the DOI separation is performed by considering the variance of the detected signals [231]. Reference events perpendicularly impinging were then assigned to the DOI layer based on their variance and the estimated boundaries that demarcated the defined DOI layers. The *mean* LUT(x, y*)* were then calculated for each DOI layer [231].

3.1.3.3 Nearest Neighbor

This method requires the acquisition of a reference data that includes a set of LDs at a series of x_i- and y_i- calibration positions as shown in Figure 44 left. The reference data is split in *training* and *test* sets. Subsequently, unknown events are assigned to a coordinate by classifying them using the Nearest Neighbor method [234]. That is, the LS difference of the LD of the event being estimated with all LDs in the *training* set. The *k* distributions in the *training* set that produce the smallest LS error are selected as the *k*-Nearest Neighbor, and the most frequently occurring coordinate within the nearest neighbor subset is assigned to the event being estimated. This procedure is repeated for all distributions in the *test* set. An advantage of using a learning system to determine the entry points of the incident annihilation photon is that small gain non-uniformities between different photodetector pixels have a small or none influence on the spatial resolution, because they are present in both *training* and *test* sets. As each photodetector array is different, each detector must be individually trained. Additionally, the *k*-Nearest Neighbor method has the advantage that for sufficiently large reference sets, the probability of misclassification approaches the theoretical minimum: the Bayes error probability [234]. Therefore, the algorithm should yield results close to the best achievable with the given data.

This method was first proposed by Maas et al. to estimate the entry point of the annihilation photons on the front surface of the detector and thus providing an automatic correction for the DOI [233]. In this case, reference data was first acquired irradiating the detector at a series of x_i- and y_i- known positions with normal incidence (see Figure 44 left); and then repeated for various angles of incidence θ (see Figure 44 right). This standard *k*-Nearest Neighbor method has been already used by several groups [235]-[237].

The *k*-NN method requires a large reference dataset acquisition for an optimal detector performance which is time consuming and also hampers the real-time implementation as all the reference samples have to be accessed for Euclidean distance computing. To overcome this, some research groups investigated several enhancements of the *k*-Nearest Neighbor method [212][238][239]. Another approach is the so-called Mean Nearest Neighbor (MNN) [240][241], which calculates the squared Euclidean distance of the LD of an event *i* to the mean LD at the x_i-, y_i- calibration positions. The interaction position of event *i* is assigned to the grid position *m* for which the calculated squared distance is smallest.

A new Self Organizing Method Neural Network-based Nearest Neighbor (SOM-NN) positioning scheme has been also proposed and allows the possibility of FPGA implementation [232]. SOMs is an unsupervised ML algorithm able to represent high-dimensional data sets in a coordinate system (usually 2D) in such a way that the topology of the original space is maintained. That is, points that are close together in the original space remain close in the reduced dimension space created. As an unsupervised learning technique, SOMs are used to find common structures and behaviors in the data, as well as to reduce the dimension of the information. In [232] the SOM-NN is used only for mapping the large reference dataset in each calibration position into a small prototype set to effectively reduce the reference samples for Nearest Neighbor position determination, so the implementation on FPGA could be simpler with a high-event processing throughput [232].

3.1.4 Machine Learning methods

Several research groups have shown the potential to use both Machine Learning techniques -including Support Vector Machine (SVM) and Gradient Tree Boosting- and Deep Learning techniques -including Multilayer Perceptron (MLP) and Convolutional Neural Networks (CNN)- for the position estimation of the annihilation photons in PET. All of them are supervised learning algorithms (see Section 2.7), thus uses a *training* set to learn models to achieve the desired output [198]. The *training* set includes the input features and true outputs, the so-called label or ground truth, and are usually obtained by acquiring reference data irradiating the detectors at x_i- and y_i- z_i- precise positions with a collimated pencil beam of 511 keV gamma-rays, as in Statistical positioning methods (see Figure 44). In the following a detailed description of the different techniques is outlined. For more details about the principles and technical aspects of these Deep Learning methods see reference [200].

3.1.4.1 Support Vector Machines

SVM is a supervised Machine Learning algorithm used for classification and regression problems. The goal of the SVM algorithm is to find the hyperplane that best separates two different classes of data points, i.e., the hyperplane with the widest margin between the two classes (see Figure 46). This margin is defined as the maximum width of the region parallel to the hyperplane that has no interior data points. The algorithm can only find this hyperplane in problems that allow linear separation; in most practical problems, the algorithm maximizes the flexible margin by allowing a small number of misclassifications.

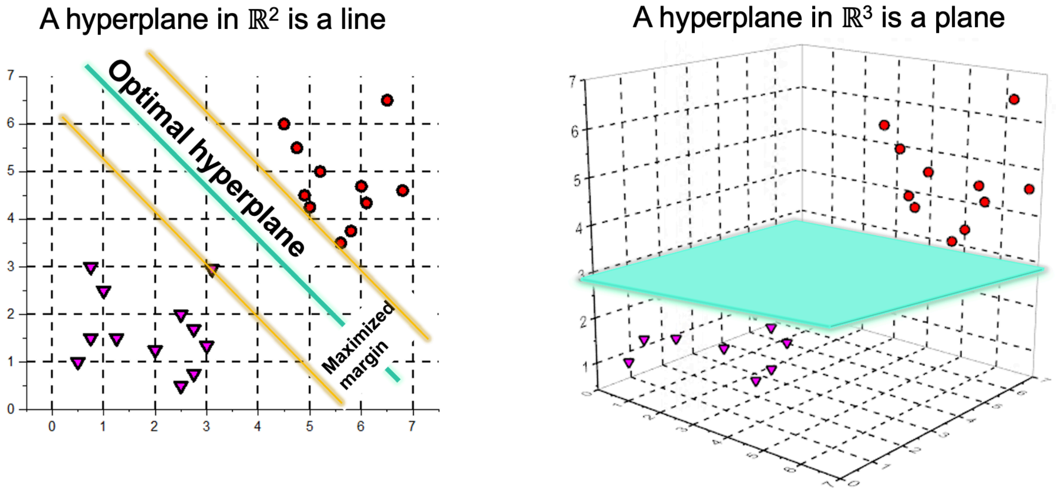

A hyperplane in $\mathbb{R}^2$ is a line

A hyperplane in $\mathbb{R}^3$ is a plane

Figure 46.- Hyperplanes in 2D and 3D spaces.

In [213] for instance, the authors applied a SVM approach to solve a regression problem for 3D position estimation of annihilation photons. In this case, *training* data was acquired from the two setups shown in Figure 44. To obtain good results, a few thousands of support vectors were required being the training speed slower than in Neural Networks with back-propagation training.

3.1.4.2 Gradient Tree Boosting

Decision trees is a predictive supervised Machine Learning method also used for classification and regression problems [242]. A decision tree consists of nodes and leaves, and it is drawn upside down with its root at the top. In Figure 47, the circles represent a condition/internal node, based on which the tree splits into branches/edges. The end of the branch that doesn't split anymore is the decision/leaf. Therefore, in a decision tree each node represents a logical divergent point where a particular characteristic of the data would be tested and then, accordingly split; the leaves represent the expected values at the point. Growing a tree involves deciding on which features to choose and what conditions to use for splitting, along with deciding when to stop [242].

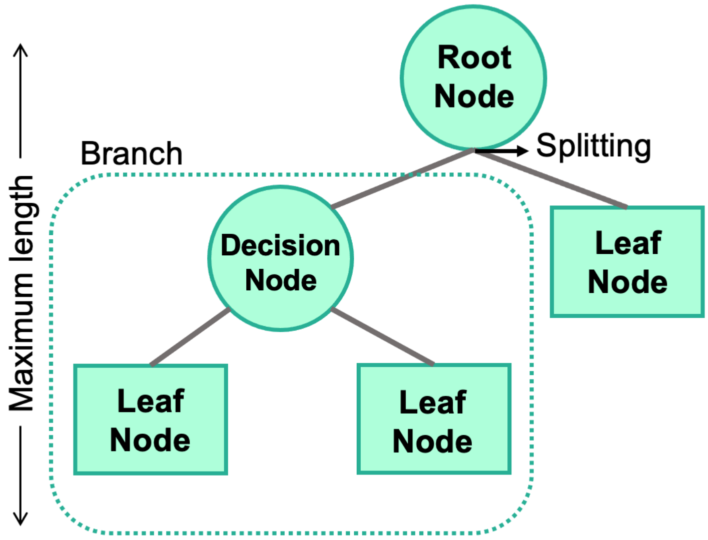

Figure 47.- Sketch of a decision tree structure.

Decision trees have an advantage over black-box models, such as NN, in terms of comprehensibility. On the one side, the logical rules followed by a decision tree are much easier to interpret than the numeric weights of the connections between the nodes in a NN. On the other side, decision trees are very simple predictors and therefore, more complex supervised Machine Learning methods based on decision trees have been proposed, such as GTB algorithms [243]. In GTBs the decision trees are created and aggregated, that is, each decision tree is built one after another to improve on the deficiencies of the previous trees and this concept is called *boosting*. The gradient part of GTB comes from minimizing the gradient of the loss function as the algorithm builds each tree [243].

GTB approaches have been already employed for the determination of the 3D photon interaction position within the crystal [214][244][245]. The ensemble decision trees are trained using acquired reference dataset containing the input features (measured detected signal in the photodetector elements) and the calibration irradiation position. The training is performed in an additive manner and the first decision tree is based on the calibration irradiation position. Every following decision tree is trained on the residuals of the previous ensemble, calculated as the difference between the irradiation position and the estimated position. Thus, every newly added decision tree corrects the results of the previous ensemble. The 3D impact coordinates of an event are fully parallelizable and computational efficient because only simple comparison between two possible outcomes is evaluated [244]. GTB models can be adapted based on the required positioning performance and memory restrictions.

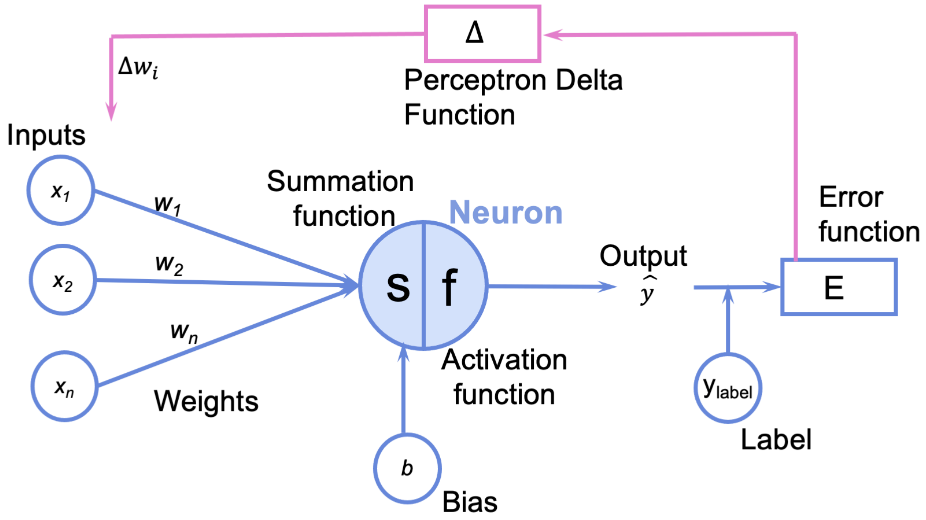

Figure 48.- Sketch of a neuron structure.

3.1.4.3 Artificial Neural Networks: Multilayer Perceptron

The perceptron (or single-layer perceptron) is a supervised Machine Learning technique developed in 1957 by Rosenblatt that illustrates how a Neural Network works [246]. It consists of a simple processing element, named neuron, that receives *n* features as input ($x = x_1, x_2, ..., x_n$) with a linked modifiable numerical value called weight, w_i (see Figure 48). The task performed by a neuron is very simple and usually is based on two actions: a summation function, *s*, and an activation function, *f*. The first one computes the weighted sum of the input features, as follows:

$$s(x) = \sum_{i=1}^{n} w_i x_i + b(x) \tag{15}$$

where, x_i is the input, w_i is its associated weight and *b(x)* is the bias. Subsequently, the result of the previous computation is passed onto the activation function *f*, which produces the output $\widehat{y}$ of the perceptron (see Figure 48). In the original perceptron, the activation function is a binary step function (threshold function), with a threshold parameter (θ), called Heaviside step function:

$$f(x) = f\big(s(x)\big) = f(x) = \begin{cases} 1, & if\ u(x) > \theta \\ 0, & otherwise \end{cases} \tag{16}$$

Since a perceptron is a supervised learning algorithm, the training step needs a *training* dataset containing the label (y_{label}), for each input set. During the training of a perceptron, the values of the weights of the neuron are modified to implement linearly separable functions following these steps over time *t* [246] (see Figure 48):

i) Initialize the weights, $w_i(t)$, and calculate the predicted output, $\widehat{y}$.
ii) Define and calculate the error function, *E,* that compares the predicted output with the label value, y_{label}.
iii) Gradient Descent for updating the weights to further reduce error. This is an iterative optimization algorithm, used to find the minimum value

for a function, in which an updated weight $w_i(t+1)$ is based on the current $w_i(t)$ and the error function as follows:

$$w_i(t+1) = w_i(t) - \eta \frac{\partial E}{\partial w_i} \tag{17}$$

where, η is the learning rate, that determines the size of the steps are taken to reach a (local) minimum. From (17) it can be written the namely Perceptron Delta Function, given by:

$$\Delta w_{ij} = w_i(t+1) - w_i(t) = \eta \cdot \delta_j(\widehat{y}, E) \cdot x_i \tag{18}$$

iv) Iteratively repeating this process updating the weights until the error is minimized.

Since a perceptron is the simplest type of Artificial Neural Networks can only classify linearly separable cases with a binary target [246]. MLP is a perceptron that teams up with additional perceptron stacked in an input layer, at least one hidden layer and, an output layer (see Figure 49 top). Each neuron behaves like a perceptron and all the units of one layer are typically connected to each unit of the succeeding layer, and hence MLP architecture is referred as Fully Connected Neural Networks (FCNN).

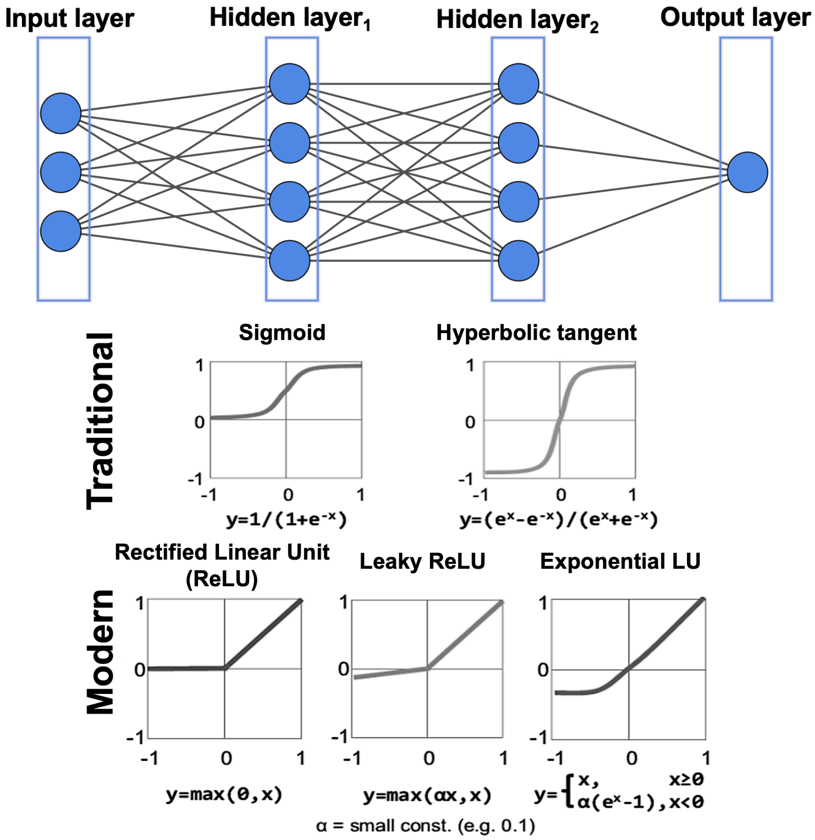

Figure 49.- Top, sketch of the Multilayer Perceptron architecture showing the input layer, two hidden layers with 4 neurons and the output layer. Bottom, the most relevant non-linear activation functions.

MLP is an interesting supervised Deep Learning technique because they are general function approximators able to resolve non-linear problems with the desired level of precision. In MLPs architectures, non-linear activation functions are used instead of the binary step activation function typically used in a perceptron, being the most typical activation functions used in MLP architectures the ones shown in Figure 49.

The training of MLP is usually accomplished by using a back-propagation algorithm. This learning algorithm belong to the groups of supervised algorithms, that is, the modification of the parameters is performed so that the network output is as close as possible to the desired output (y_{label}). The process presents two phases (see Figure 50) [247]:

i) *Feedforward propagation*. The weights of the network are fixed, and the input signal is propagated through the network layer by layer. The forward phase finishes with the computation of a loss function.

ii) *Backforward propagation*. The loss function is propagated through the network in the back direction. The network weights are updated so as to minimize a cost function in a statistical sense. In the simplest case, the cost function matches the loss function. The optimization problem is performed by computing the Gradient Descent (see Equation (17)) on the Neural Networks using the chain rule. Since back-propagation uses Gradient Descent, activation function must be a differentiable function. All the activation functions shown in Figure 49 are used for training MLPs and, thus they are differentiable. There are three popular variants of Gradient Descent, which differ in how much data they use to compute the gradient of the cost function: batch gradient descent, Stochastic Gradient Descent (SGD) and mini-batch gradient descent. Mini-batch gradient descent is typically the algorithm of choice when training an ANN, however, it does not guarantee good convergence and furthermore, it offers a few of challenges [248]. Therefore, different algorithms have been proposed by the Deep Learning community to deal with the aforementioned challenges: Momentum [249], Nesterov Accelerated Gradient (NAG) [250], Adaptative Gradient Descent (AdagGrad) [251], Adadelta [252], Root Mean Squared Propagation (RMSprop) or, Adaptative Moment Estimation (Adam) [253].

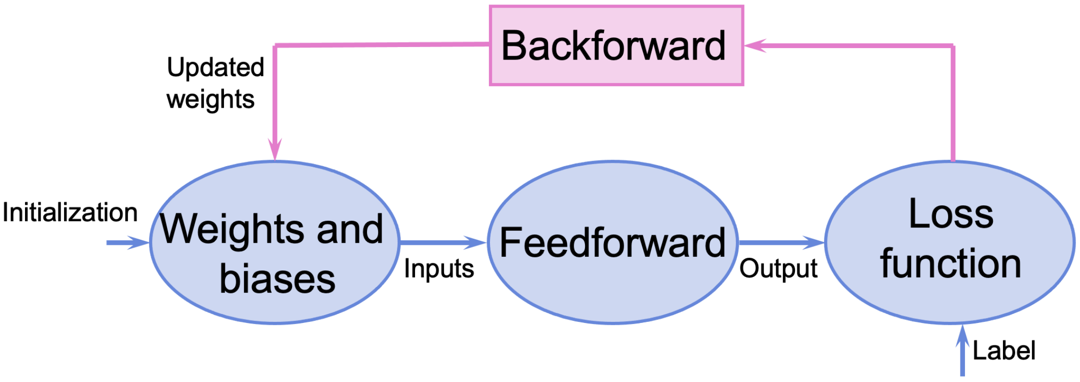

Figure 50.- Diagram of the back-propagation algorithm used for the training of MLPs.

The use of Neural Networks for the estimation of 3D annihilation photon interaction position in monolithic-based PET detector was first investigated in 1999 using a Multilayer Perceptron [254]. The MLPs are universal approximator functions since they can learn the transfer function that describes the scintillation LDs in each monolithic scintillation crystal. To accomplish this, no feature extraction is necessary as the networks can automatically learn the optimal features from a great number of input-label pairs, consisting of light output measurements from the set of photodetectors for known irradiation positions. This approach has already been studied by several research groups [237][241][254]-[262]. One of the main advantages of NN techniques compared to other methods is that, once trained, inference by forward propagating events through the network is fast and parallelizable when high computational resources are used. The increase in speed and availability of these computational resources (GPUs, supercomputer clusters, and cloud computing) has made the use of NN for 3D impact position estimation an increasingly efficient process that may end up being implemented in PET system.

3.1.4.4 Convolutional Neural Networks

Convolutional Neural Networks (CNN) are a special type of FCNN that significantly reduces the number of parameters in a Deep Neural Network with many units without losing too much in the quality of the model. CNN have found applications in image and text processing where they beat many previously established benchmarks.

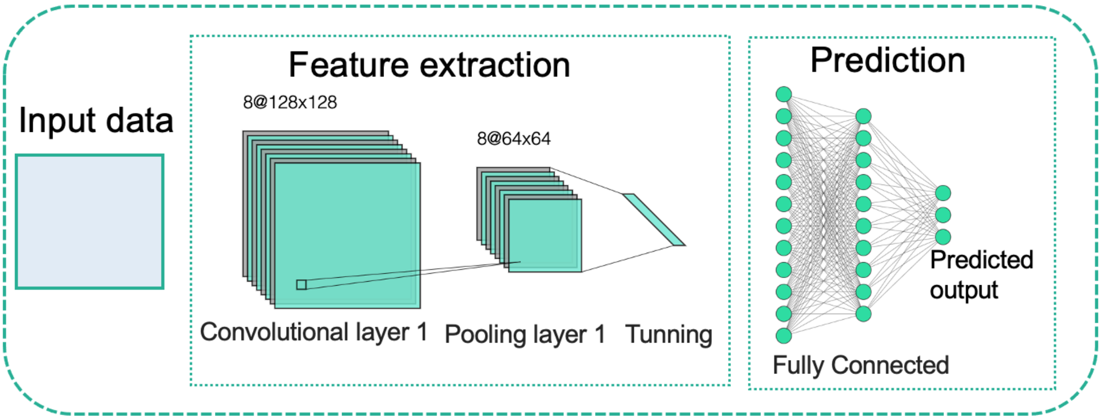

Figure 51.- Sketch of a simple structure of CNN based on a convolutional layer, a pooling layer and a fully connected layer.

CNN optimize the performance of the NN by using multilayer structures. In general, the most used layers are introduced in the following (see Figure 51):

i) *Convolutional layer*. It is used to extract critical features for getting a good prediction from the input images, which means reducing images into forms that are easier to process.

ii) *Pooling layer.* It is used to enhance the resolution of feature maps. In other words, it aims to reduce the size of matrix generated by a convolutional layer.

iii) *Fully connected layer (FC)*. The output features of the final convolutional or pooling layer it is typically flattened and connected to one or more FCNN that forms the final output. A basic structure of a FC layer, as displayed in Figure 51, is usually a fast method for learning nonlinear combinations of the high-level properties generated from convolutional layers. In that space, the FC layer will learn about a possible non-linear function.

CNN have been also used for the 3D photon position estimation [216][263]-[267]. Since CNN are usually applied to the processing of imagery instead of numerical data, the event-position-estimation task is converted from a numerical analysis-based one to an image processing by creating Tagged Image Files Format (TIFF) of optical photon distribution detected by the photosensors.

3.2 Calibration methodology of PET systems

The use of monolithic-based detectors in PET scanners requires a calibration stage that includes measurements, procedures and methods, to provide accurate 3D positioning and energy measurements of the impinging annihilation photon in the correct units [98]. The main goal of the calibration stage is to correct the non-uniformities produced by:

i) Edge effects,
ii) Light collection loses due to optical coupling mismatches,
iii) Different gains in photosensor or readout channels,
iv) Scintillation crystal LY abnormalities or other defects.

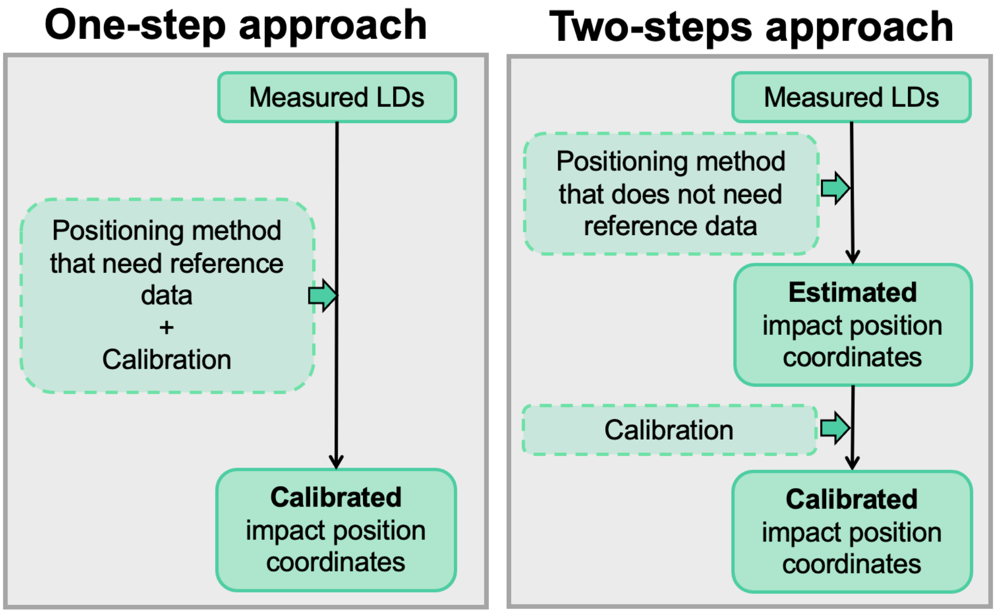

Figure 52.- Different calibration approaches depending on the positioning method selected.

Regarding impact positioning, the calibrated coordinates can be obtained following two different approaches (see Figure 52). In the *one-step calibration approach*, position estimation methods that need reference data are used, and thus directly providing calibrated impact position coordinates. In this case, the calibration includes acquisitions and procedures to obtain the reference data. In the *two-step calibration approach*, position estimation methods that do not need reference data are used to provide an estimation of the impact position coordinates. In this case, the calibration includes acquisitions, procedures and also methods to rectify the previous estimated coordinates in order to correct the edge effects and give the calibrated impact position coordinates in the correct units. Some calibration methods, such as bilinear [269], 2D polynomial [270] or 1D polynomial [271] interpolations have been already developed and implemented. In this doctoral thesis, a novel methodology based on the so-called Voronoi diagrams together with the Natural Neighboring interpolation method has been proposed and validated for monolithic-based PET detectors (see Section 4 in Chapter II for more details) [1].

At the detector level, the calibration procedure for monolithic-based detectors has traditionally been performed acquiring experimental data by moving a collimated pencil beam of 511 keV across the surface of the detector by employing different hardware setups (see Figure 53). For example, using a radioactive point source and a small pixel scintillation crystal as reference detector (see Figure 53 left). Careful alignment of the point source with the reference crystal is required to obtain useful collimated calibration beam and, moreover, the crystal and source must be moved together for scanning the crystal surface. Other possibility is to use a point source attached to a pinhole collimator and a large scintillator crystal as reference detector (see Figure 53 right). The detector under study must be moved to scan the pencil beam across the crystal surface of the monolithic crystal.

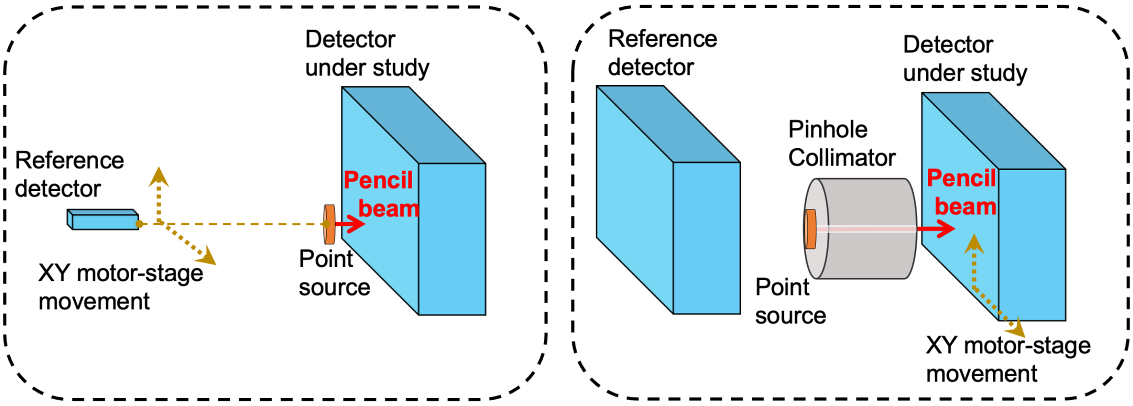

Figure 53.- Typical hardware setups used for calibration data acquisition when using monolithic-based PET detectors.

It should be noted that when calibrating full PET systems based on monolithic-based PET detectors, the process might require complex hardware setups. Therefore, it could be carried out using an auxiliary setup and individually acquire data for each detector conforming the system [273]. Each detector can be calibrated separately and later assembled in the system. Over the years after the system installation, examinations to control possible detector performance variances are performed and, if important alterations are found, recalibrations are usually suggested. In that case, the use of an auxiliary setup to individually acquire data for each detector conforming the system would imply the extraction, calibration and mounting of all detector modules in the scanner.

For practical use of monolithic crystals in commercial PET scanners, there is a major need for simpler and faster calibrations, also intended to be applied in assembled systems, i.e., with the detectors already mounted in the PET scanner.

Several groups have proposed different acquisition setups, procedures and methods to achieve these requirements, as described in the following paragraphs. For example, it has been proposed the use of a fan beam collimator instead a pencil beam collimator (see Figure 54 left) to obtain faster reference data [215][244]. However, this approach is still a time-consuming process that requires individual calibration of non-assembled detectors, which does not allow for easy recalibration once the modules are assembled in a system.

Other procedures aim to calibrate the detectors with the system already assembled have been proposed, such as the one consisting of acquiring reference data by slowly spiraling a point source close to the detectors and measuring coincidences between the closest detector and a detector on the other side of the ring. This procedure was developed and evaluated to obtain reference data to train NN for all detector modules in a PET system [274]. A different methodology based on Self-Organizing Maps has also been suggested [272]. The advantage of this method is that the *training* data can be acquired using a static uncollimated point source, thus allowing the data collection in a short period of time and with the detectors already assembled in the system (Figure 54 right). This methodology was successfully applied for monolithic block detectors in a SPECT system and could also be extended to PET systems [272].

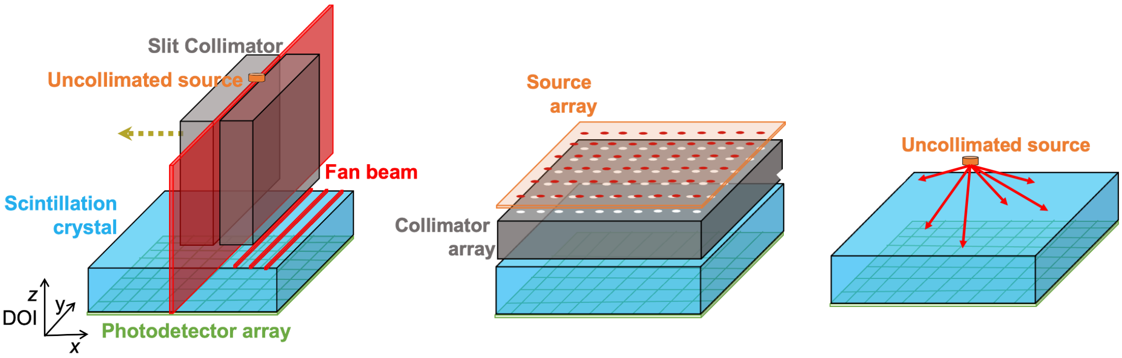

Figure 54.- Different proposals to facilitate the calibration process and reduce calibration times. Left, slit collimator generating a fan beam position. Center, array of 10×10 sources attached to an array of 10×10 parallel holes, generating an array of 10×10 gamma-ray pencil beams. Right, uncollimated source to produce homogeneous irradiation of the block.

It has been also proposed to employ an array of collimated sources, which can be obtained placing a multi-hole collimator and an array of sources in front of the monolithic block so that, annihilation photons pass through the holes (see Figure 54 center) [133]. This arrangement allows the acquisition of all the calibration positions at the same time and, therefore, reduces the detector calibration times and complexity. Different calibration methods have made use of this approach to rectify the estimated impact position and obtain calibrated data [269][270][271]. One of the main advantages of using the array of collimated sources is the possibility to perform the calibration with the detectors already mounted in the final system, thus facilitating and optimizing the process [275][276]. However, in most of the cases, the detectors are usually individually calibrated in the assembled system, which is still a difficult task, especially for PET scanners based on a large number of monolithic detectors [277] . A modified version of that procedure, that significantly reduces the calibration times, has been proposed during this thesis [2]. The method suggests the calibration of only few detectors and allows the correction for the possible differences among other detectors without the need of acquiring individual data (see Section 5.1 of Chapter II).

Other methodology proposed in the literature to obtain calibration data with the system already assembled but also reducing complexity and acquisition times is the so-called software-collimated calibration method [278]. It consists of moving a uncollimated point source placed against the entrance face of the scintillator, to obtain calibration datasets. After the acquisition, coincidence events are processed, and they are electronically collimated using software tools [279]. In this thesis, this approach has been used for the calibration of a PET insert for small animals based on a single scintillator crystal annulus (see Section 5.2 of Chapter II) [3].

Note that all the previous approaches require the acquisition of some experimental data. Recently, it has been proposed a novel method consisting of using simulated data to obtain the responses of each photodetector for a given 3D interaction position and use it for the training process of Neural Networks [260][280]. This procedure has been successfully applied to a dedicated PET system for brain imaging based on 60 monolithic-based detectors [280]. This method is feasible, robust and accurate, because of the improvement of the capabilities of the different simulation platforms and machine learning techniques, which allow its implementation easily and no requiring per-detector experimental calibration. This approach has also been applied but for the generation of LUT for ML positioning method [281].

II Objectives and contribution to PET technique

The second Chapter of this dissertation describes the main objectives pursued during the course of this doctoral work, including the candidate’s contribution to the PET imaging field.

The advantages reported in PET detector designs based on monolithic crystals triggered the interest in implementing them in PET scanners. However, more complex tasks are usually required to accurately obtain the 511 keV annihilation photon interaction position. Herein, the main objective of this PhD work is the development and validation of different monolithic-based PET detector configurations, position estimation methods and calibration procedures to overcome the shortages of these designs. Then, apply these new methodologies for the construction of PET system prototypes. To accomplish these goals, the following specific objectives were defined:

- i) Software development and implementation of methods for an accurate determination of 3D annihilation photon impact position.
- ii) Acquisition of experimental data and comparison of methods using different detector configurations.
- iii) Assembly of different PET system prototypes.
- iv) Application of the developed software methods in those PET systems.
- v) Validation of PET systems performance.

In the following sections, the major aspects of the implemented position estimation methods and calibration procedures are reported. Also, a detailed description of the main research projects in which the candidate has contributed within the timeframe of this thesis, is reported.

4 Contribution to position estimation and calibration procedures

Along the course of this doctoral work, two main approaches to accurately determine 3D impact position in monolithic-based PET detectors have been proposed, developed and experimentally validated.

First, it has been studied the use of analytical position estimation methods in monolithic detectors. As previously described, a calibration methodology is required when using those positioning methods to correct for the inhomogeneous compression that affects the flood maps and provide the calibrated impact position coordinates in the correct units. As an example, Figure 55 left shows a flood map measured using a 11×11 collimated ^{22}Na sources normally impinging to a monolithic detector. This flood map was obtained by estimating the 2D impact coordinates using the RTP algorithm. All the maxims can be clearly identified. The separation of the collimated sources is accurate in the central region, while compression effects due to the truncation of the LDs at the edges are observed since the distance between the last two columns/rows of sources is reduced compared to the central ones. When using calibration methods based on bilinear [269], 2D polynomial [270] or 1D polynomial [271] interpolations, compression effects are reduced but artifacts are generated close to the edges of the crystal (see Figure 55 center) and, therefore, the effective crystal volume considered for reconstruction decreased [271].

During this thesis, a novel calibration methodology based on the so-called Voronoi diagram and Natural Neighbor interpolation has been developed. For simplify, the latter will be referred to as Voronoi calibration. Voronoi diagram is a mathematical segmentation that divide the plane in convex polygons, known as Voronoi cells, which are delimited by the point of the plane closest to the cell surroundings (see Figure 56) [282]. Let $P = \{p_1, p_2, \ldots, p_n\}$ a set of n sites (points) in the plane, the Voronoi cells for a site $p \in P$ is the set of all points in the plane that have p as nearest site [282]. The Voronoi diagram *Vor(P)*, is the subdivision of the plane into Voronoi cells for all $p \in P$ (see Figure 56) and can be computed from the Delaunay triangulation *DG(P)* (see Figure 56).

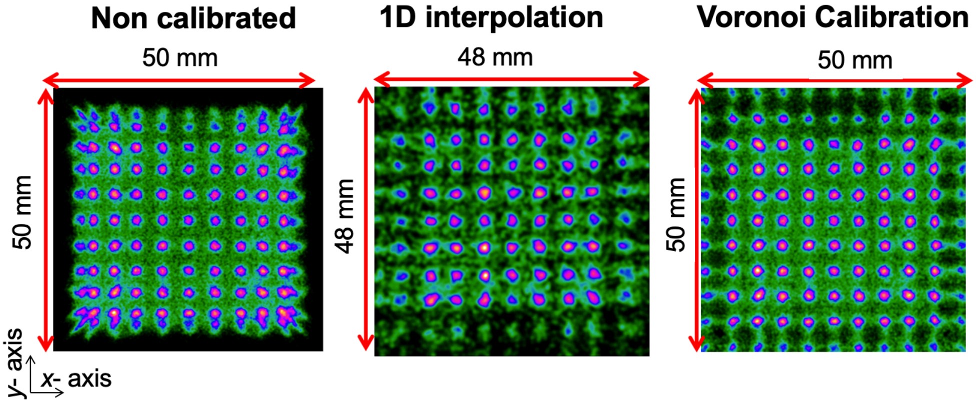

Figure 55.- Flood maps measured using an array of 11×11 collimated ^{22}Na radioactive sources. From left to right, non-calibrated, calibrated using the 1D interpolation method and calibrated using Voronoi calibration methodology.

The Voronoi calibration implemented during this thesis provides calibrated 3D impact position and energy of the interactions of the annihilation photons. Figure 57 shows a diagram illustrating the steps of the method. The detector calibration consists of acquiring experimental data by irradiating the detectors at x_i- and y_i-precise calibration positions, obtaining a calibration map, and subsequently generating the Voronoi diagram composed by several Voronoi regions equal to the number of calibration positions. Voronoi factors for the 3D position and energy are calculated for each region, and the corresponding LUTs are obtained using the Natural Neighbor interpolation method [283]. Figure 55 right shows the flood map obtained after Voronoi calibration, and it can be seen that the edge effects are reduced without the presence of artifacts (see Figure 55 right). Notice that the Voronoi calibration also provide calibrated DOI and energy. The method has been implemented using MATLAB software since it provides specific functions that allow the generation of the Voronoi diagrams and application of the Natural Neighbor interpolation.

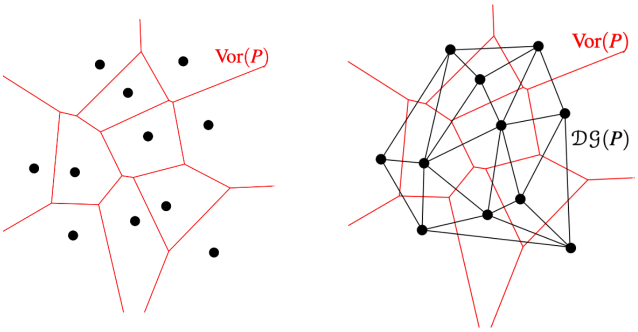

Figure 56.- Representation of Voronoi diagram and the so-called Delaunay triangulation (the dual graph of the Voronoi diagram).

This methodology was first validated at the detector level by acquiring data with an LYSO monolithic crystal of 50×50×15 mm^3 dimensions coupled to an array of 12×12 SiPMs. The photodetector array was connected to a custom electronic system that included a projection readout circuit that sum signals in the row and column directions, thus reducing the number of signals from 144 (12×12) to only 24 (12+12). The detector was calibrated by acquiring data from an array of 11×11 collimated ^{22}Na point sources. The methodology was compared with the calibration approach based on 1D polynomial interpolations for different crystal surface treatments. The article [1], enclosed as part of this thesis, explains the details of the experimental procedure, implementation of the method, calibration process and most relevant experimental results obtained with the developed methodology.

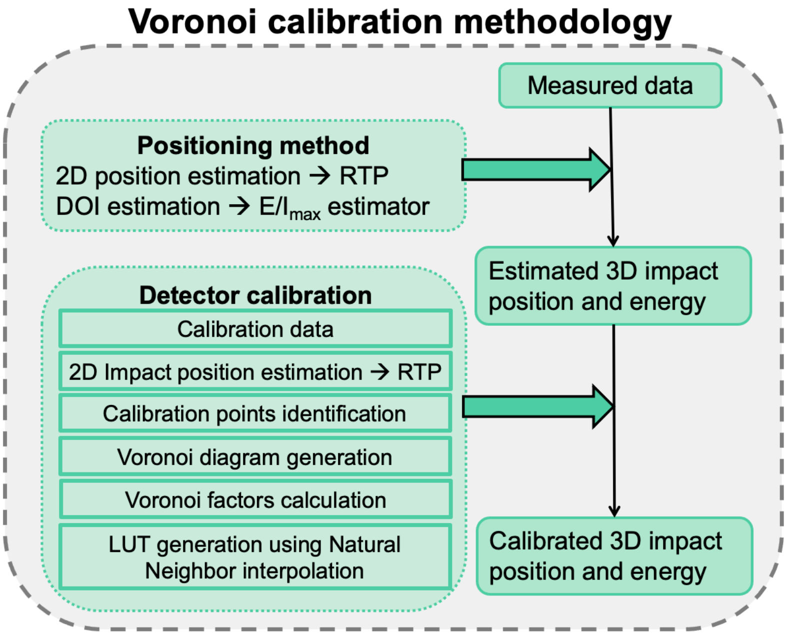

Figure 57.- Schematic steps of the Voronoi calibration methodology.

The Voronoi calibration was also validated at the detector level using LYSO monolithic crystals of 51.5×51.5×3 mm^3 (very high aspect ratio), read out using the lateral faces 51.5×3 mm^2 by means of 1×16 SiPM elements [284]. This detector block design was envisaged for its application in PET systems with multiple separated crystal layers, so each layer can work as a PET or as a Compton camera.

When validating the Voronoi methodology, the work also focused on its applicability at system level. The Voronoi calibration has been applied to a PET system prototype with a modular configuration, following a *standard procedure,* in which each detector is individually calibrated; and two *alternative procedures* developed during the thesis to reduce calibration times and facilitate the process (see Section 5.1 for more details) [2]. Moreover, the Voronoi calibration method was slightly adapted to be used in an edge-less PET system for small animals based on a single scintillator annulus crystal (see Section 5.2 for more details) [3].

Secondly, since supervised Deep Learning algorithms have already demonstrated the power to resolve big non-linear problems, along the course of this thesis, a position estimation method using a Neural Network technique has been proposed. The NN has been implemented using TensorFlow, a Python-friendly open source library that streamline and facilitate the development of NN. The implemented method consists of using a MLP architecture for each coordinate, named MLP_X, MLP_Y and MLP_Z, for the *x*-, *y*- and *z*- coordinates, respectively. The inputs of each MLP are the SiPMs summed column and row signals and the outer value corresponds to the predicted *x*-, *y*- and *z*- coordinate for the MLP_X, MLP_Y and MLP_Z, respectively (see Figure 58). The number of hidden layers and nodes used in the MLPs architectures depends on the detector under evaluation.

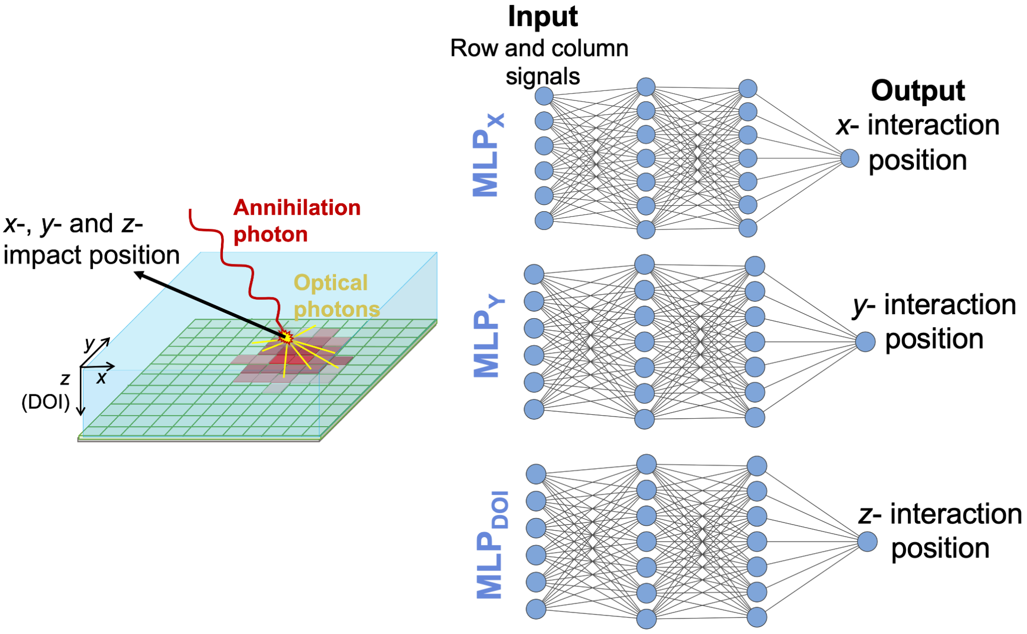

Figure 58.- Sketch of MLP architectures used for the *x*-, *y*- and *z*- positioning estimation.

The implemented NN technique has been used for the *x*- and *y*- annihilation photon position estimation in a novel detector configuration based on gluing monolithic crystals using a high-refractive optical compound. Article [4], enclosed as part of this thesis, shows the experimental validation of the NN technique at the detector level. This approach has been used in a dedicated breast PET scanner, recently built at i3M (see Section 5.3 for more details).

Furthermore, this NN has also been applied for the *x*-(monolithic) and *DOI*- annihilation photon position estimation in semi-monolithic-based detectors [106] that are going to be employed for the construction of preclinical [104] and a TB PET [285] scanner that are currently under development at i3M. The external surface is 25.4×25.4 mm^2 in both cases. The semi-monolithic array is composed by 24 slabs of 25.4×1×12 mm^2 for the preclinical scanner and by 8 slabs of 25.4×3×20 mm^2 for the TB system (see Figure 59). Two independent MLPs were used, named MLP_X and MLP_{DOI}, with the number of input the SiPM projection signals in the monolithic direction and the output, the *x*-(monolithic) and DOI- coordinates, $x_{predicted}$ and $DOI_{predicted}$, respectively. In a first step, the NN technique was validated at the detector level by acquiring reference data by moving a pencil beam generated with a pinhole collimator. Different crystal geometries, surface treatments and SiPM models were tested to evaluate the impact on the position accuracy and spatial resolution [106]. Notice that the selection of the best configuration is a compromise between the spatial capabilities (linearity, spatial resolution), detector timing resolution and sensibility, among others. In a further step, it has been proposed to reduce calibration time, *training* data was acquired using a fan beam along the monolithic and DOI directions, instead of using the pencil beam. Figure 59 shows the results obtained with the semi-monolithic detector configurations employed for the construction of the preclinical and TB scanners. In these results, the bias parameter was defined as the difference between the predicted impact coordinate and the known mechanical beam position. The spatial resolution has been obtained as the FWHM of the Gaussian fit of the $x_{predicted}$ or $DOI_{predicted}$ accumulative distribution.

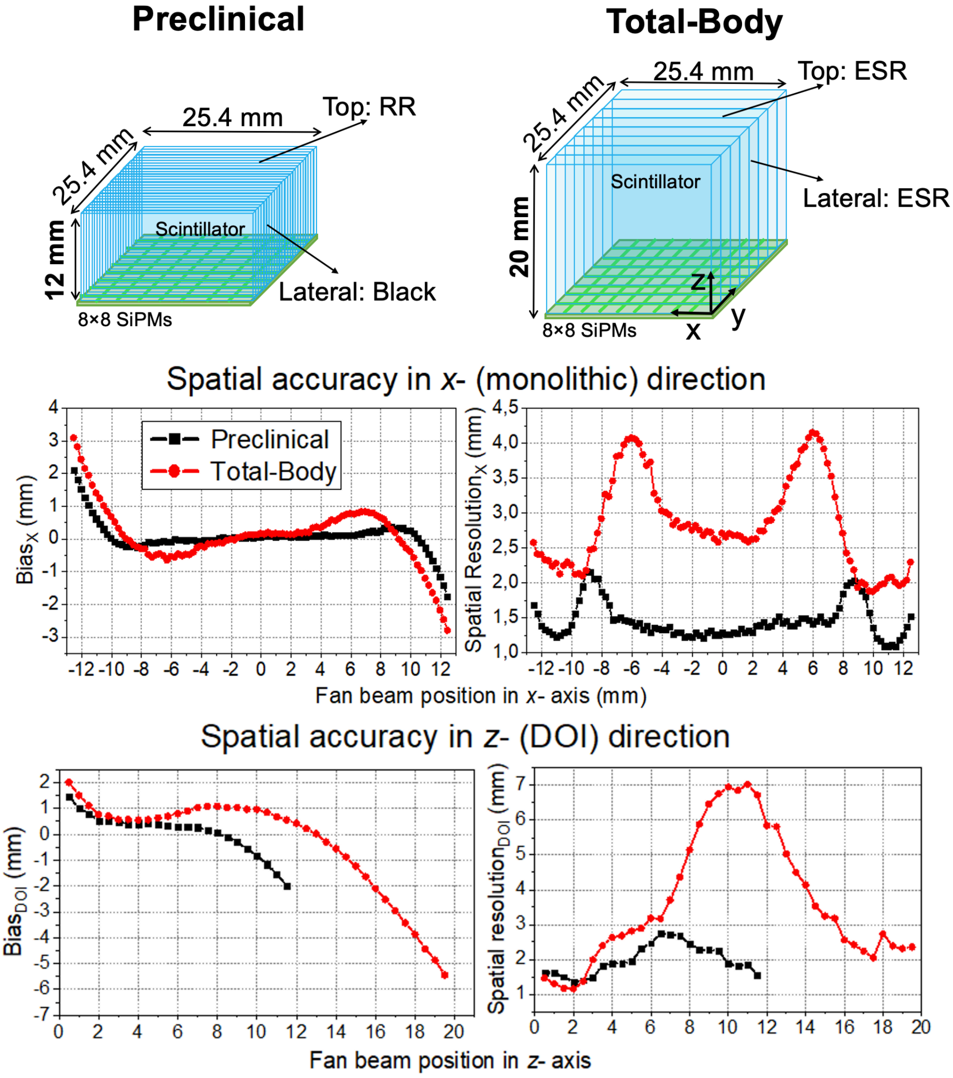

Figure 59.- Top, sketches of the semi-monolithic configurations for the preclinical (Compton camera) and Total-Body PET scanners under development at i3M. Center, bias and spatial resolution of the *x*- (monolithic) coordinate. Bottom, bias and spatial resolution of the *z*- (DOI) coordinate.

5 Contribution to research projects

One of the main goals of this thesis has been to demonstrate the potential of the developed methods, not only at single-detector level, but also in full assembled PET scanners prototypes. The methods described in the previous section have been applied to several systems which form part of different projects as described in the following paragraphs.

5.1 ProsPET

ProsPET is a Spanish National project awarded by the Spanish Ministerio de Economia y Competitividad and co-financed by the European Union through the European Regional Development Fund (ERDF) in January 2016. The project lasted for two years and was leaded by i3M in collaboration with the *Hospital La Fe* in Valencia. The main objective of the *ProsPET* was to develop a reliable system for the accurate diagnosis of Prostate Cancer (PCa) based on Molecular Imaging.

The most frequently used method for imaging the prostate is transrectal ultrasound tests (TRUST). However, this process has a clinical sensitivity of around 60%, more reliable for large and advanced tumors. Yet, the development of new specific radiotracers for prostate imaging allowed the use of molecular imaging for monitoring and treatment of PCa. However, WB-PET systems are not the most appropriated for PCa due to their limited spatial resolution and sensitivity. For this reason, a dedicated PET system for prostate imaging (see Figure 60) was proposed since it could offer several advantages compared to WB-PET systems (as mentioned in Section 2.6.3).

The axial length of the proposed system is 50 mm; and the inner and outer diameters are 416 and 446 mm, respectively. The scanner is composed of 24 detectors based on an LYSO monolithic crystal of 50×50×15 mm^3 coupled to an array of 12×12 SiPMs, arranged in a single ring (see Figure 60). All sides of the scintillation crystal were polished, and the four lateral walls were painted black to reduce undesired reflections. The entrance side of the scintillator was covered with a RR layer. The electronic part of the detector includes our custom projection readout system that reduces the 144 SiPM signals to only 24 signals [286]. The 12 SiPM signals of each row and column of the photosensor array were summed and pre-amplified before transferring to the DAQ. Figure 60 shows a photograph of one of the detectors used in this scanner.

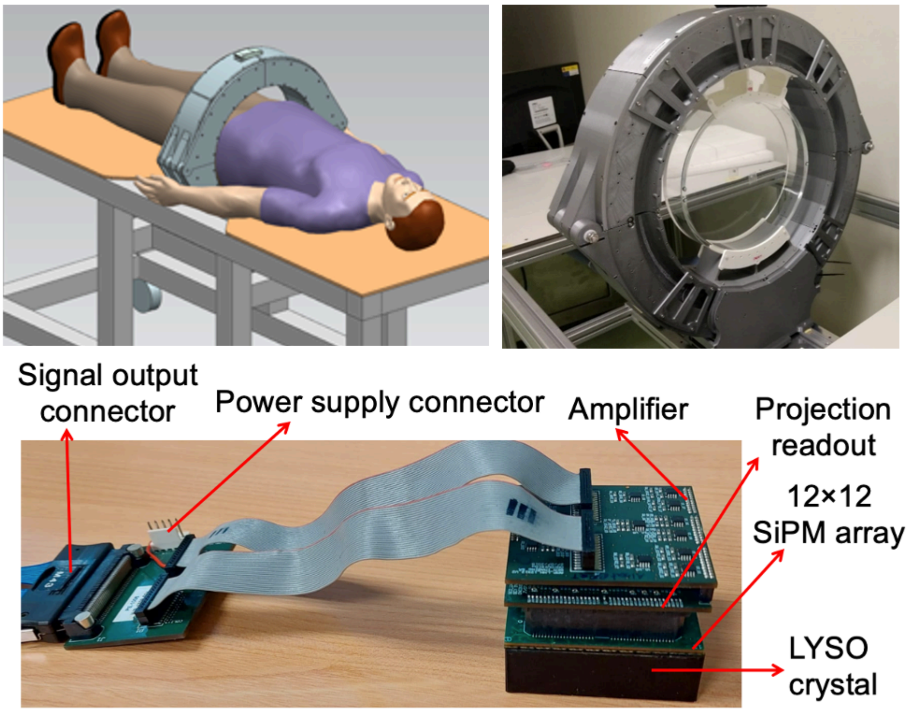

Figure 60.- Top, sketch of the *ProsPET* system and photograph of the system acquiring data using a large uniform activity phantom. Bottom, monolithic-based detector used in the *ProsPET* system.

Article [1], enclosed in this thesis, provides detailed information on the detector performance in terms of 3D spatial and energy resolution before and after applying the Voronoi calibration methodology. The Voronoi calibration methodology was applied to correct the 3D impact position estimation and energy in the whole detector volume. The calibration of the complete PET system was performed with the detectors already assembled and two different procedures have been followed:

i) *Standard calibration procedure*. Each detector block is individually calibrated by placing a 11×11 collimated ^{22}Na source array attached to each, obtaining the calibration map and applying the Voronoi calibration method. Therefore, a LUT was directly generated for each detector module.

ii) *Alternative procedure*. This method only requires the acquisition of calibration data with the 11×11 sources array for (at least) three random detector modules of the system; and a uniform measurement of each detector in the system that can be easily obtained by placing a relatively large uniform activity phantom at the center of the scanner FOV as shown in Figure 60. A mean calibration map was obtained averaging the calibration map measured with the three random detectors, and it was slightly modified for each detector module as a function of their uniform measurement. This novel strategy has been proposed during this thesis with the goal of simplify and accelerate the calibration process.

Article [2], also included as part of this thesis, provides details about the system performance when using the previous two approaches for the scanner calibration.

5.2 ScintoTube

ScintoTube is a project funded by the National Institute of Health (NIH) in USA. It was granted in September 2020 and has a duration of 5 years. The project is leaded by the i3M in collaboration with the University of Virginia and, supported by the multinational company Bruker.

The main objective of the *ScintoTube* project is to develop a PET insert for small animals able to surpass state-of-the-art sensitivity while improving spatial resolution. To accomplish this, a novel design concept using a single scintillation crystal (annulus), instead of the typical modular pieces, has been investigated. The spatial resolution improvement expected by implementing this scintillator approach was first demonstrated using experimental data from a PET system for small animals based on a ring of monolithic blocks. When suppressing the events near to the edge of the crystal (that suffer compression effect), the spatial resolution of the reconstructed image increases in a factor of 25% compared to the case employing all the events, see [121] for more details.

During this thesis, the first prototype, named *ScintoTube I*, based on a LYSO scintillator annulus with an inner circular face but ten facetted outer faces was designed to simplify the mechanics related to the photosensor coupling and electronics readout. This design was compared with the typical modular configuration through simulations, including both nuclear and optical tracking. Its feasibility was demonstrated as shown in [121].

The *ScintoTube I* exhibited an inner diameter of 62 mm, and an axial length of 52 mm (see Figure 61 top). The outer faces were 26×52 mm^2 each. The crystal thickness varied between 9 and 10 mm. Ten custom Printed Circuit Boards (PCBs) allowing the allocation of 3 arrays of 8×8 SiPMs were coupled to the outer flat face of the crystal. To simplify the characterization of this first prototype, each PCB is populated with only one SiPM array, thus reducing the axial FOV of the system to 25.8 mm. Each PCB includes our custom reduction readout system based on passive components that add the signals of each row and column of the SiPM array [286], reducing the signals of each PCB transferred to the DAQ, from 64 SiPM signals to only 16. The Voronoi calibration methodology has been modified to its exploitation in this novel system design. Calibration data was experimentally obtained by placing the ^{22}Na source attached to the inner face of the tube at known positions but, in this case, without collimator as the small inner diameter of the system made it difficult to use it. Therefore, the calibration positions were obtained for each source position applying a software-collimation method in a post-processing step as described in [278]. Both the *x*-(transaxial) and *y*-(axial) coordinates and the energy are affected by the photon DOI and therefore, the Voronoi calibration methodology was modified as described in [285]. Article [3], enclosed in this thesis, presents the experimental validation of this modified calibration methodology, showing the system performance in terms of 3D spatial and energy resolutions, system sensitivity, count rate capabilities, and reconstructed image quality.

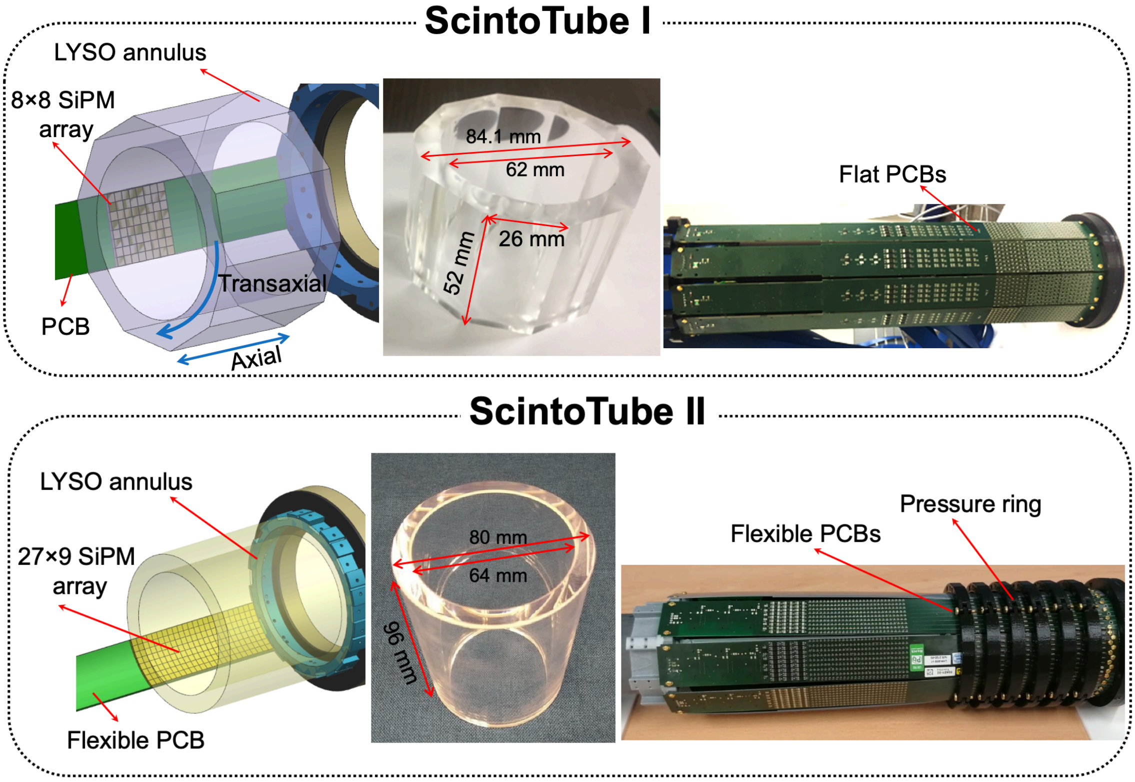

Figure 61.- Sketch of the systems, and photographs of the LYSO annulus and constructed scanners. Top, *ScintoTube I* and, bottom, *ScintoTube II*.

Unfortunately, the faceted outer faces inferred some challenges because the critical angle is determined from the normal of each photodetector plane and then, the different acceptance angle of the scintillation light into the photosensors caused undesired effects on the LD shapes at the facet joints (see Figure 62). This effect was alleviated using the proposed calibration procedure; however, some degradation of the spatial resolution remained at the facetted joins and then, the quality of the reconstructed images was not fully optimized.

To solve this problem, a second prototype, named *ScintoTube II*, with both the inner and outer faces using a cylindric shape was proposed [289]. The system has been recently built using a modified version of the custom PCBs that allows the SiPMs to be coupled to the outer cylindrical face of the tube (see Figure 61 bottom). The Voronoi calibration was also applied to this scanner and a NEMA evaluation is being currently carried out.

It should be noticed that these developed PET inserts make use of a electronics technology compatible with the high magnetic fields found in MRI systems, together with radiofrequency shielding based on carbon fiber composites, see reference [290] for more details.

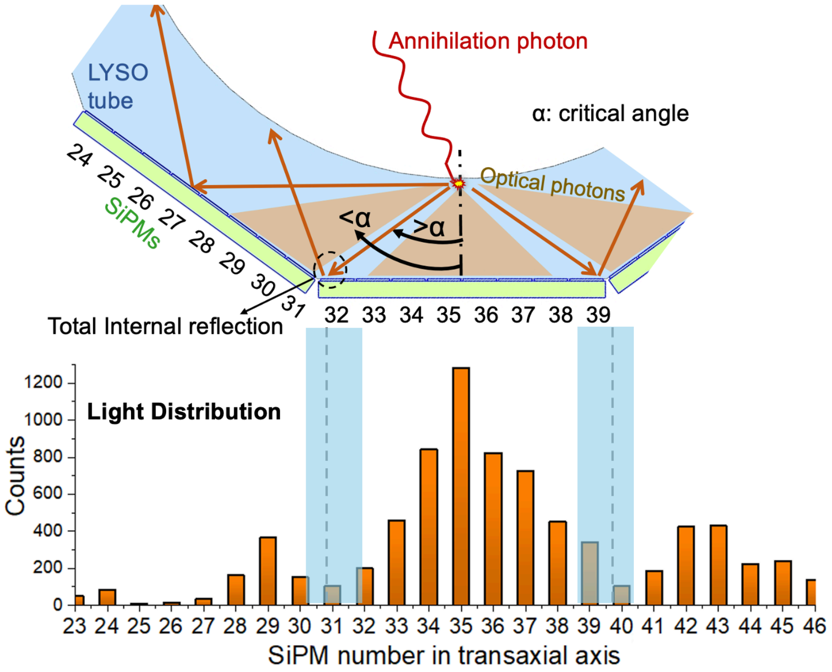

Figure 62.- LDs for one annihilation photon impact inside the LYSO tube using experimental data. Some optical photons are not collected by the photosensors since they suffer total internal reflection at the facet joints, producing gaps in the LDs.

5.3 DeepBreast

DeepBreast is the acronym of a Spanish National project leaded by i3M and funded by the Ministerio de Economía y Competitividad and co-financed by the European Union through the European Regional Development Fund (ERDF). The project was granted in June 2020 and has a duration of 3 years. The goal is to develop a dedicated breast PET system, named *DeepBreast* to increase system sensitivity and to reduce edge effects, inspired by the *ScintoTube* project but for humans and larger dimensions therefore. This can be accomplished by gluing monolithic scintillation crystals using a compound with a refractive index similar to the scintillator one.

Several works have already demonstrated that gluing the scintillators provides good spatial linearity and resolution at the interfaces that interconnect monolithic crystals [127][128]. However, some optical photons still undergo internal reflections at these regions due to the mismatch between the refractive index of the compound and the scintillation material, and therefore, the shape of the LD is not fully preserved. Nevertheless, the use of Deep Leaning techniques for the estimation of the annihilation photons inside the crystal may help reducing these effects. Therefore, the goal of this project is to build a system based on 14 curved monolithic LYSO crystals glued together using a high refractive index compound (Meltmount, n=1.7) (see Figure 63) thus eliminating the gaps in the transaxial axis and allowing the light transmission between adjacent crystals. Also, a major objective is to implement Deep Learning techniques for the impact position estimation to reduce the edge effects as much as possible.

The feasibility of this approach was first evaluated at the detector level, using two LYSO crystals of $33\times25.4\times10$ mm^3 side-by-side optically glued by of the Meltmount compound. NN were implemented for impact estimation based on two MLP, named MLP_X and MLP_Y that predict the *x*-(transaxial) and *y*-(axial) impact coordinates of the annihilation photons, respectively. For the training process, experimental data was acquired using a fan beam instead a pencil beam to reduce calibration times. Article [4] enclosed in this thesis shows the experimental results of the detector performance when using the NN technique and an analytical method for impact position estimation. Moreover, the Meltmount configuration was compared to two additional coupling methods: optical grease (refractive index n =1.46) between crystals and isolated blocks using black paint and air interface.

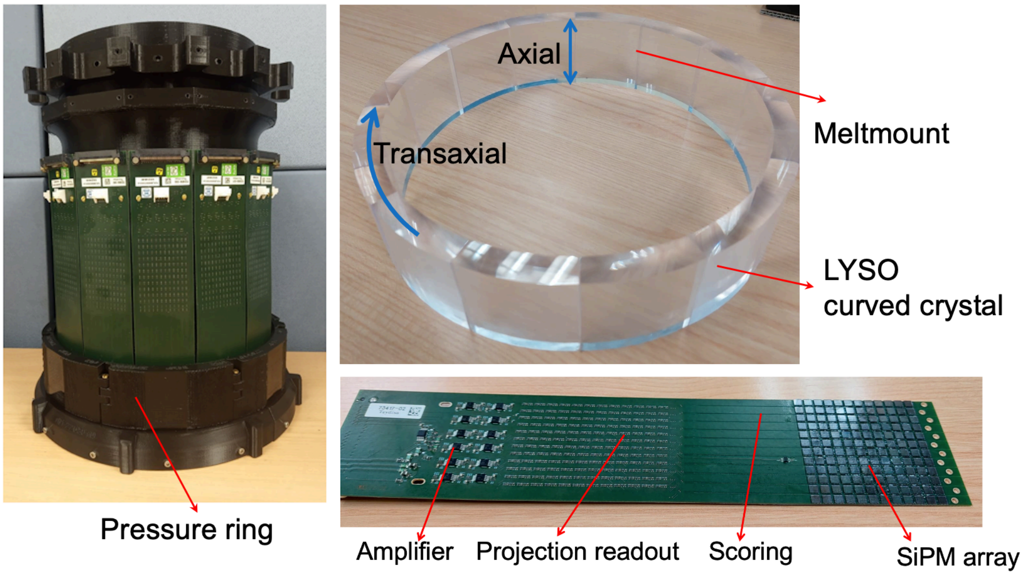

Figure 63.- Left, photograph of the *DeepBreast* system. Right, photograph of the LYSO annulus and one of the PCB including the SiPMs and the readout circuit.

The *DeepBreast* system is composed by 14 curved monolithic LYSO crystals glued together using Meltmount material and coupled to custom flexible PCBs that contain 12×12 SiPMs (see Figure 63). Pressure rings were used to bend the PCBs ensuring the coupling between the crystal and the photosensor surface. The system was recently built with inner diameter of 200 mm, outer diameter of 225 mm; and axial length of 50 mm. A Neural Network technique based on two independent MLPs for the *x*- (transaxial) and *y*- (axial) coordinates was implemented. *Training* data was obtained by acquiring experimental data using a ^{22}Na source placed in between a custom slit collimator (composed of two tungsten disks (see Figure 64)). The tungsten plates were mounted at a thin separation (0.4 mm) generating a fan beam radiation in 360°. For *training* data acquisition of the MLP_X, the slit collimator was mounted in a rotational motor and data was acquired rotating it in steps of 0.8° in the transaxial direction (*x*- axis). For *training* data of the MLP_Y, the slit collimator was mounted in a linear motor stage and it was moved in steps of 0.5 mm in the axial direction (*y*- axis). Regarding DOI and energy, the Voronoi calibration methodology was employed to obtain DOI values in mm and energy values in keV.

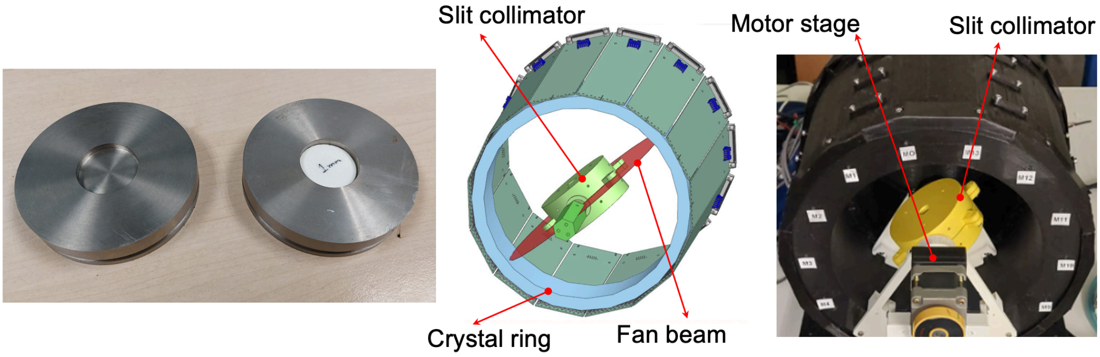

Figure 64.- Left, photograph of the tungsten plates used for the custom slit collimator. Center, sketch of the calibration setup used for the calibration of the transaxial axis. Right, photograph of the setup.

We are currently carrying out the system performance evaluation based on a modified version of the NEMA protocol for WB-PET, and it is planned to be submitted for publication soon. Figure 65 left shows the radial, tangential and axial reconstructed spatial resolution (FWHM) as a function of the radial position. It can be appreciated that homogenous spatial resolution is found for all the radial positions since DOI information allows the reduction of parallax errors. Figure 65 right shows the sensitivity obtained with the *DeepBreast* system with a 30% energy windows.

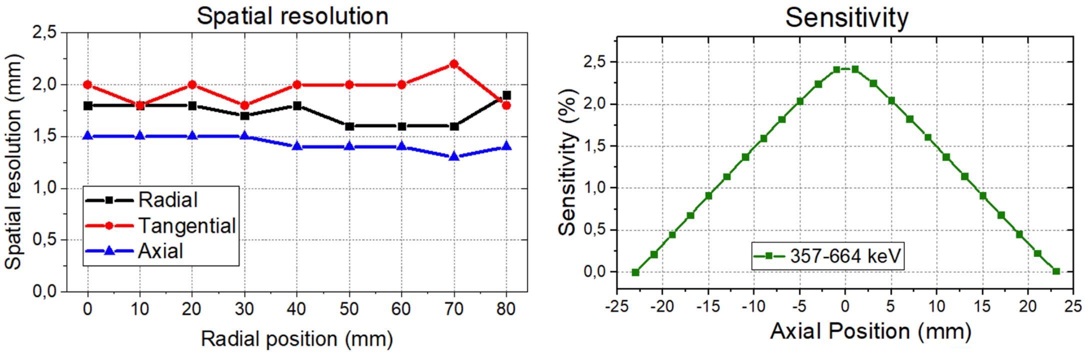

Figure 65.- Left, *DeepBreast* FWHM spatial resolution with DOI information. Right, *DeepBreast* sensitivity obtained with a ^{22}Na point source.

III Scientific Research

Chapter III includes the four scientific peer-reviewed articles which have been selected to compile this PhD thesis and in which the candidate is the first author. Notice that to avoid confusions with the numbering in figures, tables and references list of the thesis, their labelling have been renamed as *[Pi.j]*, where *i* denotes the paper and *j* the figure, table or reference particular number.

The main candidate´s contribution to the research field is supported by the selected articles and focus on the implementation and application of novel approaches to accurately determine the 3D photon impact in monolithic-based PET detectors. Different position estimation methods and calibration procedures have been developed in different software platforms (C++, MATLAB, Python, ROOT). The candidate has also experimentally validated these methods by participating in the design of the tests as well as on hardware implementation. This includes the assembly process of all the detector configurations and PET scanners and the acquisition of the experimental data. Moreover, the candidate has contributed to the data analysis and the interpretation of the subsequent results.

6 Calibration of gamma ray impacts in monolithic-based detectors using Voronoi diagrams

Authors: Marta Freire, Andrea González-Montoro, Filomeno Sánchez, José M. Benlloch and Antonio J. González.

Published: IEEE Transactions on Radiation and Plasma Medical Sciences, 2019, Vol. 4, No. 3, p. 350-360. Doi: 10.1109/TRPMS.2019.2947716

Summary: This article explains the methodology and implementation at detector level of the Voronoi calibration technique developed during this thesis. The method has the primary objective of reducing edge effects in monolithic-based PET detectors, allowing to calibrate the entire crystal volume, (see Section 4 of Chapter II).

In this article, the Voronoi method has been validated using experimental data acquired with a LYSO monolithic crystal of 50×50×15 mm^3 coupled to an array of 12×12 SiPMs. The implemented calibration method has been compared in terms of 3D spatial and energy detector performance with the commonly used 1D polynomial method. Our methodology has been proven to be superior since indeed the total volume of the detector could be accurately calibrated. Moreover, experimental data using different surface crystal treatments using black paint, RR, Teflon or ESR have been measured to evaluate the detector performance in each case. In particular, the best overall performance was obtained when the

LYSO lateral walls were black painted and the RR layer was added to the entrance of the crystal, with a spatial resolution of 1.6±0.1 mm FWHM and an energy resolution of 17.5%.

As a result of those studies, we decided to apply the Voronoi calibration method to a dedicated prostate PET system [2], and to a small-animal PET insert [3].

Calibration of Gamma Ray Impacts in Monolithic-Based Detectors Using Voronoi Diagrams

Marta Freire, Andrea Gonzalez-Montoro, Filomeno Sanchez, Jose M. Benlloch and Antonio J. Gonzalez.

Abstract— *Molecular imaging systems, such as PET, use detectors providing energy and 3D interaction position of a gamma ray within a scintillation block. Monolithic crystals are becoming an alternative to crystal arrays in PET. However, calibration processes are required to correct for non-uniformities, mainly produced by the truncation of the scintillation light distribution at the edges.*

We propose a calibration method based on Voronoi diagrams. We have used 50×50×15 mm^3 *LYSO blocks coupled to a 12×12 SiPMs array. We have first studied two different interpolation algorithms; Weighted Average Method (WAM) and Natural Neighbor (NN). We have compared them with an existing calibration based on 1D monomials. Here the crystal was laterally black painted and a retroreflector (RR) layer added to the entrance face. The NN exhibited the best results in terms of XY impact position, depth of Interaction and energy, allowing us to calibrate the whole scintillation volume. Later, the NN interpolation has been tested against different crystal surface treatments, allowing always to correct edge effects. Best energy resolutions were observed when using reflective layers (12-14%). However, better linearity was observed with the treatments using black paint. In particular, we obtained best overall performance when lateral black paint is combined with the RR.*

Index Terms— *Gamma ray detectors, Positron Emission Tomography, Monolithic crystals, SiPM, Calibration processes, Voronoi diagrams.*

1. Introduction

Radiation detectors are extensively used in the field of nuclear and atomic physics, characterizing particles interacting with them. This requires precise determination of their deposited energy and 3D impact coordinates. These quantities are accurately estimated employing calibration procedures addressing non-uniformity responses of the detectors [P1.1]-[P1.3]. In particular, γ-ray detectors are of special interest in both high energy and medical physics. They are key components of molecular imaging systems, such as gamma cameras, Single Photon Emission Computed Tomography (SPECT) or Positron Emission Tomography (PET) scanners [P1.4].

In the particular case of PET, providing accurate reconstructed process requires: *i)* precise determination of the energy, XY planar coordinates as well as Depth of Interaction (DOI) of the γ-ray within the scintillation crystal; *ii)* timing calibration when this information is included in the reconstruction process; and *iii)* a correction of non-uniformities, as a result of the different detector components or manufacturing processes between different blocks [P1.5]-[P1.7] .

Radiation detectors for PET are, in most of the cases, based on pixelated or monolithic scintillation crystals coupled to high-density photodetectors [P1.8]. The advantages of each scintillator configuration have been extensively described in the literature, see for instance [P1.9] and references therein. On the one hand, in pixelated based detectors, the estimation of the 2D photon interaction position is basically carried out by identifying the pixel that provides the maximum signal value. Photon DOI estimation typically requires additional hardware [P1.10][P1.11] or the use of algorithms such as Maximum Likelihood [P1.12]. Notice that DOI information is especially important for small aperture scanners configurations such as in small animal imaging or organ-dedicated systems [P1.13], since it allows one to correct for the parallax error [P1.14]. On the other hand, in monolithic based detectors, the generated distribution of scintillation photons covers many photosensors and the position of the photodetector element with the maximum signal does not always correspond to the estimated centroid of the scintillation light distribution (LD). However, it is possible to characterize the LD profiles allowing to directly estimate the 3D coordinates of the γ-ray interaction [P1.15]. As a drawback, there might be scintillation light reflection from inner faces of the scintillator, as well as truncation of the LD as a result of the finite detector size, producing a mispositioning of the γ-ray impact. This effect, known as edge effect or bias, is typically characterized by a shift in the impact position determination towards the crystal center that becomes stronger at the edges of the block.

The most accurate approach for the estimation of the impact position in monolithic blocks would be to readout every photosensor element. Statistical methods, such as maximum-likelihood algorithms (ML) [P1.16], *k*-nearest neighbor (*k*-NN) methods [P1.17][P1.18], have been proposed. These methods make it possible to determine the photon impact position by comparison of the LD shape at different interaction positions with a set of calibration data stored in Look-Up Tables. Recently, it has been demonstrated the possibility to apply artificial neural-network (ANN) [P1.21] or gradient tree boosting algorithm (GTB) [P1.19][P1.20] for this purpose. However, those methods typically require large acquisitions times, and hardware with accurate positioning capabilities. As an alternative, analytical methods that model the relation between the source position and the measured photodetector pixel signals, using for example weighted least-squares (WLS), can be employed without prior calibration dataset [P1.22][P1.23]. These methods could also be applied when using reduction readout schemes which reduce the complexity and cost when compared to reading out every single photosensor element [P1.24].

Electronic configurations based on networks of passive components have been proposed to reduce the number of readout channels. The most traditional is the so-called Anger logic [P1.25], that returns only four output signals allowing to implement the Center of Gravity (CoG) algorithm to estimate the XY interaction position. A modification of the resistive-network, providing the collected charge (scintillation photons) for all rows and columns of the photosensor arrays, permits to better measure the centroid of the LD and makes it possible to additionally estimate the photon DOI [P1.26]. However, the edge effect is still present in the peripheral region of the detector when statistical and analytical methods are used, especially when some type of reflection treatment is applied to the crystal faces. Modifications of the CoG, such as the so-called Raise-to-Power (RTP) algorithm

[P1.27], allows one to partially mitigate that effect, but the need of calibration procedures is still required.

The edge effect of the estimated XY positions (Anger logic, CoG, RTP, etc), can be further reduced by means of bilinear [P1.28], 2D polynomial [P1.29] or 1D polynomial [P1.30] interpolation methods using calibration masks. These approaches have been applied in several systems based on monolithic crystals [P1.5][P1.6][P1.30]. However, while the interpolation between mask points is well achieved, extrapolation beyond the outmost point sources (mask holes) may lead to some artifacts and, typically, events at the edges are rejected reducing system sensitivity.

Improvements on the calibration procedure for monolithic-based PET detectors would enhance their performance. This work focuses on the development of a calibration method to accurately determine 3D position and energy of γ-ray impacts for the whole monolithic crystal volume and, thus, also increasing system sensitivity. The proposed method is based on the mathematical structures called Voronoi diagrams [P1.31]. Those diagrams are currently being used for automatic target volume definition during treatment planning in radiotherapy [P1.32], image correction of deformable motion in PET image reconstruction [P1.33] or, in pixelated-based PET detectors, for energy calibration procedures [P1.34] and crystal identification in a multiple-layer configurations [P1.35]. Moreover, Voronoi diagrams are also used in sports [P1.36][P1.37], chemistry [P1.38][P1.39], astronomy [P1.40], medicine [P1.41] and image processing [P1.42].

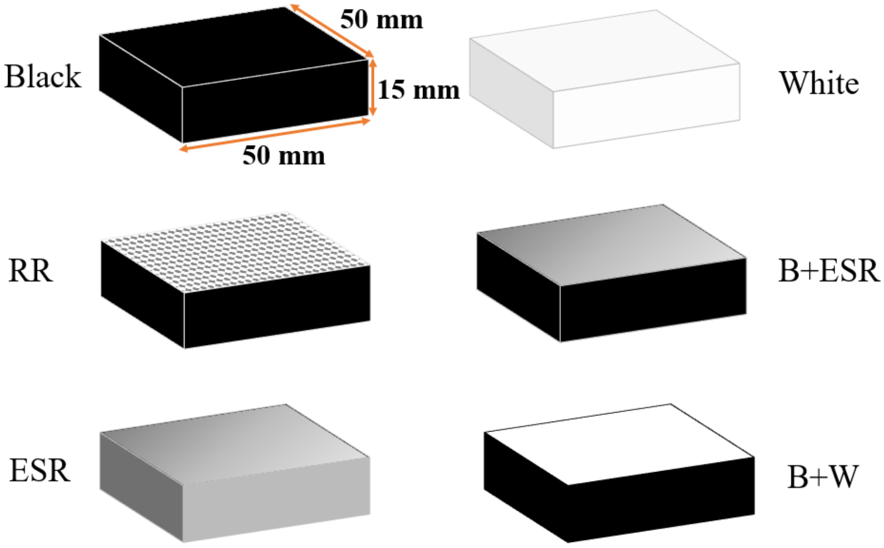

Figure P1.1. Sketch of the six different surface crystal treatments.

2. Materials and Methods

A. Detector block

Two thick LYSO monolithic scintillators with dimensions of 50×50×15 mm^3 have been used, see Figure P1.1. All crystal faces are polished and one of the 50×50 mm^2 surface (exit face) coupled to a photosensor array by means of optical grease (BC-630, Saint Gobain) to reduce light transmission losses. We have tested six different treatments on the same crystals, as depicted in Figure P1.1 and described in Table P1.1, namely: i) *Black*: all faces, except the one coupled to the photosensor coated with absorbent black paint; ii) *RR*: lateral faces black painted and a retroreflector layer added to the entrance face of the crystal using optical grease; iii) *ESR*: Enhanced Specular Reflector (ESR) layer coupled to lateral and entrance faces using an optical clear adhesive film; iv) *White*: all faces, except the one coupled to the photosensor, white painted; v) *Black and ESR* (B+ESR): lateral faces black painted and ESR layer coupled at the entrance face with optical clear adhesive film; and vi) *Black and White* (B+W): lateral faces black painted and entrance face white painted.

Name	**Surface** *Entrance/Lateral*	**Reflection type** *Entrance/lateral*
Black	Black/Black	No reflection
RR	RR/Black	Retroreflection/No reflection
ESR	ESR/ESR	Specular/Specular
White	White/White	Diffuse/Diffuse
B+ESR	ESR/Black	Specular/No reflection
B+W	White/Black	Diffuse/No reflection

Table P1.1. Characteristics of the six different surface treatments under study

For each study the same crystal and SiPM aray was used. They were coupled using optical grease (Rhodorsil Paste 7). Each SiPM array (ARRAYC-30035-144P-PCB, SensL/OnSemi) was composed by 12×12 photosensors and covering an approximate area of 50×50 mm^2. Each individual photosensor has an active area of 3×3 mm^2 and the pitch is 4.2 mm in both directions. Each array is typically operated at a bias voltage of 31 V, 6.5 V over the breakdown voltage. Since SiPMs are sensitive to temperature variations, the detectors are kept at stable temperatures of approximately 15ºC-18ºC, also reducing dark noise contributions.

The detector readout provides information for each row and column of the SiPM array allowing to characterize the scintillation LD profiles. This readout provides a reduction from 144 SiPMs output signals to only 24. The 24 signals are digitized using custom ADC boards (12-bit precision), using an integration window of about 250 ns. All acquisitions were performed in coincidence mode using an identical reference detector, and a coincidence window of 5 ns. The digitized and synchronized signals are sent to a workstation where they are processed (see description below).

B. Calibration method based on Voronoi diagrams

Figure P1.2 shows a schematic of the steps followed during the data calibration. First, using the signals provided by the analog readout, the 3D photon impact coordinates and energy of each coincidence event are estimated applying the RTP algorithm. XY coordinates are calculated by raising the 12 digitized signals for each projection to the power of two [P1.43][P1.44], before CoG calculation. The DOI coordinate, Z, is estimated for each event as the average for rows and columns (*r,c*) of the ratio of the sum of all 12 signals (photon energy, *E*) to its maximum value $(E/I_{max})_{r,c}$ [P1.26]. This process is labelled as RTP2 in Figure P1.2 (a).

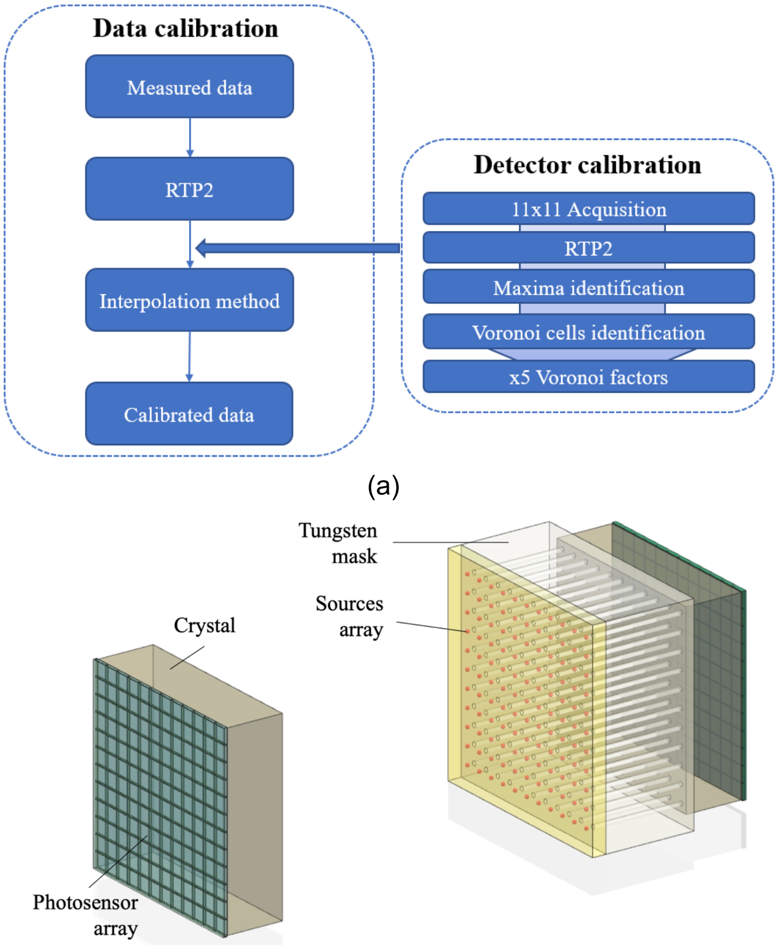

(a)

(b)

Figure P1.2. (a) Schematic steps of the data calibration using Voronoi diagrams. (b) Sketch of the measurement proccesses.

1) Detector calibration procedure: Reference data sets, named calibration maps, have been acquired for each crystal treatment using an array of 11×11 ^{22}Na sources that covers an area of 46×46 mm^2. The first row of sources is located at 2 mm from the crystal border and the pitch is 4.6 mm. The sources were mechanically collimated using a tungsten mask of 24 mm thickness and 1.2 mm drilled holes, see Figure P1.2 (b). An array with a smaller pitch would have implied overlapping of the sources at the edges of the flood maps. During data processing, each detector area is binned in 600×600 pixels. Once the calibration map has been acquired, the detector calibration is done as follows:

1) 3D photon impact coordinates (and energy) result in flood maps as the one shown in Figure P1.3 (a). All 121 calibration sources were correctly identified. A software collimation in the range of 1° (depending on the study) was applied between both detectors helping to better determine the distribution centroids. That means that only events whose line of

response (LOR) is contained within this specific angle are considered [P1.46].

2) The centroid of each measured source $(x_{source}^{floodmap}, y_{source}^{floodmap})$ in the flood map of the 121 calibration sources are calculated searching the maximum intensity values, depicted with the overlying open white squares in Figure P1.3 (a).

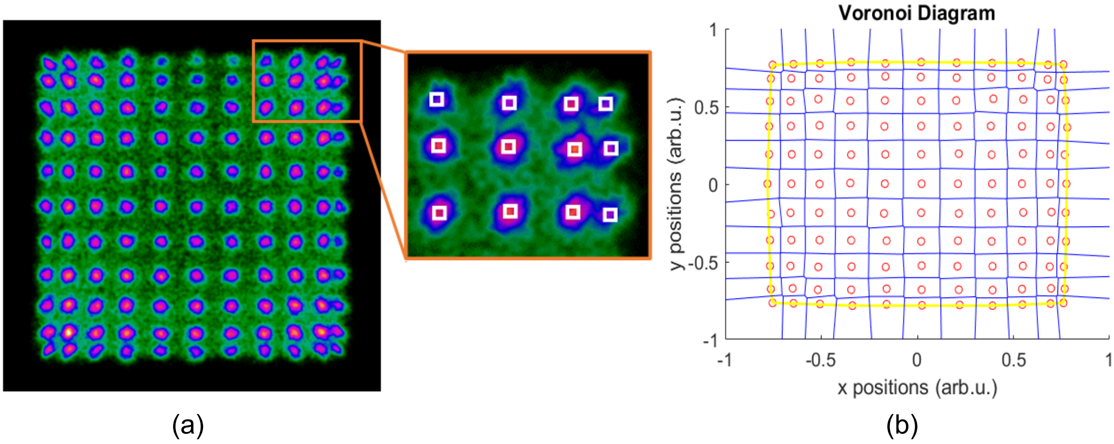

(a) (b)

Figure P1.3. (a) Flood map of an array of 11×11 collimated ^{22}Na sources and representation of the calculated centroids of the sources for one section of the flood map. (b) Voronoi diagrams of the 121 Voronoi points. The yellow line delimits the “intuitive interior” of the 121 Voronoi points, named convex hull.

The detector calibration method is based on Voronoi diagrams. These diagrams, also known as Dirichlet tessellation, are defined as the partitioning of the plane into various convex polygons T_i, named Voronoi cells, each of them containing one generating point, named Voronoi point. An arbitrary point lies within a specified Voronoi cell if, and only if, the distance from this point to the Voronoi point of its associated polygon is smaller than all other distances between this point and the remaining Voronoi points [P1.31]. This can be mathematically expressed as:

$$V(X) = \{T_i\}_{i=1\ldots m} \qquad (1)$$

where $T_i = \{x \in \mathbb{R}^2 \mid d(x,x_i) < d(x,x_j), i \neq j\}$, *V(X)* is the Voronoi diagram generated by *X*, with *X* the set of the *m* Voronoi points, and *d(x, xi)* the Euclidean distance on $\mathbb{R}^2$. In our case, since we are using a calibration mask of 11×11 sources (*m* = 121), the crystal surface is divided into 11×11 Voronoi cells, see Figure P1.3 (b). The yellow line delimits the “intuitive interior” of the 121 Voronoi points, named convex hull. In the present work, the Voronoi diagrams have been computed using a specific MATLAB function (*voronoi*) [P1.47].

Once the Voronoi cells are determined, 5 Voronoi factors for each Voronoi cell, one for X, one for Y, one for energy and two for Z, are independently calculated. For the XY and energy:

$$VoronoiFactor^{(X,Y,E)} = \frac{(x,y,E)_{source}^{known}}{(x,y,E)_{source}^{floodmap}} \qquad (2)$$

Here $(x,y,E)_{source}^{known}$ and $(x,y,E)_{source}^{floodmap}$ correspond to known and measured XY coordinates and energy of each calibration source. Regarding the energy correction, a Gaussian fit to the energy spectra of each Voronoi cell was applied providing the photopeak value in ADC units, $(E)_{source}^{floodmap}$. We have used the central cell, $(E)_{source}^{known}$, to convert the ADC units to 511 keV. For the DOI calibration, we have obtained the limits of the E/I_{max} histograms of each Voronoi cell, named *a* and *b*, are obtained by using the analytical expression for the DOI distribution [P1.26].

$$DOI(z) = A \cdot exp^{-\alpha z}\left[erf\left(\frac{b-z}{\sqrt{2}\sigma_{int}}\right) - erf\left(\frac{a-z}{\sqrt{2}\sigma_{int}}\right)\right] \quad (3)$$

To calibrate the measured E/I_{max} units to *mm* we have considered two Voronoi factors for each Voronoi cell ($VoronoiFactor^{(Z1,Z2)}$) correspond to the two parameters of a linear fit considering the limits $a-\sigma_{int}$ and $b+\sigma_{int}$ equal to 0 and 15 mm (crystal thickness), respectively.

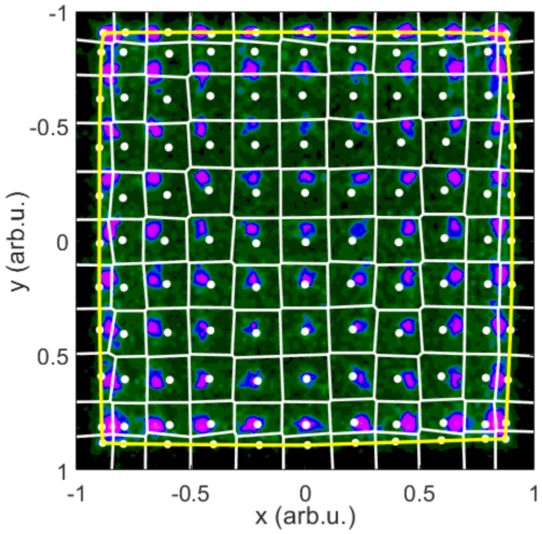

Figure P1.4. Flood map for an array of 9×9 ^{22}Na sources overlaying with the Voronoi diagram obtained during the detector calibration (11×11 centroids, represented with white circles). The yellow line depicts the convex hull.

2) Interpolation methods: Once the Voronoi factors are calculated, each recorded event *(x, y)* is added to its corresponding Voronoi cell. However, they are calibrated by interpolation of the Voronoi factors of the closest cells, as depicted in Figure P1.4 and Figure P1.5. Thus, the chosen interpolation method plays an important role. They cannot be indiscriminately used and, therefore, it is important to understand their principles and limitations. Moreover, the events near the edge should not be discarded, so the selected method must allow one to also extrapolate the events that are beyond the convex hull, represented again in Figure P1.4 by the yellow line.

Two different interpolation methods have been studied:

i) Weighted Average Method (WAM) of the Voronoi factors. Each calibration factor of one recorded event (f^j) corresponding to each position coordinate and to the energy, is calculated as follows:

$$f^j = \sum_{i=1}^{n} \frac{w_i(x,y)}{\sum_{i=1}^{n} w_i(x,y)} \times VoronoiFactor_i^j, \; 1 \le j \le 5 \qquad (4)$$

where, $w_i = [1/([d_i(x,y)]^k)]$, $d_i(x,y)$ is the distance between the recorded data point and the Voronoi points and k is a chosen exponent. For each recorded event inside the convex hull, three closest Voronoi points have been selected (*n* = 3; at left, right, up or down), see Figure P1.5 (a). The calibration factors of the recorded events that are located outside the convex hull are determined directly from the Voronoi factors of their associated Voronoi cell, without any interpolation from the closest cells. We have tested different *k* values (not shown here), suggesting the best results for the squared power (*k* = 2) and therefore, for simplicity, we are only providing these results in this work.

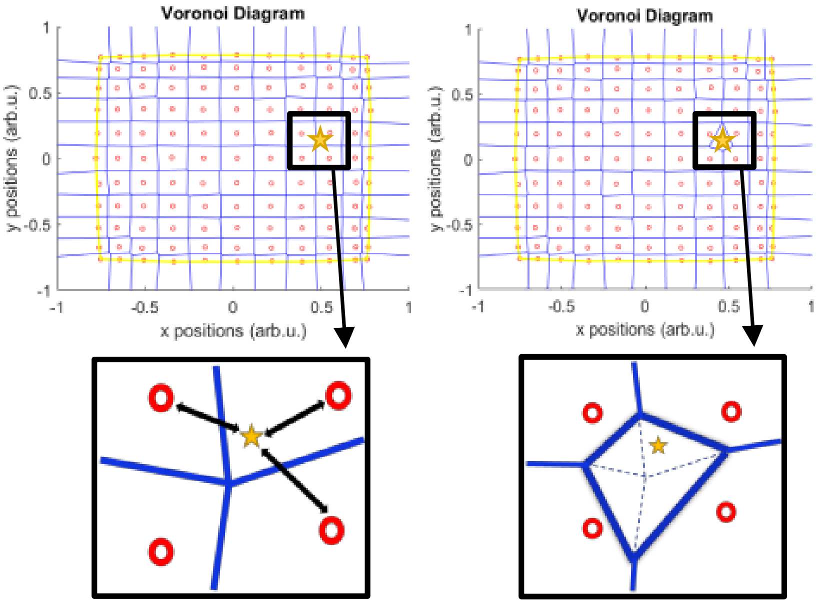

(a) (b)

Figure P1.5. Sketch of interpolation methods using Voronoi diagrams. A new event is shown as a yellow star. (a) Scheme of the data interpolation using WAM taking into account the three closest Voronoi points to the recorded data. The recorded event is calibrated considering the distance with its three closest Voroni cells. (b) Scheme of the data interpolation using NN method. The recorded event is calibrated considering the area of natural neighbor cells.

ii) Natural Neighbor (NN) method of the Voronoi factors*.* In the present work, this interpolation has been made with a specific MATLAB function (*scatteredInterpolant*) [P1.48]. The recorded event *(x, y)* is added as a new Voronoi point and, therefore, generates a new cell that intersects with certain Voronoi cells of the former set of 121 ones, named natural neighbors, see Figure P1.5 (b). The interpolation is a weighted average area of the natural neighbors of the recorded data, where f^j is calculated as follows:

$$f^j = \sum_{i=1}^{n} w_i(x,y) \times VoronoiFactor_i^j \,, 1 \le j \le 5 \quad (5)$$

where $w_i = \frac{area\,[T_i(x,y)]}{area\,[T(x,y)]}$, $T(x,y)$ is the Voronoi cell of the recorded event and $T_i(x,y)$ the natural neighbors cells. Moreover, the calibration factors of the events located outside the convex hull are calculated using an extrapolation method based on a least squares approximation of the gradient at the boundary of the convex hull [P1.47].

In the WAM, weights are distance-based and, therefore, the weights assigned to each Voronoi cell diminishes as the distance from the recorded data to the Voronoi point increases. In the NN interpolation, weights are area-based and, therefore, depend on the area of the NN cells which are inside of the new Voronoi cell. Here, larger areas result in larger influence of the corresponding Voronoi factor on the interpolation value.

The calibrated data for each recorded are calculated multiplying the estimated 3D coordinates and energy event (x_{med}, y_{med}, z_{med}, E_{med}) by its appropriate calibration factor (f^j), as follows:

$$\begin{gathered} x_{cal} = x_{med} \times f^X \\ y_{cal} = y_{med} \times f^Y \\ z_{cal} = f^{Z1} \times z_{med} + f^{Z2} \\ E_{cal} = E_{med} \times f^E \end{gathered} \tag{6}$$

C. Experimental validation

To validate the calibration data process carried out using the 11×11 ^{22}Na sources array (4.6 mm pitch), a second set of data has been acquired using another array but with 9×9 ^{22}Na sources (5 mm pitch). The studied cases are:

1) Comparison of Voronoi interpolation methods and 1D monomial approach. The 1D monomial interpolation [P1.30] also makes use of the 11×11 sources array to perform the calibration. We have used the crystals with RR treatment, since they have been successfully tested before [P1.43]. The 9×9 ^{22}Na sources array was placed in front of the crystal under evaluation. The position of these sources is different from those used during the calibration (11×11). Having sources outside the convex hull (less than 2 mm to the crystal edge) would have been challenging to resolve. The reference detector was located at 416 mm and just software collimation of 0.6º (total aperture) was applied.
2) Crystal surface treatments. The aim here was to test the calibration using the NN interpolation method for the six different crystal treatments because as it will be shown in the results section, it exhibited the best performance in the case i). In order to reduce possible random coincidences, the 9×9 ^{22}Na sources were additionally collimated using a tungsten mask with 1.2 mm in diameter drilled holes in a 24 mm thick block. The collimator was attached to the entrance face of the detector under calibration. The reference detector was placed at 110 mm and a software collimation of 1.1º (total aperture) was applied after the calibration.

Concerning the XY calibration, we have evaluated the central row and column of the 9×9 ^{22}Na sources array (see horizontal and vertical yellow bands in Figure P1.6 (a) left), before and after calibration, for all cases. The known mechanical source position defines the true position of the sources. The centroid of each source in the flood maps is calculated using a multi-Gaussian fit. Several parameters have been used to evaluate the performance of the XY calibration:

1) Bias: difference between measured and true source position.
2) Linearity: mean distance between sources. We have also calculated the Confidence Intervals (CI). We provide the 65% CI, this is a range where one can be 65% certain it contains the mean value.
3) Spatial resolution: FWHM of the Gaussian distributions.
4) Bias resolution coefficient (R_{bias}): product of the bias and the FWHM value at each source position. We are introducing this figure of merit as an estimation of the global performance of the XY calibration method.

Regarding the DOI calibration, we have calculated the lower and upper limits, *a* and *b*, for the DOI histograms for three regions of interest (ROI) of the flood maps, namely central, lateral and corner (see yellow squares in Figure P1.6), using Eq. (3).

Finally, the energy calibration has been evaluated with the sources located along one diagonal in the flood maps (see also diagonal yellow band in Figure P1.6) both before and after calibration. The energy resolution is calculated as $\Delta E(FWHM)/E_{centroid}$ using a Gaussian plus a linear distribution.

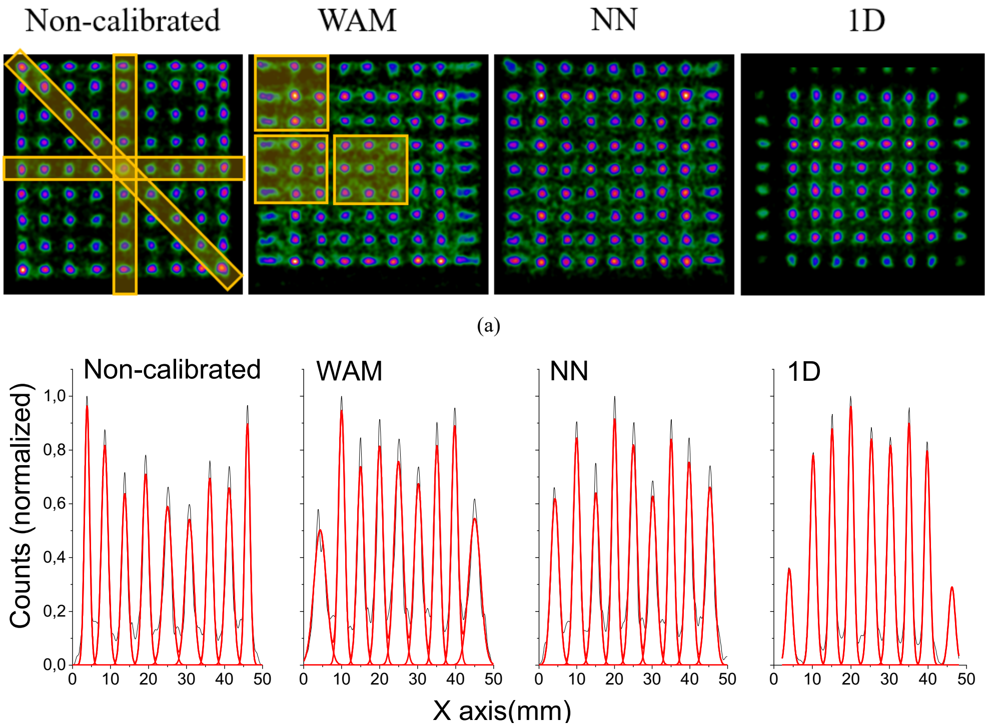

(a)

(b)

Figure P1.6. (a) Flood maps for an array of 9×9 ^{22}Na sources acquired with the RR crystal. From left to right: non-calibrated and calibrated using WAM, NN and 1D approaches. (b) Profile for the central row of sources for each case.

3. Results

A. Comparison of Voronoi interpolation and 1D monomial

The non-calibrated flood map of the 9×9 ^{22}Na sources array acquired with the RR crystal is shown in Figure P1.6 (a) left. A slight shift of the sources along the Y axis is observed due to a misalignment of the array positioning system. We have calibrated the 3D impact positions and energy using the interpolation methods described above (named WAM and NN), and the 1D monomial approach, also shown in Figure P1.6 (a). The profiles of the central row of sources, together with a multi-Gaussian fit (red line), are shown in Figure P1.6 (b).

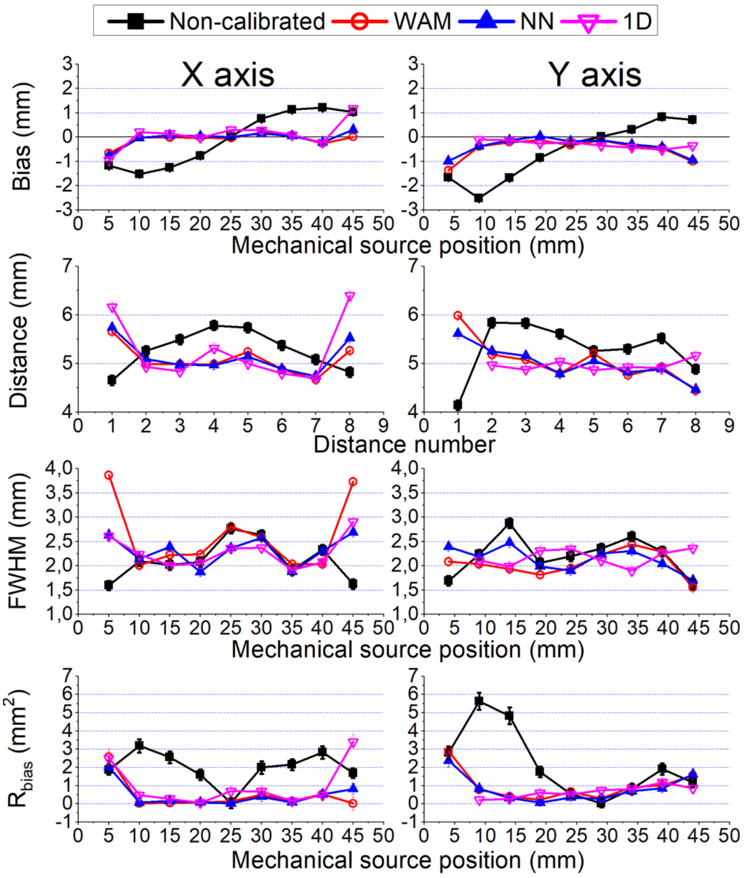

Figure P1.7. From top to bottom for the four studied cases: the bias as a function of the mechanical source position, the distance between sources, the spatial resolution FWHM as a function of the mechanical source position and Rbias coefficient as a function of the mechanical source position. Left panels for the central row and right panels for the central column.

Figure P1.7 shows the bias, distances between sources, spatial resolution (FWHM) and the R_{bias} coefficient, for the four studied cases. The panels on the left correspond to the central row (X-axis) of the flood maps and the panels on the right to the central column (Y-axis). The average standard deviation (X and Y axes) of the bias is 1.15 mm for the non-calibrated data. This value is reduced to 0.34 mm, 0.33 mm and 0.35 mm for the calibrated data using the WAM, NN and 1D approaches, respectively.

The linearity and confidence intervals are listed in Table P1.2 for both X and Y axes. More accurate values are obtained with the Voronoi approaches, closer to the actual value of 5 mm (see also Figure P1.7). The average linearity for the X and Y axes is 5.3±0.2, 5.1±0.2, 5.1±0.1 and 5.2±0.2 mm, for the non-calibrated data and WAM, NN and 1D cases, respectively.

Dataset	**Linearity (mm)** **X**	**CI (mm)** **X**	**Linearity (mm)** **Y**	**CI (mm)** **Y**
Non-cal.	5.3±0.1	[5.14, 5.42]	5.3±0.2	[5.10, 5.50]
WAM	5.1±0.1	[4.98, 5.19]	5.0±0.2	[4.89, 5.21]
NN	5.1±0.1	[5.01, 5.25]	5.0±0.1	[4.88, 5.13]
1D	5.3±0.2	[5.03, 5.50]	4.96±0.04	[4.92, 5.00]

Table P1.2. linearity and ci for the central row (X) and central column (Y) for the non-calibrated data, calibrated data using the WAM interpolation, NN interpolation and 1D approach.

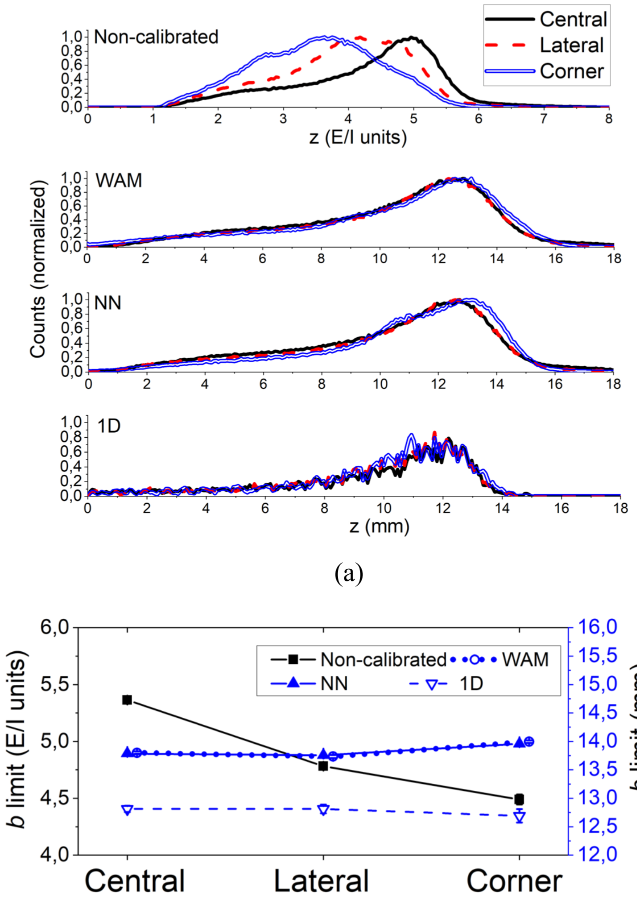

(a)

(a) (b)

Figure P1.8. (a) DOI distributions. From top to bottom: for the non-calibrated data in arbitrary units (E/I units), and WAM, NN and 1D in mm units. (b) *b* values for the non-calibrated data and WAM, NN, 1D approaches.

The spatial resolution FWHM as a function of the mechanical source position is also depicted in Figure P1.7. FWHM values of the non-calibrated sources closest to the crystal edge diminish for both X and Y axes due to the image compression. FWHM values worsen for the sources closest to the edge in the X-axis when the WAM is applied. However, this effect is reduced using the NN or the 1D approaches. The average FWHM for the X direction obtained for the non-calibrated, WAM, NN and 1D cases is 2.1±0.4, 2.6±0.7, 2.3±0.3 and 2.3±0.3 mm, respectively; and 2.2±0.4, 2.0±0.3 and 2.1±0.3 and 2.2±0.2 mm in the Y direction.

The R_{bias} coefficients are shown in the bottom panels of Figure P1.7. The average R_{bias} for the X and Y axes is 2.1±0.1, 0.7±0.4, 0.6±0.3 and 0.8±0.2 mm^2 for the non-calibrated, WAM, NN and 1D cases, respectively.

The DOI profiles for the non-calibrated (E/I units) and calibrated data (mm units), for the three studied regions of interest, are shown in Figure P1.8.The DOI histograms for the non-calibrated data showed different shapes depending on the analysed detector area (see Figure P1.8 (a) top panel). After DOI calibration, the histograms resembled the expected one. That means a larger amount of events at the crystal entrance (15 mm side) and lower closer to the photosensor side (0 mm). This happens for the three ROI and calibration approaches. Figure P1.8 (b) shows the determined upper limits, named *b*, for the three regions of interest.

In Figure P1.9 we depict the photopeak centroid position, normalized to the central one, for the 9 sources across the diagonal. The non-calibrated data exhibited lower photopeak values of about 13±1% at the crystal edges. After energy calibration, all interpolation methods returned differences as small as 5±1% at the edges, and below 2±1% in the central region. The energy resolution for the whole scintillation volume resulted in 17.4±0.2%, 13.3±0.1%, 13.0±0.1% and 13.2±0.1%, for the non-calibrated, WAM, NN and 1D approaches, respectively.

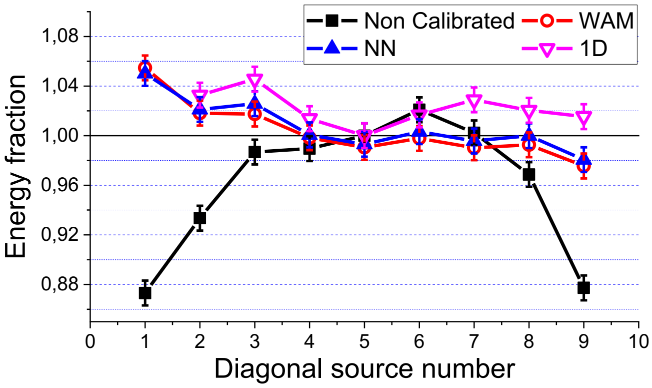

Figure P1.9. Energy photopeaks for the diagonal of sources for the four studied cases.

B. Crystal surface treatments

We have obtained non-calibrated data of the 9×9 ^{22}Na sources array for the six different crystal treatments. The NN interpolation method was used to calibrate the 3D impact positions and energy for all crystal treatments. Figure 10 left shows the flood maps of the non-calibrated data, and on the right side the calibrated flood maps. The profiles for the central column (Y-axis) of each flood map are also shown at the sides.

Figure P1.11 shows the bias values as a function of the mechanical source position for the central row (left) and column (right) for each treatment. The top panels depict the values for the non-calibrated data. The largest bias value is observed for the sources closest to the edge for the White treatment. The bottom panels show the bias values after calibration. Figure P1.12 (a) shows the average standard deviation for the X and Y axes of the bias for each treatment before and after calibration. The largest value (1.5±0.2 mm) obtained for the White treatment is reduced to 0.3±0.1 mm after calibration, as also found for other treatments.

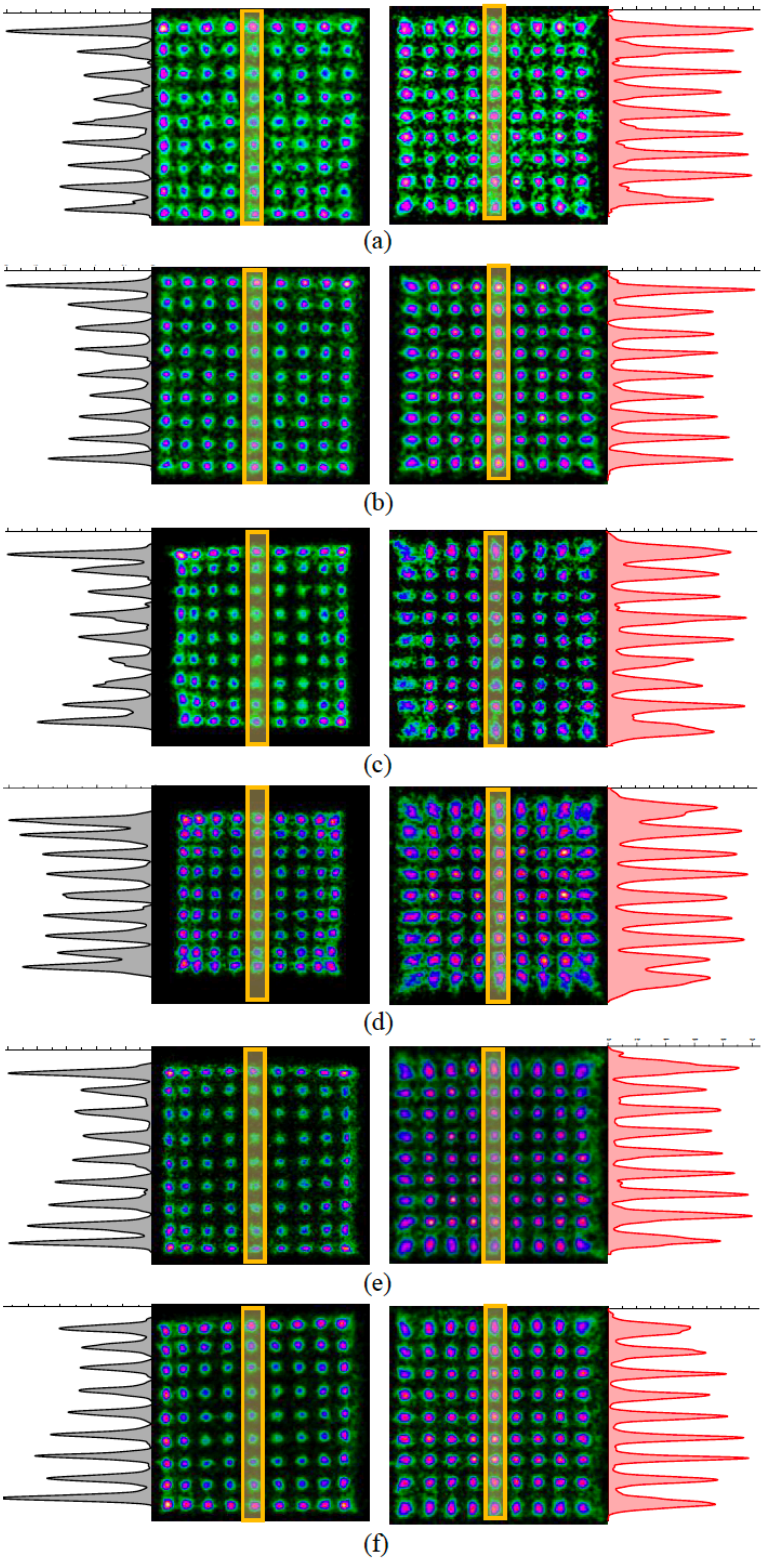

Figure P1.10. Flood maps for the 9×9 ^{22}Na sources array and profiles for the central column. Left, non-calibrated data. Right, calibrated data using NN interpolation. (a) Black crystal, (b) RR crystal, (c) ESR crystal, (d) White crystal, (e) B+ESR crystal and (f) B+W crystal.

Figure 12 (b) depicts the average linearity. Some excess of the linearity in the non-calibrated data is observed for the treatments including lateral walls black painted. This is the opposite for both specular (ESR) or diffused reflection (White) treatments. The average linearity for all calibrated cases agrees well with the actual value of 5 mm.

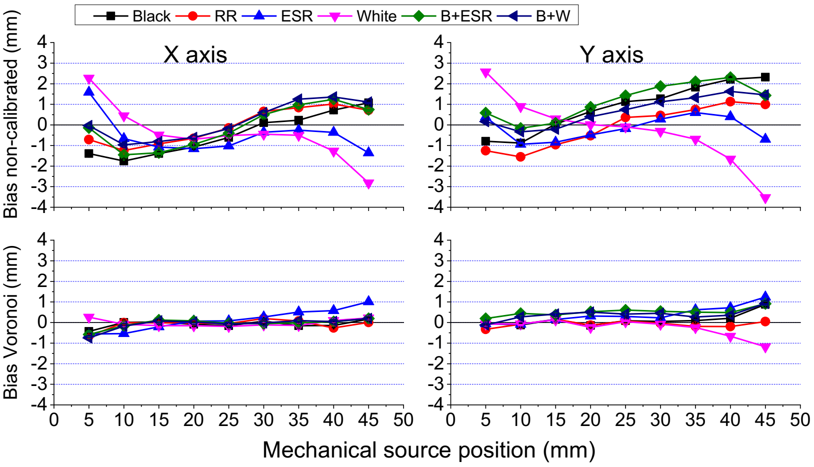

(a) (b)

Figure P1.11. Bias values as a function of the mechanical source position for the non-calibrated data (top) and for the calibrated data using NN interpolation (bottom) for all treatments. (a) For the central row and (b) for the central column.

The average spatial resolution FWHM is plotted in Figure P1.12 (c). Regarding the calibrated spatial resolution FWHM, the best value is obtained when using the RR treatment (about 1.6±0.1 mm on average). This value is slightly better than that obtained in the previous section IIIA due to the additional mechanical collimation (see Discussion for more details). The worst spatial resolution is observed when reflective materials are used (ESR and White) approaching 2.2±0.1 mm.

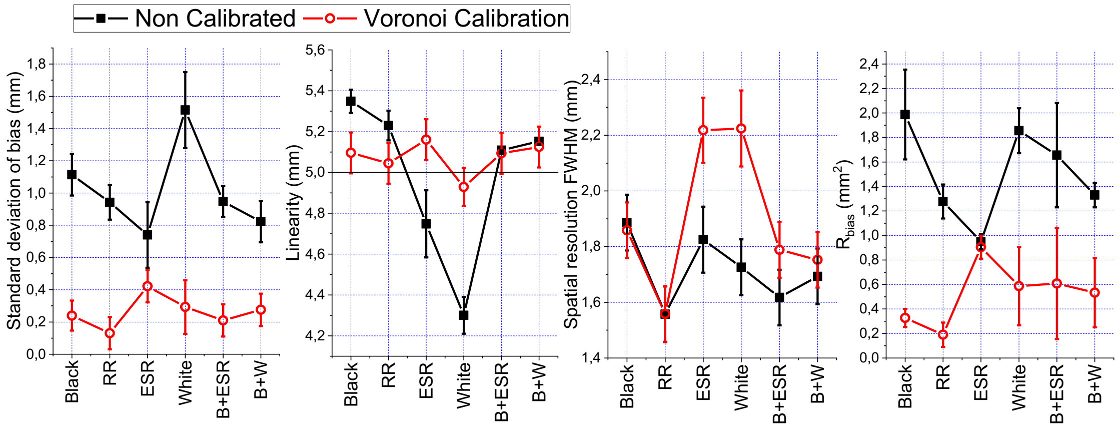

(a) (b) (c) (d)

Figure P1.12. Average parameters calculated for each treatment, for both non-calibrated and NN calibrated data. (a) Standard deviation of bias. (b) Linearity. (c) Spatial resolution FWHM. (d) Rbias coefficient.maps for the 9×9 ^{22}Na sources array and profiles for the central column. Left, non-calibrated data. Right, calibrated data using NN interpolation. (a) Black crystal, (b) RR crystal, (c) ESR crystal, (d) White crystal, (e) B+ESR crystal and (f) B+W crystal.

The average R_{bias} coefficient for each treatment is shown in Figure P3.12 (d). The calibrated data exhibit results nearing zero. In particular, the RR treatment results in 0.2±0.1 mm^2, whereas the ESR treatment shows the highest value of 0.9±0.1 mm^2.

The energy resolution for the whole scintillation volume before and after calibration is plotted in Figure P1.13 (a). In contrast to the spatial resolution, ESR and White treatments exhibited the best energy resolution (12-14%). A deterioration to 16-17% is observed when the lateral black paint is used in combination with other reflective materials, and to about 22% if the entire block is black, most likely due to a poorer collection of scintillation photons Figure P1.13 (b) shows the photopeak variation for each treatment as a function of the γ-ray impact position for a diagonal of sources across the detector surface. The largest variation of the photopeak positions is observed at the detector edges reaching 24%, 22%, 7%, 11%, 17% and 29% (±1%) for the Black, RR, ESR, White, B+ESR and B+W treatments, respectively. After calibration these values are significantly reduced to only: 5%, 2%, 1%, 2%, and 2% (±1%), respectively.

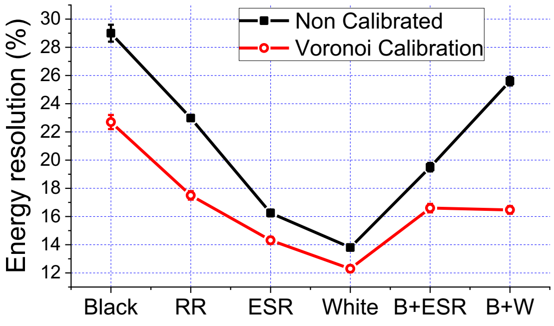

(a)

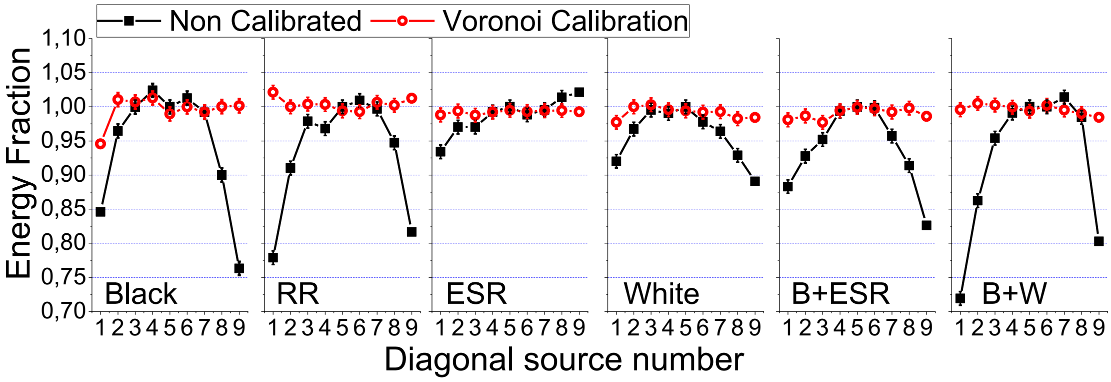

(b)

Figure P1.13. (a) Energy resolution for the whole detector for each treatment both non-calibrated and after calibration. (b) Photopeaks variation referred to the central one, for the diagonal of sources for all cases studies. From left to right: Black, RR, ESR, White, B+ESR, and B+W.

Figure 14 depicts the DOI histograms corresponding to each treatment, before and after calibration. The non-calibrated data is plotted in E/I units and all other data using the NN interpolation in millimeters. The treatments with reflective material show a shift of the DOI histograms to higher values, due to the increase of collected energy affecting the estimator (E/I). After calibration, there is a good agreement in between all distributions. Indeed, Figure P1.15 shows the determined lower and upper limits, a and b, for the three ROI. The upper limits exhibit a position dependence. After calibration, most of the treatments showed almost no variation of these parameters independently of the studied region. This indicates the possibility to also calibrated the photon DOI with this methodology. The larger variation in the non-calibrated data was observed for the ESR treatment, which is nevertheless reduced after data calibration.

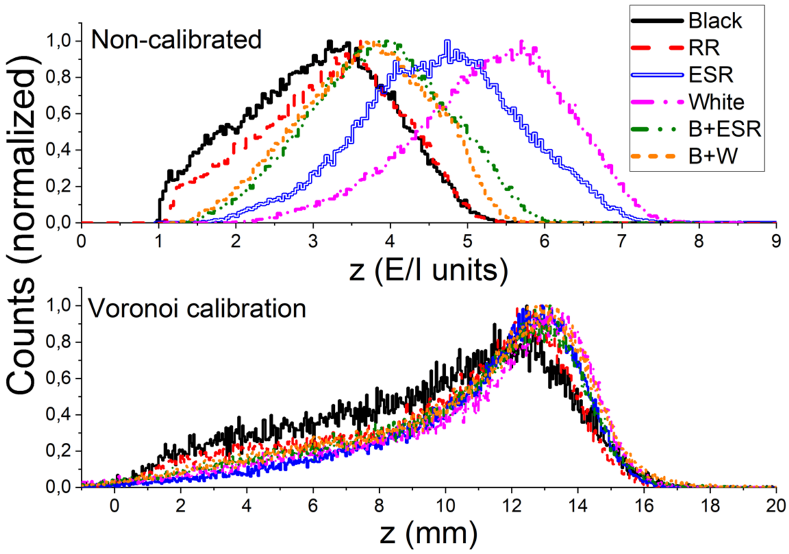

Figure P1.14. DOI distributions for the whole crystal volume. Non-calibrated data is depctied in arbitrary units (top). Calibrated DOI distributions are in mm (bottom).

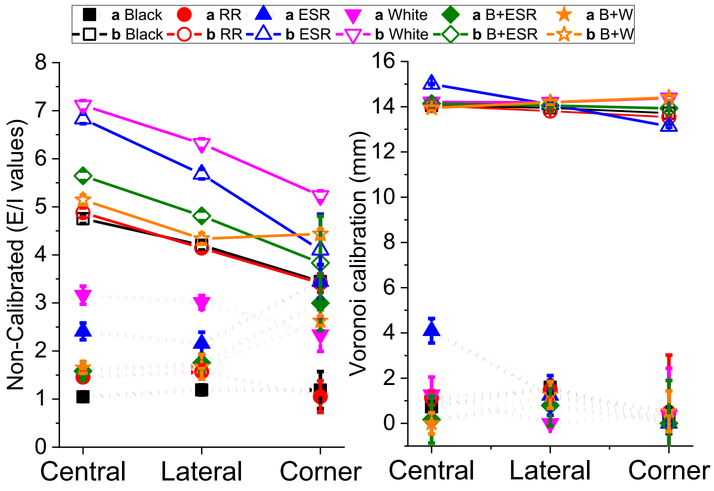

(a) (b)

Figure P1.15. *a* and *b* values for the central, lateral and corner regions for each treatment. (a) Non-calibrated data and (b) calibrated data using NN.

4. Discussion

In this work we have introduced a calibration method based on Voronoi diagrams to accurately determine the energy and 3D impact positions in γ-ray detectors based on monolithic scintillation crystals.

In a first set of experiments, we have evaluated the WAM, NN and 1D calibration methods using a 9×9 ^{22}Na sources array acquired with the RR crystal (lateral black painted and a RR layer at the entrance). On the one hand, the non-calibrated image shows the inward compression at the edges of the crystal due to the truncation of the LD. This results in an overestimation of the spatial resolution FWHM values of the sources closest to the crystal edge, as expected. Interestingly, the linearity of this non-calibrated data did not show a large mispositioning of the sources at the edges. We assumed this happened because the sources at the edges are at 5 mm from the crystal edge, where this effect is less pronounced given the photosensor density (12×12 SiPMs), surface treatment, readout granularity (12+12 signals), crystal aspect ratio (15 mm thickness and 50 mm size) and RTP2 calculation of the estimated impact position. On the other hand, when the 1D approach is applied, we observed that it is hard to resolve data that occurs beyond the outermost calibration sources. In particular, the upper row of the 1D approach is almost vanished, due to the slight shift of the 9×9 array with respect to the detector center (see Figure P1.6).

The interpolation methods based on Voronoi diagrams made it possible to calibrate the whole scintillation volume, thus increasing the detector sensitivity. When the WAM was applied, the FWHM values of the sources closest to the X edge worsened. This was caused because these sources are located between two Voronoi cells (see Figure P1.4) and, thus, this method has some position challenges, producing an elongation of the sources. On the Y-axis, the sources closest to the edge are not located between two Voronoi cells (see Figure P1.4) due to the aforementioned 9×9 sources array shift and, therefore, this elongation was not observed. However, when the NN interpolation method was applied, the elongation was not shown in any axis; providing a correct interpolation in both directions.

The different shapes of the non-calibrated DOI distributions for the three ROIs are produced by a stronger scintillation light truncation towards the crystal edges and corners. After calibration, DOI distributions for all regions exhibited a similar behavior. The use of a RR layer, when compared to a totally black painted crystal, is characterized by an excess of the slope of the exponential attenuation curve [P1.49]. Regarding the photopeak energy dependency with the impact position, a larger photopeak variation at the crystal corners was found in the non-calibrated data, especially for configurations using black painted walls, as expected. This is because in monolithic crystals with black painted walls, there is a scintillation light collection dependence with the γ-ray impact position due to the scintillation light truncation at the edges and, thus, certain losses of light transferred and collected at the photosensors. These effects were compensated after calibration.

Summarizing, the accuracy on the impact determination (FWHM, bias, distance) using the NN interpolation performs better than the other tested approaches, especially recovering impacts at the edges of the crystal without deteriorating the FWHM, as it occurs for the WAM interpolation. Independently of the used interpolation method, an improvement on the energy and DOI performance is always observed. It is worth mentioning that the calibration of data described in this work could be implemented in reconfigurable devices such as FPGA (Field Programmable Gate Arrays), by means of look-up-tables for each Voronoi factor and detector unit.

After the validation of the Voronoi interpolation methods, in particular when using the NN approach, an additional study was carried out for different crystal treatments. Notice that in this study we used an additional mechanical collimation as compared with the previous study in order to better resolve the sources at the edges of the crystals. In the non-calibrated images is discernible how the compression effect increases when the White treatment is used. Thus, larger bias values of these data are obtained at the edges. However, for all treatments, this bias is significantly reduced when the data is calibrated using the NN interpolation. Moreover, the linearity for all the treatments agrees well with the actual value. We found the best FWHM for the RR treatment. A deterioration of the calibrated spatial resolution FWHM for the ESR and White treatments is observed, most likely due to the fact that the LD is no longer preserved, and the stronger edge effect. In contrast to the spatial resolution behavior, ESR and White treatments exhibited the best energy resolution (12-14%) due to the larger collection of optical photons. This light collection increase also causes a shift of the measured DOI histograms to higher values. However, after DOI calibration we observed a general good qualitative agreement of all profiles with the expected gamma ray attenuation distribution. For all cases we made it also possible to calibrate the *a* and *b* parameters for the entire block.

5. Conclusions

We have described and validated a calibration method for monolithic crystals of large dimensions based on analytic calculations. We have combined this with high density photosensors arrays and readout electronics. Such readout makes use of a reduction scheme of signals resulting in the number of rows plus columns of the photosensor arrays. This has been shown to be a good sampling to return accurate energy and 3D impact coordinates of the γ–rays in monolithic blocks. The aim of the article has been to calibrate these measured energy and impact coordinates to the expected values. This has been done using the so-called Voronoi diagrams and interpolation methods. We have studied few interpolation methods, but in this article, we have shown the two that achieved better performance, named WAM ($k=2$) and NN.

We have first evaluated the two interpolation methods and compared them with an additional approach based on 1D monomial that we have successfully used in former detector designs and systems. The tested interpolations are used not only for the XY impact position but also for the energy and now for the photon DOI. If we compared to the 1D method, both procedures based on the Voronoi diagrams allowed one to calibrate the whole scintillation volume, without rejecting events at the detector edges, increasing the system sensitivity. Nevertheless, we observed some better calibration performance when using the NN method.

Finally, we made use of the NN interpolation method to evaluate the response of the described methodology to six different crystal treatments. Although black paint is widely used to preserve the light distribution expecting more accurate 3D impact determination, other crystal treatments that enhance the light extraction using diffuse or specular reflectors are also possible. We have demonstrated that it is possible to use the NN interpolation with a variety of crystal treatments. Therefore, the selection of the crystal treatment would be a trade-off of the aimed system geometry and application.

References

[P1.1] V. N. Solovov, et al., “Position reconstruction in a dual phase xenon scintillation detector,” *IEEE Trans. on Nucl. Sci.*, vol. 59, no. 6, pp. 3286-3293, 2012.

[P1.2] W. A. Peters, et al., “Performance of the versatile array of neutron detectors at low energy (VANDLE),” *Nucl. Instrum. Meth. A*, vol. 836, pp. 122-133, 2016.

[P1.3] Z. Zhang, et al., “The calibration and electron energy reconstruction of the BGO ECAL of the DAMPE detector,” *Nucl. Instrum. Meth. A*, vol. 836, pp. 98-104, 2016.

[P1.4] K. Asari, S. K. Vijayan and D. Radhakrishnan, “A new approach for nonlinear distortion correction in endoscopic images based on least squares estimation,” *IEEE Trans. on Med. Imag.*, vol. 18, no. 4, pp. 345-354, 1999.

[P1.5] M. Dahlbom, “Technology,” in *Physics of PET and SPECT Imaging*, CRC Press, Boca Raton, 2017.

[P1.6] J. M. Benlloch, et al., “Scanner calibration of a small animal PET camera based on continuous LSO crystals and flat panel PSPMTs,” *Nucl. Instrum. Meth. A*, vol. 571, no. 1-2, pp. 26-29, 2007.

[P1.7] F. Sánchez, et al., “ALBIRA: a small animal PET/SPECT/CT imaging system,” *Med. Phys.*, vol. 40, no. 5, pp. 051906, 2013.

[P1.8] S. España, et al., “DigiPET: sub-millimeter spatial resolution small-animal PET imaging using thin monolithic scintillators,” *Phys. Med. Biol.*, vol. 59, no. 13, pp.3405, 2014.

[P1.9] T. K. Lewellen, “The challenge of detector designs for PET,” *Am. J. Roentgenol.*, vol. 195, no. 2, pp. 301-309, 2010.

[P1.10] P. Bruyndonckx, et al., “Towards a continuous crystal APD-based PET detector design,” *Nucl. Instrum. Meth. A*, vol. 571, no. 1-2, pp. 182-186, 2007.

[P1.11] M. Ito, S. J. Hong, and J. S. Lee, “Positron emission tomography (PET) detectors with depth-of-interaction (DOI) capability,” *Biomed. Eng. Lett.*, vol. 1, no. 2, pp. 70, 2011.

[P1.12] S. An et al., “ Development of a New PET Detector With Depth-Encoding Capability Using Wavelength-Shifting Fiber Readout,” *IEEE Trans. Radiat. Plasma Med. Sci.,* vol. 1, no. 3, pp. 206-211, 2018.

[P1.13] M.S. Lee, K. Y. Kim, G. B. Ko, J. S. Lee, “Prototype pre-clinical PET scanner with depth-of-interaction measurements using single-layer crystal array and single-ended readout,” Phys. Med. Biol., vol. 62, no. 10, pp. 3983-3996, 2017

[P1.14] A. J. González, F. Sánchez, and J. M. Benlloch, “Organ-dedicated molecular imaging systems,” *IEEE Trans. Radiat. Plasma Med. Sci.*, vol. 2, no. 5, pp. 388-403, 2018.

[P1.15] Z. Gu, et al., “A DOI detector with crystal scatter identification capability for high sensitivity and high spatial resolution PET imaging,” *IEEE Trans. on Med. Imag.*, vol. 63, no. 3, pp. 740-747, 2015.

[P1.16] Ling, T., T. K. Lewellen, and R. S. Miyaoka, “Depth of interaction decoding of a continuous crystal detector module,” *Phys. Med. Biol.,* vol. 52, no. 8, pp. 2213, 2007.

[P1.17] W. C. Hunter, H. H. Barrett, and L. R. Furenlid, “Calibration method for ML estimation of 3D interaction position in a thick gamma-ray detector,” *IEEE Trans. Nucl. Sci*., vol. 56, no. 1, pp. 189-196, 2009.

[P1.18] H. T. Van Dam, et al., “Improved nearest neighbor methods for gamma photon interaction position determination in monolithic scintillator PET detectors,” *IEEE Trans. Nucl. Sci*., vol. 58, no. 5, pp. 2139-2147, 2011.

[P1.19] G. Borghi, et al., “Experimental Validation of an Efficient Fan-Beam Calibration Procedure for *k*-Nearest Neighbor Position Estimation in Monolithic Scintillator Detectors,” *IEEE Trans. Nucl. Sci*., vol. 62, no. 1, pp. 57-67, 2015.

[P1.20] F. Müller, D. Schug, P. Hallen, J. Grahe and V. Schulz, “Gradient Tree Boosting-Based Positioning Method for Monolithic Scintillator Crystals in Positron Emission Tomography,” ,” *IEEE Trans. Radiat. Plasma Med. Sci.,* vol. 2, no. 5, pp. 411-421, 2018.

[P1.21] F. Müller, D. Schug, P. Hallen, J. Grahe and V. Schulz, “novel DOI Positioning Algorithm for Monolithic Scintillator Crystals in PET based on Gradient Tree Boosting,” *IEEE Trans. Radiat. Plasma Med. Sci.,* vol. 3, no. 4, pp. 465-474, 2019.

[P1.22] Y. Wang, et al., “3D position estimation using an artificial neural network for a continuous scintillator PET detector,” *Phys. Med. Biol.*, vol. 58, no. 5, pp. 1375, 2013.

[P1.23] Z. Li, M. Wegrowski, P. Bruyndonckx, G. Vandersteen, “Nonlinear least-squares modeling of 3D interaction position in a monolithic scintillator block,” *Phys. Med. Biol.*, vol. 55, no. 21, pp. 6515, 2010.

[P1.24] T. Ling, T. H. Burnett, T. K.Lewellen, and R. S. Miyaoka, "Parametric positioning of a continuous crystal PET detector with depth of interaction decoding," *Phys. Med. Biol.*, vol. 53, no. 7, pp. 1843, 2008.

[P1.25] S. Krishnamoorthy, et al., “Performance evaluation of the MOLECUBES β-CUBE—a high spatial resolution and high sensitivity small animal PET scanner utilizing monolithic LYSO scintillation detectors,” *Phys. Med. Biol.*, vol. 63, no. 15, pp. 155013, 2018.

[P1.26] H. O. Anger, “Sensitivity, resolution, and linearity of the scintillation camera,” *IEEE Trans. Nucl. Sci*., vol. 13, no. 3, pp. 380-392, 1966.

[P1.27] C. W. Lerche, et al., “Dependency of energy-, position-and depth of interaction resolution on scintillation crystal coating and geometry,” IEEE Transactions on Nuclear Science 55.3 (2008): 1344-1351.

[P1.28] Pani, R., et al., “Position algorithm for monolithic scintillation crystals based on charge projection readout,” *J. Instrum.*, vol. 11, no. 01, pp. C01061, 2016.

[P1.29] M. M. Fernandez, et al., “A flat-panel-based mini gamma camera for lymph nodes studies,” *Nucl. Instrum. Meth. A*, vol. 527, no. 1-2, pp. 92-96, 2004.

[P1.30] F. Sanchez, et al., “Design and tests of a portable mini gamma camera,” *Med. Phys.*, vol. 31, no. 6, pp. 1384-1397, 2004.

[P1.31] M. Seimetz, et al., “Correction algorithms for signal reduction in insensitive areas of a small gamma camera,” *J. Instrum.*, vol. 9, no. 05, pp. C05042, 2014.

[P1.32] F. Aurenhammer, “Voronoi diagrams—a survey of a fundamental geometric data structure,” *ACM Comput. Surv.*, vol. 23, no. 3, pp. 345-405, 1991.

[P1.33] J.B. Davis, et al., “Assessment of 18F PET signals for automatic target volume definition in radiotherapy treatment planning,” *Radiother. Oncol.*, vol. 80, no. 1, pp. 43-50, 2006.

[P1.34] I. S. Klyuzhin, and V. Sossi, “PET image reconstruction and deformable motion correction using unorganized point clouds,” *IEEE Trans. on Med. Imag.*, vol. 36, no. 6, pp. 1263-1275, 2017.

[P1.35] H. Alva-Sánchez, et al., “Energy calibration of individual crystals in a LYSO pixelated array for microPET detection modules using Voronoi diagrams,” *Nucl. Instrum. Meth. A*, vol. 596, no. 3, pp. 384-389, 2008.

[P1.36] H. Semmaoui, et al., “Crystal identification based on recursive-least-squares and least-mean-squares autoregressive models for small animal PET,” *IEEE Trans. Nucl. Sci.*, vol. 55, no. 5, Oct. 2008.

[P1.37] D. Cervone, L. Bornn, and K. Goldsberry, “NBA court realty,” in *10th MIT Sloan Sports Analytics Conference*, 2016.

[P1.38] S. Fonseca, J. Milho, B. Travassos, D. Araújo, “Spatial dynamics of team sports exposed by Voronoi diagrams,” *Hum. Mov. Sci.*, vol. 31, no. 6, pp. 1652-1659, 2012.

[P1.39] L. Andronov, I. Orlov, Y. Lutz, J. L. Vonesh, and B. P. Klaholz, “ClusterViSu, a method for clustering of protein complexes by Voronoi tessellation in super-resolution microscopy,” *Sci. Rep.*, vol. 6, pp. 24084, 2016.

[P1.40] P. Felfer, A. V. Ceguera, S. P. Ringer, “Detecting and extracting clusters in atom probe data: A simple, automated method using Voronoi cells,” *Ultramicroscopy*, vol. 150, pp. 30-36, 2015.

[P1.41] J. Roshanian, Y. Shabnam, and M. Ebrahimi, “Star identification based on euclidean distance transform, voronoi tessellation, and k-nearest neighbor classification,” *IEEE Trans. Aerosp. Electron. Syst.*, vol. 52, no. 6, pp. 2940-2949, 2016.

[P1.42] C. Duyckaerts, and G. Godefroy, “Voronoi tessellation to study the numerical density and the spatial distribution of neurones,” *J. Chem. Neuroanat.*, vol. 20, no. 1, pp. 83-92, 2000.

[P1.43] A. Martínez, J. Martínez, H. Pérez-Rosés, and R. Quirós, “Image Processing using Voronoi diagrams,” in *IPCV*, Las Vegas Nevada, USA, 2007.

[P1.44] A. González-Montoro, et al., “Performance study of a large monolithic LYSO PET detector with accurate photon DOI using retroreflector layers,” *IEEE Trans. Radiat. Plasma Med. Sci.,* vol. 1, no. 3, pp. 229-237, 2017.

[P1.45] A. Gonzalez-Montoro, and A. J. González, “Performance comparison of large-area SiPM arrays suitable for gamma ray detectors,” *Biomed. Phys. Eng. Express*, vol. 5, no. 4, pp. 045013, 2019.

[P1.46] R. Pani, et al., “Continuous DOI determination by Gaussian modelling of linear and non-linear scintillation light distributions,” in *Proc. IEEE NSS-MIC*, Valencia, Spain, 2011, pp. 3386-3389.

[P1.47] A. González-Montoro, et al., “Novel method to measure the intrinsic spatial resolution in PET detectors based on monolithic crystals,” *Nucl. Instrum. Meth. A*, vol. 920, pp. 58-67, 2019.

[P1.48] MATLAB. (2018). *version 9.5 (R2018b)*. Natick, Massachusetts: The MathWorks Inc.

[P1.49] I. Amidror, “Scattered data interpolation methods for electronic imaging systems: a survey,” Journal Elec. Imag. Vol. 11, no. 2, pp. 157-176, 2002.

[P1.50] A. González-Montoro, “Design and implementation of PETdetectors based on monolithic crystals and SiPMs,” Ph.D. dissertation, Dept. Atomic, Molecular and Nuclear Physic, Valencia Univ., Valencia, Spain, 2018.

Acknowledgments

The authors would like to thank members of Bruker NMI in Valencia for their support in brainstorming of ideas

7 Reducing Calibration Time in PET Systems Based on Monolithic Crystals

Authors: Marta Freire, Gabriel Cañizares, Andrea González-Montoro and Antonio J. González.

Published: Frontiers in Medicine, 2021, vol. 8, p. 734476. Doi: 10.3389/fmed.2021.734476

Summary: This article presents the experimental implementation of the Voronoi calibration method in a dedicated prostate PET system composed by monolithic-based PET detectors (constructed at i3M), with particular emphasis on techniques that minimize calibration procedures. The system has been built under the *ProsPET* Spanish National Project and it has been installed at the hospital La Fe in Valencia (See Section 5.1). The scanner is composed of a ring of 24 LYSO monolithic crystals of 50×50×15 mm^3 coupled to an array of 12×12 SiPMs and the projection readout circuit. The crystals present black paint on the lateral sides and include a RR layer at the top face as this was the treatment exhibiting the best overall detector performance in the previous article [1].

The Voronoi calibration method has been applied to the detectors after having been mounted in the system. A standard calibration procedure, in which each detector is individually calibrated, has been compared to two novel alternative calibration procedures, namely *TEST1* and *TEST2*, which have been developed with the goal of reducing the calibration time and complexity of the standard

method. Experimental data has been acquired and subsequently calibrated, applying the standard procedure and the two implemented alternative calibration procedures. A comparison of these approaches has been performed by analyzing the system spatial resolution, high count rates capabilities and image quality. The results show that the *TEST2* approach reduces the calibration times by approximately 80% compared to that of the standard one, without system performance degradation. Therefore, this method solves one of the principal problems of using monolithic-based detectors in PET scanners.

Reducing Calibration Time in PET Systems Based on Monolithic Crystals

Marta Freire, Gabriel Cañizares, Sara Echegoyen, Andrea Gonzalez-Montoro and Antonio J. Gonzalez.

Abstract— *In the past years, the gamma-ray detector designs based on the monolithic crystals have demonstrated to be excellent candidates for the design of high-performance PET systems. The monolithic crystals allow to achieve the intrinsic detector resolutions well below state-of-the-art; to increase packing fraction thus, increasing the system sensitivity; and to improve lesion detectability at the edges of the scanner field of view (FOV) because of their intrinsic depth of interaction (DOI) capabilities. The bottleneck to translate to the clinical PET systems based on a large number of monolithic detectors is eventually the requirement of mechanically complex and time-consuming calibration processes. To mitigate this drawback, several methods have been already proposed, such as using non-physically collimated radioactive sources or implementing the neuronal networks (NN) algorithms trained with simulated data. In this work, we aimed to simplify and fasten a calibration process of the monolithic based systems. The Normal procedure consists of individually acquiring a 11 × 11* ^{22}*Na source array for all the detectors composing the PET system and obtaining the calibration map for each module using a method based on the Voronoi diagrams. Two reducing time methodologies are presented: (i) TEST1, where the calibration map of one detector is estimated and shared among all others, and (ii) TEST2, where the calibration map is slightly modified for each module as a function of their detector uniformity map. The experimental data from a dedicated prostate PET system was used to compare the standard calibration procedure with both the proposed methods. A greater similarity was exhibited between the TEST2 methodology and the Normal procedure; obtaining spatial resolution variances within 0.1 mm error bars and count rate deviations as small as 0.2%. Moreover, the negligible reconstructed image differences (13% deviation at most in the contrast-to-noise ratio) and almost identical contrast values were reported. Therefore, this proposed method allows us to calibrate the PET systems based on the monolithic crystals reducing the calibration time by approximately 80% compared with the Normal procedure.*

Keywords— *Positron emission tomography, monolithic crystals, calibration, total-body PET, whole-body PET*

1. Introduction

In the PET detectors, two main types of scintillator crystals are usually employed namely, pixelated and monolithic. The advantages and disadvantages of each one are extensively described elsewhere [P2.1]. They offer intrinsic resolutions that are well below the state-of-the-art and an improvement of the system sensitivity, as they do not contain zero detection zones, unlike the pixelated crystals. But the most significant feature of monolithic crystals is their inherent access to the light distribution (LD) profile of the scintillation events which allows to retrieve, in addition to the planar impact coordinates (*x,y*), accurate photon depth of interaction (DOI) information, unlike the pixelated crystals that require additional components to provide 3D positioning information [P2.2][P2.3]. The DOI information permits to correct for the parallax errors, which strongly affect the systems with small apertures (i.e., small animal and organ dedicated scanners), but also at the edges of the field of view (FOV) in the human size scanners. Both width and position of the source profile improve when applying the DOI correction independently of the system diameter [P2.4][P2.5]. Recently, the monolithic crystals are employed in the PET scanners achieving high sensitivity and spatial resolution [P2.6]-[P2.8]. Moreover, regarding cost, analyzing the different providers for scintillator crystals and studying the price differences between the several pixel arrays and monolithic crystals with similar volumes, it can be concluded that they are cheaper than the traditional pixelated scintillators for the pixel sizes smaller than 1.5 mm×1.5 mm, as the ones used in the pre-clinical PET imaging.

To accurately determine the energy and 3D impact position in the monolithic-based PET detectors, the calibration processes accounting for the possible non-uniformities or edge effects are required [P2.9]. The non-uniformities arise from different gains in the photosensors or readout channels, and eventually by the crystal light yields abnormalities. The edge effects result from the scintillation light truncation toward the crystal edges, reducing the accuracy of the photon impact coordinates determination and energy discrimination. For the pixelated-based detectors, the flood maps are easily and quickly found, since one source can be placed at the center of the PET scanner providing information of all the pixel elements. However, for the monolithic-based detectors, the calibration processes are typically based on scanning a collimated small size source across the entire monolithic surface while recording the measured and mechanical/known source positions [P2.1]. This procedure must be applied for each detector module of the PET scanner, which results in the time-consuming calibrations and requires using entangled hardware set-ups [P2.9]. For one single detector, the measurement for obtaining reference data might last about 30 min even when using the high activity sources.

Multiple methods have been proposed to ease the calibration processes in the monolithic assemblies; such as using reference data corresponding to a line of irradiation points instead of singular points [P2.10][P2.12][P2.13], utilizing an array of collimated sources [P2.10], or using non-physically collimated sources [P2.11][P2.12]. An alternative approach, not requiring the calibration for each detector block of the PET system, is to carry out an accurate simulation of the detector responses either for Neural Networks (NN) training [P2.13][P2.14] or for the generation of look-up-tables (LUTs) to be applied using the maximum likelihood expectation maximization methods (MLEM) [P2.15].

In this work, we propose an approach to apply the detector calibration process based on the Voronoi diagrams [P2.10] in the PET scanners based on a large number of monolithic detectors. The proposed methodology significantly reduces the calibration times while accounts and corrects for the possible differences among each individual detector module. Shortly, the method suggests using the combined accurate calibration of few detectors, to be applied after some tuning provided by uniform radiation, to all the other detectors. In the following, we describe this rather simple methodology, but never studied before in detail, and its experimental validation employing data from a prostate dedicated clinical PET scanner [P2.16].

2. Materials and methods

A. Materials

Data were experimentally acquired using a clinical PET specifically designed for prostate imaging. The scanner is composed of a single ring with 24 detectors [P2.16], each one comprising a LYSO:Ce ($Lu_{1.8}Y_2SiO_5$:Ce) monolithic crystal of 50×50×15 mm^3 with the lateral surfaces black painted (absorbent paint) and the entrance face, such as a retroreflector layer [P2.10][P2.17], as shown in the images of the system in Figure P2.1. Each scintillation crystal is coupled to a photosensor array of 12×12 silicon photomultipliers (SiPMs) with 3×3 mm active area and 4.2 mm pitch (52% active are coverage) by means of optical grease (BC-630, Saint Gobain, France). The readout scheme provides the row and column SiPM signals, thus allowing to determine the 3D photon impact coordinates within the crystal [P2.4][P2.18]. The detector output signals are fed into a data acquisition (DAQ) system based on the 12-bit analog-to-digital converters (ADCs) with 1 GB ethernet connection, and the summed signal of either all SiPM rows or columns, was fed into a trigger board that allows coincidences within a 5 ns coincidence window. Further details about the system can be found in the reference [P2.16].

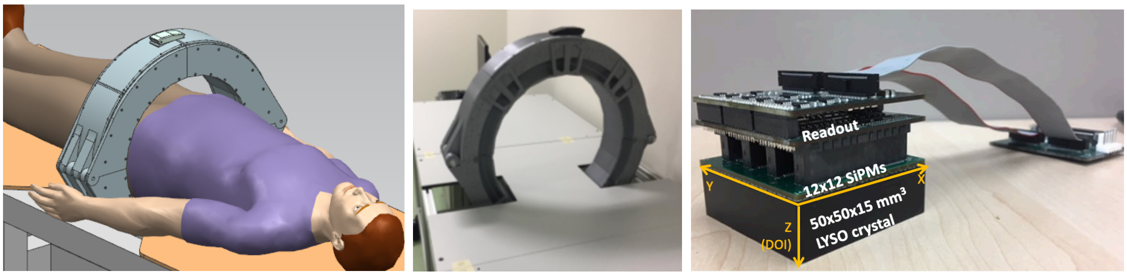

Figure P2.1. The sketch (left) and photograph (right) of the prostate dedicated PET system used during the calibration tests.

The planar impact coordinates (x, y) were calculated using the rows and column SiPM signals by applying a modified version of the center of gravity algorithm (COG) in which the row and column values are risen to the power of 2 to improve the system linearity [P2.19]. The DOI value was estimated as E/I_{max} where E is the energy calculated as the sum of the rows or columns, and I_{max} is the maximum value of the row or column, respectively [P2.12].

B. Calibration Process

Instead of sequentially moving individual radioactive sources across the crystal surface, which requires long calibration times, we used an array of 11×11 ^{22}Na radioactive sources (4.6 mm pitch and 1 mm in diameter, total activity ~10 μCi) placed at the known positions. A 30 mm thick tungsten collimator, with drilled holes of 1.2 mm in diameter, was accurately aligned with the sources and placed at each crystal entrance. The acquired reference data were later post-processed using a software collimation method (defined as a trade-off between the statistics and spatial resolution) that rejects the lines of response (LORs) with angles larger than 1.2 degrees measured from the detector normal [P2.2]. These two-steps, acquisition and collimation, resulted in the accurate flood maps composed by 121 measured positions as those shown in Figure P2.2 (left).

The calculated 3D photon impact position and energy were calibrated using a method based on the Voronoi diagrams. The flood map of the 11×11 ^{22}Na sources (as shown in Figure P2.2) is used to generate a Voronoi diagram, thus permitting the partition of the crystal surface into 121 Voronoi cells and the extraction of five Voronoi factors for each cell [P2.10]. The VoronoiFactor$_X$ and VoronoiFactor$_Y$ were calculated as the deviation of the measured source position to the mechanical position and the VoronoiFactor$_E$ was determined as the deviation of the energy photopeak value in the channels to the value corresponding to the central Voronoi cell. Finally, we determined the lower and upper limits (*a* and *b* parameters) and sigma (σ_{int}) of the E/I$_{max}$ histogram for each Voronoi region using the DOI analytical expression extracted from the reference [P2.14] (as shown in Figure P2.2). Two Voronoi factors were calculated corresponding to the limits a-σ_{int} and b+σ_{int} and then, considered to be equal to 0 and 15 mm (crystal thickness) to calibrate the measured E/I$_{max}$ into millimeters. As shown in the reference [P2.10] for more detail of the process. These Voronoi factors were used to obtain five LUTs: two corresponding to the planar XY coordinates {LUT$_X$, LUT$_Y$}, two to the DOI {LUT$_{DOI1}$, LUT$_{DOI2}$}, and another one corresponding to the energy {LUT$_{Energy}$}. These LUTs are finally used to calibrate every impact. Data from the subjects or phantoms are off-line calibrated applying the calculated LUTs in an event-by-event process that includes a correction to the true LOR (parallax error compensation).

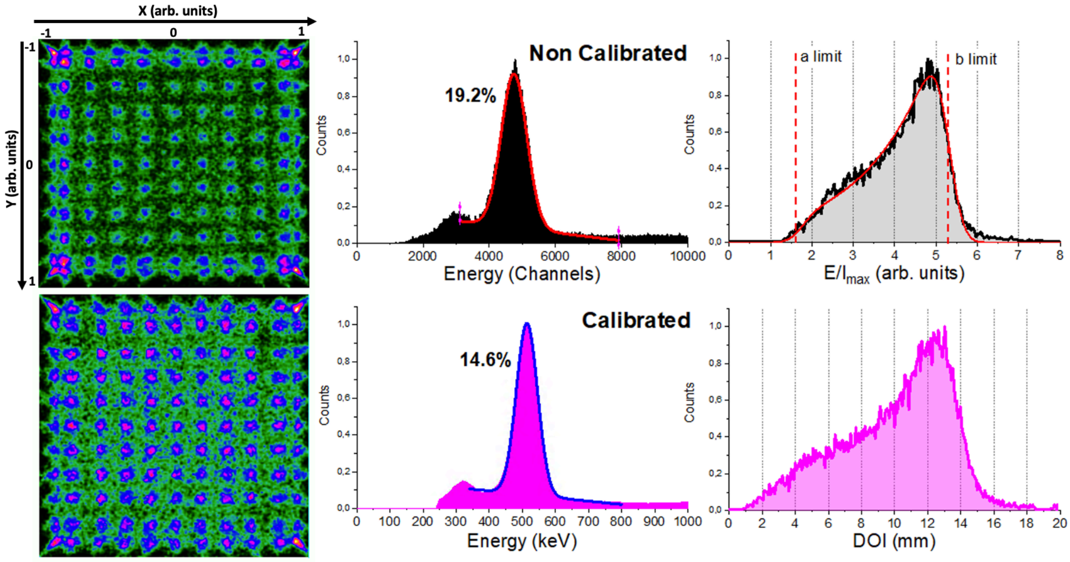

Figure P2.2. From left to right, the image flood maps of the 11 × 11 ^{22}Na collimated sources before (top) and after (bottom) calibration using the Normal method, energy spectra, and depth of interaction (DOI) distribution for the whole detector

We have tested three different calibration methods, a conventional one detector-by-detector calibration, and two proposed modifications to shorten the calibration times:

i) *Normal*, the 24 detectors of the PET scanner were individually calibrated as described above. This means, that a set of 5 individuals

{$\mathrm{LUT}_{X,Y,DOI1,DOI2,Energy}$} is generated from the flood map of each detector module. This calibration is considered as the ground-truth for comparison purposes. Figure P2.2 shows the flood map of the 11×11 ^{22}Na sources, the energy and DOI histograms for one detector module of the prostate dedicated PET before (top panels) and after (bottom panels) calibration. Acquisition using the described array and activity might last about 2–3 h per detector, thus 48–72 h for the whole system without stop (at least 6 working days). Notice that the higher activities and the use of non-encapsulated sources, such as ^{18}F could accelerate these processes but potentially increase the radiation associated risk.

ii) *TEST1*, the calibration set of only one random detector is carried out and, therefore only its {$\mathrm{LUT}_{X,Y,DOI1,DOI2,Energy}$} are generated and shared among the other detectors without further corrections. With this approach, a total process calibration time of ~ 3 h for the entire scanner was required. We have evaluated this method for two random detectors: *T1* and *T1B*, corresponding to the detectors M2 and M6, respectively.

iii) *TEST2,* three random detectors of the PET scanner were individually calibrated and, to avoid an outlier detector performance, an averaged reference calibration map was obtained using the mean values of the calibration positions of the three detectors (as shown in Figure 3 left). Thereafter, the calibration maps for each other detector were determined applying a shift map to such reference calibration map. The shift map was generated for each detector using their uniformity maps (as shown in Figure P2.3) acquired placing a relatively large uniform activity phantom at the center of the scanner FOV. Event accumulation can be observed at the edges of the uniform map due to the truncation of the LD closer to the edge of the monolithic crystal. The *x* and *y* coordinates for these regions were plotted, as shown in Figure P2.2, and a linear fit was used to estimate the slope following that event accumulation. The intersection of the lines allowed us to calculate the coordinates of the four corners. Then, four shift factors with respect to the reference ones were calculated and a natural neighbor interpolation methodology considering the four corners was applied to obtain the shift map for the entire surface. The shift map for each module was applied to the reference calibration map to obtain the new calibration map corresponding to each detector. Finally, the calibration maps were used to determine the Voronoi factors according to the reference (20). The Voronoi factors corresponding to the DOI and energy, were calculated using the uniformity measurements. A total calibration time of ~ 10 h was consumed as: the uniformity acquisition (~1 h) plus the three detectors calibration maps (6–9 h). For this case, three sets of three different detectors were used defining: *T2*, *T2B*, and *T2BB*, in particular detectors [M1, M9, and M21], [M5, M18, and M24], and [M7, M15, and M20] were used, respectively.

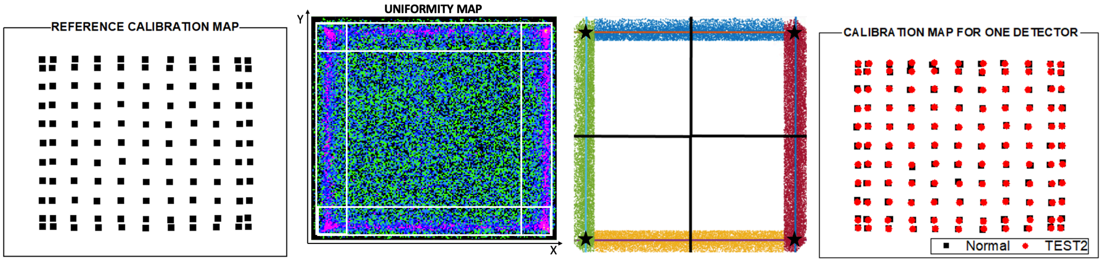

Figure P2.3. From left to right, a reference calibration map obtained as the average of the calibration positions of three random detectors, example of a detector uniform map for one detector used to obtain the calibration map in *TEST2*, surface partition obtained from the four corners calculated as the intersection of the lines following the event accumulation and calibration positions obtained for one detector in the Normal calibration and after applying the *TEST2*.

C. Evaluation of the Calibration Processes

The calibration accuracy of the proposed methods was evaluated by comparing the LUTs for *TEST1* and *TEST2* with the ground truth provided by the *Normal* case for each detector module of the prostate PET system. Thus, the correlation factors (CF) corresponding to X, Y, DOI1, DOI2, and energy, respectively, were determined for each detector module as:

$$CF^{i}_{X,Y,DOI1,DOI2,Energy} = \frac{(VoronoiFactor\ value^{i}_{X,Y,DOI1,DOI2,Energy})_{TEST}}{(VoronoiFactor\ value^{i}_{X,Y,DOI1,DOI2,Energy})_{Normal}} \qquad (1)$$

where, *i* goes from 1 to 121 (each Voronoi diagram contains 121 values because 11×11 sources array was used for the calibration). Notice that, the range of values for the VoronoiFactorX and VoronoiFactorY is [−1, 1] in arb. units; for the VoronoiFactorE it is [0, ~10000] in channels and for the VoronoiFactorDOI1, DOI2, it is [1, 8] in arb. units (as shown in Figure P2.2 top). The mean of the 121 CFi values was calculated, obtaining five *CF* values corresponding to X, Y, DOI1, DOI2, and energy for each detector module. Finally, the mean of the *CF* values of all detector modules were calculated and considered as a good estimator of the validity of the two proposed approaches. In addition, the three calibration methods were compared using the reconstructed images from the following datasets:

i) Data of a small size ^{22}Na source (0.25 mm in diameter and ~ 22 µCi activity) scanned across the radial axis of the scanner. The spatial resolution was estimated as the full width at half of the maximum (FWHM) of the source profiles.

ii) Data acquired during the evaluation of the noise equivalent count rate (NECR) of the system. This dataset was used to provide hints about the count rates capabilities of the system as a function of the calibration method. Sub-optimal calibration of the detectors might lead to a decrease in the count rates.

iii) Data acquired using a custom designed image quality (IQ) phantom made out of Polymethyl methacrylate (PMMA) with an outer diameter of 135 and 103 mm height. The IQ phantom contains six capillaries with diameters of 20, 15, 12, 9, 6, and 4.5 mm and 60 mm height each placed inside a warm background. A capillaries-to-background concentration ratio of 38 was used.

The reconstruction of the acquired data was performed using the Customizable and Advanced Software for Tomographic Reconstruction (CASToR) platform [P2.21] and the ordered subset expectation maximization (OSEM) algorithm, with voxels sizes of 1×1×1 mm and virtual detector pixels of 1×1 mm. During the reconstruction process, three iterations and two subsets were used when the small size sources were imaged, whereas eight iterations and two subsets were employed for the image quality phantom. Additionally, both the attenuation and normalization corrections were applied. For the attenuation correction, the transmission information of a previous CT acquisition was used. The normalization was applied using data of an annulus filled with fluorodeoxyglucose (FDG) (as shown in reference [P2.11]) and processed using the three different calibration approaches.

We have quantitatively evaluated the reconstructed IQ phantom calculating the contrast-to-noise ratio (CNR) and the contrast for all cases as:

$$CNR = \frac{Mean\ hot\ spot\ VOI - BackGround\ level}{Background\ standard\ deviation} \quad (2)$$

$$Contrast\ (\%) = 100 \times \frac{Mean\ hot\ spot\ VOI - Background\ level}{Mean\ hot\ spot} \quad (3)$$

where VOI stands for the Volume of Interest selected. Then, 12 VOIs were drawn distributed along the uniform warm area of the phantom to obtain the background level and SD. To calculate the *mean hot spot* values, six VOIs were defined fitting each capillary dimension but with a centered height of 25 mm.

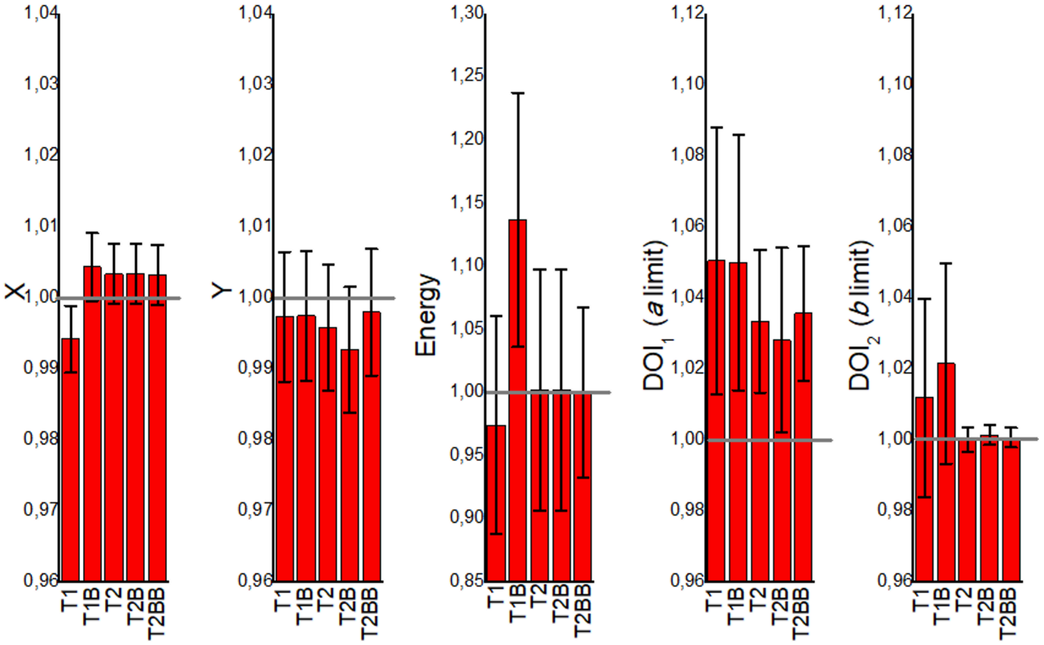

Figure P2.4. Mean CFi values obtained from the VoronoiFactorX, VoronoiFactorY, VoronoiFactorE, VoronoiFactorDOI1 and VoronoiFactorDOI2 for all detectors and calibration positions, and for all proposed calibration cases.

3. Results

A. Detector Accuracy

Figure P2.4 shows the mean values for the CFi parameters namely X and Y positions, energy, and DOI limits. The mean values are calculated for all 24 detector and for all 121 calibration positions within each detector block. The error bars are calculated as the SD of all these 24×121 values. The T2, T2B, and T2BB cases are typically close to 1, meaning that they reflect well the ground truth. However, the T1 and T1B cases are in general further from 1.

B. Reconstructed Images

Figure P2.5 depicts the FWHM values (radial, tangential, and axial) of the reconstructed images of the ^{22}Na source versus the off-radial position. For the case closer to the center of the FOV (1 cm), all the cases exhibit very similar values. However, worse FWHM values are observed for the *T1* and *T1B* cases at radial positions far from the center, especially at the edges (12 cm) resulting in an elliptical shape of the sources.

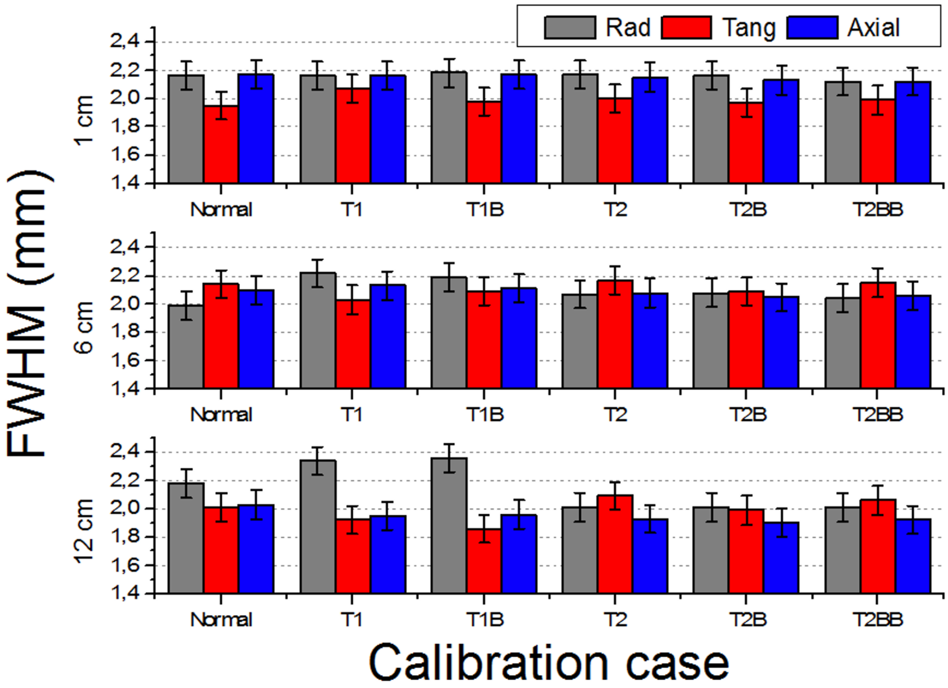

Figure P2.5. Reconstructed full width at half of the maximum (FWHM) (three components: radial, tangential, and axial) of the 1 mm in diameter source at off-radial positions 1, 6, and 12 cm.

Figure P2.6 depicts the count rate capabilities of the system for each calibration method. In general, there is a better agreement for the *TEST2* approaches with respect to the *Normal* case. Some deviations are observed for the NECR curves regarding the *TEST1* cases (also for the True and Scatter/random ones but not shown here) at high activities. We have calculated the ratios of the NECR for the *Normal* case with respect to all others. The average ratio for the *T2*, *T2B,* and *T2BB* cases is as small as 0.2, 0.1, and 0.1%, respectively, with SDs of about 1% only. However, we found the ratios of 7 and 2% for the *T1* and *T1B*, respectively.

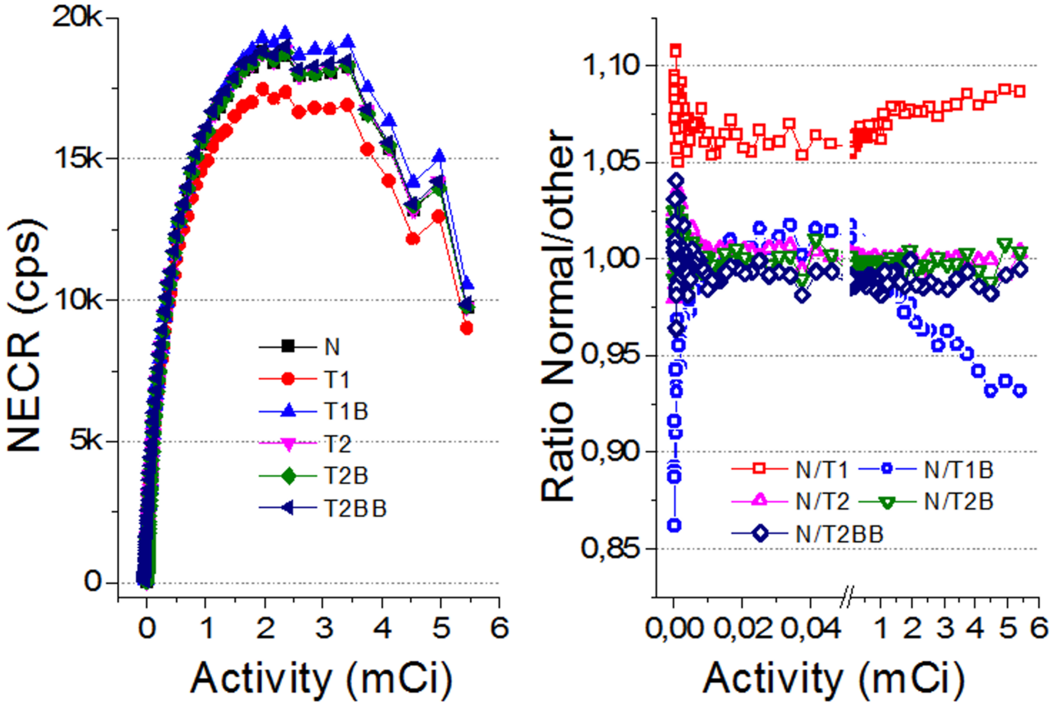

Figure P2.6. (Left) The noise equivalent count rate (NECR) curves for all the evaluated cases. (Right) Ratio of the NECR values for Normal with respect to all others. Notice there is a break between 0.5 and 0.6 mCi to expand the axis for lower values.

Figure P2.7 shows the reconstructed IQ phantom after applying the described calibration processes for all the cases. Qualitatively, the images and profiles are very similar. Slightly less uniform background is observed for the *TEST1* cases, as it can also be appreciated in the shown slice and projection at the bottom panels.

We observe the CNR values that are in general poor, most likely due to low acquisition times (Figure P2.8). Comparing the results obtained between *Normal* and the other methods, the CNR for *T1* and *T1B* are, on average, 28.5% lower. However, the *TEST2* cases exhibit similar values for the 4.5- and 6-mm rods, and better for the larger capillaries. An average improvement for all rods and tests of 8.4% is observed. We hypothesize that the improvement of CNR for the *TEST2* cases might be due to an improvement in the background uniformity caused by the averaging of three detector blocks.

4. Discussion

In this work, we have studied the possibility to reduce the calibration time for monolithic-based PET systems. Different works are proposed to obtain reference dataset using the line sources and slit collimators or uncollimated sources without detector performance degradation, avoiding irradiating the crystal at a large number of known entry points across the entire surface, and thus, reducing the time calibration [P2.6]-[P2.11][P2.22]-[P2.24]. Moreover, the use of simulated data for NN training or for LUT generation for ML position estimation [P2.12][P2.13] allows for calibration time reduction. However, most of these methods demand higher computational requirements to be efficient.

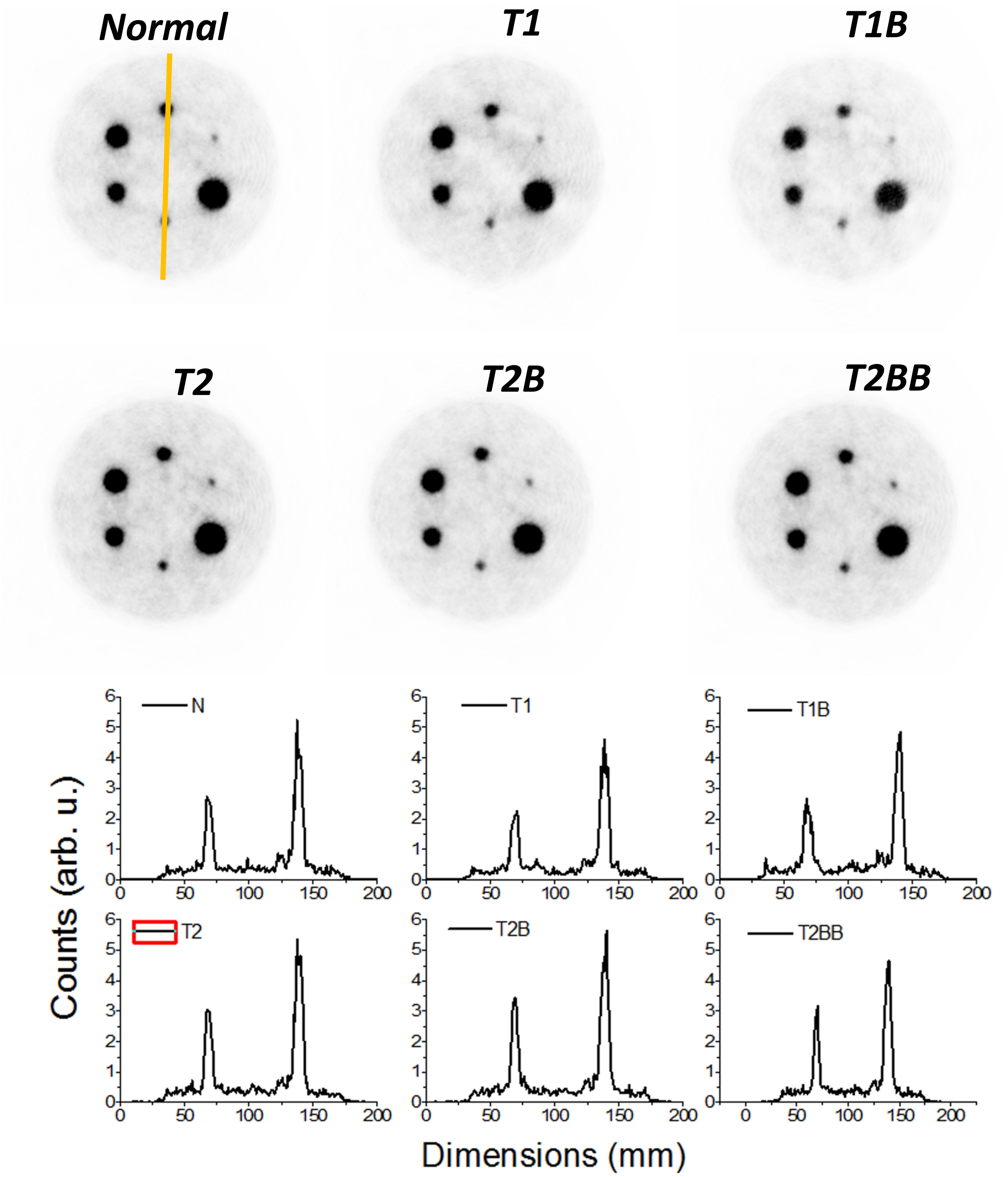

Figure P2.7. Top panels, reconstructed images of the IQ phantom. Only 15% of the low colour scale was used. Bottom panels, profiles along the smallest the marked rods in the Normal case.

In our approach, the calibration data are acquired using an array of collimated sources, instead of sequentially scanning individual radioactive sources across the crystal surface, which reduce the calibration times somewhat; however, in the *Normal* procedure each detector needs to be independently calibrated, which still leads to high time-consuming. Therefore, we have proposed two new calibration routines named *TEST1* and *TEST2* that reduce the calibration time from standard calibration of all 24 detectors of our prostate PET system (~72 h) to just 10 h in the case of *TEST2* and 3 h in the case of *TEST1* (as shown in Table P2.1). Notice that the times were estimated considering the activity of a source that can be typically found in the instrumentation laboratories and, therefore, higher activity sources would linearly improve the process. Using the high radioactivity sources and two screw bar and step motors would allow to create a robotic instrument to speed up the calibration acquisition and to prevent the radiation hazard at the same time. However, for the PET systems already installed in the research laboratories or clinical sites, introducing such a hardware setup is sometimes difficult.

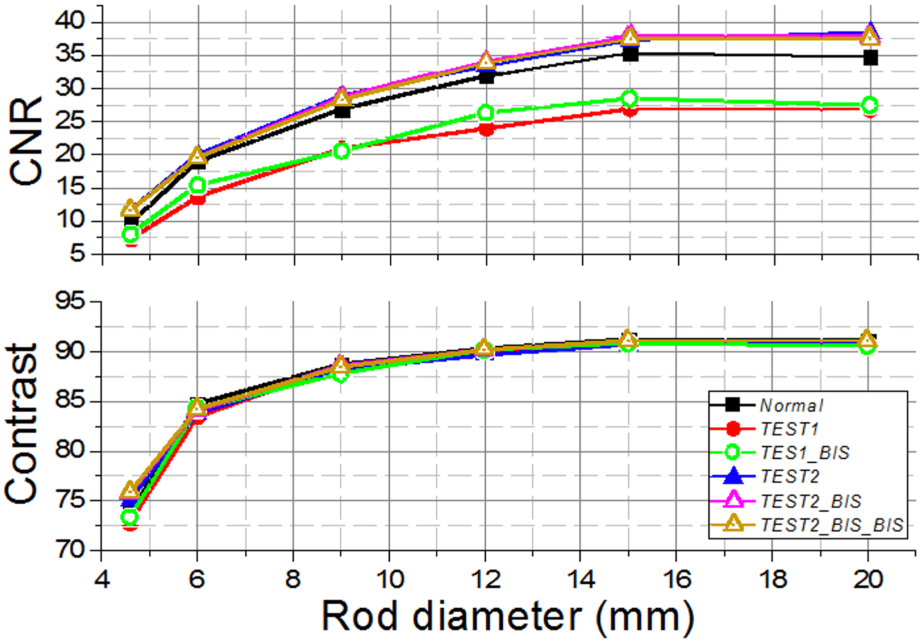

Figure P2.8. The contrast-to-noise ratio (CNR) (Top) and the contrast (Bottom) curves for the different Normal, TEST1, and TEST2 cases acquired using the prostate dedicated PET system.

An important implication of this reduction is that allow one to perform the calibration in one single working journey without the requirement of stopping, thus avoiding the additional complications. The uniform flood maps are obtained routinely during the PET calibration processes when for instance the normalization is performed. By reducing the calibration time without impacting the PET system performance, on the one hand, we are also minimizing the technical personnel exposure to radiation and, on the other hand, reducing the calibration cost associated to the supply of radioactive sources. An FDG dose used for calibration (370 MBq) costs approximately 275 € at our institution and lasts only for 1 day. Moreover, the proposed methodology simplifies the associated hardware, even if a low percentage of detectors are to be normally calibrated, such as in the *TEST2* (3/24 detectors), in comparison with calibrating all of them individually.

Our findings when comparing the results of the *TEST1* tests with the *Normal* case, showed some underperformance, as expected. Using one-detector calibration induces some errors due to many factors in the other 23 blocks, such as non-uniformities in the light collection, wrong coupling alignments of the photosensor and crystal, to name but a few. We observed that the reconstructed 1 mm sources show a worst performance for *T1* and *T1B* when they are far from the center FOV. Regarding the CNR, with the three different sets of detectors somehow still to be understood, the CNR values outperformed those exhibited the Normal calibration. The *TEST1* cases are about 28% worst on average.

	Steps/Tasks				**Maximum Calibration time**
	Acquisitions		**Computational Time**		
	11×11 ^{22}Na sources array (∼10 μCi in total)	***Uniformity***	***Shift map***	***LUT generation***	
Normal	24 detectors×(2-3 hours/detector)≈72 hours	1 hour	-	24 detectors×(1 min/detector) ≈ 20 min	72.3 hours
TEST1	2-3 hours	1 hour	-	1 min	3 hours
TEST2	3 detectors×(2-3 hours/detector)≈9 hours	1 hour	24 detectors×(24 seconds/detector) ≈10 min	24 detectors×(1 min/detector)≈20 min	10.5 hours

Table P2.1. Estimation of calibration time processes for the different methods.

The *TEST2* methodology might be the key to exploit the use of large PET scanners based on the monolithic crystals because it has demonstrated the capabilities to significantly reduce the calibration times without system degradation, enabling to calibrate a system with very low computational cost and in a reasonable time-period in a clinical domain. For a system, such as the MINDView PET insert with 60 detectors blocks of 50 × 50 × 20 mm monolithic LYSO crystals [P2.13], we struggled with a 10 days calibration process using the high activities of FDG sources, when calibrating 2–3 detectors simultaneously.

Obviously, the proposed methods require the detectors of each system to behave relatively similar, which is the case of commercially available PET scanners, since they go through the quality assessment tests during the manufacturing process. In our case, the assembly of all 24 detectors building the PET system was carried out following the same procedure, the readout electronics components have very small tolerances, and all the crystals and SiPM arrays are provided by the same manufacturer.

5. Conclusion

We have proposed two new methodologies to reduce the calibration times for the monolithic-based PET systems and validated them using data acquired in a dedicated system for prostate imaging built of 24 monolithic crystals with 15 mm thickness each. The *TEST2* method, based on calibrating few detector blocks and then, making some fine tuning using the uniform calibration maps (routinely obtained when the corrections based on uniform radiation are applied), has shown the possibility of simplifying and accelerating the calibration process without system performance degradation and without high computational cost. Therefore, this proposed method allows to solve one of the obstacles to translate to the clinics large monolithic-based PET scanners.

References

[P2.1] Gonzalez-Montoro A, Gonzalez AJ, Pourashraf S, Miyaoka RS, Bruyndonckx P, Chinn G, et al. Evolution of PET detectors and event positioning algorithms using monolithic scintillation crystals. IEEE Trans Rad Plasma Med Sci. (2021) 5:282. doi: 10.1109/TRPMS.2021.3059181.

[P2.2] Gonzalez-Montoro A, Pierce LA, Hunter WJC, Gonzalez AJ, Miyaoka R., Validation of photon collimation techniques for monolithic PET detector calibration. IEEE Trans Rad Plasma Med Sci. (2020). doi: 10.1109/TRPMS.2020.3043397.

[P2.3] Du J, Ariño-Estrada G, Bai X. and Cherry SR Performance comparison of dual-ended readout depth-encoding PET detectors based on BGO and LYSO crystals. Phys Med Biol. (2020) 65:5030. doi: 10.1088/1361-6560/abc365

[P2.4] Gonzalez AJ, Aguilar A, Conde P, Hernandez L, Moliner L, Vidal LF, et al. A PET Design Based on SiPM and Monolithic LYSO Crystals: Performance Evaluation. IEEE Trans Nucl Scie. (2016) 63:2471–77. doi: 10.1109/TNS.2016.2522179

[P2.5] Mohammadi I, Castro JFC, Correia PMM, Silva ALM. and Veloso FCA Minimization of parallax error in positron emission tomography using depth of interaction capable detectors: methods and apparatus. Biomed Phys Eng Express. (2019) 5:06200. doi: 10.1088/2057-1976/ab4a1b

[P2.6] Mikhaylova E, Tabacchini V, Borghi G, Mollet P, D'Hoe E, Schaart DR. Optimization of an ultralow-dose high-resolution pediatric PET scanner design based on monolithic scintillators with dual-sided digital SiPM readout: a simulation study. Phys Med Biol. (2017) 62:8402. doi: 10.1088/1361-6560/aa8eb2

[P2.7] Sanaat A, Ashrafi-Belgabad A, Zaidi H. Polaroid-PET: a PET scanner with detectors fitted with Polaroid for filtering unpolarized optical photons— a Monte Carlo simulation study. Phys Med Biol. (2020) 65:235044. doi: 10.1088/1361-6560/abaeb8

[P2.8] Sanaat A, Arabi H, Ay MR, Zaidi H. Novel preclinical PET geometrical concept using a monolithic scintillator crystal offering concurrent enhancement in spatial resolution and detection sensitivity: a simulation study. Phys Med Biol. (2020) 65:045013. doi: 10.1088/1361-6560/ab63ef

[P2.9] España S, Marcinkowski R, Keereman V, Vandenberghe S, Van Holen R. DigiPET: Sub-millimeter spatial resolution small-animal PET imaging using thin monolithic scintillators. Phys Med Biol. (2014) 59:3405–20. doi: 10.1088/0031-9155/59/13/3405

[P2.10] Freire M, Gonzalez-Montoro A, Sanchez F, Benlloch JM, Gonzalez AJ. Calibration of gamma ray impacts in monolithic-based detectors using voronoi diagrams. IEEE Tran Rad Plasma Med Sci. (2019) 4:350–60. doi: 10.1109/TRPMS.2019.2947716

[P2.11] España SK, Deprez van Holen R, Vandenberghe S. Fast calibration of SPECT monolithic scintillation detectors using un-collimated sources. Phys Med Biol. (2013) 58:4807–25. doi: 10.1088/0031-9155/58/14/4807

[P2.12] Fan P, Wang S, Wu Z, Liu Y, Ma T. Monolithic PET detector calibration using uncollimated source and gamma interaction position distribution constrain. In: Proc. IEEE NSS/MIC (2017). p. 1–5. doi: 10.1109/NSSMIC.2017.8532720

[P2.13] Iborra A, Gonzalez AJ, Gonzalez-Montoro A, Bousse A. and Visvikis D Ensemble of neural networks for 3D position estimation in monolithic PET detectors. Phys Med Biol. (2019) 64:5010–3. doi: 10.1088/1361-6560/ab3b86

[P2.14] Sanaat A, Zaidi H. Depth of interaction estimation in a preclinical PET scanner equipped with monolithic crystals coupled to SiPMs using a deep neural network. Appl Sci. (2020) 10:4753. doi: 10.3390/app10144753

[P2.15] Park JH, Lee S. Monte carlo simulations-based maximum-likelihood position estimation for monolithic scintillation detectors. J Korean Phys Soc. (2019) 74:812–5. doi: 10.3938/jkps.74.812

[P2.16] Cañizares G, Gonzalez-Montoro A, Freire M, Lamprou E, Barrio J, Sanchez F, et al. Pilot performance of a dedicated prostate PET suitable for diagnosis and biopsy guidance. EJNMMI Phys. (2020) 7:38. doi: 10.1186/s40658-020-00305-y

[P2.17] Gonzalez-Montoro A, Aguilar A, Cañizares G, Conde P, Hernandez L, Vidal LF, et al. Performance study of a large monolithic LYSO PET detector with accurate photon DOI using retroreflector layers. IEEE Trans Rad Plasma Med Scie. (2017) 1:229–37. doi: 10.1109/TRPMS.2017.2692819

[P2.18] Gonzalez AJ. Gonzalez-Monotoro, A, Vidal LF, Barbera J, Aussenhofer S, Hernandez L, et al. Initial Results on the MINDView PET Insert Inside the 3T mMR. IEEE Trans Rad Plasma Med Sci. (2019) 3:343–51. doi: 10.1109/TRPMS.2018.2866899

[P2.19] Pani R, Bettiol M, Preziosi E, Cinti MN, Borrazzo C, Pellegrini R et al. Position algorithm for monolithic scintillation crystals based on charge projection readout. J Inst. (2016) 11:C01061. doi: 10.1088/1748-0221/11/01/C01061

[P2.20] Solovov VN, Belov VA, Akimov DY, Araujo HM, Barnes EJ, Burenkov AA, et al. Position reconstruction in a dual phase xenon scintillation detector. IEEE Trans Nucl Sci. (2012) 59:3286–93. doi: 10.1109/TNS.2012.2221742

[P2.21] Merlin T, Stute S, Benoit D, Bert J, Carlier T, Comtat C, et al. CASToR: a generic data organization and processing code framework for multi-modal

Data availability statement

The raw data supporting the conclusions of this article will be made available by the authors, without undue reservation.

Author contributions

MF has designed the experiments, the calibration of all detectors, and elaborated the draft manuscript. SE has analyzed part of the data. GC has taken care of the normalization correction and reconstruction of the data. AG-M has supervised the calibration processes and conducted the experimental data acquisitions. AG has managed the different contributions, wrote the final manuscript, and interpreted the results. All authors contributed to the article and approved the submitted version.

Funding

This work was supported in part by the Spanish Ministerio de Ciencia e Innovación under Grant No. PID2019-107790RB-C21 and co-funded by the European Union ERDF funds (European Regional Development Fund [ERDF]) of the Comunitat Valenciana 2014-2020, with reference IDIFEDER/2018/032 (High-Performance Algorithms for the Modeling, Simulation, and early Detection of diseases in Personalized Medicine). This work was in part also supported by the Imagen Molecular de Alta Sensibilidad (IMAS) project launched by the Conselleria de Sanitat Universal i Salut Pública of the Goverment of Valencia Region, announced in the BOE 328, December 28, 2020, co-funded at 50% by the ERDF. AG-M was supported by Valid Program for Researchers in Postdoctoral Phase of the Ministry of Labor and Social Economy (Generalitat de Valencia) and the EU Social Fund. MF was supported by the Program for Researchers in Predoctoral Phase of the Ministry of Labor and Social Economy (Generalitat de Valencia) and the EU Social Fund.

8 Experimental validation of a rodent PET scanner prototype based on a single LYSO crystal tube

Authors: Marta Freire, Andrea González-Montoro, Gabriel Cañizares, Ahmadreza Rezaei, Johan Nuyts, Stuart S. Berr, Mark B. Williams, José M. Benlloch and Antonio J. González.

Published: IEEE Transactions on Radiation and Plasma Medical Sciences, 2022, Vol. 6, No. 6, p. 697-706. Doi: 10.1109/TRPMS.2021.3124448

Summary: This article reports on the experimental validation of the *ScintoTube I* PET insert, a prototype constructed under the *ScintoTube* project in collaboration with the University of Virginia (see Section 5.2). The main goal of the project is to enhance the system sensitivity and to reduce the edge effect in the transaxial axis. To achieve this objective, it has been proposed to build an edge-less PET system using a single LYSO annulus crystal instead of a modular system configuration. Along the course of the PhD work, the system has been completely assembled. Moreover, the Voronoi calibration method has been adapted to accurately determine the 3D interaction position and energy of the annihilation photons in this novel design.

This article shows a detailed description of the system design, the calibration methodology and its experimental evaluation. Data was collected using point sources, phantoms (high count rates) and, subsequently calibrated using the

implemented Voronoi method. An average energy resolution of 23.4 ± 1.8% and a system spatial resolution of 1.4±0.2 and 1.3±0.4 mm FWHM has been achieved for the radial and axial directions, respectively. A system sensitivity of 3.8% at the system center and a maximum NECR at 40.6 kcps for 0.27 mCi have been obtained. The NEMA image quality have been reconstructed and all the capillaries are well resolved. These results demonstrate the feasibility of the edge-less approach.

Experimental Validation of a Rodent PET Scanner Prototype Based on a Single LYSO Crystal Tube

Marta Freire, Andrea Gonzalez-Montoro, Gabriel Cañizares, Ahmadreza Rezaei, Johan Nuyts , S. Berr, Mark B. Williams, Jose M. Benlloch , and Antonio J. Gonzalez .

Abstract— *Improving sensitivity and spatial resolution in small animal positron emission tomography imaging instrumentation constitutes one of the main goals of nuclear imaging research. These parameters are degraded by the presence of gaps between the detectors. The present manuscript experimentally validates our prototype of an edge-less preclinical PET system based on a single LYSO:Ce annulus with an inner diameter of 62 mm and ten outer facets of 26 × 52 mm^2. Scintillation light is read out by arrays of 8 × 8 SiPMs coupled to the facets, using a projection readout of the rows and columns signals. The readout provides an accurate depth of interaction (DOI). We have implemented a calibration that mitigates the DOI-dependency of the transaxial and axial impact coordinates, and the energy photopeak gain. An energy resolution of 23.4 ± 1.8% was determined. The aver- age spatial resolution of 1.4 ± 0.2 and 1.3 ± 0.4 mm FWHM were achieved for the radial and axial directions, respectively. We found a peak sensitivity of 3.8% at the system center, and a maximum NECR at 40.6 kcps for 0.27 mCi. The image quality (IQ) was evaluated using reconstructed images of an array of sources and the NEMA IQ phantom was also studied.*

Index Terms— *Calibration, monolithic scintillators, positron emission tomography, silicon photomultipliers (SiPMs).*

1. Introduction

Positron emission tomography (PET) is the molecular imaging technique of choice due to its significantly superior sensitivity when compared to other imaging modalities, such as single-photon emission tomography (SPECT) [P3.1], [P3.2] or gamma cameras [P3.3].

Most commercial PET scanners are composed of multiple detector blocks typically arranged in a cylindrical configuration to maximize detection area and geometrical sensitivity [P3.4]–[P3.7]. PET detector blocks are responsible for efficiently stopping and converting the incoming 511-keV annihilation photons into measurable electric signals that are later used for the image reconstruction process to provide a visual representation of the radiotracer distribution inside the object or patient under study.

In PET scanners based on the aforementioned modular approach, there are always unavoidable finite distances, called gaps, between detectors in both axial and transaxial planes [P3.8]. The drawbacks associated to these gaps are twofold: first, they cause losses in the system ability to detect annihilation events, resulting in decreased sensitivity and negatively impacting the overall performance of the scanner; and second, modular detectors have edges and, regardless of the scintillator technology used (monolithic crystals or pixelated arrays -specifically for crystal pixel sizes smaller than the photosensor active area), they suffer from edge effects that degrade the spatial resolution toward those edges [P3.9].

To mitigate these limitations, it has been already proposed to construct so-called edge-less PET scanners [P3.10]–[P3.12] in which the scintillation material is made of a single continuous piece instead of modular pieces attached together. This idea was first proposed in 1988; Genna and Smith [P3.13] described an SPECT design based on a single NaI(Tl) scintillation block of 31 cm in diameter. Following this concept, an SPECT system using the same crystal type but with significantly smaller size was built with a field of view (FOV) of just 25.6 mm in diameter for imaging small rodents [P3.14] and, a 26.5-cm diameter brain PET scanner, based on a single NaI(Tl) scintillator, was constructed and evaluated [P3.15]. More recently, it was presented in a simulation study showing the feasibility of a PET scanner based on a continuous cylindrical scintillator shell designed for small animal or dedicated human imaging [P3.16]. The reported system uses novel fast scintillation materials and the photosensors are coupled to both inner and outer faces of the cylinder. Finally, a cylindrical LYSO annulus of 58.5 and 48.5 mm, outer and inner diameters, respectively, was built and tested [P3.17]. Supporting the edge-less idea, Stolin et al. [P3.12] showed in another simulation study the image quality (IQ) improvement of an LYSO tube with a cylindrical inner face of 50 mm in diameter and an external face composed of 12 facets. In the present work, we show the experimental realization and pilot tests of an edge-less small-animal PET insert following an earlier design study mostlybased on simulations [P3.8]. To simplify the complex electronics, we have decided to use an LYSO scintillator with an inner circular face but a facetted outer face. As it will be described in detail below, it makes use of the silicon photomultiplier (SiPM) photosensor technology mounted in a printed circuit board (PCB) compatible with the magnetic fields found in magnetic resonance imaging (MRI) systems [P3.18], together with a radiofrequency shield based on carbon fiber composites [P3.19]. The experimental results of this work are reinforced with Monte Carlo simulations, including both nuclear and optical processes. We present here the system performance in terms of 3-D spatial and energy resolutions, system sensitivity, count rate capabilities, and reconstructed IQ.

2. Materials and Methods

A. System Architecture and Data Acquisition

Our design is based on a single LYSO:Ce ($Lu_{1.8}Y_2SiO_5$:Ce) scintillator crystal that defines an axial length of 52 mm. The LYSO:Ce bolus was 62 mm in diameter and was fabricated by Proteus (Ohio, USA) [P3.20]. A unique aspect of this design is the outer face of the annulus which was cut to generate 10 flat faces of 26×52 mm^2 each, with a maximum crystal diameter of 84.1 mm (see Figure P3.1 (a)), thus the crystal thickness varies between 9 and 10 mm. All crystal faces of the annulus were polished, with the inner face and endcaps painted black (see Figure P3.1 (b)) to minimize undesired scintillation light reflections [P3.21].

For the readout electronics, we designed PCBs (see Figure P3.1(c)) with capability to allocate three arrays of 8 × 8 SiPM elements. In particular, we used S14161 (Hamamatsu Photonics, Japan) SiPM arrays with 50-μm cell size, an active area of 3×3 mm^2, and a pitch of 3.2 mm. The photosensor array has dimensions of 25.8×25.8 mm^2 matching well the facets of the scintillation ring and was coupled to the crystal using optical grease [P3.20]. To simplify the characterization of the prototype, we have populated each PCB with only one SiPM array. The SiPM arrays were biased at 42 V and placed in the middle of the axial length of the crystal as depicted in Figure P3.1(a). Thus, the axial FOV of the system is 25.8 mm. The row and column projection readout was implemented providing 8+8 analog output signals for each SiPM array.

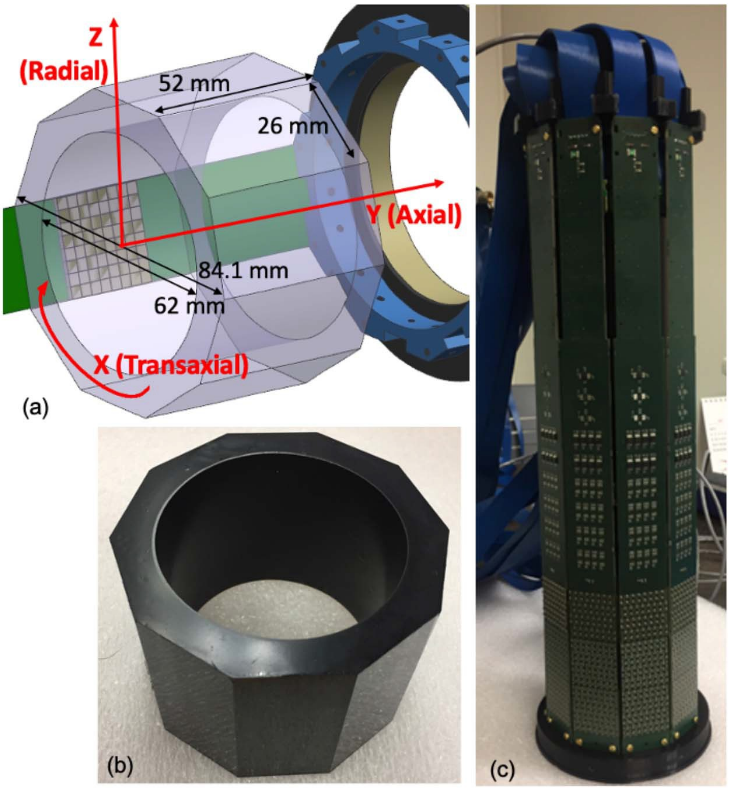

Figure P3.1. (a) Sketch showing the crystal dimensions and photosensor array position. (b) Photograph of the scintillation crystal with black painted inner faces and endcaps (there is no paint on the outer faces). (c) Photograph of the whole PET scanner without the outer housing.

All analog signals, the temperature reading signal (each detector block includes a temperature sensor) and trigger signal (determined as the sum of the row signals from a facet) are fed into a data acquisition (DAQ) system using multicoaxial cabling. The DAQ system is based on ten analog to digital converters (ADC) with 12-bit precision and an integration win- down of 250 ns. The analog pulses have rise and decay times of 25–50 and 200–300 ns, respectively. Additionally, the system includes a custom-made trigger board that receives the trig- ger signal, determines its arrival time using a leading-edge discriminator and decides on the validation of an event accordingly to the programmed firmware (coincidence map) and coincidence window [P3.19]. Each ADC is fed with 16 energy signals (eight column + eight row signals).

The architecture of the acquisition system works in such a way that when a coincidence event is detected (within a 9 ns coincidence window), all ADC channels of the two involved arrays (eight column+eight row signals) plus the adjacent ones at left and right, are sent to the workstation and processed. Thus, for every coincidence the projections of 48 rows and 48 columns are considered (see Figure P3.2 (a)). Every detector has allowed coincidences with its five opposite blocks.

In this configuration, the light distribution (LD) produced by each incident gamma ray is shared among several SiPM. The detector readout is based on a highly multiplexed scheme (high capacitance noise), as previously mentioned, in which the pho- ton timing information is obtained through the combination of several SiPMs and thus degraded. The temporal resolution of the system in the 2–3 ns scale which is not useful for time-of-flight (TOF) applications in rodents.

This PET design meets the requirements for operation inside high magnetic field as used in MRI. The PCBs have been designed, based on our previous experience, avoiding the presence of connectors and components containing ferromagnetic materials such that the generation of eddy currents induced by magnetic gradient fields is minimum. Moreover, they are placed between two carbon fiber structures reducing radiofrequency field (RF) cross-talk between the PET insert and the MRI RF. Specifically, the shielding consists on a Faraday cage made out of three overlapping carbon fiber sheets of approximately 200-μm thickness each, that helps to prevent electronic noise from both the B1 field and the Eddy currents arising from the switching gradient field. This is a design with high potential for MRI compatibility [P3.19], [P3.23]. The inner diameter of the PET insert is roughly 60 mm which leaves plenty of space to accommodate the RF coil and animal. During DAQ, the PET system was enclosed and kept at a stable temperature of 23°C using vortex tubes. The temperature was monitored using temperature sensors placed at the PCBs (near the SiPM arrays) which are read and used to generate a PID controller that manages the output air temperature [P3.19].

Data was acquired in coincidence mode using different radioactive sources. The evaluation of the spatial resolution and system sensitivity were performed using ^{22}Na small spherical sources with activities of ~515 kBq (0.25 mm in diameter) and ~290 kBq (1 mm in diameter), respectively. For imaging evaluation purposes, we used an array of 11×11 ^{22}Na sources (1 mm in diameter each) separated 4.6 mm and with a total activity of ~400 kBq. Additionally, ^{18}F was used for the evaluation of count rates capabilities and IQ during the system evaluation.

B. Data Processing: Coincidence Event Identification

The digitized values of all SiPM rows and columns, the coincidence detection time (timestamps), and facet numbers (0–9) associated to the detection of a coincidence event are encoded in binary format and sent to the workstation. The estimation of the 3-D photon impact coordinates, including depth of interaction (DOI) information and energy consists on a three-step process as described as follows.

1) The projection of the 48 columns of SiPMs, containing transaxial information of the coincidence detection are merged together to estimate the transaxial coincidence coordinates, x_1 and x_2. Two sets of eight rows projections (from the arrays containing x_1 and x_2) are used to obtain the axial coincidence coordinates, y_1 and y_2 as shown in Figure P3.2 (b). Only those events for which $|x_1 - x_2|$ is larger than the distance defined by 24 SiPMs were considered.

2) The absolute maximum of the projected columns, which is close to the center of the LD of one event, is first obtained. The signal of 30 SiPMs (±15 SiPMs on each side of the maximum) are considered to estimate x_1. The second maximum is then found, and the same process is applied to estimate x_2. For the impact position estimation, the digitized SiPM values were raised to the power of 2 (the RTP method) [P3.24], before calculation of the center of gravity (COG). The effect of, including more or less SiPMs for the COG estimation, was studied ensuring the best tradeoff between positioning and homogeneity in the flood maps. Then, y_1 and y_2 are estimated (the RTP method) using SiPM projection values of the rows.
3) The energy is estimated as the sum of the projected value of the eight rows of SiPMs belonging to x_1 and x_2 positions. The DOI coordinate (defined as z coordinate) is also calculated using these rows, as the ratio of the energy (E) to the maximum row value (I_{max}), the E/I_{max} method [P3.25].

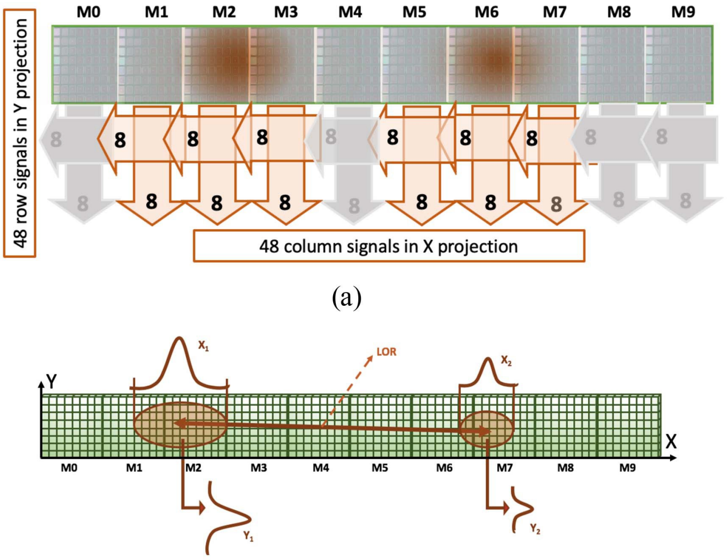

(a)

(b)

Figure P3.2. (a) Projection readout implemented providing 8+8 signals for each SiPM array. The dark areas represent the scintillation light generated due to the interaction of the annihilation photon with the scintillator material. In this example, the coincidence event has been detected by the arrays corresponding to M2 and M6. The signals of these arrays plus the signals from the adjacent ones (M1 and M3 for the event detected at M2; and M5 and M7 for the event detected at M6) are also processed. (b) x and y projections of a coincidence event. The xi coordinates (along the ring) are calculated as the projection of the columns while the yi coordinates (along the axial axis of the scanner) as the projections of the rows containing the maximum value of the distribution. Notice that both sketches show the tube unfolded.

C. Calibration Methodology

Due to the finite size of the design in the axial direction, the LDs exhibit truncation in the y-axis (axial axis), thus impacting the y_i calculation. Moreover, due to optical reflections at the facet joints (limit angle variances), there are some light losses along the x-axis (transaxial axis) that affect the estimation of the x_i coordinates [P3.26]. In addition, spatial variations in light collection loses due to optical coupling mismatches, photosensor efficiency or, scintillation light yield differences in different parts of the crystal require the calibration of the system.

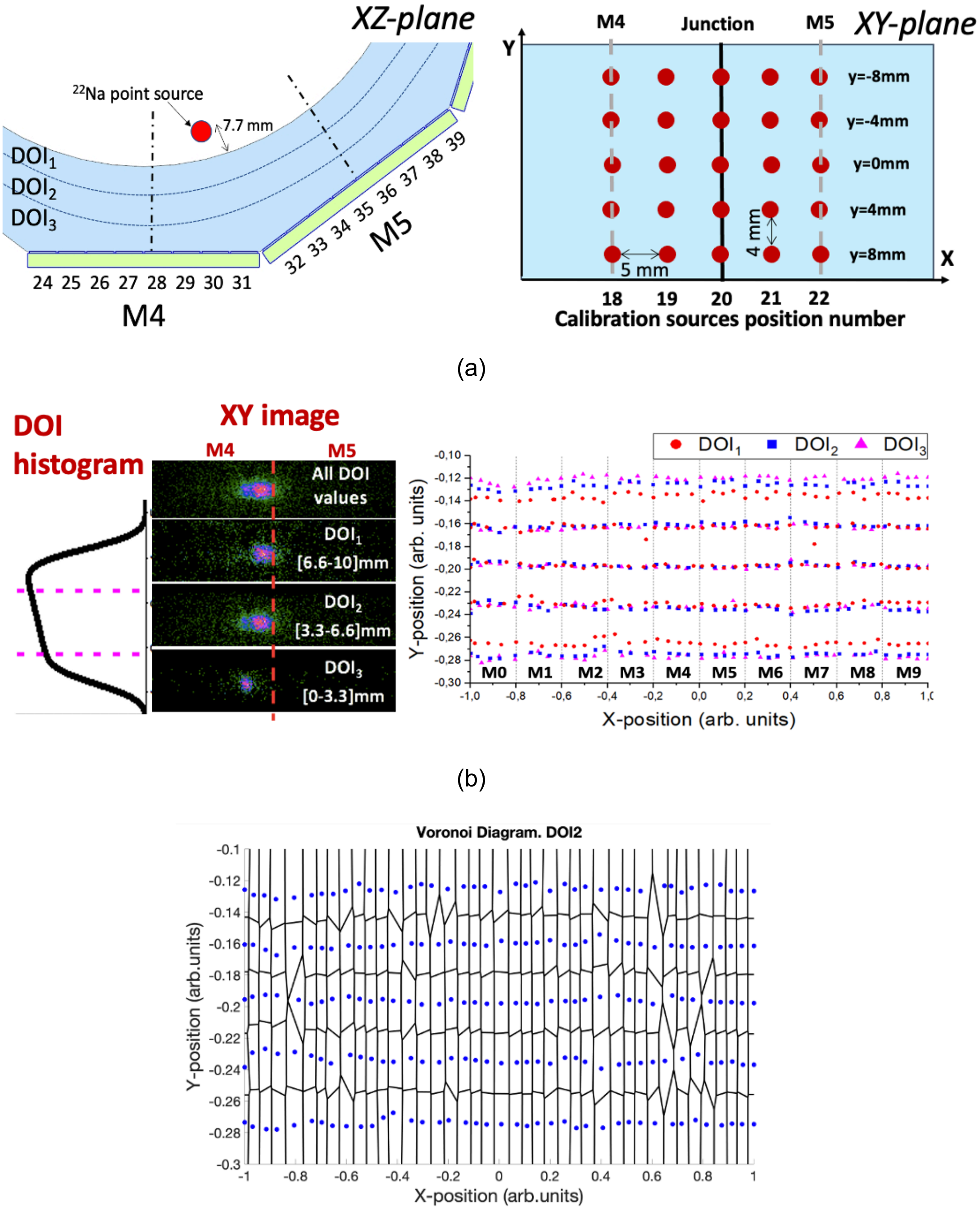

(a)

(b)

(c)

Figure P3.3. (a) Schematic of a calibration source close to the junction between two facets on XZ-plane and schematic of different calibration source positions on XY-plane, (b) Flood maps (x and y coordinates) of the source number 20 at y=0 mm; including, from top to bottom, all DOI values, DOI1 (impact at the entrance of the scintillator), DOI2 and DOI3 (impacts closer to the photosensor) and measured impact position as a function of the DOI layer for the 200 calibration positions; and (c) Voronoi Diagram of the measured source positions for DOI2 layer.

The calibration method applied for this system is based on a computational geometry technique named Voronoi diagrams [P3.21]. Voronoi diagrams divide the plane in regions, known as Voronoi cells, which are delimited by the point of the plane closest to the cell surroundings. The number of regions corresponds to the number of points contained in the plane which in our case are the calibration points. Figure P3.3 of [P3.22] provides an example of a Voronoi diagram including a description of the mathematical terminology.

The calibration procedure is a two-step process. The first step, named Tube Calibration, consists of the generation of look-up-tables (LUTs) by acquiring calibration data placing the ^{22}Na source (1 mm in diameter) at 7.7 mm from the inner face of the tube (see Figure P3.3 (a)). A matrix of 200 calibration positions was obtained acquiring data of the source at known positions in the step of 5-mm across the *x*-axis and in steps of 4-mm across the *y*-axis (see Figure P3.3 (a)).

Both the x_i and y_i coordinates (see Figure P3.3 (b)), and the photopeak position are impacted by the facetted geometry as well as by the photon DOI. To account for this dependency, the DOI information was used to modify the conventional calibration procedure [P3.21] as follows: the DOI distribution for each calibration source position has been used to split the acquired calibration data of each source in three layers as a function of the photon DOI (see Figure P3. 3 (b)) [P3.26]. Three pairs of $x_{Calibration}$ and $y_{Calibration}$ coordinates (see Figure P3.3(b)], and corresponding photopeak positions, were estimated for each calibration position. Then, a Voronoi diagram was generated for each set of calibration corresponding to each DOI layer (see Figure P3.3 (c)) and Voronoi factors [P3.21] were determined for each layer generating three LUTs: $\{LUT_{X,Y,E}^{DOI1}$, $LUT_{X,Y,E}^{DOI2}$, $LUT_{X,Y,E}^{DOI3}\}$, by using the natural neighbor interpolation (see the block named Tube Calibration in Figure P4.4 (a)). Regarding the calibration of the z coordinate, the E/I$_{max}$ distributions for each calibration position (including the events of the three DOI layers) were fitted using an empirical equation as shown in [P3.25]. The fitting pro- vides the limits of the histogram, namely, a and b that are used to calibrate the DOI values into millimeters. In this case, only one LUT was generated: $\{LUT_Z^{AllDOI}\}$.

The second step of the calibration procedure, named Data Correction, consists of correcting each event $(x_iy_iz_iE_i)_{Estimated}$ to obtain $(x_iy_iz_iE_i)_{Corrected}$ by using the generated LUTs. For the *z* coordinates the $\{LUT_Z^{DOI}\}$ was directly applied. For the *x* and *y* coordinates and energy, two different methods have been studied:

i) Discrete method (*DM*). Voronoi factors for each $\{LUT_{X,Y,E}^{DOIn}\}$, n=1,2,3, were considered.

ii) Interpolation method (*IM*). Each $\{LUT_{X,Y,E}^{DOIn}\}$, n=1,2,3, was distance-based weighted using the Voronoi factors corresponding to the two nearest LUTs (see Figure P3.4(a)). Both linear and quadratic interpolations were tested without observing significant differences and therefore, for simplicity, only results using the linear case are shown in this work.

Notice that, after calibration, the corrected 3-D impact coordinates are in metric units while the energy is in keV. In order to avoid including Compton scattered event, a Gaussian fit to the energy spectrum was determined and only those events that are within the standard deviation from the computed photopeak mean were considered for image reconstruction.

The continuous DOI information was included to also correct the parallax error. As shown in the Data Projection process in Figure P3., the intersection of the line that connects two points $(x_iy_iz_i)_{Corrected}$ with the cylindrical inner face of the tube was calculated resulting in the true coordinates $(x_iy_iz_i)_{Projected}$.

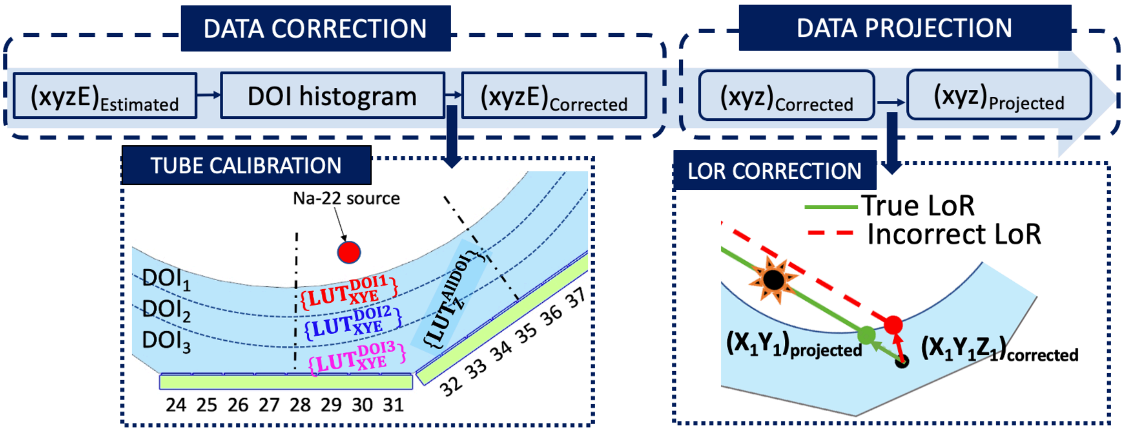

Figure P3.4. Block diagram of the data processing. Left, calibration procedure or both the 3D coordinates and energy. Right, correction of the parallax error.

D. Image Reconstruction

The data were discretized in virtual crystals pixels of 0.75 and 1 mm in transaxial and axial directions, respectively, and the image reconstruction was performed using the ray-tracing Joseph projector [P3.27]. In particular, List-Mode ordered subsets expectation maximization (OSEM) reconstruction was applied with an isotropic voxel size of $0.5 \times 0.5 \times 0.5$ mm^3. Different combinations of iterations and subsets were tested, namely: 5, 3, 2, and 1 iterations, and 30, 20, 10, and 1 subsets. A Gaussian smoothing of 1.2-mm FWHM was also applied to the data, except for the spatial resolution analysis.

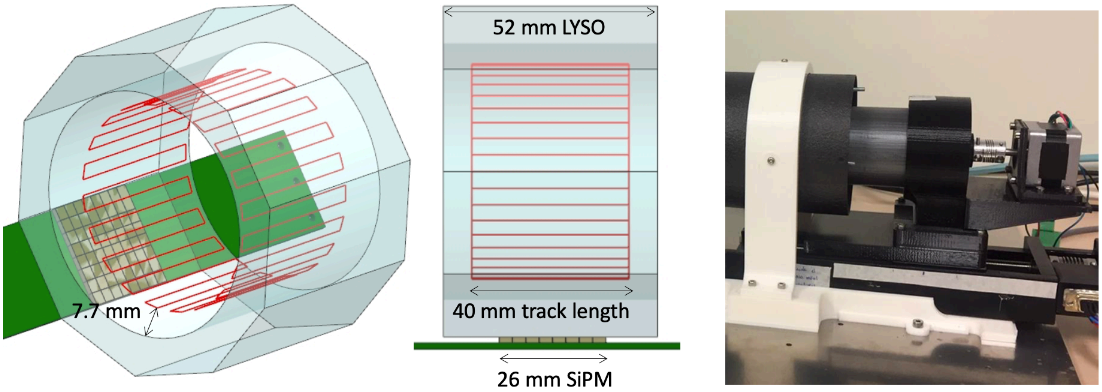

(a)

(b)

Figure P3.5. (a) Sketch of the photosensors, LYSO tube and movement of the ^{22}Na source (red line) during the normalization data acquisition. Note that the rotated angle of the acquisition is less than the one represented on the sketch; and (b) Photograph of the normalization acquisition setup.

E. Normalization

Normalization data were collected by placing the 0.25 mm ^{22}Na source at 7.7 mm from the inner face of the tube and axially displacing it 40 mm. Note that at the end of the dis- placement a rotation of 1.8° was included (see Figure P3.5 (a)). The sensitivity sinogram was computed comparing the measured data to the analytic projections of a cylinder shell of uniform activity, and later back-projected along all LORs. The calculated sensitivity image was used during the reconstruction process. For estimation of the tracer activity 3 iterations and 20 subsets were applied for reconstruction.

F. Detector performance

To study the detector performance, all the 200 measured calibration sources were analyzed. However, we are only reporting the evaluation of selected sources placed at the center of the *y*-axis and at five different positions across the *x*-axis of the detector since this data set represents the behavior of the full system due to the cylindrical symmetry of the design. In particular, we are showing the results obtained for the source positions 18 to 22 (both included), which are placed at the center of the facets named as M4 and M5, respectively, source number 20 was placed exactly between those facet centers (at the facet joint) and source positions 19 and 21 were at 6.5 mm from the facet center (see Figure P3.3 (a)).

Energy spectra were obtained for each one of these positions and for each one of the DOI layer. The photopeak position and energy resolution were also evaluated for each source. The latter was estimated as the ratio of the FWHM of the distribution to the photopeak position. This evaluation was performed both before and after applying the calibration described in the previous section.

E/I_{max} distributions were obtained for each one of these source positions and fitted using the empirical equation shown in [P3.25]. The sigma parameter of the fitting is a good estimator of the DOI resolution when the scintillation entrance faces are painted black since the LD is preserved. Note however, that providing an accurate estimation of DOI resolution requires lateral incident experiments, which is highly challenging with the current geometry.

G. System Performance and Image Quality

Regarding system spatial resolution, measurements of the 0.25-mm diameter ^{22}Na point source were acquired at various radial and axial positions. The emission data were normalized, arc-corrected, and grouped in the axial direction with a span of 5 in order to reduce the noise, and finally, were organized in sinograms with radial, angular, and axial sampling of 0.375 mm, 1.385°, and 0.5 mm, respectively. The spatial resolutions were then obtained as the mean resolutions computed along radial and axial profiles in each measured sinogram projection angle in the direct plane in which the point source was positioned. The reported resolutions ignore the positron range of the source and assume the system resolution and point-source width added in quadrature.

Experimental data for the sensitivity estimation was acquired by moving the ^{22}Na source (1 mm in diameter) across the system *y*-axis in steps of 2 mm. Data was analyzed by applying a 30% and a 50% energy window at the photopeak. A measurement of the background activity was also obtained. Regarding count rate capabilities, data was acquired placing a cylinder of high-density polyethylene with dimensions of 25 mm in diameter and 70-mm length, at the center of the FOV (cFOV). The phantom has a drilled hole of 3.2 mm at a radial offset of 10 mm and was filled with 330 µCi of ^{18}F. Data was acquired for 10 s every 30 min for a total time of 12 h. Acquired data was processed following the small animal

NEMA NU 4 standard procedure [P3.28]. The true coincidence rate was estimated as the area within the peak, and the random and scattered events were estimated using the background of the distribution. The system noise equivalent count rate (NECR) was studied as a function of the source activity. The reconstructed IQ was first evaluated acquiring data from an 11×11 ^{22}Na array source. Experimental data was recon- structed using iterations and subsets sequences of 4/10, 2/5, and 1/1. DOI information and normalization corrections were also included during the reconstruction process. Four different cases of calculating the photon impact were analyzed.

1) Standard COG algorithm and standard calibration process without splitting the calibration data in three DOI layers.
2) RTP algorithm (power = 2) and standard calibration process, without splitting the calibration data in three DOI layers.
3) RTP algorithm and DOI-dependent calibration process using the DM (RTP algorithm+DM).
4) RTP algorithm and DOI-dependent calibration process using the IM (RTP algorithm+IM).

The IQ was evaluated as the Gaussian FWHM, by analyzing the sources profiles of the transaxial view of the reconstructed image of the sources array. Moreover, the image deformation closer to the edges of the FOV was qualitatively evaluated for each case.

In a further step, the IQ was also evaluated using the Micro-PET IQ phantom proposed in the NEMA NU 4 standard [P3.28]. The IQ phantom is a 50-mm long and 30-mm diameter PMMA cylinder. The first half of the cylinder offers a large cavity of 30 mm in diameter fillable with an ^{18}F (uniformity region) that comprises of two smaller 15-mm long cavities separated from that volume to be filled with water and air (cold regions). The second half of the phantom contains five smaller rods of 1, 2, 3, 4, and 5 mm in diameter, radially aligned around the phantom length axis, thus providing an interconnection to the first half-cylinder filled with an isotope. The IQ phantom was filled with a total activity of 82 µCi of ^{18}F and acquired for a total time of 30 min. The data were calibrated using the RTP algorithm + IM and reconstructed using iterations and subsets sequences of 5/3, 2/10, and 2/1 and including normalization correction. We have calculated relative recovery coefficients (RRCs) as follows:

$$RRC = \frac{Mean\ Hot\ Spot\ VOI}{Mean\ Background\ VOI} \quad (1)$$

where VOI stands for volume of interest. For the hot spots, five cylindrical VOIs with diameters equal to the physical diameter of the phantom rods and 10-mm height, were drawn centered at each rod. For the background measurement, a cylindrical VOI with 25 mm in diameter and 5-mm height was drawn in the center volume of the uniform region of the IQ phantom.

H. Simulations

In order to support the experimental results regarding energy performance and sensitivity, simulations of this edge-less design were carried out using Gate v7.2 platform [P3.29]. A parallelizable detector dead time of 1 µs [P3.30] was used and the simulations include both nuclear and optical events. An energy resolution of 25% was implemented, allowing coincidences of a detector with its five opposites modules. All the LYSO scintillation process characteristics, as the Light Yield and the scintillation spectrum, were included in the simulation, as well as the PDE of the SiPM. The 95% of the scintillation light that reach to the LYSO tube surface was absorbed, being the rest randomly scattered.

Specifically, a study of the energy resolution was performed using the simulations to better understand the impact on light collection due to the reflection at the facet joints. Moreover, the sensitivity results were also simulated considering an energy window of 30% or 50%.

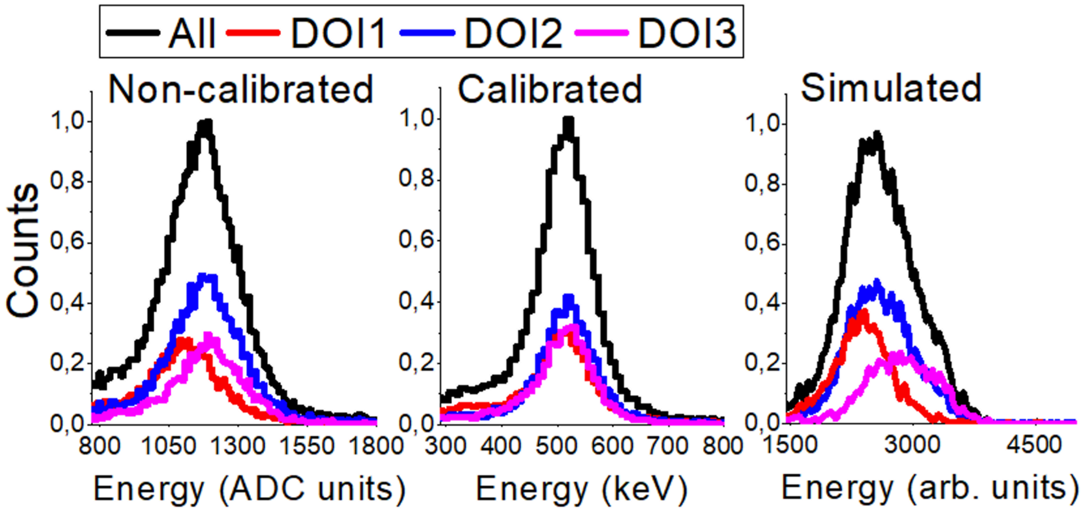

(a) (b) (c)

Figure P3.6. Energy spectra as a function of DOI position for source position number 20 for (a) non-calibrated data, (b) calibrated data, and (c) simulated data.

3. Results

A. Detector performance

Figure P3.6 shows the energy spectra before calibration (a), after calibration using the RTP + IM method (b), and simulated (c); for source position number 20, for the three DOI layers. A DOI dependency of the photopeak energy position is observed for the measured data of source number 20; corroborated by simulated data. After detector calibration, the photopeak value is precisely positioned at 511 keV.

Figure P3.7(a) and (b) show the noncalibrated and calibrated photopeak position value and the energy resolution as a function of the DOI layer for sources 18 to 22. The black dashed line represents the same calculations, but without the DOI layer selection. Figure P3.7(c) shows the estimated energy resolution after calibration of the experimental data as a function of the axial position. The average energy resolution was 23.4 ± 1.8%, with best values of 21.0 ± 1.3% at the axial center, worsening to about 25.0±2.1% at the edges, most likely due to scintillation light losses.

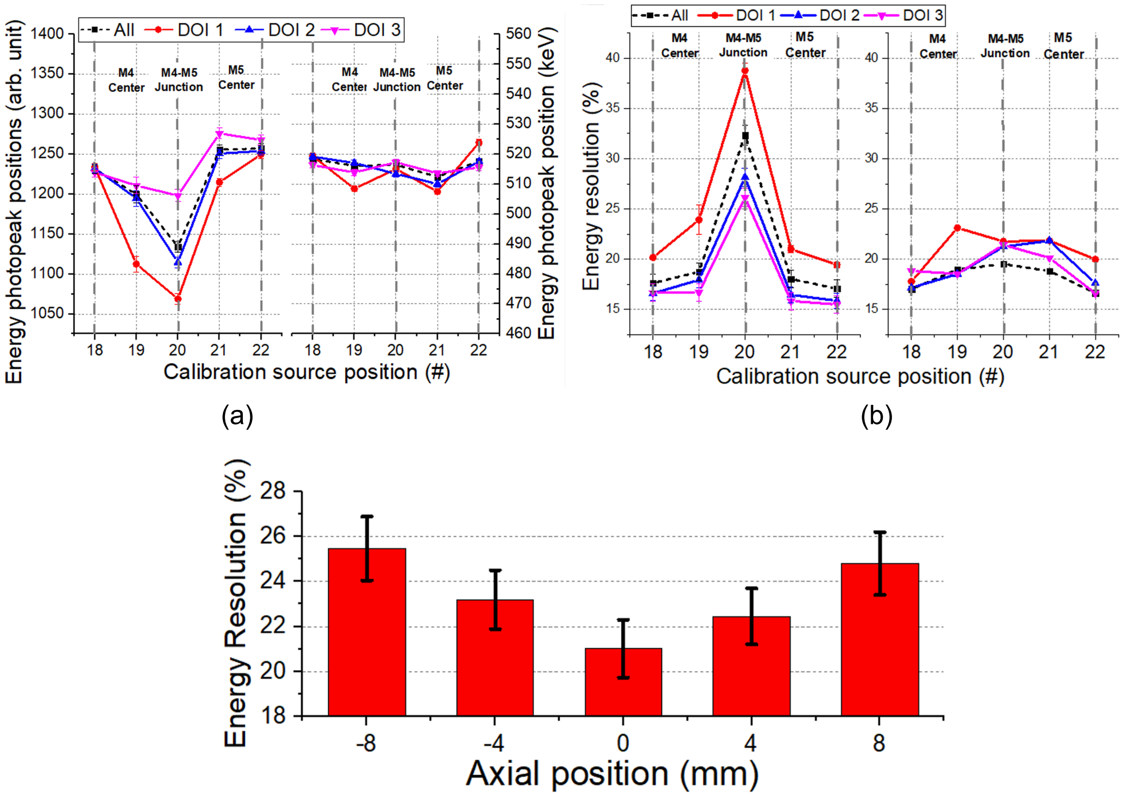

(a)

(b)

(c)

Figure P3.7. (a) Energy photopeak position as a function of the DOI for the non-calibrated (left) and calibrated (right) data, (b) energy resolution for the non-calibrated (left) and calibrated (right) data as a function of the DOI, and (c) overall energy resolution for source position 18 to 22.

The estimated DOI resolution values after calibration for position numbers 18 to 22 are depicted in Figure P3.8. On average, the estimated DOI resolution of the system is 1.8 ± 0.8 mm FWHM.

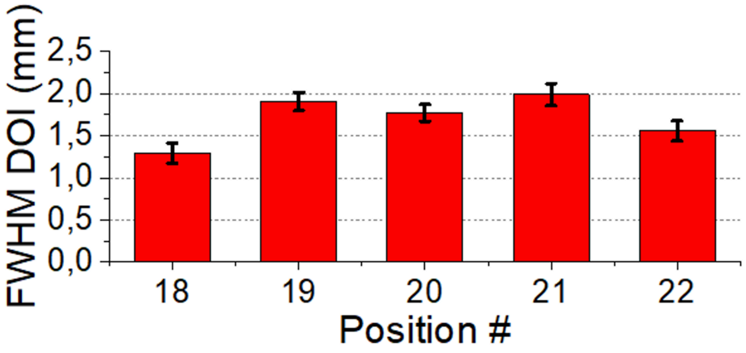

Figure P3.8. Estimated DOI resolution for source position 18 to 22.

B. System Performance and Image Quality

The acquired data with the 0.25-mm diameter ^{22}Na source was processed using the RTP+IM positioning method. Figure P3.9 (a) depicts the sinogram of the ^{22}Na source centered at the expected sinogram data bin and computed as the projection of the point-source reconstruction center. Deformations and defragmentation in the radial and axial plots are most likely due to residual calibration issues.

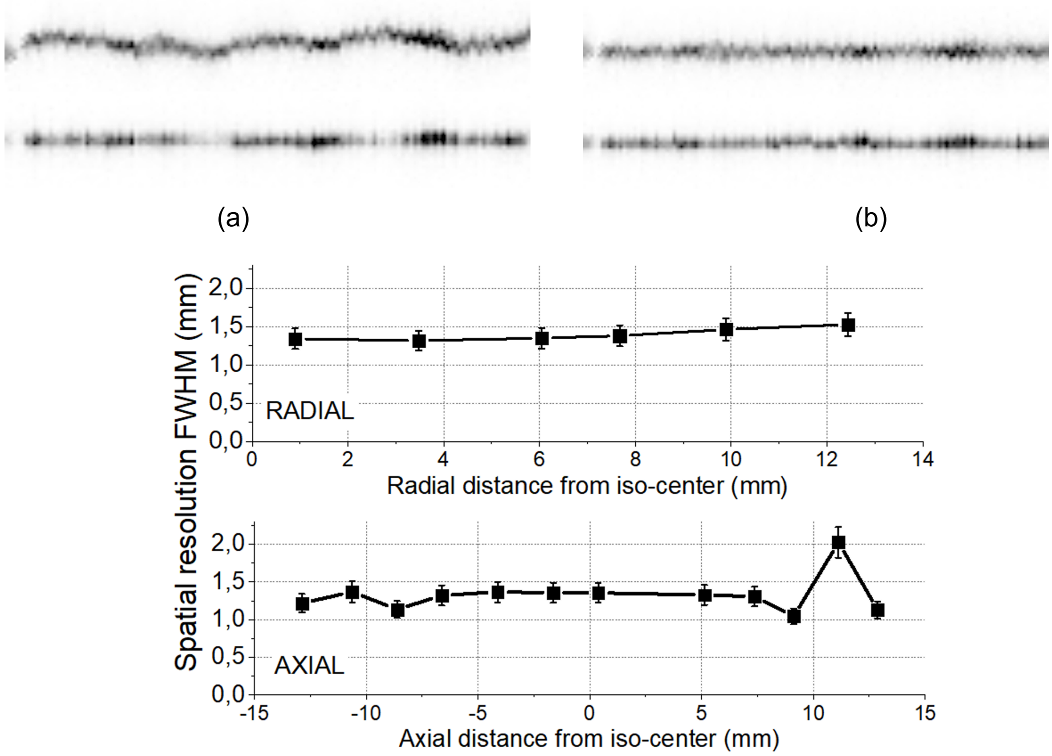

(a) (b)

(c)

Figure P3.9. (a) Radial (top) and axial (bottom) sinogram views of the ^{22}Na point-source (0.25 mm in diameter) measurements centered at the expected data-bin, and (b) after correction by centering each view at the maximum emission count. (c) Mean radial (top) and axial (bottom) spatial resolutions values computed over all projection angles for each ^{22}Na point-source positioning, these values are determined from sinogram profiles and not reconstructed images.

Figure P3.9 (b) depicts, the same sinogram after centering the measurements at the data bin with the most counts in each projection angle. Figure P3.9 (c) shows the spatial resolutions obtained at varying radial and axial positions, respectively, using the sinogram profiles and not reconstructed images. Notice that the system is intended to be used as a PET insert, so by including the RF coil, the useful diameter is reduced to 30 mm. Regarding the radial component, a degradation of just 10% is observed at the useful FOV edge, when compared to the cFOV. For the axial component, an outlier data point is found at 11.5 mm radial distance, probably due to some small crystal damage or bad painting in this region. Mean values of 1.4 ± 0.2 mm and 1.3 ± 0.4 mm FWHM in the radial and axial dimensions were obtained, respectively.

Figure P3.10 (a) depicts the calculated sensitivity for 30% (black symbols) and 50% (red symbols) energy windows. Both simulated (open symbols) and experimental results (full symbols) are shown. An experimental sensitivity of 3.8% was estimated at the system center for the 50% energy window, whereas the simulation predicted about 5.4%. Figure P3.10 (b) shows the experimental results for the total counts, random plus scatter, trues, and NECR values as a function of the source activity. The curves follow the typical behavior of linearity at lower activities. The NECR peak was reached at 40.6 kcps for an activity of 270 µCi.

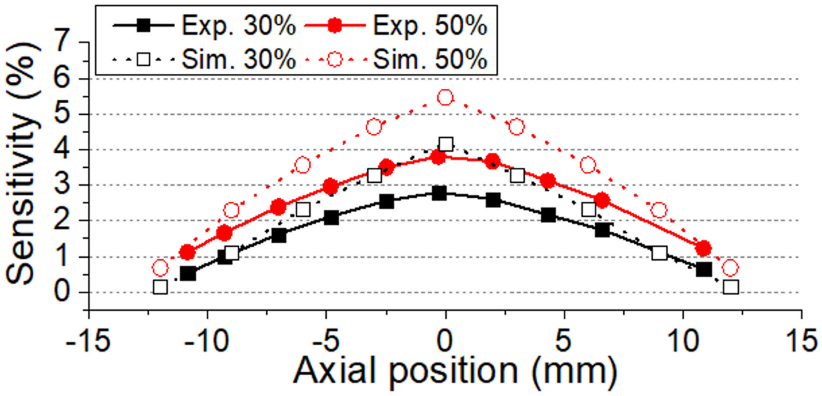

(a)

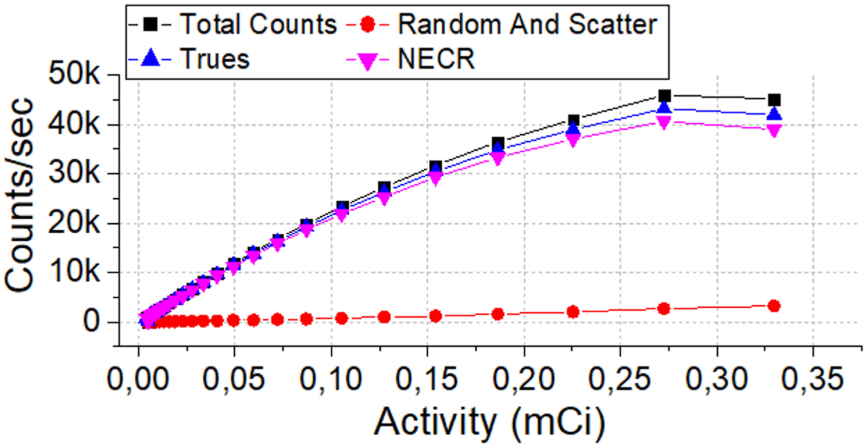

(b)

Figure P3.10. (a) Experimental and simulated system sensitivity for the energy window of 30% and 50%, and (b) count rate measurements.

Concerning the evaluation of the four impact determination methods and calibration processes, Figure P3.11 (a) shows the transaxial views of the reconstructed array of sources. The red circle indicates the area/volume covered during the normalization process (44.6 mm in diameter). Figure P3.11 (b) plots the projection of one row of sources for all cases. Average FWHM spatial resolution values of the sources of 2.11±0.54, 1.23±0.51, 1.06±0.15, and 0.97±0.12 mm were obtained for the COG, RTP, RTP+DM, and RTP+IM, respectively.

Moreover, we have calculated the peak to valley ratio of all source profiles and mean values of 0.07±0.02, 0.22±0.12, 0.20±0.06, and 0.21±0.06 were reported for the COG, RTP, RTP+DM, and RTP+IM cases, respectively.

The IQ was studied using the NEMA IQ phantom. Figure P3.12 (a) shows a photograph of the phantom inserted in the PET system with the reconstructed image. The acquired data was calibrated using the RTP + IM case and reconstructed (normalization corrected) with a sequence of iterations/subsets of 5/3, 2/10, and 2/1. Notice that no scatter, random, or attenuation corrections were applied to this data. The profiles of the 1 and 3 mm rods are also shown. Figure P3. 12(b) shows the measured RRC values as a function of the diameter rod.

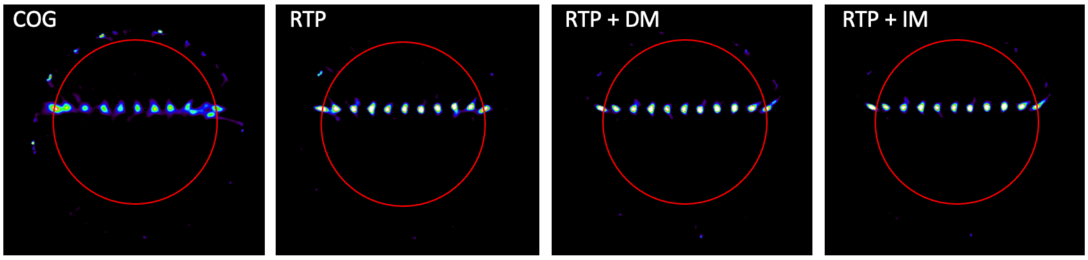

(a)

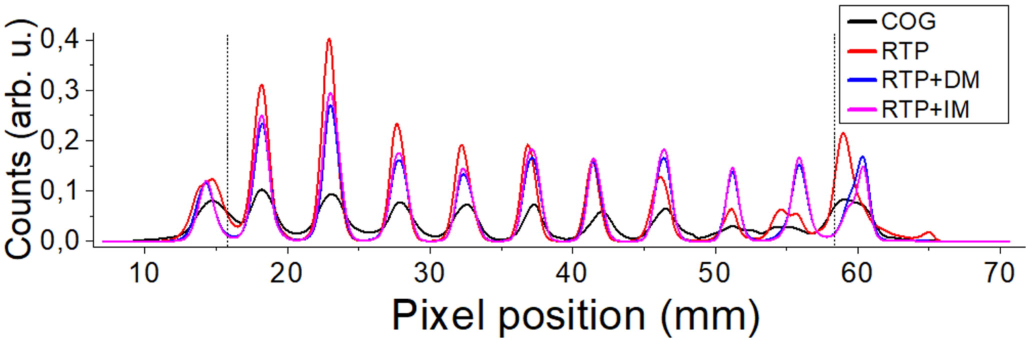

(b)

Figure P3.11. Analysis of the reconstructed array (a) from left to right: COG, RTP, RTP+DM, and RTP+IM, respectively. The red circle shows the limit of the calibration normalization, and (b) projections of the central row of the coronal view of sources for all cases.

4. Discussion

The present work describes and validates a small-animal PET design based on a novel edge-less (single monolithic) LYSO:Ce scintillator with a high potential for MRI compatibility. The aim of this design is twofold: first, to enhance state-of-the-art PET system sensitivity by avoiding the typical modular structure with axially and transaxially gaps; and second, enhance spatial resolution by exploiting monolithic-based detectors ability to provide accurate 3-D photon impact positioning while mitigating the drop-off in PET performance by suppressing the edges in the transaxial plane.

Our prototype is based on a single LYSO:Ce annular scintillator with an axial length of 52 mm and an outer face that has been cut generating ten flat faces of 26×52 mm^2 each. Having flat outer faces simplified photosensor coupling, thus overcoming complex PCB implementations. An outer annular surface has the challenge of coupling the photosensor in the circular surface unless using the endcaps for data reading [P3.17]; but this comes at the cost of missing DOI information. The main challenges associated to the faceted design are the large number of internal light reflections at the joints between facets which increase the DOI dependency of the data and the nonuniform thickness of the scintillator (thicker at the joints). To mitigate these drawbacks, we have implemented a highly accurate position and energy calibration process as a function of the DOI impact information (three layers of 3 mm thick each in our case, see Figs. P3.3 and P3.6). Note that more DOI layers are not required due to the DOI resolution of the system which was estimated to be 1.8±0.8 mm FWHM. Moreover, to reduce the number of light reflections in the annulus walls, especially at the junction between facets, both the inner face and endcaps of the annulus were polished and painted black. Based on our previous experience, the use of absorbent black paint, despite preserving the LD profiles and thus improving DOI resolution, improves the determination accuracy of the impact photon position, but reduces the energy performance.

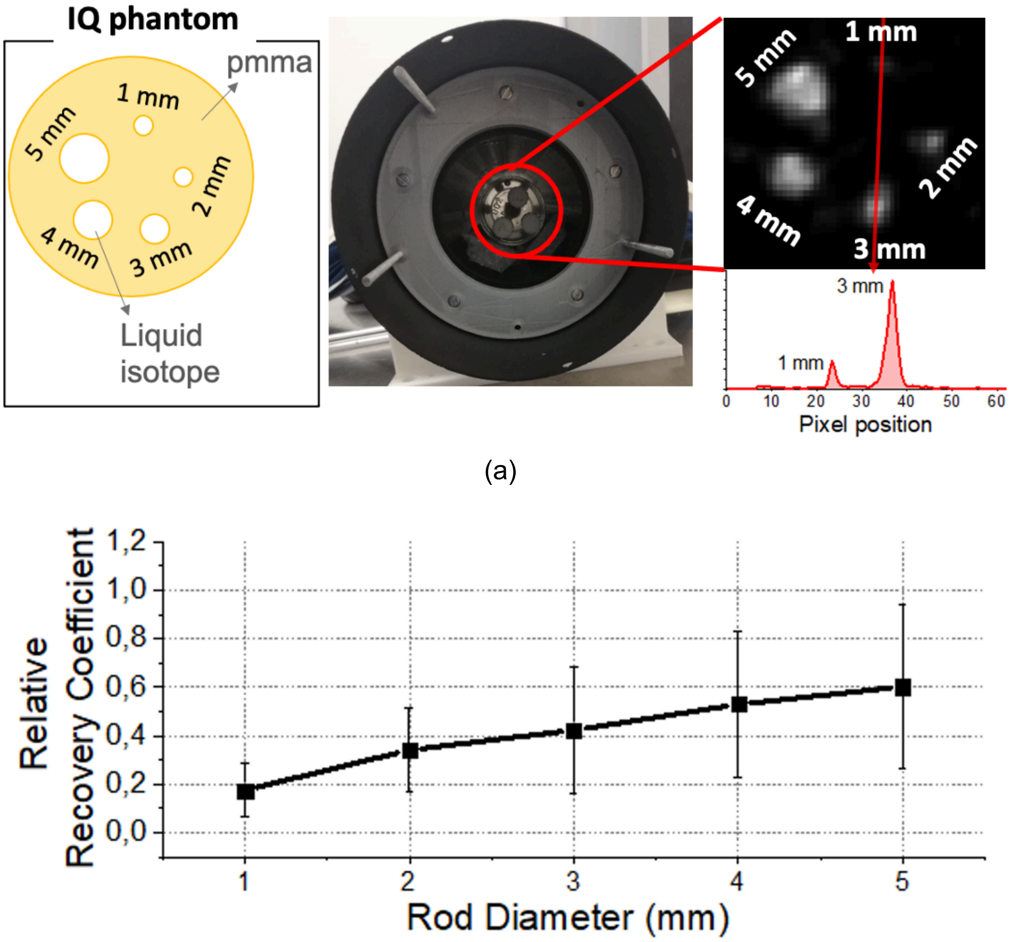

(a)

(b)

Figure P3.12. (a) Photograph of the system including the IQ phantom and reconstructed image of the rods showing the profiles across the 1 and 3 mm rods, and (b) measured relative recovery coefficient values.

If using reflective treatments, instead of black paint, the amount of light reaching the photosensor will increase, therefore enhancing the energy and timing performance. To explore this, we are currently investigating the use of retroreflector materials to enhance the light collection at the photosensor while preserving the LD (required by our methodology to estimate the DOI) and, also, the use of using white reflective paints combined with neural network algorithms for 3-D event positioning. This scintillator surface treatment decision for this first prototype was a compromise between impact detectability and the use of analytical methods for impact position determination.

Regarding evaluation at the detector level, we observed a strong dependency of the impact position accuracy and energy resolution as a function of the DOI. For the x and y photon impact positioning, we analyzed both the use of standard COG and RTP methods, concluding that the use of the RTP algorithm is key to providing accurate positioning. Small differences between the *x* and *y* calibration as a function of the DOI for the DM and IM methods were observed. The photopeak position and energy resolution dependency with the photon DOI is shown in Figs. P3.7 and P3.8. Impacts closer to the entrance face of the scintillator (DOI1) present lower gain impacting on the energy resolution. Identical behavior was observed for all the calibration sources at a given axial position. The photopeak position and DOI histograms exhibit also a dependency on the source position location along the *x*-axis with a worse characterization at the joints. To achieve highly accurate reconstructed images, the *x* and *y* photon impact positions and energy were calibrated using the DOI-dependent calibration methodology (see Figure P3. 4(a)), and then the LORs were also corrected using the continuous DOI information (see Figure P3.4(b)). Figs. P3.7 and P3.8 demonstrate the improvement of the calibration methodology (RTP+IM, including the DOI-dependent calibration process), which results on an average energy resolution of 23.4±1.8% for the entire annulus and a DOI resolution of 1.8±0.8 mm FWHM.

As shown in Figure P3.9 (c), average spatial resolution values of 1.4±0.2 mm FWHM and 1.3±0.4 mm FWHM were achieved for the radial and axial dimensions using the ^{22}Na source, respectively. Even with the small dimensions of the scintillation tube and relatively wide FOV, there is still a high homogeneity of the spatial resolution across the whole FOV. However, the facets on the external face of the tube cause some light losses due to internal reflections, degrading the spatial resolution of the system.

The study of the system sensitivity shows a mismatch between the simulation and experimental data (see Figure P3.10 (a)). We hypothesize that these discrepancies might arise from some data transfer capability differences between the experimental and simulated system. Using acquired data, the system exhibited a sensitivity of 3.8% at the system center for a 50% energy window. As shown in Figure P3.10 (b), the NECR curve follows the expected behavior as a function of measured activity, being linear at lower activities. The NECR peak was reached at 40.6 kcps for an activity 270 µCi, which is acceptable for a small animal PET imaging.

The IQ was also evaluated. Figure P3.11 shows the reconstructed image of the array of multiple ^{22}Na sources by applying the four different event positioning and calibration combinations. As described above, the calibration of *x* and *y* coordinates as a function of its DOI played an important role for the IQ assessment. Artifacts observed at the limits of the FOV for the COG method were totally removed using the RTP+IM method. Moreover, the best average spatial resolution value, for one row of sources, was obtained for the RTP+IM case (0.97±0.12 mm FWHM). Regarding the peak-to-valley parameter, the best overall combination (higher peak-to-valley value but a small standard deviation) was also obtained for the RTP+IM case. Additionally, the NEMA IQ phantom was calibrated with the RTP+IM method and reconstructed. Some artifacts can be observed due to the loss of light produced by the faceted exit faces. As shown in Figure P3.12 (b), the measured RRC values follow the expected behavior, but were a little lower than expected because attenuation correction was not applied. Table P3.1 summarizes the most relevant performance parameters of the state-of-the-art small animal inserts. As can be seen the performance reported with our edge-less design is comparable [P3.33].

One of the limitations of the edge-less concept is the scintillator crystal growth process that constrains the maximum size of the piece. Lutetium-based scintillator ingots have approximated maximum dimensions of ~90-mm diameter and ~150-mm height. For the maximum possible outer diameter of 90 mm, the inner diameter of the scintillation piece may be in the range of ~60–70 mm, to ensure a thickness of at least 10 mm. These dimensions are well suited only for mice and other small rodents, thus confining the design to the small animal research field. It may be possible to increase the size of the scanner without having gaps and thus expand this technology to human-size scanners for the clinic, by optically gluing multiple scintillation sections using matching high refractive index materials. Feasibility for this has been shown by simulations [P3.31], [P3.32].

Finally, although not shown in this work, we are confident about the high potential MR compatibility of this prototype, since it uses design principles applied in prior prototypes already working immersed in high magnetic fields [P3.19], [P3.23].

System	Modality	Detector	S. Res (mm)	DOI	FOV Trans/Axial
NuPET (Cubresa)	Insert	1.2×1.2×4 top ×6 bottom LYSO	0.9-1.3	yes	59/67
HALO 3.0 (Inviscan)	PET/MRI Insert	1.5×1.5×6 LYSO	1.1	no	75/80
PET insert (MR solutions)	Insert	1.4×1.4×4 top ×6 (bottom) LYSO	0.8	yes	45-60/150
NanoScan (Mediso)	PET/MRI	1.12×1.12×13 LYSO	1.5	no	45.94 -120/94
SimPET (Scintica)	Insert	1.2×1.2×10 LYSO	0.8	no	65/55
MRI/PET (SynchroPET)	Insert	2.3×2.3×8 LYSO	1.8	no	44.85/25,26
Albira Si (Bruker)	Insert	50×50×10 LYSO monolithic	0.7-1.0	yes	80-46/148
Edge-less	Insert	LYSO monolithic tube	1.4	yes	30/26

Table P3.1. State-of-the-art commercial small animal PET systems.

5. Conclusions

The present manuscript validates and characterizes a novel edge-less small-animal PET insert design based on an LYSO:Ce annular scintillator.

A method for coincident event identification in the scintillation tube based on the LD profiles is provided including a modified version of the conventional calibration method based on Voronoi diagrams, which already demonstrated to correct for typical edge effects [P3.21]. The methodology introduces a calibration procedure, that is, DOI-dependent, allowing to mitigate the DOI-dependency of the *x*- and *y*-axis, as well as the energy photopeak gain, thus demonstrating the advantage of performing DOI-dependent position and energy calibrations. The proposed edge-less PET prototype behaves as expected, minimizing event positioning challenges. Reported results at detector and system-level demonstrate the feasibility of using an edge-less PET scanner.

For the next design, we planned to enhance the system performance using a completely cylindrical geometry and a novel implementation of the photosensors around the external cylindrical face using flexible PCBs. The NU-4 procedures will be applied for its characterization.

We are optimistic this edge-less design may open a new era of high sensitivity and high-performance PET scanners.

References

[P3.1] C. Kuntner and D. Stout, “Quantitative preclinical PET imaging: Opportunities and challenges,” *Front. Med.*, vol. 2, no. 1, p. 12, 2014.

[P3.2] M. S. Judenhofer and S. R. Cherry, “Applications for preclinical PET/MRI,” *Seminar Nucl. Med.*, vol. 43, no. 1, pp. 19–29, 2013.

[P3.3] N. Seshadri, L. I. Sonoda, A. M. Lever, and K. Balan, “Superiority of 18F-FDG PET compared to 111In-labelled leucocyte scintigraphy in the evaluation of fever of unknown origin,” *J. Infect.*, vol. 65, no. 1, pp. 71–79, 2012.

[P3.4] S. España, R. Marcinkowski, V. Keereman, S. Vandenberghe, and R. Van Holen, “DigiPET: Sub- millimeter spatial resolution small-animal PET imaging using thin monolithic scintillators,” *Phys. Med. Biol.*, vol. 59, no. 13, p. 3405, 2014.

[P3.5] Y. Yang *et al.*, “A prototype high-resolution small-animal PET scan- ner dedicated to mouse brain imaging,” *J. Nucl. Med.*, vol. 57, no. 7, pp. 1130–1135, 2016.

[P3.6] S. Yamamoto *et al.*, “Development of an ultrahigh resolution SiPM based PET system for small animals,” *Phys. Med. Biol.*, vol. 58, no. 21, pp. 7875–7888, 2013.

[P3.7] F. Godinez, K. Gong, J. Zhou, M. S. Judenhofer, A. J. Chaudhari, and R. D. Badawi “Development of an ultra high resolution PET scanner for imaging rodent paws: PawPET,” *IEEE Trans. Radiat. Plasma Med. Sci.*, vol. 2, no. 1, pp. 7–16, Jan. 2018.

[P3.8] A. J. Gonzalez *et al.*, “Feasibility study of a small animal PET Insert based on a single LYSO monolithic tube,” *Front. Med.*, vol. 5, p. 328, Nov. 2018.

[P3.9] A. Gonzalez-Montoro *et al.*, “Evolution of PET detectors and event positioning algorithms using monolithic scintillation crystals,” *IEEE Trans. Radiat. Plasma Med. Sci.*, vol. 5, no. 3, pp. 282–305, May 2021.

[P3.10] S. S. Berr, S. Majewski, A. J. Gonzalez, M. B. Williams, A. Gonzalez-Montoro, and R. A. Martí, “Novel PET scanner based on an edgeless, continuous scintillator tube (ScintoTube^{TM})," presented at the World Molecular Imag. Congr. (WMIC), Philadelphia, PA, USA, Sep. 2017.

[P3.11] S. Xie *et al.*, "LOR-PET: A novel PET camera constructed with a monolithic scintillator ring," in *Proc. IEEE NSS-MIC Conf.*, Atlanta, GA, USA, 2017, pp. 1–3.

[P3.12] A. V. Stolin, P. F. Martone, G. Jaliparthi, and R. R. Raylman, "Preclinical positron emission tomography scanner based on a monolithic annulus of scintillator: Initial design study," *J. Med. Imag.*, vol. 4, no. 1, 2017, Art. no. 011007.

[P3.13] S. Genna and A. P. Smith, "The development of APSECT, an annular single crystal brain camera for high efficiency SPECT," *IEEE Trans. Nucl. Sci.*, vol. 35, no. 1, pp. 654–658, Feb. 1988.

[P3.14] A. L. Goertzen, D. W. Jones, J. Seidel, K. Li, and M. V. Green, "First results from the high-resolution mouse SPECT annular scintillation camera," *IEEE Trans. Med. Imag.*, vol. 24, no. 7, pp. 863–867, Jul. 2005.

[P3.15] R. Freifelder, J. S. Karp, M. Geagan, and G. Muehllehner, "Design and performance of the HEAD PENN-PET scanner," *IEEE Trans Nucl. Sci.*, vol. 41, no. 4, pp. 1436–1440, Aug. 1994.

[P3.16] K. J. Wilson, R. Alabd, M. Abolhasan, D. R. Franklin, and M. Safavi-Naeini, "Localisation of the lines of response in a continuous cylindrical shell PET scanner," in *Proc. Annu. Int. Conf. IEEE Eng. Med. Biol. Soc.*, 2019, pp. 4844–4850.

[P3.17] J. Xu *et al.*, "A preclinical PET detector constructed with a monolithic scintillator ring," *Phys. Med. Biol.*, vol. 64, no. 15, 2019, Art. no. 155009.

[P3.18] W. Gsell *et al.*, "Characterization of a preclinical PET insert in a 7 Tesla MRI scanner: Beyond NEMA testing," *Phys. Med. Biol.*, vol. 65, no. 24, 2020, Art. no. 245016.

[P3.19] A. J. Gonzalez *et al.*, "Initial results on the MINDView PET insert inside the 3T mMR," *IEEE Trans. Radiat. Plasma Med. Sci.*, vol. 3, no. 3, pp. 343–351, May 2019.

[P3.20] "Silicone Grease Datasheet," BC-630 Data Sheet, Saint-Gobain, Courbevoie, France, 2017. [Online]. Available: https://www.crystals.saint-gobain.com/sites/imdf.crystals.com/files/documents/bc-630.pdf

[P3.21] M. Freire, A. Gonzalez-Montoro, F. Sanchez, J. M. Benlloch, and A. J. Gonzalez, "Calibration of gamma ray impacts in monolithic-based detectors using voronoi diagrams," *IEEE Trans. Radiat. Plasma Med. Sci.*, vol. 4, no. 3, pp. 350–360, May 2020.

[P3.22] A. Gonzalez-Montoro, L. A. Pierce, W. C. J. Hunter, A. J. González, and R. S. Miyaoka, "Validation of photon collimation techniques for monolithic PET detector calibration," *IEEE Trans. Radiat. Plasma Med. Sci.*, early access, Dec. 9, 2020, doi: 10.1109/TRPMS.2020.3043397.

[P3.23] A. J. Gonzalez *et al.*, "Next Generation of the Albira Small Animal PET Based on high density SiPM arrays," *IEEE Nuclear Sci.Symp. Medical Imaging Conf.(NSS/MIC),* San Diego, CA, USA, 2015, doi: 10.1109/NSSMIC.2015.7582085.

[P3.24] R. Pani *et al.*, "Position algorithm for monolithic scintillation crystals based on charge projection readout," *J. Instrum.*, vol. 11, no. 1, 2016, Art. no. C01061.

[P3.25] A. Gonzalez-Montoro *et al.*, "Performance study of a large monolithic LYSO PET detector with accurate photon DOI using retroreflector layers," *IEEE Trans. Radiat. Plasma Med. Sci.*, vol. 1, no. 3, pp. 229–237, May 2017.

[P3.26] A. Gonzalez-Montoro *et al.*, "Detector block performance based on a monolithic LYSO crystal using a novel signal multiplexing method," *Nucl. Instrum. Methods Phys. Res.*, vol. 912, pp. 372–377, Dec. 2018.

[P3.27] P. M. Joseph, "An improved algorithm for reprojecting rays through pixel images," *IEEE Trans. Med. Imag.*, vol. 1, no. 3, pp. 192–196, Nov. 1982.

[P3.28] *Performance Measurements of Small Animal Positron Emission Tomographs*, NEMA Standard NU 4-2008, 2008.

[P3.29] *Gate V7.2 User Guide*. [Online]. Available: http://wiki.opengatecollaboration.org/index.php/Users_Guide_V7 (Accessed: 2016).

[P3.30] S. Jan *et al.*, "GATE: A simulation toolkit for PET and SPECT," *Phys. Med. Biol.*, vol. 49, no. 19, pp. 4543–4561, 2004.

[P3.31] R. Vinke and C. S. Levin, "A method to achieve spatial linearity and uniform resolution at the edges of monolithic scintillation crystal detector," *Phys. Med. Biol.*, vol. 59, no. 12, pp. 2975–2995, 2014.

[P3.32] M. Morrocchi *et al.*, "Evaluation of event position reconstruction in monolithic crystals that are optically coupled," *Phys. Med. Biol.*, vol 61, no. 23, pp. 8298–8320, 2016.

[P3.33] R. S. Miyaoka and A. L. Lehnert, "Small animal PET: A review of what we have done and where we are going," *Phys. Med. Biol.*, vol. 65, no. 24, 2020, Art. no. 24TR04.

9 Performance evaluation of side-by-side optically coupled monolithic LYSO crystals

Authors: Marta Freire, Sara Echegoyen, Andrea González-Montoro, Filomeno Sánchez and Antonio J. González.

Published: Medical Physics, 2022, Vol. 49, p. 5616-5226. Doi: https://doi.org/10.1002/mp.15792

Summary: The main goal of the *DeepBreast* project, a Spanish National grant led by i3m, is to boost the sensitivity and reduce edge effects in dedicated PET scanners following an edge-less approach (see Section 5.3). We proposed the construction of a system for breast imaging based on monolithic curved crystals glued together with a high refractive index adhesive and, implementing NN techniques for the 3D photon impact position estimation.

This article shows the experimental validation of the detectors by using two LYSO crystals of 33×25.4×10 mm^3 optically glued with Meltmount adhesive (refractive index, n=1.70), and coupled to a 12×12 SiPM array. For comparison, the same detector configuration has been tested for two additional coupling cases: optical grease (n = 1.46) in between crystals, and isolated crystals using black paint with an air gap at the interface.

A NN algorithm based on two MLPs has been implemented for the *x*- and *y*-impact position estimation. Moreover, the NN technique has been compared with

an analytical conventional method. Experimental data have been acquired for each detector configuration by moving a fan beam across the detector surface. The results suggest that optically coupling together scintillators with a high refractive index adhesive allows the transmission of the optical photon between adjacent crystals, thus reducing edge effects, especially when the NN technique is applied.

Due to such results, this approach has been used for designing the *DeepBreast* system. The system has been recently constructed and experimental data for the NN training have been already acquired.

Performance evaluation of side-by-side optically coupled monolithic LYSO crystals

Marta Freire, Sara Echegoyen, Andrea González-Montoro, Filomeno Sánchez, Antonio J. González

Abstract— *Background: Significant interest has been recently shown for using monolithic scintillation crystals in molecular imaging systems, such as positron emission tomography (PET) scanners. Monolithic-based PET scanners result in a lower cost and higher sensitivity, in contrast to systems based on the more conventional pixelated configuration. The monolithic design allows one to retrieve depth-of -interaction information of the impinging 511 keV photons without the need for additional hardware materials or complex positioning algorithms. However, the so-called edge-effect inherent to monolithic-based approaches worsens the detector performance toward the crystal borders due to the truncation of the light distribution, thus decreasing positioning accuracy.*

Purpose: The main goal of this work is to experimentally demonstrate the detector performance improvement when machine-learning artificial neural- network (NN) techniques are applied for positioning estimation in multiple monolithic scintillators optically coupled side-by-side.

Methods: In this work, we show the performance evaluation of two LYSO crystals of 33 × 25.4 × 10 mm^3 optically coupled by means of a high refractive index adhesive compound (Meltmount, refractive index $n = 1.70$). A 12 × 12 silicon photomultiplier array has been used as photosensor. For comparison, the same detector configuration was tested for two additional coupling cases: (1) optical grease ($n = 1.46$) in between crystals, and (2) isolated crystals using black paint with an air gap at the interface (named standard configuration). Regarding 2D photon positioning (XY plane), we have tested two different methods: (1) a machine-learning artificial NN algorithm and (2) a squared-charge (SC) centroid technique.

Results: At the interface region of the detector, the SC method achieved spatial resolutions of 1.7 ± 0.3, 2.4 ± 0.3, and 2.6 ± 0.4 mm full-width at half -maximum (FWHM) for the Meltmount, grease, and standard configurations, respectively. These values improve to 1.0 ± 0.2, 1.2 ± 0.2, and 1.2 ± 0.3 mm FWHM when the NN algorithm was employed. Regarding energy performance, resolutions of 18 ± 2%, 20 ± 2%, and 23 ± 3% were obtained at the interface region of the detector for Meltmount, grease, and standard configurations, respectively.

Conclusions: The results suggest that optically coupling together scintillators with a high refractive index adhesive, in combination with an NN algorithm, reduces edge-effects and makes it possible to build scanners with almost no gaps in between detectors.

Keywords— monolithic scintillator, neural network, optical coupling, PET, position estimation

1. Introduction

The two most prevalent geometry configurations of scintillation crystals used on conventional gamma-ray scanners are the pixelated and the monolithic [P4.1].

Pixelated crystal configurations are the most extended configuration in positron emission tomography (PET) scanners, since it allows for a relatively easy pixel identification. Nevertheless, monolithic scintillators offer lower cost, higher sensitivity, and provide intrinsic depth-of-interaction (DOI) information of the gamma-ray interaction within the scintillator, thus enabling the possibility to correct for parallax errors [P4.2]. Moreover, monolithic- based designs allow one to accurately characterize the scintillation light distributions (LDs) and, thus spatial resolutions of 1 mm have already been obtained [P4.3]. As a consequence of all these features, a significant interest has grown over the recent years for using gamma- ray scanners based on monolithic crystals for both academic and commercial purposes [P4.4]–[P4.11].

In both the pixelated and monolithic approaches, the gaps in between detectors decrease system sensitivity. Moreover, the performance of monolithic scintillators tends to be compromised toward the crystal edges (border effect) [P4.12] due to the strongest truncation of the LD in these areas. Therefore, data recorded at the edges have a poorer performance and are eventually discarded [P4.13]-[P4.15], thus, reducing the useful detector volume and consequently decreasing the system sensitivity.

Several methods have been developed to mitigate border effects, some of them are based on weighted centroid methods [P4.16] or squared-charge (SC) centroids [P4.17]. Recently, the development of multichannel photosensor-readout application-specific integrated circuits combined with silicon photomultipliers (SiPMs) enabled the possibility to build highly granular, scalable, and large arrays for position sensitive gamma-ray detectors [P4.18]–[P4.20]. These developments allowed for an exhaustive characterization of the 3D spatial detector response, paving the way for new positioning algorithms, such as maximum- likelihood (ML) methods [P4.21][P4.22], nonlinear data fit [P4.23], k-NN technique [P4.24][P4.25], Voronoi-based calibration methods [P4.26], and machine-learning artificial neural-network (NN) algorithms [P4.27]–[P4.29]. However, these new algorithms only partially alleviate edge-artifacts and, thus, these effects are still present [P4.30], particularly when using thick scintillators. The use of bigger monolithic crystals would be a good approach; however, this presents some limitations in crystal growth size and geometrical flexibility in ring construction. A proposed solution is to optically couple side-by-side monolithic crystals [P4.31][P4.32]. A previous simulation study demonstrated that using optical coupling compounds with refractive index approaching the refractive index of the scintillation crystal allows the scintillation light to spread through the crystal junctions almost preserving the shape of the LD and, therefore, reducing substantially edge-artifact [P4.31]. In addition to this, optically coupling monolithic crystals reduces the gaps in between detectors, thus increasing sensitivity; and overcomes the challenges in using large scintillator volumes. Other authors have experimentally evaluated the use of optical adhesive to couple LYSO monolithic blocks, and generated look up tables followed by a least-squares minimization and ML methods for event positioning [P4.32]. They have also concluded that the adoption of optically coupled monolithic crystals can be a useful and feasible method to improve the uniformity of performances in the whole sensitive area [P4.32].

In this work, we have experimentally evaluated, as a proof-of-concept, the performance of a detector based on a 12×12 SiPM array and two LYSO crystals of 33×25.4×10 mm^3 optically coupled by means of a high refractive index compound (refractive index n = 1.70). This configuration was compared to two additional coupling methods, namely: (1) optical grease (refractive index n = 1.46) between crystals and (2) isolated blocks using black paint and air interface. For XY event positioning, we have tested two different methods: (1) SC centroid technique, which is a modified Anger logic procedure that has demonstrated enhanced linearity and spatial resolution [P4.16], and (2) machine-learning artificial NN algorithm. The performance of the optically coupled system was evaluated in terms of spatial linearity and resolution (including DOI determination) as well as energy performance.

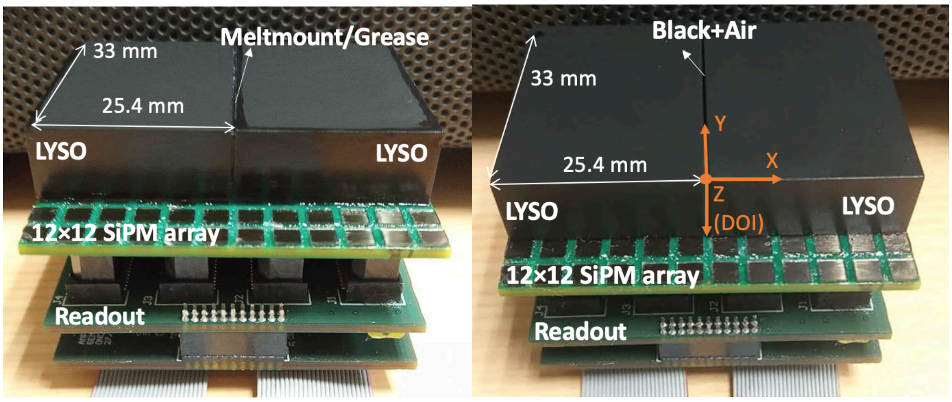

(a) (b)

Figure P4.1. Detector configurations used in this work. (a) Meltmount or grease configuration, where all lateral faces were black painted except the interface one that was used to coupled crystals. (b) Standard configuration, where all the lateral faces of the crystal were black painted.

2. Materials and methods

For the experimental setup, two $(LuY)_2SiO_5$ (LYSO) crystals of 33×25.4×10 mm^3 with refractive index of 1.81 from EPIC Crystals Co., Ltd, China, were used. All crystal faces were polished and black painted except one of 33×10 mm^2 that was rough. The two crystals were coupled along this face.

Three configurations were tested; in the first one, a high refractive index compound named “Cargille Meltmount” ($n_{Meltmount}$=1.70) was used [P4.35]. Meltmount is a thermal plastic material, thus its viscosity is inversely dependent on the temperature. Therefore, it was heated to 70°C on a hotplate to decrease its viscosity. The two sides of the crystals to be glued were also heated to avoid sudden temperature changes when applying the Meltmount compound. When the targeted temperature was reached, the Meltmount compound was spread in the side of one of the crystals using a spatula and was immediately attached to the side of the other crystal. Then, the coupled crystals cooled down to room temperature. For the second configuration, named optical grease, the crystals were coupled together using “SS-988 Non-Curing Optical Coupling Gel - V-788 Offset” (n_{grease} = 1.46) from Silicone Solutions [P4.33]. For the third configuration, named standard configuration, these side faces of the crystal were black painted and placed together letting an air gap between them. For all cases, the gap between the two faces was 0.5 mm (Figure P4.1). Table P4.1 summarizes the refractive index and optical properties of the different used compounds.

Material	Optical properties at the interface	Refrective index
LYSO	-	$n_{LYSO} = 1.81$
Black paint	Absorption	-
Grease	Partial transmission	$n_{grease} = 1.46$
Meltmount	Partial transmission	$n_{Meltmount}= 1.70$
Air	Partial transmission	$n_{air} = 1.00$

Table P4.1. Refractive index and optical properties of the materials used in this work.

In all cases, the exit face of the crystals was coupled by means of optical grease to a 12×12 SiPMs array (SensL, now OnSemi) with 3×3 mm^2 active area each and a pitch of 4.2 mm. Each SiPM array was directly connected to a readout circuit that provides output signals for each column (c_i) and row (r_i) of the photosensor array [P4.6] Notice that only the eight central rows were covered by scintillation crystals and, thus, only those were read out (Figure P4.1). These signals are digitized using custom analog-to-digital converter (ADC) boards (12-bit precision and 250 ns integration time) providing information for both *x* and *y* projections of the LD.

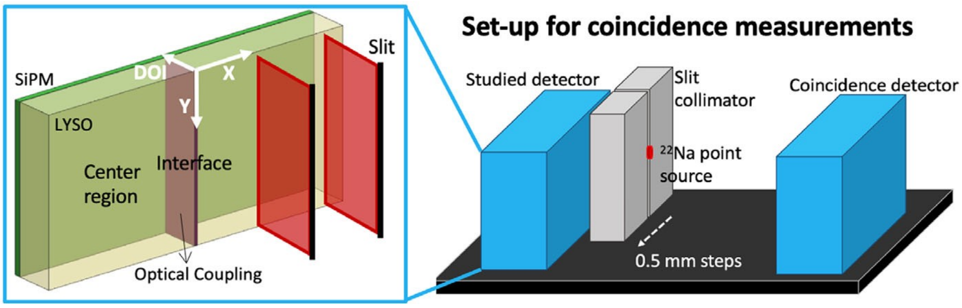

Figure P4.2. Sketch of the experimental set-up showing the ^{22}Na point source in front of the slit collimator (thickness of 30 mm), the studied detector composed by two LYSO crystals coupled to an array of 12×12 SiPMs and the reference detector for coincidence measurements. The fan beam was scanned on 0.5 mm steps in both the *x*- and *y*-directions.

The detector performance was studied through coincidence measurements using a reference detector based on a LYSO crystal of 50×50×15 mm^3. The reference detector was coupled to an identical 12×12 SiPMs array. Coincidence data were acquired using a ^{22}Na pencil beam (450 μm slit) generated using a ^{22}Na source of 1 mm in diameter with an activity of about 7 μCi, attached to a mechanical collimator composed of two tungsten blocks of 56×56×30 mm^3 separated by the slit (Figure P4.2). The slit collimator was moved in steps of 0.5 mm along the *x* and *y* directions. For the scan along the *y* direction, the studied detector was rotated 90°.The acquisition time was 1000 s for each slit position. We have scanned the slit along each direction started and ended outside the crystal to ensure that the entire scintillation volume was scanned. Plotting the number of events as a function of the slit position, the borders of the crystals can be found, and the real position of the slit determined. A total of 101 slit positions in *x* direction and 64 positions in *y* direction covered the detector under study (see Figure P4.2).

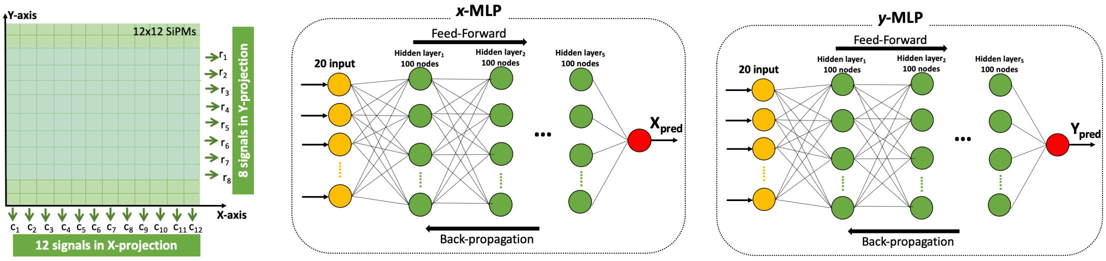

Figure P4.3. Each MLP was trained using the slit measurement along *x* and *y* direction, respectively. The MLPs contain 20 inputs, corresponding to the signals along *x* and *y* projections, 5 layers, 100 nodes each, and one output corresponding to the predicted coordinate.

A. XY positioning, DOI and energy estimation

For the 2D positioning of the scintillation events in the crystals, the *x* and *y* coordinates were calculated using both the SC and the NN positioning methods. For the NN method, one multilayer perceptron architecture (MLP) was used for each direction, named *x*-MLP and *y*-MLP, respectively (see Figure P4.2). Both MLPs contain 5 hidden layers and 100 nodes. The inputs of the networks are the digitized SiPM projection signals, thus 12 signals for *x*-projection and 8 signals for *y*-projection were included. The slit measurement along the *x*- and *y*-directions was used to train the *x*-MLP and the *y*-MLP, respectively. Two filters were applied to the data:

- Energy filter. The energy was calculated for each individual event as the mean of the sum of signals for *x* and *y* projections. For each slit position, only the events that fell within ±15% of the energy spectra photopeak were considered.

- Position filter. The coordinates were pre-estimated using the center of gravity (CoG) algorithm [P4.34]. The CoG_X and CoG_Y ensemble distribution of each slit position was obtained for the scanning along *x*- and *y*- directions, respectively. Events outside the 10% of the peak ensemble distribution along each direction were removed in order to discard events that have suffered Compton scatter, or other interactions, before photoelectric absorption [P4.35].

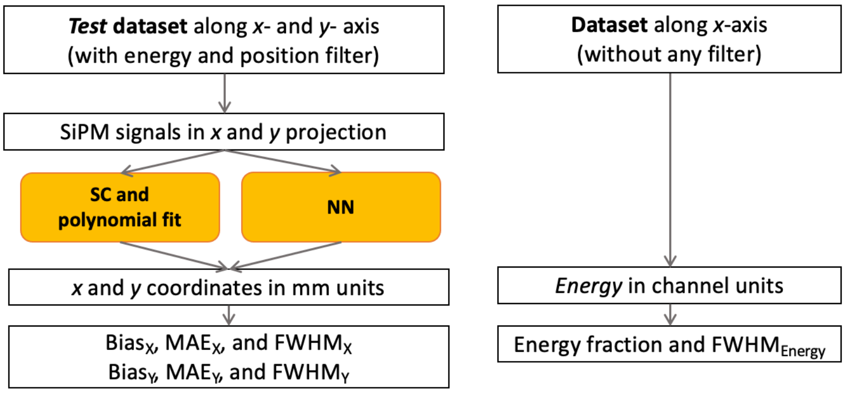

Figure P4.4. Diagram of the dataset employed and calculated parameters for the detector evaluation in terms of spatial and energy performance.

After these pre-filters, the dataset, that contains about 7k events per slit position, was split into three datasets: *train* (50%), *evaluation* (5%) and *test* (45%). Each MLP was trained using the *train* dataset by the Adagrad optimizer using rectified linear activation function (RELU) and the Root Mean Squared Median (RMSE) loss function:

$$RMSE = \sqrt{\frac{\sum_{i=1}^{N}(pos_{real}(i) - pos_{pred}(i))^2}{N}} \qquad (1)$$

where, *N* is the number of events, pos$_{real}$ is the real position of the slit in mm and pos$_{pred}$ is the predicted position also in mm. After training, the MLP was evaluated using the *evaluation* dataset to avoid overfitting.

In the SC algorithm, the x_c and y_c coordinates from the *test* dataset were first estimated using the following equations [P4.17]:

$$x_c = \frac{\sum_{i=1}^{i=12} c_i^2 x_i}{\sum_{i=1}^{i=12} c_i^2} \qquad (2)$$

$$y_c = \frac{\sum_{i=1}^{i=8} r_i^2 y_i}{\sum_{i=1}^{i=8} r_i^2} \qquad (3)$$

where, c_i and r_i are the digitized signals for the projected columns and rows respectively, and x_i and y_i are the SiPMs positions on the detection surface. Acquired data moving the slit along the *x*- and *y*-directions was used to calibrate the estimated x_c and y_c coordinates into mm units. The position profile was fitted using a gaussian distribution and the centroid of each measurement was recorded. The slit real position was plotted versus the estimated centroids and a 3rd polynomial fit was used to convert the measured units to mm (see sketch in Figure P4.3).

The gamma-ray energy (*E*) was calculated as the mean of the sum of signals for *x* and *y* projections. The gamma-ray impact DOI was estimated by using its correlation with the width of the LD profiles and a model of the light transport in the crystal. It is calculated as the average of the ratio of the energy to the maximum signal value (E/I_{max}) for *x* and *y* projections [P4.36].

B. Spatial and energy performance

For each tested configuration, the *x* and *y* coordinates from the *test* dataset along the *x*-axis and *y*-axis (containing the LD profiles after energy and position filter) were calculated using the two studied positioning methods (see sketch in Figure P4.4). The following parameters along each direction were calculated for each slit measurement:

- Bias$_X$ and Bias$_Y$, calculated as the difference between the estimated position, $x_{estimated}$ *or* $y_{estimated}$, and the known position, x_{real} *or* y_{real}:

$$Bias_X = \frac{1}{N} \times \sum_{i=1}^{i=N}(x_{estimated}(i) - x_{real}(i)) \qquad (4)$$

$$Bias_Y = \frac{1}{N} \times \sum_{i=1}^{i=N}(y_{estimated}(i) - y_{real}(i)) \qquad (5)$$

- Mean average error, MAE_X and MAE_Y was calculated following the equations:

$$MAE_X = \frac{1}{N} \times \sum_{i=1}^{i=N} |x_{estimated}(i) - x_{real}(i)| \quad (6)$$

$$MAE_Y = \frac{1}{N} \times \sum_{i=1}^{i=N} |y_{estimated}(i) - y_{real}(i)| \quad (7)$$

  where *N* is the number of events for each slit measurement.

- Spatial resolution, FWHMX and FHWMY, calculated as the FWHM of the gaussian fit to the $x_{estimated}$ and $y_{estimated}$ distribution, respectively.

Regarding the DOI performance, we have plotted the E/I_{max} histograms for each slit measurement of the dataset along *x*-axis (with only energy filter applied) and fitted them using the following analytical expression [P4.37]:

$$DOI\ (z) = A\ \times\ e^{-\alpha z}\left[erf\left(\frac{b-z}{\sqrt{2}\sigma_{int}}\right) - erf\left(\frac{a-z}{\sqrt{2}\sigma_{int}}\right)\right] \quad (8)$$

where α is the attenuation coefficient of the material, *A* is the amplitude, σ_{int} is the standard deviation of the distribution which relates to the DOI FWHM as $2.3\times\sigma_{\text{int}}$, erf is the Gaussian error function, and *a* and *b* are the lower and upper limits of the distribution.

Regarding energy performance, a Gaussian fit to the energy spectra (without any filter) was applied to the data at each slit position of the dataset along *x*-axis to obtain the photopeak position ($E_{photopeak}$) in energy channels. The photopeak position value corresponding to the slit at the center crystal ($E_{photopeak,center}$) was used to calculate the energy fraction parameter for each slit position, as $E_{photopeak}/E_{photopeak,center}$. Notice that this parameter was calculated for each side of the interface separately. The energy resolution was obtained as $\Delta E(FWHM)/E_{photopeak}$.

For each configuration, the average and standard deviation of the parameters described in this section were also calculated.

3. Results

A. Light Distribution

The shape of the measured LD varies depending on the detector configuration [P4.31]. For the standard configuration (see experimental examples for one gamma ray impact at 0.5 mm to the left of the interface in Figure P4.5), most of the generated scintillation light is absorbed by the black paint and therefore the LD is truncated. When the crystals were coupled using the high refractive index compound, the light can travel to the neighbor crystal and be collected by the SiPMs located at the right of the interface (see Figure P4.5 (a)). However, there is not glue compound, to our knowledge, perfectly matching the refractive index of the LYSO scintillator and therefore, some scintillation light is still reflected at the interface by this index unmatching. The amount of light transmitted to the neighbor crystal depends on the difference of such refractive indexes between the crystal and the coupling compound. The outcome of this reduced transmission is a discontinuity in the LDs (see Figure P4.5 (b)) that needs to be modeled in the detector calibration.

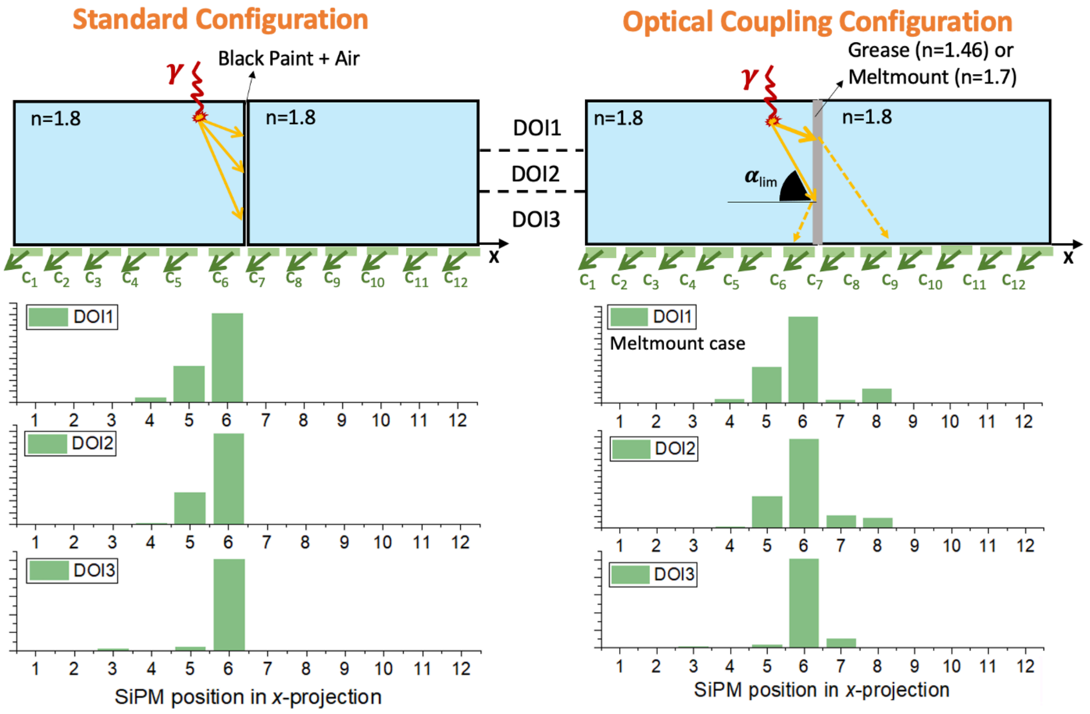

(a) (b)

Figure P4.5. Example of LD profiles for impacts near the interface (0.5 mm) for different DOI positions. (a) LD profiles for the standard configuration. (b) LD profiles for the Meltmount configuration.

B. Spatial and energy performance

The bias_X, MAE_X, and FWHM_X values along the x-axis are shown in Figure P4.6 for both the SC and NN positioning estimation methods. The values corresponding to slit positions belonging to the range between –3 and 3 mm, named the interface region, are shown in Figure P4.7. It can be observed that bias_X, MAE_X, and FWHM_X are significantly improved near the optical coupling interface when using Meltmount compound.

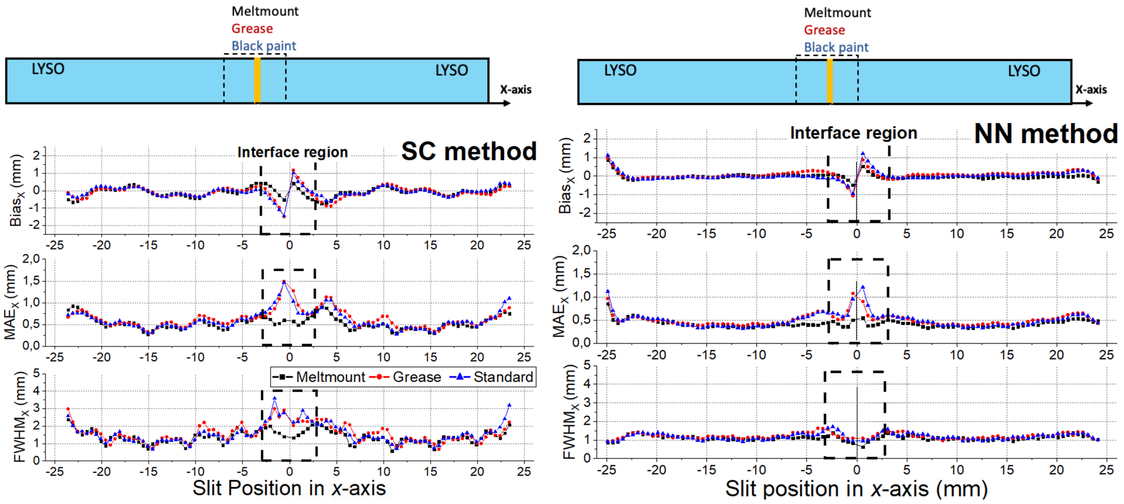

(a) (b)

Figure P4.6. Bias_X, MAE_X and FWHM_X as a function of the slit position along the *x*-axis for the three configurations, using SC (a) and NN (b) position estimation methods.

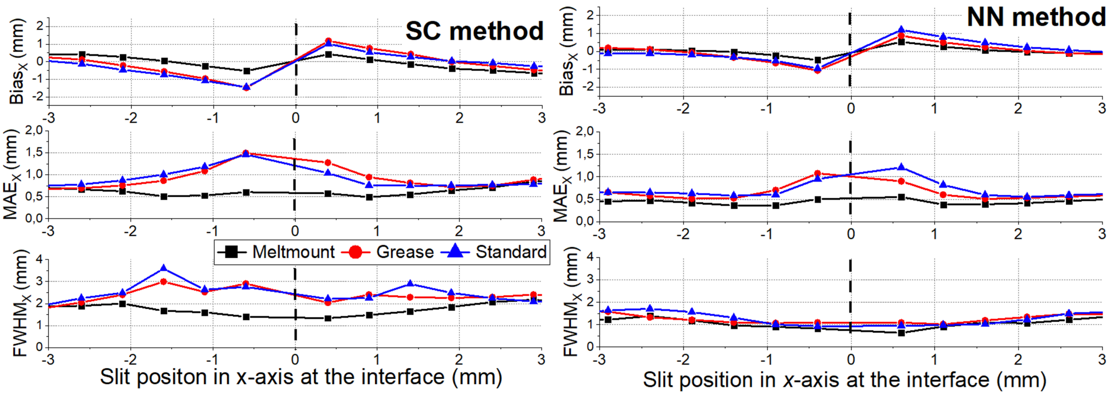

(a) (b)

Figure P4.7. Bias$_X$, MAE$_X$ and FWHM$_X$ as a function of the slit position at the interface region along the *x*-axis for the three configurations, using SC (a) and NN (b) position estimation methods.

Figure P4.8 shows the average values of the |bias$_X$|, MAE$_X$, and FWHM$_X$ for the slit positions at the interface region (3 mm from the optical coupling to each side) as well as their standard deviation (error bars) for each configuration. Using the SC method, a spatial resolution of 1.7±0.3, 2.4±0.3, and 2.6±0.4 mm FWHM was obtained for the Meltmount, grease, and standard configurations, respectively. Lower values are found when the impact positions are estimated using the NN and when the crystals are optically coupled using Meltmount, achieving a FWHM$_X$ of 1.0 ± 0.2 mm.

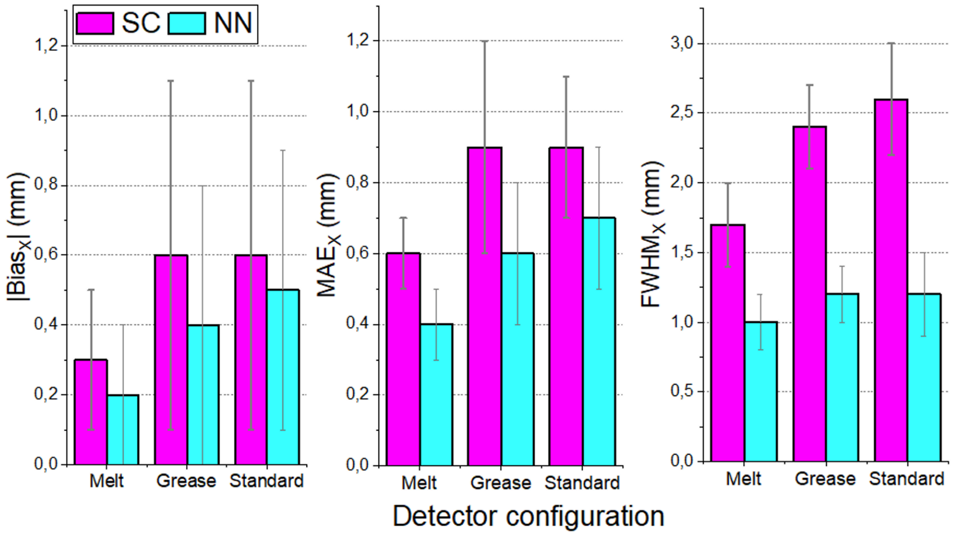

Figure P4.8. Average and standard deviation (error bars) values of the bias$_x$, MAE$_x$ and FWHM$_x$ corresponding to the slit positions at the interface region for each position estimation method.

The bias$_Y$, MAE$_Y$, and FWHM$_Y$ values for the slit position along the *y*-axis are plotted in Figure P4.9. The mean values of the parameters for all slit positions along *y*-axis and their standard deviations are shown in Figure P4.10. Best values were found for NN method for all the configurations, as it occurs along *x*-axis.

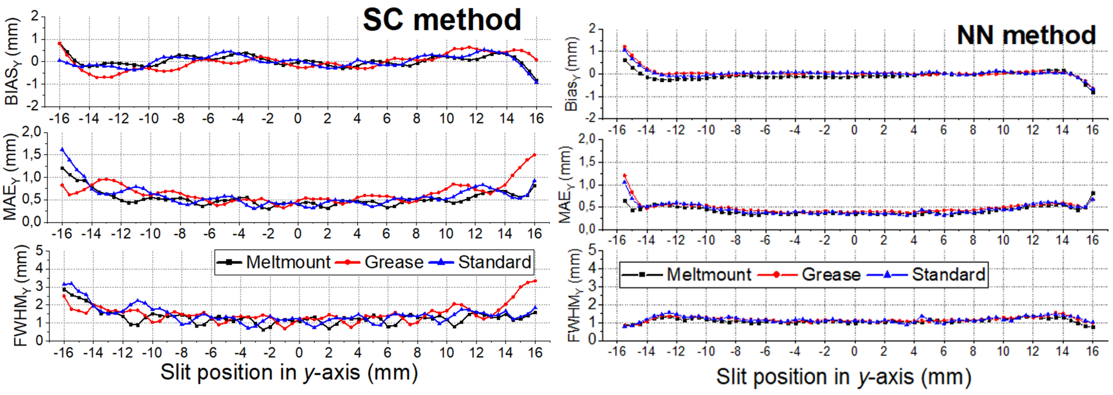

(a) (b)

Figure P4.9. Bias$_Y$, MAE$_Y$ and FWHM$_Y$ as a function of the slit position along the *y*-axis for the three configurations, using SC (a) and NN (b) position estimation methods.

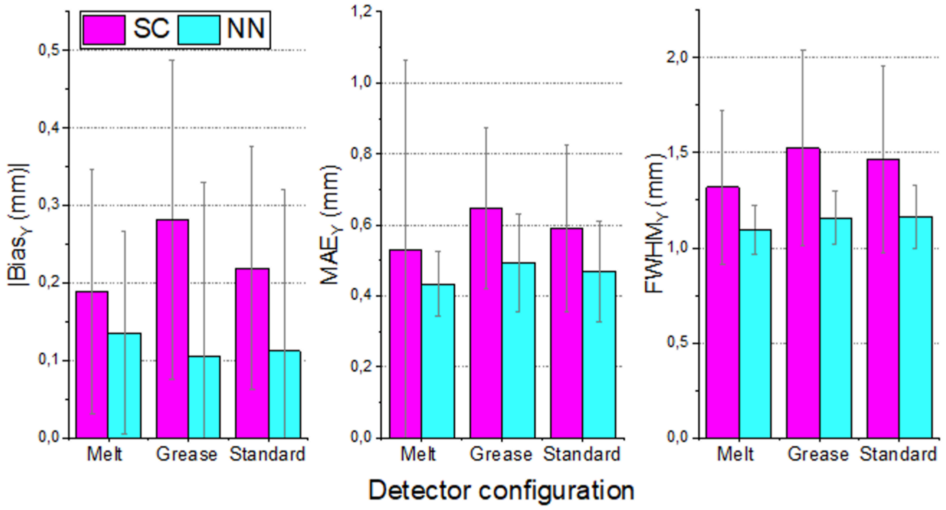

Figure P4.10. Average and standard deviation (error bars) values of the bias$_Y$, MAE$_Y$ and FWHM$_Y$ corresponding to all the slit positions in *y*-axis for each position estimation method.

The left panel in Figure P4.11 shows the DOI histograms (in arbitrary DOI units) measured for one slit position at the crystal center (15 mm from the optical coupling) and other at the interface (1 mm from the optical coupling) for the Meltmount, grease, and standard configurations. The profiles were fitted using Equation (8), see green lines.

Figure P4.12 (a) shows the energy spectra (normalized to the maximum value) corresponding to one slit position at the center region as well as at the interface region for the three studied configurations, in ADC units. The energy fraction and resolution are also shown in Figure P4.12 (b). For all configurations near the coupling inter- face, more energy losses are observed compared to the center of each crystal (energy fraction values close to 1). However, for the Meltmount configuration, these losses are lower compared to the other configurations. Moreover, better energy resolution values were obtained at the interface region for the Meltmount configuration. Figure P4.12 (c) shows the average and standard deviation values for slit positions at the interface region. The standard configuration exhibited lower (20% on average) photopeak values. These differences are reduced when using grease as optical coupling and are almost vanished using Meltmount. Average energy resolutions at the interface region of 18±2%, 20±2%, and 23±3% were measured for the Meltmount, grease, and standard configurations, respectively.

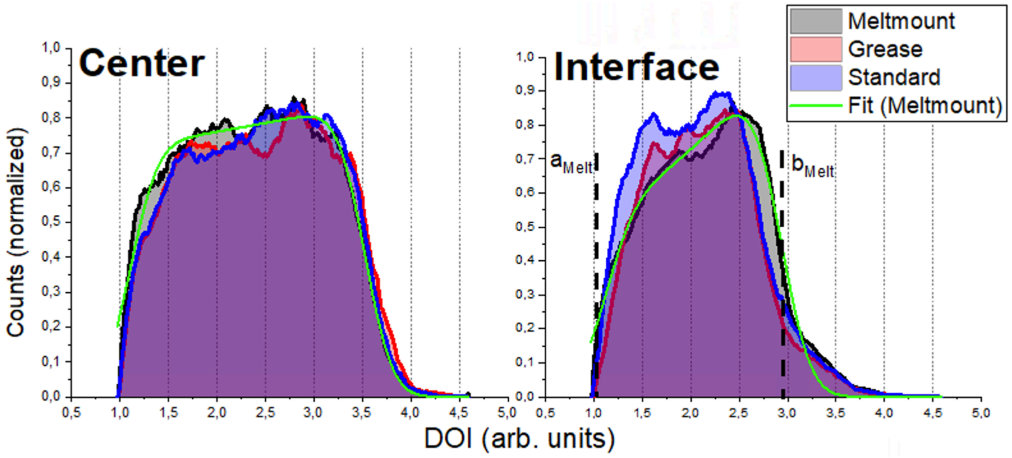

Figure P4.11. DOI histograms (in arbitrary DOI units) measured for one slit position at the crystal center (15 mm from the optical coupling) and other at the interface (1 mm from the optical coupling) for the Meltmount, grease and standard configurations. The profiles were fitted using Equation (8), see green lines.

4. Discussion

In this work, we have experimentally evaluated the performance achieved when coupling two monolithic LYSO crystals using Meltmount ($n_{Meltmount}$=1.7), optical grease (n_{grease}=1.46), and air (standard configuration) between them, in terms of spatial (including DOI) and energy performance. In all cases, the crystals were coupled to a 12×12 SiPMs array and read out with a circuit that provides each row and column signals of the photosensor.

For the planar coordinates (XY), two positioning estimation methods were compared, named SC and NN. Figure P4.8 shows that the |biasX|, MAEX, and FWHMX improved near the interface for the case with smaller mismatch with the refractive index of the crystal, that is, Meltmount configuration. In this case, the total internal reflection is minimal, allowing a better LD characterization and thus, reducing the edge-effect, as expected. Moreover, the NN technique improves the spatial performance along *x*- and *y*-axis compared to the SC method (Figure P4.8 and P4.10). The NNs are able to learn the LD shapes from all the samples of the training data, and thus, a higher spatial accuracy is expected in contrast to SC method, despite having applied a third polynomial fit to mitigate border effects. However, quite similar performance in terms of $bias_X$, MAE_X, and $FWHM_X$ has been obtained for the grease and standard configuration at the interface region (Figure P4.6). We hypothesize that such a similar behavior is explained by the filter of 10% in positions that may be masking the differences of these two configurations. Higher LD truncation in the interface region for standard configuration should pro- duce a deterioration of spatial parameters with respect to the grease configuration. The best values (lowest mean and standard deviation) were reported for the Meltmount configuration and NN method, obtaining an $|bias_X|$ of 0.2 ± 0.2 mm and a $FWHM_X$ of 1.0 ± 0.2 mm at the interface region; thus, achieving a uniform spatial resolution. In other experimental work, a |bias| of 0.4 mm and a FWHM of 2.1 mm was obtained at the transition region between four LYSO crystals glued together with Meltmount and applying both ML and least-squares minimization positioning estimation methods [P4.32] In other study, a |bias| of 0.5 mm and a FWHM of 1.5 mm near the optical coupling (n_{grease} = 1.7) was reported using the ML positioning estimation and simulated data [P4.31]. We assume that the improvement in spatial performance obtained in our work is due to the use of machine-learning artificial NN techniques for positioning estimation.

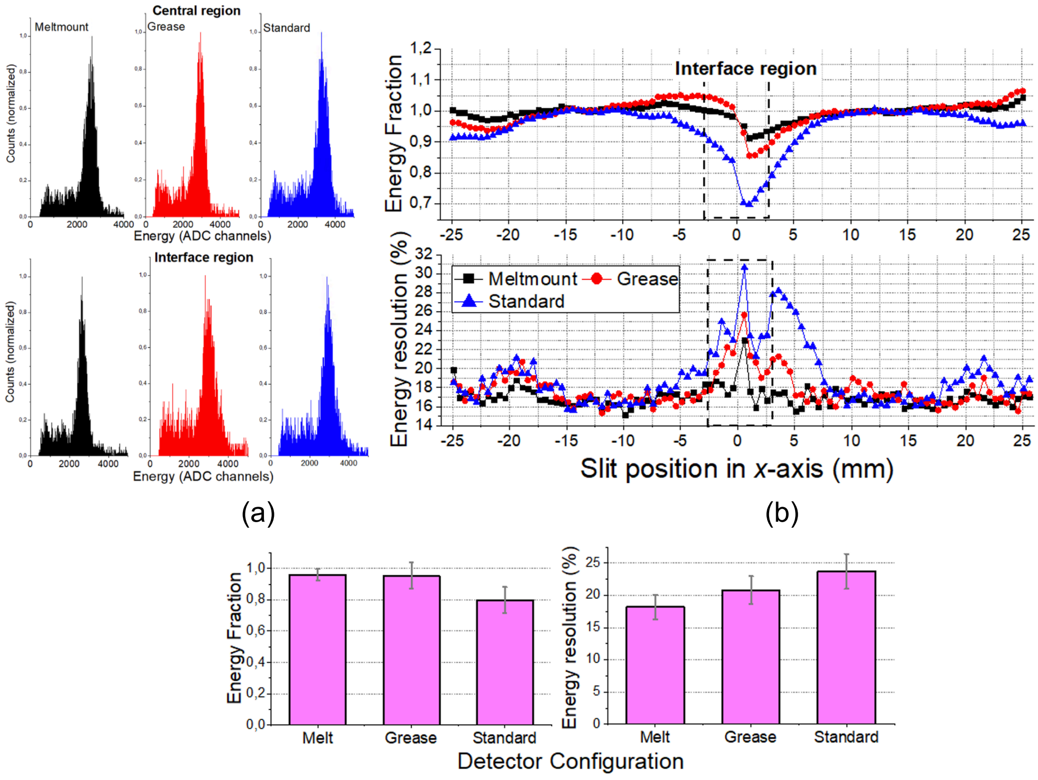

(a) (b)

(c)

Figure P4.12. (a) Energy spectra for one slit at the center of one crystal and at the interface region. (b) Energy fraction and resolution as a function of the slit position along the *x*-axis. (c) Average and standard deviation (error bars) values of energy fraction and resolution for slit positions at the interface region.

Concerning DOI performance at the interface region, narrower DOI histograms were obtained for grease and standard configurations (Figure P4.11), because in these cases, the LD is no longer preserved, either by internal reflections or its truncation. However, for the Meltmount configuration, the LD is almost preserved and, there- fore, the measured DOI histogram follows the shape of the theorical DOI distribution [P4.2]. Out of the scope of this work, lateral incident experiments would be required to accurately estimate the DOI resolution for each configuration.

Regarding energy performance, Figure P4.12 shows that in the Meltmount and grease configurations, some optical photons will be collected by the neighbor crystal, thus reaching an energy fraction closer to the unit. However, it is uncleared the origin of the observed asymmetric behavior around the interface region for the standard configuration (Figure P4.12 (b)). Probably, some inhomogeneities on the crystal and/or on the SiPM array could explain this behavior. For instance, an electronic read-out or paint coupling problem for column 9 of the SiPM array (Figure P4.5) could explain the asymmetric energy performance behavior we have observed for the standard configuration. Moreover, the best average energy resolution value was obtained for Meltmount configuration, improving the energy performance at the interface region.

Table P4.2 summarizes the obtained spatial and energy parameter values for each configuration at the inter- face region. Overall, the Meltmount configuration and NN technique allow to reduce border effects in terms of an improved spatial and energy performance.

	Spatial				**Energy**
	$\lvert \text{bias}_X \rvert$ (mm)		**FWHM$_X$ (mm)**		**Resolution (%)**
	SC	**NN**	**SC**	**NN**	
Meltmount	0.3±0.2	0.2±0.2	1.7±0.3	1.0±0.2	18±2%
Grease	0.6±0.5	0.4±0.4	2.4±0.3	1.2±0.2	20±2%
Standard	0.6±0.5	0.5±0.4	2.6±0.4	1.2±0.3	23±3%

Table P4.2. Spatial and energy performance obtained at the interface region for each configuration.

5. Conclusions

We have experimentally studied the effect of gluing two monolithic LYSO crystals of 33×25.4×10 mm^3 using a high refractive index compound. We have demonstrated the edge-effect reduction when optically coupling side-by-side scintillation crystals using a compound with a refractive index $n_{\text{Meltmount}}=1.7$. We have also shown that compression effects are further reduced when using NN techniques for the gamma-ray impact position estimation in contrast to analytical methods.

It can be concluded that this approach helps increasing the light transfer between adjacent crystals in monolithic detectors, improving the uniformity of spatial and energy performance. In this way, the design and implementation of molecular imaging scanners with minimum gaps among detector blocks would be possible, enhancing the system sensitivity and performance. In order to extrapolate this approach to PET systems, monolithic crystals that are curved could be glued together, ensuring no gaps between blocks in the transaxial axis. Our team is currently building a dedicated breast PET system based on a ring made out of 14 monolithic curved surface LYSO crystals glued together using Meltmount and read out using flexible Printed Circuit Boards (PCBs) coupled to SiPM photosensors.

References

[P4.1] Del Guerra A, Belcari N, Bisogni MG. Positron emission tomography: its 65 years. La Rivista del Nuovo Cimento. 2016;39:155- 223.

[P4.2] Gonzalez-Montoro A, Benlloch JM, Gonzalez AJ, et al. Performance study of a large monolithic LYSO detector with accurate photon DOI using retroreflector layers. Trans Radiat Plasma Med Sci. 2017;1(3):229-237.

[P4.3] González-Montoro A, Sánchez F, Bruyndonckx P, Cañizares G, Benlloch JM, González AJ. Novel method to measure the intrinsic spatial resolution in PET detectors based on monolithic crystals. Nucl Instrum Meth A. 2019;920:58-67.

[P4.4] Schaart DR, Van Dam HT, Seifert S, et al. A novel, SiPM-array based, monolithic scintillator detector for PET. Phys Med Biol. 2009;54:3501-3512.

[P4.5] Maas MC, Van Der Laan DJ, Schaart DR, et al. Experimental characterization of monolithic-crystal small animal PET readout by APD arrays. IEEE Trans Nucl Sci. 2006;53(3):1071-1077.

[P4.6] Gonzalez AJ, Aguilar A, Conde P, et al. A PET detector based on SiPM and monolithic LYSO crystals: performance evaluation. IEEE Trans Nucl Sci. 2016;63:2471-2477.

[P4.7] Cabello J, Barrillon P, Barrio J, et al. High resolution detectors based on continuous crystals and SiPMs for small animal PET. Nucl Instrum Meth A. 2013;718:148-150.

[P4.8] Sánchez F, Orero A, Soriano A, et al. ALBIRA: a small ani- mal PET/SPECT/CT imaging system. Med Phys. 2013;40(5): 051906.

[P4.9] Moliner L, González AJ, Soriano A, et al. Design and evaluation of the MAMMI dedicated breast PET. Med Phys. 2012;39:5393- 5404.

[P4.10] Krishnamoorthy S, Blankemeyer E, Mollet P, Surti S, Van Holen R, Karp JS. Performance evaluation of the MOLECUBES β-CUBE— a high spatial resolution and high sensitivity small animal PET scanner utilizing monolithic LYSO scintillation detectors. Phys Med Biol. 2018;63(15):155013.

[P4.11] Gonzalez-Montoro A, Gonzalez AJ, Pourashraf S, et al. Evolution of PET detectors and event positioning algorithms using mono- lithic scintillation crystals. IEEE Trans Radiat Plasma Med Sci. 2021;5:282-305.

[P4.12] Maas MC, Schaart DR, Van Der Laan DJ(J), et al. Mono- lithic scintillator PET detectors with intrinsic depth-of-interaction correction. Phys Med Biol. 2009;54(7):1893-1908.

[P4.13] Conde P, González AJ, Hernández L, et al. Statistical moments of scintillation light distribution analysis with dSiPMs and monolithic crystals. In 2013 IEEE Nuclear Science Symposium and Medical Imaging Conference (2013 NSS/MIC). 2013, October. (pp. 1-4). IEEE.

[P4.14] Seifert S, Van Dam HT, Huizenga J, et al. Monolithic LaBr3:Ce crystals on silicon photomultiplier arrays for time-of-flight positron emission tomography. Phys Med Biol. 2012;57:2219-2233.

[P4.15] Conde P, Iborra A, González AJ, et al. Minimization of border effects in monolithic scintillators using neural networks, based on MR-compatible SiPM arrays. In EJNMMI Phys. 2014; (Vol. 1, No. 1, pp. 1-2). SpringerOpen.

[P4.16] Vaska P, Petrillo MJ, Muehllehner G. Virtual PMTs: improving centroid positioning performance near the edges of a gamma camera detector. IEEE Trans Nucl Sci. 2001;48:645-649.

[P4.17] Pani R, Vittorini F, Cinti MN, et al. Revisited position arithmetics for LaBr 3:Ce continuous crystals. Nucl Phys B Proc Suppl. 2009;197:383-386.

[P4.18] Pani R, Nourbakhsh, S, Pani P, et al. Continuous DOI determina- tion by Gaussian modelling of linear and non-linear scintillation light distributions. In 2011 IEEE Nuclear Science Symposium Conference Record (2011, October). (pp. 3386-3389). IEEE.

[P4.19] Di Francesco A, Bugalho R, Oliveira L, et al. TOFPET 2: a high-performance circuit for PET time-of-flight. Nucl Instrum Meth A. 2016;824:194-195.

[P4.20] Nadig V, Schug D, Weissler B, Schulz V. Evaluation of the PET- sys TOFPET2 ASIC in multi-channel coincidence experiments. EJNMMI Phys. 2021;8:30.

[P4.21] Lerche ChW, Ros A, Monzó JM, et al. Maximum likelihood posi- tioning for gamma-ray imaging detectors with depth of interaction measurement. Nucl Instrum Meth A. 2009;604:359-362.

[P4.22] Pierce LA, Pedemonte S, Dewitt D, et al. Characterization of highly multiplexed monolithic PET/gamma camera detector modules. Phys Med Biol. 2018;63:075017.

[P4.23] Zhi L, Wedrowski M, Bruyndoncx P, Vandersteen G. Non- linear least-squares modeling of 3D interaction position in a monolithic scintillator block. Phys Med Biol. 2010;55:6515- 6532.

[P4.24] Van Dam HT, Seifert S, Vinke R, et al. Improved nearest neighbor methods for gamma photon interaction position determination in monolithic scintillator PET detectors. IEEE Trans Nucl Sci. 2011;58:2139-2147.

[P4.25] Aldawood S, Thirolf PG, Miani A, et al. Development of a Compton camera for prompt-gamma medical imaging. Radiat Phys Chem. 2017;140:190-197.

[P4.26] Freire M, Gonzalez-Montoro A, Sanchez F, Benlloch JM, Gonzalez AJ. Calibration of gamma ray impacts in monolithic- based detectors using Voronoi diagrams. IEEE Trans Radiat Plasma Med Sci. 2020;4:350-360.

[P4.27] Conde P, Iborra A, Gonzalez AJ, et al. Determination of the interaction position of gamma photons in monolithic scintillators using neural network fitting. IEEE Trans Nucl Sci. 2016;63:30- 36.

[P4.28] Gostojic´A, Tatischeff V, Kiener J, et al. Characterization of LaBr3:Ce and CeBr3 calorimeter modules for 3D imag- ing in gamma-ray astronomy. Nucl Instrum Meth A. 2016;832: 24-42.

[P4.29] Ulyanov A, Morris O, Roberts OJ, et al. Localisation of gamma- ray interaction points in thick monolithic CeBr3 and LaBr3:Ce scintillators. Nucl Instrum Meth A. 2017;844:81-89.

[P4.30] Babiano V, Caballero L, Calvo D, Ladarescu I, Olleros P, Domingo-Pardo C. γ-Ray position reconstruction in large mono- lithic LaCl3(Ce) crystals with SiPM readout. Nucl Inst Meth A. 2019;931:1-22.

[P4.31] Vinke R, Levin CS. A method to achieve spatial linearity and uni- form resolution at the edges of monolithic scintillation crystal detectors. Phys Med Biol. 2014;59:2975-2995.

[P4.32] Morrocchi M, Hunter WCJ, Del Guerra A, et al. Evaluation of event position reconstruction in monolithic crystals that are optically coupled. Phys Med Biol. 2016;61:8298-8320.

[P4.33] Silicone Solutions. SS-988 Non-Curing Optical Coupling Gel- V-788 Offset DATASHEET from https://siliconesolutions.com/ media/pdf/SS-988TDS.pdf. Accessed 2020.

[P4.34] Landi G. Properties of the center of gravity as an algorithm for position measurements. Nucl Instrum Meth A. 2002;485:698-719.

[P4.35] Ling T, Lewellen TK, Miyaoka RS. Depth of interaction decod- ing of a continuous crystal detector module. Phys Med Biol. 2007;52:2213. https://www.cargille.com/mounting-media/

[P4.36] Pani R, et al. Continuous DOI determination by Gaussian mod- elling of linear and non-linear scintillation light distributions. In Proceedings of IEEE NSS-MIC. 2011.

[P4.37] Lerche CW, Ros A, Herrero V, et al. Dependency of energy-, position- and depth of interaction resolution on scintillation crystal coating and geometry. IEEE Trans Nucl Sci. 2008;55(3):1344- 1351.

Acknowledgments

This work was supported in part by the Spanish Ministerio de Ciencia e Innovación under grant no. PID2019-107790RB-C21 and by the National Institute of Health under grant no. 1R01EB029450-01. Action co-financed by the European Union through the Programa Operativo del Fondo Europeo de Desarrollo Regional (FEDER) of the Comunitat Valenciana (IDIFEDER/2021/004).

M. Freire was supported by the BEFPI Program for Researchers in Predoctoral Phase of the Generalitat Valenciana. A. Gonzalez-Montoro is supported by VALi+d Program for Researchers in Postdoc- toral Phase of the Ministry of Labor and Social Economy (Generalitat Valenciana) and the EU Social Fund.

IV Discussion

PET is one of the most powerful Nuclear Molecular Imaging technique in which positron-emitter radiotracers are introduced to the patient, decaying by emitting two annihilation photons that are detected by specific detectors located around the subject body. The measured data is image reconstructed to determine the distribution of such radiotracer inside the patient. The functional information obtained by PET has multiple indications and particularly in oncology, as it allows for an accurate staging, therapy response assessment and eventually early detection of recurrent diseases.

Currently, most of commercial PET systems are built using detectors blocks based on pixelated crystals. However, the use of monolithic crystals in PET detectors has shown the potential to provide accurate 3D spatial resolution, including DOI estimation capabilities, good energy response, and promising timing resolutions. Moreover, their production cost is more affordable than pixelated crystals since monolithic blocks are easy to manufacture because less crystals cutting, polishing and surface processing are required.

Monolithic-based detectors have been already implemented in some commercial organ dedicated and preclinical PET systems (see Table 6 and Table 7). Nevertheless, they have not yet been widely exploited in the clinical field, mainly because they usually require more complex and time-consuming calibration procedures than pixelated-based PET detectors to accurately obtain the 511 keV annihilation photon interaction position.

In pixelated crystals, detector calibration is relatively easy and can be quickly performed for all modules by placing one radioactive source at the center of the PET scanner to provide information of all the crystal pixel elements. However, for monolithic crystals, the calibration typically requires scanning a collimated small size source across the entire monolithic surface while recording the measured LDs and mechanical positions (see Section 3.2 of Chapter I). This procedure must be applied for each detector module building the PET scanner. Moreover, in monolithic-based configurations, edge effects, produced by truncation or reflection of scintillation light at the borders of the crystals need to be also characterized. This complicates returning precise estimations of the 3D interaction position of the annihilation photons in the entire crystal.

In the last decade, several efforts have been pursued to implement positioning methods and calibration procedures addressing those challenges (see Section 3) [98]. The main objectives of this PhD thesis are: i) to develop methodologies to accurately retrieve the impact positions of annihilation photons in monolithic-based detectors and, ii) to efficiently apply these new methods in different PET systems designs. In particular, two novel methodologies have been proposed, implemented and experimentally validated.

The first technique uses positioning algorithms based on analytical methods that does not require the use of reference data, specifically the RTP method and E/I_{max} estimator for the determination of (*x*-, *y*-) and *z*- impact positions, respectively. These positions need to be modified to provide calibrated coordinates and to correct for the non-uniformities arising from edge effects. To accomplish that, the Voronoi calibration methodology based on the so-called Voronoi diagrams and Natural Neighbor interpolation was proposed and implemented (see Section 4 of Chapter II). This technique allows for the calibration of the 3D impact coordinates and photon energy.

The Voronoi calibration was first implemented and validated at the detector level using different detector block configurations [1][284]. In all cases, the calibration map was obtained acquiring data from an array of 11×11 ^{22}Na sources that allows us to retrieve all the calibration positions without the use of complex hardware setups, thus facilitating the procedure and reducing calibration times. One of the detector configurations consisted of a monolithic LYSO with 50×50×15 mm^3 dimensions, with lateral sides black painted and a RR film added to the entrance side [1]. The crystal was coupled to an array of 12×12 SiPMs making use of the projection readout circuit. Edge effects are successfully corrected when applying Voronoi calibration. Moreover, the proposed method has demonstrated to be superior compared to another calibration approach, the so-called 1D polynomial, previously employed in some PET scanners co-developed at i3M, since all the events were accurately calibrated without the presence of artifacts. Therefore, there is no need to remove events at the edges of the crystal, as it might happen when applying 1D polynomial calibration method, thus boosting the detection efficiency [1].

The Voronoi calibration was carefully also applied to data acquired for different crystal surface treatments also using a 50×50×15 mm^3 LYSO crystal coupled to an array of 12×12 SiPMs and the projection readout circuit [1]. After calibration, better spatial and DOI performance has been achieved when the laterals were painted black because the LD is preserved, however, better energy resolution is reached when using diffuse or specular reflectors since they enhance the amount of light extraction (see Section 2.3.2 of Chapter I) [1]. Therefore, it can be concluded that the selection of the crystal treatment is a tradeoff between the aimed system geometry and application. Moreover, the results obtained when using analytical-based positioning methods including the proposed Voronoi calibration are comparable with state-of-the-art works. For example, for the case in which the lateral sides of the crystal were painted black and the top side was covered with ESR, a detector spatial resolution (FWHM) of 1.6±0.1 mm was obtained after Voronoi calibration [1]. This value is close to the spatial resolution values of 1.23 mm and 1.15 mm obtained when applying the Mean Nearest Neighbor method and Neural Networks, respectively, for a detector block based on a 50×50×16 mm^3 LYSO crystal with the same surface treatment and coupled to an array of 8×8 SiPMs [241].

During this thesis, the Voronoi calibration was validated using a second detector configuration that consisted of a LYSO crystal of 51.5×51.5×3 mm^3 laterally read out by coupling a 16×1 SiPMs array to the four lateral sides of 51.6×3 mm^2 dimensions [284]. The results showed that the edge effects are extensively reduced when the Voronoi calibration was applied, thus also demonstrating its potential for other detector configuration designs.

Due to the excellent results achieved using the Voronoi calibration, it was applied to the *ProsPET* system [277]. This scanner was installed at the Hospital La Fe in Valencia and it was composed by a single ring of 24 LYSO monolithic crystals of 50×50×15 mm^3 coupled to photodetector arrays of 12×12 SiPM (see Section 5.1 of Chapter II) [277]. After calibration, the scanner achieved an average detector spatial resolution values of 1.6±0.1 mm FWHM and an energy resolution of 17.5%, as well as accurate DOI capabilities [1]. The system calibration was performed when all the detector modules were already assembled. However, two different calibration strategies were proposed and compared. First, a standard procedure based on individually calibrating each detector by acquiring data using an array of 11×11 ^{22}Na sources and subsequently obtaining a set of LUTs for each detector module was employed. This process still requires acquiring data from each detector module, being a tedious and time-consuming task. To alleviate this, in this doctoral thesis, a second more practical methodology was proposed based on using only 3 calibration maps obtained measuring the array of sources for 3 random detectors, and the uniformity map of the 24 detectors [2]. This last measurement can be easily obtained for all the modules at the same moment by placing a uniform activity phantom at the center of the scanner FOV. Notice that this is the same routine measurement performed to apply the normalization correction required for PET image reconstruction (see Section 2.4 of Chapter I). The implemented approach was experimentally evaluated in the *ProsPET* system [2]. The calibration times was significantly reduced by approximately 80% compared with the standard procedure with no degradation of the system performance and no need to increase the computational cost [2]. This methodology has the potential to calibrate the system in a reasonable short time-period in the clinical domain and therefore, might be the key to exploit the use of conventional large PET scanners based on monolithic crystals. Herein, by reducing the calibration time, technical personnel exposure to radiation is also minimized and, the calibration cost associated to the supply of radioactive sources also reduced.

Making use of the experience obtained during the implementation of the Voronoi calibration in the *ProsPET* scanner, the Voronoi calibration was also applied to the *ScintoTube I*, a PET insert for small animals developed within the context of an international project (see Section 5.2). The main goal of the project is to experimentally demonstrate the boosting in the system sensitivity and the reduction of edge effects inherent to a novel PET design concept that uses a single (continuous) annular scintillation crystal, instead of the conventional block detectors. The *ScintoTube I* prototype was constructed as a proof-of-concept to experimentally show the feasibility of the proposed edge-less approach. To simplify the implementation process, an LYSO scintillator annulus with an inner circular face but facetted outer faces was proposed, allowing an easy coupling of the outer faces to flat SiPM arrays. This specific design was already evaluated using robust simulation studies [121][288], and one of the objectives of this thesis has been the assembly, calibration and performance validation of the proposed scanner [3]. The *x*-, *y*- and DOI- annihilation photon impact coordinates were estimated using an analytical method [287] and calibrated applying a modified version of the aforementioned Voronoi calibration for this peculiar system design. The facetted geometry of this prototype produces optical reflections at the facet joints (due to variances in the limit angle) that causes a dependency of the *x*-impact coordinate and energy photopeak position with the photon DOI. The implemented calibration allows us to provide accurate 3D impact position and energy considering this DOI dependency, as demonstrated in [287]. Calibration data was experimentally acquired when the system was completely assembled by moving a small size ^{22}Na source across the inner face of the crystal using a motor stage. In addition, an exhaustive experimental evaluation of the *ScintoTube I* prototype was performed. A peak sensitivity of 3.8% at the system center, and a maximum NECR at 40.6 kcps for 0.27 mCi was achieved. Moreover, all rods (from 1 mm to 5 mm) of the NEMA IQ phantom could be clearly resolved. These results demonstrated the feasibility of the edge-less approach and validated the Voronoi calibration methodology in this novel design [3]. Notice that, in this first prototype the surfaces of the annulus were painted black to avoid undesired reflections that degrade spatial performance, resulting in an energy resolution of 23.4±1.8%. Other surface treatments could be employed in order to improve that value. For example, in a recent experimental work published by other group [126], the sides of an LYSO annulus crystal were treated with specular reflector achieving an energy resolution 12.3%. However, preliminary results showed that rods of 1 mm were barely resolved. It should be mentioned that the edge-less approach has been also validated for SPECT scanners [122][123], and even images of small animals were obtained [122].

The faceted design of the *ScintoTube I* was recently modified and a second insert with both inner and outer faces being cylindrical, named *ScintoTube* II, was proposed. This updated design may allow us to correct the undesired effects on the LD pattern at the facet junctions caused by the faceted outer faces (see Section 5.2 in Chapter II), which degraded the reconstructed image quality. The system has been assembled and calibrated [289] and it has been installed at University of Virginia, where experimental tests with mice are planned to be done in the next months.

In all previous studies, analytical positioning methods together with the Voronoi calibration methodology were employed for an accurate determination of the annihilation photon impact position, since its implementation is easier. However, different studies pointed that supervised Machine Learning and Deep Learning methods, such as Neural Networks algorithms, can enhance the spatial performance of PET detectors compared to analytical or statistical methods [237][241]. For this reason, a second strategy for impact positioning but employing NN techniques was investigated, with particular interest in its practical and feasible application to full PET scanners based on monolithic crystals and their calibration.

During the thesis, the NN technique was first implemented and evaluated at the detector level using two monolithic LYSO scintillation blocks of 33×25.4×10 mm^3 side-by-side optically coupled using the Meltmount material, a high refractive index compound ($n_{Meltmount} = 1.7$) [4]. This detector approach was studied for the *DeepBreast* project, that proposes in addition to the use of NN techniques for the impact position estimation, a novel system design for breast imaging based on gluing curved monolithic crystals (see Section 5.3). As we have mentioned, the potential of gluing monolithic crystals using a high refractive compound, such as Meltmount, has been already exhibited but only analytical and statistical methods for impact position estimation were tested [127][128]. One of the objectives of this thesis has been to further improve the spatial capabilities of glued monolithic crystals using NN techniques. Specifically, a NN algorithm based on two MLP architectures, named MLP_X and MLP_Y, has been implemented during this thesis, returning the *x*- and *y*- impact positions in millimeters, respectively. An exhaustive experimental study was reported comparing the case of gluing the crystals with Meltmount with the case (i) in which the coupling is optical grease ($n_{grease} = 1.46$) and, (ii) the crystal are isolated using black paint and air between them [4]. Moreover, the NN technique was compared to a simple analytical method. The best results were obtained for the Meltmount configuration when applying the NN technique, resulting in a spatial resolution (FWHM) of 1.0±0.2 mm. Notice that better spatial resolution was obtained compared to a previous work also based on gluing LYSO crystals with Meltmount, in which a spatial resolution of 2.1 mm FWHM was achieved applying Least Square (analytical) and MLE (statistical) positioning methods [128].

Due to these promising results, it was decided to build the *DeepBreast* PET system by laterally gluing 14 curved monolithic LYSO crystals with Meltmount and to implement the NN technique for impact determination (see Section 5.3). It should be mentioned that the use of curved monolithic crystals instead of blocks is not a common approach, but a WB-PET and a dedicated breast scanner, both of them based on NaI(Tl) scintillator, were built at the University of Pennsylvania [291][292]. Moreover, although the advantages of gluing monolithic crystals have been already demonstrated at the detector level [127][128], not published work has been found showing the feasibility of this approach in a full PET system. During the course of this thesis the assembly process and calibration of the *DeepBreast* system was carried out (see Section 5.3). The scanner has an inner and outer diameter of 200 mm and 224 mm, respectively; and an axial length of 50 mm. The inner, top and bottom sides of the ring were painted black to avoid undesirable reflections. The outer faces of the crystals were successfully coupled to custom flexible PCBs containing 12×12 SiPMs. Each PCB also contains a projection readout circuit and then, a total of 12+12 signals are digitized. The *x*-(transaxial) and *y*-(axial) impact positions were determined using a NN technique based on two MLP, MLP_X and MLP_{DOI}, respectively. For training the MLPs, a novel setup was proposed allowing for the generation of the experimental data with the scanner already mounted, thus facilitating the process and reducing the calibration time. The DOI coordinates were estimated using the E/I_{max} estimator and then calibrated employing the Voronoi calibration, which was also used for the energy calibration. Experimental data from a ^{22}Na point source at different radial positions of the scanner was successfully reconstructed. A measured system spatial resolution (FWHM) of 1.8 mm, 2 mm and 1.5 mm was achieved at the center FOV for the radial, tangential and axial directions, respectively. These values remain almost constant when radially moving from the center to the edges of the scanner FOV, since DOI information was used to determine the correct LOR, and thus parallax errors are mitigated. In a very similar dedicated breast PET scanner based on monolithic blocks so-called *MAMMI,* the radial component of the spatial resolution degrades from 1.9 mm to 7 mm at the edge of the FOV [194]. This is because the crystals were coupled to PMTs followed by a modified version of the Anger resistor network that reduces the number of signals to only 5, including certain DOI information. The preliminary results obtained with *DeepBreast* scanner are very promising and a modified version of the NEMA protocol is being under development.

In all the previous studies, the use of monolithic-based PET detector was exploited, mainly focusing on their spatial capabilities but not on their timing capabilities. During the last period of the thesis, an alternative detector configuration, the so-called semi-monolithic detector was also studied. This configuration is based on an array of scintillation slabs, so that optical photons are distributed along one dimension of the photosensor area (monolithic direction), but they are confined along the other direction (pixelated direction). Therefore, it combines the inherent DOI determination capabilities of monolithic crystals, and the improved timing resolution of pixelated ones (see Section 2.3.1.3 of Chapter I) [105]. The semi-monolithic detector is intended to be used in two novel systems that require simultaneous DOI and TOF capabilities, namely: a TB-PET system and, a PET-Compton scanner. Both systems are currently under development at i3M (see Section 5 of Chapter II). The benefits of this configuration have been already demonstrated with simulated and experimental studies by several groups [100]-[105]. In most of the published works, analytical or MLE methods were employed for the *x*-(monolithic) and DOI impact position estimation inside the detector [100]-[103]. Recently, a supervised machine learning method using GTB was also published as shown in [105]. During this this thesis, the NN technique already validated in previous detectors have been implemented in this novel detector design. The NN technique based on two MLPs architectures, MLP_X and MLP_{DOI} for the *x*-(monolithic) and DOI determination, respectively, was validated at the detector-level using different semi-monolithic crystal dimensions, surfaces treatments and photosensor models. An exhaustive study of the spatial capabilities when using the implemented NN technique was performed for a semi-monolithic detector composed by 8 slabs of $25.8\times25.8\times20$ mm^3 coupled to an array of 8×8 SiPMs and read out using the TOFPET2 ASIC from PETsys Electronics [106]. The training process was performed by using experimental data acquired by moving a pencil beam in the *x*-(monolithic) and DOI directions. Spatial resolution values (MAE) of 1.3 mm and 2.2 mm for the *x*-(monolithic) and DOI directions, respectively, were achieved for the case in which the lateral and top sides of the crystal were covered with specular reflector. These values are comparable with the results obtained when using the GTB method and a very similar semi-monolithic detector design [105].

Regarding the applicability of the NN technique to the systems based on semi-monolithic crystal that are under development at i3M, we investigated the alternative use of a fan beam collimator instead of the pinhole collimator for the experimental acquisition of the training data in order to speed up the process (see Section 4 of Chapter II). However, further research will be necessary to be able to predict the annihilation photon impact position on all the detectors of the PET scanner without the need to acquire fan-beam measurements for each detector block.

V Conclusions

Medical Imaging techniques generate visual representations of the human body, allowing the clinicians to accurately diagnose, monitor or treat different medical conditions. Among the large variety of Medical Imaging modalities, this PhD thesis is focused on the development of novel methodologies for PET scanners. In recent years, the progress in the technology of PET detectors based on monolithic scintillators has made them suitable candidates to replace traditional detector blocks based on pixelated scintillators. However, practical techniques to operate with monolithic detectors are required, especially for retrieving annihilation photon interactions with high precision and, thus, obtain superior quality of tomographic images. The main objective of this thesis was to propose, implement and validate positioning estimation methods and calibration techniques for using monolithic-based detectors in PET systems installed in clinical environments.

This PhD thesis is presented through four peer-reviewed papers and shows a detailed study of two proposed and developed strategies, for the accurate determination of the annihilation photon impact position, one based on analytical methods and another based on Deep Learning algorithms. On the first one, it has been implemented a Voronoi calibration methodology that corrects the 3D annihilation photon impact position previously estimated using analytical methods. On the second one, a supervised Deep Learning algorithm using a Neural Network technique has been developed for detectors based on monolithic and semi-monolithic crystals, showing that this approach improves the overall spatial detector capabilities. Both of them have been first successfully validated at the detector level, demonstrating its capabilities to retrieve the annihilation photon impact position with high precision.

A translation of the research from the laboratory to the clinical and preclinical environments has been performed by applying the two strategies developed during this thesis to the different research lines followed by the group. The Voronoi calibration methodology was successfully applied to a prostate dedicated PET system, the *ProsPET*, installed at Hospital La Fe in Valencia; and also, to a preclinical PET insert, the *ScintoTube I,* installed at the University of Virginia. Moreover, a novel procedure to speed up the calibration process was developed and also applied to the *ProsPET* system, reducing and facilitating the calibration process, and thus, dealing with one of the main drawbacks of employing monolithic-based PET systems in a clinical environment. Finally, the Neural Network technique was implemented in the *DeepBreast* system using a novel procedure that reduces calibration times, allowing to acquire training data with the system totally assembled, and determine annihilation photon impact positions with a very high precision.

Therefore, the two strategies developed during this thesis for an accurate determination of the annihilation photon impact position, have successfully demonstrated the possibility to use monolithic-based detectors in PET system in the clinical and preclinical fields, significantly increasing the value of this powerful functional imaging system.

Bibliography

[1] M. Freire, et al., “Calibration of gamma ray impacts in monolithic-based detectors using voronoi diagrams,” IEEE Trans. Radiat. Plasma Med. Sci. **4**, 350-360, 2019.

[2] M. Freire, et al., “Reducing Calibration Time in PET Systems Based on Monolithic Crystals,” Front. Med. **8**, 734476, 2021.

[3] M. Freire, et al., “Experimental validation of a rodent PET scanner prototype based on a single LYSO crystal tube,” IEEE Trans. Radiat. Plasma Med. Sci. **6**, 697-706, 2021.

[4] M. Freire, et al., “Performance evaluation of side-by-side optically coupled monolithic LYSO crystals,” Med. Phys. **49**, 5616-5626, 2022.

[5] J.L. Prince and J. Links, “Medical Imaging Signals and Systems,” Upper Saddle River: Pearson Prentice Hall **37**, 2006.

[6] J.D. Schuijf, J.J Bax and E.E. van der Wall, “Anatomical and functional imaging techniques: basically similar or fundamentally different?,” Neth. Heart J. **15**, 43-44, 2007.

[7] H. Kasban, M.A.M. El-Bendary and D.H. Salama “A comparative study of medical imaging techniques,” Int. J. Inf. Sci. Intell. Syst. **4**, 37-58, 2015.

[8] M. Desco and J.J. Vaquero, “Más de un siglo de imagen médica,” Arbor **177**, 337-364, 2004.

[9] N.S. Kaltoft, et al., “Hybrid FDG PET/MRI vs. FDG PET and CT in patients with suspected dementia–A comparison of diagnostic yield and propagated influence on clinical diagnosis and patient management,” Plos One **14**, e0216409, 2019.

[10] A. Alavi, T.J. Werner and P.F. Høilund-Carlsen, “PET-based imaging to detect and characterize cardiovascular disorders: unavoidable path for the foreseeable future,” J. Nucl. Cardiol. **25**, 203-207, 2018.

[11] W. C. Roentgen, "On a New Kind of Rays," Nat. **53**, 1896.

[12] G.N. Hounsfield, “Computerized transverse axial scanning (tomography): Part 1. Description of system,” Br. J. Radiol. **46**, 1016-1022, 1973.

[13] S. Ruben, M.D. Kamen and W.Z. Hassid, “Photosynthesis with radioactive carbon. II. Chemical properties of the intermediates,” Jam. Chern. Soc. **62**, 1940.

[14] National Research Council (US) and Institute of Medicine (US) Committee on State of the Science of Nuclear Medicine. Advancing Nuclear Medicine Through Innovation. Washington (DC): National Academies Press (US); 2007. 2, Nuclear Medicine. Available from: https://www.ncbi.nlm.nih.gov/books/NBK11471/

[15] M.E. Phelps, et al., “Application of annihilation coincidence detection to transaxial reconstruction tomography,” J. Nucl. Med. 1**6**, 1975.

[16] M.M. Ter-Pogossian, et al., “Positron emission transaxial tomograph for nuclear imaging (PETT),” Radiol. **114**, 1975.

[17] V. Varadarajan, et al., “Role of Imaging in Diagnosis and Management of COVID-19: A Multiorgan Multimodality Imaging Review,” Front. Med, 2013, 2021.

[18] H. Jung, “Basic physical principles and clinical applications of computed tomography,” Prog. Med. Phys. **32**, 1-17, 2021.

[19] P. Bama Aivarasi and R. Vasuki, “An overview to medical imaging techniques and non-invasive MRI medical system-as a scientific diagnostic tool,” Int J Recent Sci Res. **8**, 22349-22353., 2017

[20] J. P. Hornak, “The Basics of MRI,” Biomed. Eng. **24**, 2–6, 2008.

[21] C.H. Liu, “Anatomical, functional and molecular biomarker applications of magnetic resonance neuroimaging,” Future Neurol. **10**, 49-65, 2015.

[22] M. Symms, “A review of structural magnetic resonance neuroimaging,” J. Neurol. Neurosurg. Psychiatry **75**, 1235-1244, 2004.

[23] D. A. Mankoff, “A definition of molecular imaging,” J. Nucl. Med. **48**, 18N, 2007.

[24] R.E. Gibson, “Molecular Imaging, Principles and Practices,” Mol. Imaging Biol. **13**, 594-598, 2011.

[25] M. L. James, S.S. Gambhir, "A molecular imaging primer: modalities, imaging agents, and applications," Physiol. Rev. **92**, 897-965, 2021.

[26] ¿Qué son la medicina nuclear y la imagen molecular?. Available from: https://s3.amazonaws.com/rdcms-snmmi/files/production/public/FileDownloads/Patients/FactSheets/What%20is%20Nuclear%20Med%20spanish.pdf

[27] G. Borghi, “From detectors towards systems: enabling clinical TOF-PET with monolithic scintillators.”, PhD thesis, Delft University of Technology, 2021.

[28] J. Lau, et al., "Insight into the Development of PET Radiopharmaceuticals for Oncology," Cancers **12**, 1312, 2020.

[29] B. J. Zitelli, “Atlas of Pediatric Physical Diagnosis,” E-Book. Elsevier Health Sciences, 2021.

[30] M. Błaszczyk, Z. Adamczewski and A. Płachcińska, “Capabilities of Modern Semiconductor Gamma Cameras in Radionuclide Diagnosis of Coronary Artery Disease,” Diagnostics **11**, 2130, 2021.

[31] P. Zanzonico, “Principles of nuclear medicine imaging: planar, SPECT, PET, multi-modality, and autoradiography systems,” Radiat. Res. **177**, 349-364, 2012.

[32] T. Beyer, et al., “A combined PET/CT scanner for clinical oncology,” J. Nucl. Med. **41**, 1369–1379, 2000.

[33] S. R. Cherry, S. R, “Multimodality imaging: Beyond pet/ct and spect/ct,” Semin. Nucl. Med. **39**, 348-353, 2009.

[34] D. W. Townsend, Multimodality imaging of structure and function,” Phys. Med. Biol. **53**, 2008.

[35] L. Martí-Bonmatí, et al., “Multimodality imaging techniques,” Contrast Media Mol. Imaging **5**, 180-189, 2010.

[36] B.H. Hasegawa, et al., “Description of a simultaneous emission-transmission CT system,” Medical Imaging IV: Image Formation **1231**, 50-60, 1990.

[37] L. Martí-Bonmatí, et al., "Multimodality imaging techniques," Contrast Media Mol Imaging **5**, 180-189, 2010.

[38] A. Z. Kyme, and RR. Fulton, "Motion estimation and correction in SPECT, PET and CT," Phys. Med. Biol. **66**,18, 2021.

[39] H. Zaidi, A. Del Guerra “An outlook on future design of hybrid PET/MRI systems,” Med. Phys. **38**, 5667-5689, 2011.

[40] S. Vandenberghe and P.K. Marsden, “PET-MRI: a review of challenges and solutions in the development of integrated multimodality imaging,” Phys. Med. Biol. **60**, 2015.

[41] W. P. Fendler, et al., “Variations in PET/MRI operations: results from an international survey among 39 active sites,” J. Nucl. Med. **57**, 2016.

[42] J. H. N. Wagner, “A brief history of positron emission tomography (PET),” Semin. Nucl. Med. **28**, 213-220, 1998.

[43] T. Jones and D. W. Townsend, “History and future technical innovation in positron emission tomography,” J. Med. Imaging **4**, 011013, 2017.

[44] P. A. M. Dirac, “A theory of electrons and protons,” Proc. Camb. Soc. **26**, 1929

[45] C. D. Anderson, “The Positive Electron,” Phys. Rev. **43**, 1933

[46] J. F. Volker, et al., “The absorption of fluoride by enamel, dentine, bone and the hydroxyapatite as shown by the radioactive isotope,” J. Bioi. Chern. **134**, 1940.

[47] J. H. Wills, “Secretion of intravenously injected fluorine in the submaxillary saliva of cats,” J. Dent. Res. **19**, 1940.

[48] C. L. Melcher, “Scintillation crystals for PET*.,” J. Nucl. Med. **41**, 1051-1055, 2000.

[49] M. N. Croll, “Nuclear medicine instrumentation. Historic perspective,” Semin. Nucl. Med. **24**, 1994.

[50] F. R. Wrenn, M.L. Good and P. Handler, “The use of positron-emitting radioisotopes for the localization of brain tumors,” Science **19**, 1951.

[51] G. L. Brownell and W.H. Sweet, “Localization of brain tumors with positron emitters,” Nucleonics **11**, 1953.

[52] S. Rankowitz, et al., “Positron scanner for locating brain tumors,” Proc. IRE Int. Com. Rec., New York, NY, 1962.

[53] H. O. Anger and A. Gottschalk, “Localization of brain tumors with the positron scintillation camera,” J. Nucl. Med. **4**, 1963.

[54] H. O. Anger and D. C. Van Dyke, “Human bone marrow distribution shown in vivo by iron-52 and the positron scintillation camera,” Science **144**, 1964.

[55] A. del Guerra, et al., “Positron Emission Tomography: Its 65 years,” Riv. Del Nuovo Cim. **39**, 2016.

[56] M. A. Steiner, "PET--The history behind the technology,", 2002.

[57] C. J. Thompson, Y. L. Yamamoto and E. Meyer, “A Position Imaging System for the Measurement of Regional Cerebral Blood Flow,” Appl. Opt. Inst. Med. V. **96**, 1976.

[58] C. W. Williams, M. C. Crabtree and S.G. Burgiss, “Design and performance characteristics of a positron emission computed axial tomograph—ECAT®-II,” IEEE Trans. Nucl. Sci. Vol. **26**, 1979.

[59] E. J. Hoffman, et al., “ECAT III—basic design considerations,” IEEE Trans. Nucl. Sci. **30**, 1983.

[60] Z. H. Cho, J. K. Chan and L. Eriksson, “Circular ring transverse axial positron camera for three-dimensional reconstruction of radionuclides distribution,” IEEE Trans. Nucl. Sci. **23**, 1976.

[61] Z. H. Cho and M. R. Farukhi, “Bismuth germanate as a potential scintillation detector in positron cameras,” J. Nucl. Med. **18**, 1977.

[62] C. L. Melcher and J. S. Schweitzer “Cerium-doped lutetium oxyorthosilicate: A fast, efficient new scintillator,” IEEE Trans. Nucl. Sci. **39**, 502–505, 1992.

[63] T. Ido, et al., “Labeled 2-deoxy-D-glucose analogs. Fluorine-18-labeled 2-deoxy-2-fluoro- D-glucose. 2-deoxy- 2-fluoro-D-man- nose, and C-14-2-fluoro-Dglucose,” J. Labelled Comp. Radiopharm. **14**, 175-183, 1978.

[64] N. A. Mullani, et al., “Dynamic imaging with high resolution time-of-flight PET camera- TOFPET I,” IEEE Trans. Nucl. Sci. **31**, 1984.

[65] M. M. Ter-Pogossian, et al., “Photon time-of-flight assisted positron emission tomography,” J. Comput. Assist. Tomogr., 227- 239, 1981.

[66] J. S. Reddin, “Performance evaluation of the SiPM-based Siemens Biograph Vision PET/CT system,” IEEE NSS-MIC Conference Proceedings, 2018.

[67] A. J. González, F. Sánchez and J. M. Benlloch, “Organ-dedicated molecular imaging systems,” IEEE Trans. Radiat. Plasma Med. Sci. **2**, 388-403, 2018.

[68] R. D. Badawi, “First human imaging studies with the EXPLORER total-body PET scanner,” J. Nucl. Med. **60**, 299-303, 2019.

[69] A. Alavi, “Unparalleled and revolutionary impact of PET imaging on research and day to day practice of medicine,” Bio-Algorithms and Med-Systems **17**, 203-212, 2021.

[70] M. L. Giger, H. P. Chan and J. Boone, “Anniversary paper: history and status of CAD and quantitative image analysis: the role of medical physics and AAPM,” Med. Phys. **35**, 5799-5820, 2008.

[71] M. L. Giger, “Ai/machine learning in medical imaging,” Mol. Imaging, 1691-1702, Academic Press, 2021.

[72] C. Beegle, “Artificial Intelligence and Positron Emission Tomography Imaging Workflow: Technologists’ Perspective,” PET Clin. **17**, 31-39, 2022.

[73] F. Pesapane, M. Codari and F. Sardanelli, “Artificial intelligence in medical imaging: threat or opportunity? Radiologists again at the forefront of innovation in medicine,” Eur. Radiol. Exp. **2**, 1-10, 2018.

[74] D. L. Bailey and J. L. Humm, “Nuclear medicine physics: a handbook for teachers and students,” Iaea, 2014.

[75] R. D. Evans, “The Atomic Nucleus,” McGraw-Hill, New York, LCCCN 55-7275, 1955.

[76] P. Moskal, et al., "Feasibility study of the positronium imaging with the J-PET tomograph," Phys. Med. Biol. **64**, 055017, 2019.

[77] C. S. Levin, “Calculation of positron range and its effect on the fundamental limit of positron emission tomography system spatial resolution,” Phys. Med. Biol. **44**, 1999.

[78] K. S. Krane, “Introductory Nuclear Physics,” John Wiley and Sons, 1995.

[79] B.S. Gopal, “Basics of PET imaging. Physics. Chemistry, and Regulations,” Springer, 2010.

[80] R. Lecomte, "Novel detector technology for clinical PET." European journal of nuclear medicine and molecular imaging **36**, 69-85, 2009.

[81] I. Mohammadi, “Minimization of parallax error in positron emission tomography using depth of interaction capable detectors: methods and apparatus,” Biomed. Phys. Eng. Express **5**, 062001, 2019.

[82] M. Ito, Mikiko, S. J. Hong, and J. S. Lee, "Positron emission tomography (PET) detectors with depth-of-interaction (DOI) capability," Biomed. Eng. Lett. **1**, 70-81, 2011.

[83] M. M. Moses, P. R. G. Virador, S. E. Derenzo, “Design of a high-resolution, high-sensitivity PET camera for human brains and small animals,” IEEE Trans Nucl Sci. **44**, 1487–91, 1997.

[84] M. Soret M, S. L. Bacharach, I. Buvat, “Partial-volume effect in PET tumor imaging,” J Nucl Med. **48**, 932–945, 2007

[85] M. E. Phelps, “PET molecular imaging and its biological applications,” New York: Springer; 2004.

[86] R. S. Miyaoka and A. Lehnert, "Small animal PET: a review of what we have done and where we are going," Phys. Med. Biol. **65**, 24 2020.

[87] H. Peng and S. L. Craig, "Recent developments in PET instrumentation," Curr. Pharm. Biotechnol. **11**, 555-571, 2010.

[88] S. Surti, “Update on time-of-flight PET imaging,” J. Nucl. Med. **56**, 98-105.

[89] D. R. Schaart, “Physics and technology of time-of-flight PET detectors,” Phys. Med. Biol. **66**, 2021.

[90] M. Conti and B. Bendriem, “The new opportunities for high time resolution clinical TOFPET,” Clin. Trans. Imaging **7**, 139-147, 2019.

[91] S. Surti, et al., “Impact of time-of-flight PET on whole-body oncologic studies: A human observer lesion detection and localization study,” J. Nucl. Med. **52**, 712–719, 2011.

[92] P. Lecoq, “Pushing the Limits in Time-of-Flight PET Imaging,” IEEE Trans. Radiat. Plasma Med. Sci. **1**, 473–485, 2017.

[93] G. F. Knoll,” Radiation Detection and Measurement,” John Wiley and Sons, New York, 3rd edition, 2000.

[94] S. R. Cherry, and M. Dahlbom “PET: physics, instrumentation, and scanners,” PET, 1-117, Springer, New York, 2006.

[95] G. Bizarri, “Scintillation mechanisms of inorganic materials: From crystal characteristics to scintillation properties,” Journal of Crystal Growth **312**, 1213–1215, 2010.

[96] C. W. E. Van Eijk, “Inorganic scintillators in medical imaging,” Phys. Med. Biol. **47**, 8, 2002.

[97] A. Nassalski, et al., “Comparative Study of Scintillators for PET/CT Detectors,” IEEE Trans. Nucl. Sci. **54**, 3–10, 2007.

[98] A. Gonzalez-Montoro, et al., “Evolution of PET Detectors and Event Positioning Algorithms Using Monolithic Scintillation Crystals,” IEEE Trans. Rad. Plasma. Med. Sci. **5**, 282-305, 2021.

[99] A. Gonzalez-Montoro, “Design and implementation of PET detectors based on monolithic crystals and SiPMs,” PhD thesis, University of Valencia, 2018.

[100] Y. H. Chung, et al., "New design of a quasi-monolithic detector module with DOI capability for small animal pet," Nucl. Instrum Methods. Phys. Res. A **593**, 588-591, 2008.

[101] Y. H. Chung, et al., "Preliminary experimental results of a quasi-monolithic detector with DOI capability for a small animal PET." Nucl. Instrum Methods.

Phys. Res. A, Accelerators Spectrometers Detectors Assoc. Equip.**621**, 590-594, 2010.

[102] X. Zhang, et al., "Performance of a SiPM based semi-monolithic scintillator PET detector," Phys. Med. Biol. **62**,19 7889, 2017.

[103] X. Zhang, et al., "Performance of long rectangular semi-monolithic scintillator PET detectors," Med. Phys. **46**, 1608-1619, 2019.

[104] N. Cucarella, et al., "Timing evaluation of a PET detector block based on semi-monolithic LYSO crystals," Med. Phys. **48**, 8010-8023, 2021.

[105] F. Mueller, et al., "A Semi-Monolithic Detector providing intrinsic DOI-encoding and sub-200 ps CRT TOF-Capabilities for Clinical PET Applications," Med. Phys., 2022.

[106] M. Freire, et al. “Position estimation methods using neural networks in semi-monolithic PET detectors”, Phys. Med. Biol., 2022.

[107] A. Kaalep, et al., "Feasibility of state of the art PET/CT systems performance harmonization," Eur. J. of Nucl. Med. Mol. Imaging **45**, 1344-1361, 2018.

[108] M. Amirrashedi , H. Zaidi and M.R. Ay, “Advances in preclinical PET instrumentation,” PET clinics **15**, 403-426, 2020.

[109] L. Bläckberg, et al., “Light spread manipulation in scintillators using laser induced optical barriers,” IEEE Trans. Nucl. Sci. **65**, 2208-2215, 2018.

[110] S. Surti and J.S. Karp, “Current status of PET technology,” Advances in PET: The Latest in Instrumentation, Technology, and Clinical Practice, 3-14, Springer, 2020.

[111] A. González-Montoro, et al., “Study of optical reflectors for a 100ps coincidence time resolution TOF-PET detector design,” Biomed. Phys. Eng. Express **7**, 065008, 2021.

[112] E. Berg, E. and S.R. Cherry, “Innovations in instrumentation for positron emission tomography,” Semin. Nucl. Med. **48**, 311-331, 2018.

[113] E. Lamprou, et al., “PET detector block with accurate 4D capabilities,” Nucl. Instrum Methods. Phys. Res. A, Accelerators Spectrometers Detectors Assoc. Equip. **912**, 132-136, 2018.

[114] M. Wang, Y. Wang and L. Wang, “Evaluation of high-resolution and depth-encoding PET detector modules based on single-ended readout with TOFPET2 ASIC,” Radiat. Detect. Technol. Methods. **5**, 451-458, 2021.

[115] I. Mohammadi, “Minimization of parallax error in positron emission tomography using depth of interaction capable detectors: methods and apparatus,” Biomed. Phys. Eng. Express **5**, 062001, 2019.

[116] N. Belcari, et al., "Design and detector performance of the PET component of the TRIMAGE PET/MR/EEG scanner., IEEE Trans. on Rad. and Plasma Med.Sci. **3**, 292-301, 2019.

[117] Stickel, Jennifer R., Jinyi Qi, and Simon R. Cherry. "Fabrication and characterization of a 0.5-mm lutetium oxyorthosilicate detector array for high-resolution PET applications," J. of Nucl. Med. **48**, 115-121, 2007.

[118] E. Lamprou, et al. "Exploring TOF capabilities of PET detector blocks based on large monolithic crystals and analog SiPMs," Phys. Med. **70**, 10-18, 2020.

[119] H. T. Van Dam, et al., “Sub-200 ps CRT in monolithic scintillator PET detectors using digital SiPM arrays and maximum likelihood interaction time estimation,” Phys. Med. Biol. **58**, 3243, 2013.

[120] P. Carra, et al., “A neural network-based algorithm for simultaneous event positioning and timestamping in monolithic scintillators,” Phys. Med. Biol., 2022.

[121] A. J. Gonzalez, et al., “Feasibility study of a small animal PET Insert based on a single LYSO monolithic tube,” Front. Med. **5**, 328, 2018.

[122] S. Genna and A. P. Smith, “The development of ASPECT, an annular single crystal brain camera for high efficiency SPECT,” IEEE Trans. Nucl. Sci. **35**, 654–658, 1988.

[123] A. L. Goertzen, et al., “First results from the high-resolution mouse SPECT annular scintillation camera,” IEEE Trans. Med. Imag. **24**, 863–867, 2005.

[124] R. Freifelder, J.S. Karp, M. Geagan and G. Muehllehner, “Design and performance of the HEAD PENN-PET scanner,” IEEE Trans Nucl. Sci. **41**, 1436–1440, 1994.

[125] K. J. Wilson, et al., “Localisation of the lines of response in a continuous cylindrical shell PET scanner,” in Proc. Annu. Int. Conf. IEEE Eng. Med. Biol. Soc., 4844–4850, 2019.

[126] J. Xu, et al., “A preclinical PET detector constructed with a monolithic scintillator ring,” Phys. Med. Biol. **64**, 2019.

[127] R. Vinke R, C.S. Levin, “A method to achieve spatial linearity and uniform resolution at the edges of monolithic scintillation crystal detectors,” Phys Med Biol. **59**, 2975-2995, 2014.

[128] M. Morrocchi, et al., Evaluation of event position reconstruction in monolithic crystals that are optically coupled,” Phys Med Biol. **61**,8298-8320, 2016.

[129] E. Roncali and S.R. Cherry, “Simulation of light transport in scintillators based on 3D characterization of crystal surfaces,” Phys. Med. Biol. **58**, 2185, 2013.

[130] M. Stockhoff, et al., “Advanced optical simulation of scintillation detectors in GATE V8. 0: first implementation of a reflectance model based on measured data,” Phys. Med. Biol. **62**, 2017.

[131] E. Roncali, M. Stockhoff and S. R. Cherry, “An integrated model of scintillator-reflector properties for advanced simulations of optical transport,” Phys. Med. Biol. **62**, 4811, 2017.

[132] E. Berg, E. Roncali and S. R. Cherry, “Optimizing light transport in scintillation crystals for time-of-flight PET: an experimental and optical Monte Carlo simulation study,” Biomed. Opt. express **6**, 2220-2230, 2015.

[133] A. González-Montoro, et al., “Performance study of a large monolithic LYSO PET detector with accurate photon DOI using retroreflector layers,” IEEE Trans. Radiat. Plasma Med. Sci. **1**, 229-237, 2017.

[134] S. R. Cherry, J. Sorenson and M. Phelps, Physics in Nuclear Medicine, Elsevier Inc, 7, 87-106, 2012.

[135] W. Jiang, C. Yamn, and M. J. Deen, "Sensors for positron emission tomography applications," *Sensors* **19**, 5019., 2019

[136] Photomultipler tubes. Basics and applications. https://www.hamamatsu.com/content/dam/hamamatsu-photonics/sites/documents/99_SALES_LIBRARY/etd/PMT_handbook_v3aE.pdf

[137] D. Renker, “New trends on photodetectors,” Nucl. Instrum. Methods. Phys. Res. A, Accelerators Spectrometers Detectors Assoc. Equip. **571**, 1-6, 2007.

[138] S. Cova, et al., “ Avalanche photodiodes and quenching circuits for single-photon detection,” Appl. Opt. **35**, 1956-1976, 1996.

[139] D. Renker, “Geiger-mode avalanche photodiodes, history, properties and problems,” Nucl. Instrum. Methods Phys. Res. A, Accelerators Spectrometers Detectors Assoc. Equip. **567**, 48–56, 2006.

[140] A. Del Guerra, et al., "Silicon Photomultipliers (SiPM) as novel photodetectors for PET," Nucl. Instrum. Methods. Phys. Res. B **648**, S232-S235, 2011.

[141] F. Acerbi and S. Gundacker, “Understanding and simulating SiPMs,” Nucl. Instrum. Methods Phys. Res. A, Accelerators Spectrometers Detectors Assoc. Equip. **487**, 16–35, 2019.

[142] D. R. Schaart, et al., “Advances in digital SiPMs and their application in biomedical imaging,” Nucl. Instrum. Methods Phys. Res. A, Accelerators Spectrometers Detectors Assoc. Equip. **809**, 31–52, 2016.

[143] D. Sanchez, “Optimized PET module for both pixelated and monolithic scintillator crystals,” PhD thesis University de Barcelona, 2021.

[144] I. Sarasola, et al., “Performance evaluation of a PET demonstrator for PET-MR imaging based on monolithic LYSO:Ce scintillators,” J. Instrum. **6**, 2006.

[145] J. M. Monzo, et al., “PETIROC2 based readout electronics optimization for Gamma Cameras and PET detectors,” J. Instrum. **12**, 2017.

[146] D. Sánchez, et al., "HRFlexToT: a high dynamic range ASIC for time-of-flight positron emission tomography," IEEE Trans. Radiat. Plasma Med. Sci. **6**, 51-67, 2021.

[147] S. Gómez, et al., "FastIC: a fast integrated circuit for the readout of high performance detectors,” J. Instrum. **17**, 2022.

[148] L. A. Pierce, et al., “Characterization of highly multiplexed monolithic PET/gamma camera detector modules,” Phys. Med. Biol. **63**, 2018.

[149] A. Gonzalez-Montoro, et al., “Detector block performance based on a monolithic LYSO crystal using a novel signal multiplexing method,” Nucl. Instrum. Methods Phys. Res. A, Accelerators Spectrometers Detectors Assoc. Equip. **912**, 372–377, 2018.

[150] C. Wanarak, W. Chewpraditkul and A. Phunpueok. "Light yield non-proportionality and energy resolution of Lu1. 95Y0. 05SiO5: Ce and Lu2SiO5: Ce scintillation crystals," Procedia Eng. **32**, 765-771, 2012.

[151] S. Tong, A.M. Alessio and P.E. Kinahan, “Image reconstruction for PET/CT scanners: past achievements and future challenges,” Imaging Med. **2**, 529, 2010.

[152] A. J. Reader and H. Zaidi., “Advances in PET image reconstruction,” PET clinics **2**, 173-190, 2007.

[153] F. H. Fahey, "Data acquisition in PET imaging," J. Nucl. Med. Technol. **30**, 39-49, 2002.

[154] L. M. Popescu, M. Samuel Matej and M. L. Robert, "Iterative image reconstruction using geometrically ordered subsets with list-mode data," IEEE Nucl. Sci. Symp. Conf. Rec. **6**, 2004.

[155] L. A. Shepp and Y. Vardi, “Maximum Likelihood Reconstruction for Emission Tomography,” IEEE Trans. Med. Imaging **1**, 113–122, 1982.

[156] H. M. Hudson and R. S. Larkin, “Accelerated Image Reconstruction Using Ordered Subsets of Projection Data,” IEEE Trans. Med. Imaging **13**, 601–609, 1994.

[157] J. M. Ollinger, “Model-based scatter correction for fully 3D PET,” Phys. Med. Biol **41**,153-176, 1996.

[158] S. D. Wollenweber, “Parameterization of a model-based 3D PET scatter correction,” IEEE Trans. Nucl. Sci **49**, 722–727, 2002.

[159] L. Theodorakis, et al., "A review of PET normalization: striving for count rate uniformity," Nucl. Med. Commun. **34**, 1033-1045, 2013.

[160] E. Vicente, et al., "Improved dead-time correction for PET scanners: application to small-animal PET," Phys. Med. Biol. **58**, 2059, 2014.

[161] M. E. Daube-Witherspoon, et al., “PET performance measurements using the NEMA NU 2-2001 standard,” J. Nucl. Med. **43**, 1398-1409, 2002.

[162] National Electrical Manufacturers Association. NEMA Standards Publication NU 2-1994: Performance measurements of positron emission tomographs. Washington, DC: National Electrical Manufacturers Association, 1994.

[163] National Electrical Manufacturers Association. NEMA standards publication NU 2-2018: Performance measurements of positron emission tomographs. Rosslyn: National Electrical Manufacturers Association; 41, 2018

[164] National Electrical Manufacturers Association NEMA standards publication NU4-2008: Performance measurements of small animal positron emission tomographs. Rosslyn: National Electrical Manufacturers Association; 2008

[165] S. Surti, R.P. Austin and S.K. Joel, "Total body PET: why, how, what for?," IEEE Trans. Radiat. Plasma Med. **4**, 283-292, 2020.

[166] S.R. Cherry, et al., "Total-body PET: maximizing sensitivity to create new opportunities for clinical research and patient care," J. Nucl. Med. **59**, 3-12, 2018.

[167] CareMiBrain imager, ONCOVISION, Valencia, Spain, https://www.oncovision.com.

[168] PET insert. Bruker, https://www.bruker.com/en/products-and-solutions/preclinical-imaging/nmi/pet-insert.html?utm_source=Advertising&utm_medium=GoogleAd&utm_campaign=BBIO-Imaging-PCI-MRI-PETInsert-H2-2022&gclid=CjwKCAiA2rOeBhAsEiwA2Pl7QykAMpgsRMqM5JPJ9XLsWjr1NmLMqL_MKsHp5PzG5pXsNH82cVckxRoCvdsQAvD_BwE

[169] M. E. Casey and R. O. Dustin, "Siemens biograph vision 600," Advances in PET, 71-91, Springer, Cham, 2020.

[170] S. Surti, and J. S. Karp, "Update on latest advances in time-of-flight PET." Physica Medica **80**, 251-258, 2020.

[171] I. Rausch et al., “Performance evaluation of the VereoS PET/CT system according to the NEMA NU2-2012 standard,” J. Nucl. Med. **60**, 561–567, 2019.

[172] S. Chen, et al., "Performance characteristics of the digital uMI550 PET/CT system according to the NEMA NU2-2018 standard," EJNMMI Phys. **7**, 1-14, 2020.

[173] M. Conti and B. Bendriem, “The new opportunities for high time resolution clinical TOF PET,” Clin. Trans. Imaging **7**, 139-147, 2019.

[174] S. Surti, et al., “Performance of Philips Gemini TF PET/CT scanner with special consideration for its time-of-flight imaging capabilities,” J. Nucl. Med. **48**, 471–480, 2007.

[175] V. Bettinardi, et al., “Physical Performance of the new hybrid PETCT Discovery-690,” Med. Phys. **38**, 5394–5411, 2011.

[176] J. B. W. Jakoby, et al., “Physical and clinical performance of the mCT time-of-flight PET/CT scanner,” Phys. Med. Biol. **56**, 2375–2389, 2011.

[177] N. C. Nguyen, et al., “Image quality and diagnostic performance of a digital pet prototype in patients with oncologic diseases: Initial experience and comparison with analog PET,” J. Nucl. Med. **56**, 1378–1385, 2015.

[178] D. F. C. Hsu, et al., “Studies of a next-generation silicon-photomultiplier-based time-offlight PET/CT system,” J. Nucl. Med. **58**, 1511–1518, 2017

[179] J. S. Reddin, et al., “Performance evaluation of the SiPM based Siemens Biograph vision PET/CT system,” IEEE NSS-MIC Conference Proceedings, 2018.

[180] J. Van Sluis, et al., “Performance characteristics of the digital biograph vision PET/CT system,” J. Nucl. Med. **60**, 1031–1036, 2019.

[181] E. Lamprou, “Development and Performance Evaluation of High Resolution TOFPET Detectors Suitable for Novel PET Scanners”, PhD Thesis, Universidad Politécnica de Valencia, 2021.

[182] G. Delso, et al., “Performance measurements of the Siemens mMR integrated whole-body PET/MR scanner,” J. Nucl. Med. **52**, 1914–1922, 2011.

[183] C. S. Levin, et al., "Design features and mutual compatibility studies of the time-of-flight PET capable GE SIGNA PET/MR system," IEEE Trans. Med. Imaging **35**, 1907-1914, 2016.

[184] H. Zaidi, et al., "Design and performance evaluation of a whole-body Ingenuity TF PET–MRI system," Phys. Med. Biol. **56**, 3091, 2011.

[185] S. R. Cherry, et al., "Total-body PET: maximizing sensitivity to create new opportunities for clinical research and patient care," J. Nucl. Med. **59**, 3-12, 2018.

[186] S. Vandenberghe, P. Moskal and J.S. Karp. "State of the art in total body PET," EJNMMI Phys. **7**, 1-33, 2020.

[187] L. Nardo, et al., "Clinical implementation of total-body PET/CT at University of California, Davis," PET clin. **16**, 1-7, 2021.

[188] D. B. Crosetto, "The 3D complete body screening (3D-CBS) features and implementation," 2003 IEEE NSS-MIC Conference Record **4**, 2003.

[189] S. Surti and J. S. Karp., "Impact of detector design on imaging performance of a long axial field-of-view, whole-body PET scanner," Phys. Med. Biol. **60**, 5343, 2015.

[190] Q. K. T. Ng, et al., “Total-body PET/CT–first clinical experiences and future perspectives.” Semin. Nucl. Med*.,* 2022.

[191] A. R. Pantel, et al., "PennPET Explorer: human imaging on a whole-body imager," J. Nucl. Med. **61**, 144-151, 2020.

[192] G. A. Prenosil, et al., "Performance Characteristics of the Biograph Vision Quadra PET/CT System with a Long Axial Field of View Using the NEMA NU 2-2018 Standard," J. Nucl. Med. 63, 476-484, 2022.

[193] R. R. Raylman, et al., “The positron emission mammography/tomography breast imaging and biopsy system (PEM/PET): design, construction and phantom-based measurements,” Phys. Med. Biol. **53**, 637, 2008.

[194] L. Moliner, et al., "Design and evaluation of the MAMMI dedicated breast PET," Med. Phys. **39**, 5393-5404, 2012.

[195] G. Akamatsu, et al., “Modified NEMA NU-2 performance evaluation methods for a brain-dedicated PET system with a hemispherical detector arrangement,” Biomed. Phys. Eng. Expres **6**, 015012, 2019.
[196] L. Moliner, et al., "NEMA Performance Evaluation of CareMiBrain dedicated brain PET and Comparison with the whole-body and dedicated brain PET systems," Sci. Rep. **9**, 15484, 2019.
[197] J. van der Laan, et al., “Simulated performance of a small-animal PET scanner based on monolithic scintillation detectors,” Nucl. Instrum. Methods Phys. Res. A, Accelerators Spectrometers Detectors Assoc. Equip. **571**, 227–230, 2007.
[198] E. Alpaydin, Introduction to machine learning. MIT press, 2020.
[199] A. T. G. Tapeh and M. Z. Naser “Artificial Intelligence, Machine Learning, and Deep Learning in Structural Engineering: A Scientometrics Review of Trends and Best Practices,” Arch. Comput. Methods Eng., 1-45, 2022.
[200] A. Barragán-Montero, et al., "Artificial intelligence and machine learning for medical imaging: A technology review," Phys. Med. **83,** 242-256, 2021.
[201] I. Castiglioni, et al., “AI applications to medical images: From machine learning to deep learning,” Phys. Med. **83**, 9-24, 2021.
[202] H. Arabiet al., “The promise of artificial intelligence and deep learning in PET and SPECT imaging,” Phys. Med. **83**, 122-137, 2021.
[203] M. Freire, et al., “Using Neural Networks for Impact Position Estimation in a PET Prototype Based on Glued Monolithic Crystals,” IEEE NSS-MIC Conference Proceedings, 1-4, 2021.
[204] D. Bruciaferri, et al., “The development of a 3D computational mesh to improve the representation of dynamic processes: The Black Sea test case,” Ocean Modelling **146**, 101534, 2020.
[205] E. Berg and S. R. Cherry, “Using convolutional neural networks to estimate time-of-flight from PET detector waveforms,” Phys. Med. Biol. **63**, 2018.
[206] A. K. Jha, et al., “Nuclear medicine and artificial intelligence: Best practices for evaluation (the RELAINCE guidelines),” J. Nucl. Med., 2022.
[207] R, Pani, et al., “Position algorithm for monolithic scintillation crystals based on charge projection readout,” J. Instrum. **11**, 2016.
[208] A. González-Montoro, et al., “Performance study of a large monolithic LYSO PET detector with accurate photon DOI using retroreflector layers,” IEEE Trans. Radiat. Plasma Med. Sci. **1**, 229-237, 2017.
[209] T. Ling, et al., "Parametric positioning of a continuous crystal PET detector with depth of interaction decoding," Phys. Med. Biol. **53**, 1843, 2008.
[210] Z. Li, et al., “Nonlinear leastsquares modeling of 3d interaction position in a monolithic scintillator block,” Phys. Med. Biol. **55**, 6515, 2010.
[211] T. Ling, T. K. Lewellen and R. S. Miyaoka, “Depth of interaction decoding of a continuous crystal detector module,” Phys. Med. Biol. **52**, 2213, 2007.
[212] H. T. Van Dam, et al., “A practical method for depth of interaction determination in monolithic scintillator PET detectors,” Phys. Med. Biol. **56**, 4135, 2011.
[213] P. Bruyndonckx, et al., “Evaluation of machine learning algorithms for localization of photons in undivided scintillator blocks for PET detectors,” IEEE Trans. Nucl. Sci. **55**, 918-924, 2008.

[214] F. Müller, et al., “A novel DOI positioning algorithm for monolithic scintillator crystals in PET based on gradient tree boosting,” IEEE Trans. Radiat. Plasma Med. Sci. **3**, 465-474, 2018.

[215] Y. Wang, et al., “3D position estimation using an artificial neural network for a continuous scintillator pet detector,” Phys. Med. Biol. **58**, 1375, 2013.

[216] M. Kawula, et al., “Sub-millimeter precise photon interaction position determination in large monolithic scintillators via convolutional neural network algorithms,” Phys. Med. Biol. **66**, 135017, 2021.

[217] H. O. Anger, “Scintillation camera,” Rev. Sci. Instr. **29**, 27–33, 1958.

[218] R. Pani, et al., “Continuous DOI determination by Gaussian modelling of linear and non-linear scintillation light distributions,” IEEE NSS-MIC Conference Record, 3386-3389, 2011.

[219] R. Pani, et al., "Preliminary evaluation of a monolithic detector module for integrated PET/MRI scanner with high spatial resolution," J. Instr. **10**, C06006, 2015.

[220] W. C. J. Hunter, “Modeling stochastic processes in gamma-ray imaging detectors and evaluation of a multi-anode PMT scintillation camera for use with maximum-likelihood estimation methods,” PhD thesis, Dept. Phys. Univ. Arizona, 2007.

[221] W. C. J. Hunter, H. H. Barrett and L. R. Furenlid, “Calibration method for ml estimation of 3d interaction position in a thick gamma-ray detector,” IEEE Trans. Nucl. Sci. **56**, 189, 2009.

[222] H. H. Barrett, et al., “Maximum-likelihood methods for processing signals from gammaray detectors,” IEEE Trans. Nucl. Sci. **56**, 725, 2009.

[223] R. S. Miyaoka, et al., “Calibration procedure for a continuous miniature crystal element (cMiCE) detector,” IEEE Trans. Nucl. Sci. **57**, 1023-1028, 2010.

[224] M. Streun, et al., “Position reconstruction in monolithic block detectors,” IEEE NSS-MIC Conference Record, 3212-3215, 2012.

[225] R. Vinke, et al., “Time walk correction for TOF-PET detectors based on a monolithic scintillation crystal coupled to a photosensor array,” Nucl. Instrum. Methods Phys. Res. A, Accelerators Spectrometers Detectors Assoc. Equip. **621**, 595-604, 2010

[226] A. Etxebeste, et al., “3D position determination in monolithic crystals coupled to SiPMs for PET,” Phys. Med. Biol. **61**, 3914, 2016.

[227] Y. Wang, et al., “An FPGA-based real-time maximum likelihood 3D position estimation for a continuous crystal PET detector,” IEEE Trans. Nucl. Sci. **63**, 37-43, 2016.

[228] Y. Wang, X. Cheng, and D. Li, “Improved statistics based positioning scheme for continuous thick crystal pet detectors,” IEEE Trans. Nucl. Sci. **60**, 1527, 2013.

[229] H. T. Van Dam, et al., “Sub-200 ps CRT in monolithic scintillator PET detectors using digital SiPM arrays and maximum likelihood interaction time estimation,” Phys. Med. Biol. **58**, 3243, 2013.

[230] X. Li, et al., “Spatial resolution performance evaluation of a monolithic crystal PET detector with Cramer-Rao lower bound (CRLB),” IEEE NSS-MIC Conference Record, 2202-2205, 2010.

[231] R. Marcinkowski, et al., “Sub-millimetre DOI detector based on monolithic LYSO and digital SiPM for a dedicated small-animal PET system,” Phys. Med. Biol. **61**, 2196, 2016.

[232] K. Deprez, R. Van Holen and S. Vandenberghe, “A high resolution SPECT detector based on thin continuous LYSO,” Phys. Med. Biol. **59**, 153, 2013.

[233] M. C. Maas, et al.,” Experimental characterization of monolithic-crystal small animal pet detectors read out by apd arrays,” IEEE Trans. Nucl. Sci. **53**, 1071, 2006.

[234] T. Cover and P. Hart, “Nearest neighbor pattern classification,” IEEE Trans. Inf. Theory. **13**, 21-27, 1967.

[235] D. R. Schaart, et al., “A novel, SiPM-array-based, monolithic scintillator detector for PET,” Phys. Med. Biol. **54**, 3501, 2009.

[236] M. C. Maas et al., “Monolithic scintillator PET detectors with intrinsic depth-of-interaction correction,” Phys. Med. Biol. 54, 1893–1908, 2009.

[237] P. G. De Acilu, et al., "Study and optimization of positioning algorithms for monolithic PET detectors blocks," J. Instrum. **7**, 2012.

[238] H. T. van Dam, et al., “Improved nearest neighbor methods for gamma photon interaction position determination in monolithic scintillator pet detectors,” IEEE Trans. Nucl. Sci. **58**, 2139, 2011.

[239] G. Borghi, et al., “Experimental validation of an efficient fan-beam calibration procedure for $ K $-nearest neighbor position estimation in monolithic scintillator detectors,” IEEE Trans. Nucl. Sci. **62**, 57-67, 2015.

[240] Y. Wang, et al., “Self-organizing map neural network-based nearest neighbor position estimation scheme for continuous crystal PET detectors IEEE Trans. Nucl. Sci. **61**, 2446-2455, 2014.

[241] M. Stockhoff, et al., “High-resolution monolithic LYSO detector with 6-layer depth-of-interaction for clinical PET,” Phys. Med. Biol. **66**, 155014, 2021.

[242] S. B. Kotsiantis, “Decision trees: a recent overview,” Artif. Intell. Rev. **39**, 261-283, 2013.

[243] A. Natekin and A. Knoll, “Gradient boosting machines, a tutorial,” Front. Neurorobot. **7**, 21, 2013.

[244] F. Müller, et al., “Gradient tree boosting-based positioning method for monolithic scintillator crystals in positron emission tomography," IEEE Trans. Radiat. Plasma Med. Sci. **2**, 411-421, 2018.

[245] C. Wassermann, et al., “High throughput software-based gradient tree boosting positioning for PET systems,” Biomed. Phys. Eng. Express **7**, 055023, 2021.

[246] R. Rojas, Neural networks: a systematic introduction, Springer Science & Business Media, 2013

[247] S. Haykin, Neural networks: A guided tour. Soft computing and intelligent systems: theory and applications, 71, 1999.

[248] S. Ruder "An overview of gradient descent optimization algorithms," arXiv preprint arXiv:1609.04747, 2016.

[249] N. Qian, “On the momentum term in gradient descent learning algorithms,” Neural Net. **12**, 145–151, 1999.

[250] Y. Nesterov, “A method for unconstrained convex minimization problem with the rate of convergence o(1/k2),” Soviet. Math. Docl. **269**, 543– 547, 1983.

[251] J. Duchi, E. Hazan and Y. Singer, “Adaptive Subgradient Methods for Online Learning and Stochastic Optimization,” J. Mach. Lear. Res. **12**, 2121–2159, 2011

[252] M. D. Zeiler, “ADADELTA: An Adaptive Learning Rate Method,”, 2012.

[253] D. P. Kingma and J. L. Ba, “Adam: a Method for Stochastic Optimization,” International Conference on Learning Representations, 1–13, 2015.

[254] D. Clément, et al., “Development of a 3D position sensitive scintillation detector using neural networks,” IEEE NSS-MIC Conference Record **3**, 1448-1452, 1998.

[255] P. Bruyndonckx, et al., “Study of spatial resolution and depth of interaction of apd-based pet detector modules using light sharing schemes,”, IEEE Trans. Nucl. Sci. **50**, 1415,2003.

[256] P. Bruyndonckx, et al., “Neural network-based position estimators for pet detectors using monolithic lso blocks,” IEEE Trans. Nucl. Sci. **51**, 2520, 2004.

[257] R. J. Aliaga, et al., “Corrected position estimation in PET detector modules with multi-anode PMTs using neural networks,” IEEE Trans. Nucl. Sci. **53**, 776-783, 2006.

[258] W. Yonggang, et al., “Electronics for monolithic scintillator PET detector modules based on neural network position estimators,” IEEE NSS-MIC Conference Record, 554-558, 2009.

[259] D. Junwei, et al., “Performance study of neural network position estimators for the monolithic scintillator PET detector modules,” IEEE NSS-MIC Conference Record, 1-4, 2010.

[260] A. Sanaat and H. Zaidi, “Depth of interaction estimation in a preclinical PET scanner equipped with monolithic crystals coupled to SiPMs using a deep neural network,” Appl. Sci. **10**, 4753, 2020.

[261] M Decuyper, et al., “Artificial neural networks for positioning of gamma interactions in monolithic PET detectors,” Phys. Med. Biol. **66**, 075001, 2021.

[262] A. Sanaat, and Zaidi**, “**Accurate estimation of depth of interaction in PET on monolithic crystal coupled to SiPMs using a deep neural network and Monte Carlo simulations,” IEEE NSS-MIC Conference Record, 1-3, 2019.

[263] L. Tao, et al., “Deep learning techniques for gamma ray interaction location estimation in monolithic scintillation crystal detectors,” 2018 IEEE NSS-MIC Conference Proceedings, 1-3, 2018

[264] P. Peng, et al., “Compton PET: a simulation study for a PET module with novel geometry and machine learning for position decoding,” Biomed. Phys. Eng. Express **5**, 015018, 2018.

[265] P. Peng, M. S. Judenhofer and S. R. Cherry, “Compton PET: a layered structure PET detector with high performance,” Phys. Med. Biol. **64**, 2019.

[266] C. Clement, et al., “Deep Learning for Predicting Gamma-Ray Interaction Positions in LYSO Detector,” IEEE EMBC, 3366-3369, 2021.

[267] G. Jaliparthi, et al., “Deep residual-convolutional neural networks for event positioning in a monolithic annular PET scanner,” Phys. Med. Biol., **66**, 145008, 2021.

[268] W. He, et al., “High-performance coded aperture gamma camera based on monolithic GAGG: Ce crystal,” Rev. Sci. Instrum. **92**, 013106, 2021.

[269] M. M. Fernandez, et al., “A flat-panel-based mini gamma camera for lymph nodes studies,” Nucl. Instrum. Methods Phys. Res. A, Accelerators Spectrometers Detectors Assoc. Equip. **527**, 92–96, 2004.

[270] F. Sanchez, et al., “Design and tests of a portable mini gamma camera,” Med. Phys. **31**, 1384–1397, 2004.

[271] M. Seimetz, et al., “Correction algorithms for signal reduction in insensitive areas of a small gamma camera,” J. Instrum. **9**, 2014.

[272] S. España, et al., "Fast calibration of SPECT monolithic scintillation detectors using un-collimated sources," Phys. Med. Biol. **58**, 4807, 2013.

[273] S. España, et al., “DigiPET: sub-millimeter spatial resolution small-animal PET imaging using thin monolithic scintillators,” Phys. Med. Biol. **59**, 3405, 2014.

[274] P. Bruyndonckx, et al., “Investigation of an in situ position calibration method for continuous crystal-based PET detectors,” Nucl. Instrum. Methods Phys. Res. A, Accelerators Spectrometers Detectors Assoc. Equip. **571**, 304–307, 2007

[275] J. M. Benlloch, et al., “Scanner calibration of a small animal PET camera based on continuous LSO crystals and flat panel PSPMTs,” Nucl. Instrum. Methods Phys. Res. A, Accelerators Spectrometers Detectors Assoc. Equip. **571**, 26–29, 2007.

[276] F. Sánchez, et al., “ALBIRA: A small animal PET/SPECT/CT imaging system,” Med. Phys. **40**, 2013.

[277] G. Cañizares, et al., “Pilot performance of a dedicated prostate PET suitable for diagnosis and biopsy guidance,” EJNMMI Phys., **7**, 1-17, 2020.

[278] A. Gonzalez-Montoro, et al., “Validation of photon collimation techniques for monolithic PET detector calibration,” IEEE Trans. Radiat. Plasma Med. Sci. **5**, 783-792, 2020.

[279] A. Gonzalez-Montoro, et al., “Novel method to measure the intrinsic spatial resolution in PET detectors based on monolithic crystals,” Nucl. Instrum. Methods Phys. Res. A, Accelerators Spectrometers Detectors Assoc. Equip. **920**, pp. 58–67, 2019.

[280] A. Iborra, et al., “Ensemble of neural networks for 3D position estimation in monolithic PET detectors,” Phys. Med. Biol. **64**, 5513–5525, 2019.

[281] J. H. Park and S. Lee, “Monte carlo simulations-based maximum-likelihood position estimation for monolithic scintillation detectors,” J Korean Phys Soc. **74**, 812–5, 2019.

[282] F. Aurenhammer “Voronoi diagrams—a survey of a fundamental geometric data structure,” ACM Comp. Surveys **23**, 345-405., 1991.

[283] I. Amidror "Scattered data interpolation methods for electronic imaging systems: a survey," J. Elect. Imag. **11**, 157-176, 2022.

[284] J. Barrio, et al., “Characterization of a high-aspect ratio detector with lateral sides readout for Compton PET.” IEEE Trans. Rad. Plasma Med. Sci. **4**, 546-554, 2020.

[285] G. Cañizares, et al., “Pilot Results of Detectors Enhancing TOF and DOI Capabilities, Suitable for TB-PET,” IEEE NSS-MIC Conference Proceedings, 1-3, 2021.

[286] A. J. Gonzalez, el al., “Method to Reduce the Number of Signals to be Read Out in a Detector,” General Equipment for Medical Imaging SA, U.S. Patent Application 15/989,892, 2019.

[287] M. Freire, et al., “Calibration methodology of an edgeless PET system prototype,” IEEE NSS/MIC, p- 1-5, 2020.

[288] A. V. Stolin, et al., “Preclinical positron emission tomography scanner based on a monolithic annulus of scintillator: initial design study,” J. Med. Imaging **4**, 011007, 2017.

[289] M. Freire, et al., “Addressing Light Distribution Truncation and 3D Impact Positioning in PET: Edgeless Approach,” IEEE NSS-MIC Conference Proceedings, 1-3, 2021.

[290] W. Gsell, et al., “Characterization of a preclinical PET insert in a 7 Tesla MRI scanner: Beyond NEMA testing,” Phys. Med. Biol. **65**, 2020.

[291] L. E. Adam, et al., “Performance of a whole-body PET scanner using curve-plate NaI (Tl) detectors,” J. Nucl. Med. **42**,1821-30, 2001.

[292] R. Freifelder, et al. "First results of a dedicated breast PET imager, BPET, using NaI (Tl) curve plate detectors," IEEE NSS Conference Record **3**, 2001.

Contributions published during the course of the PhD thesis

Peer-reviewed publications

1. **M. Freire**, A. González-Montoro, F. Sánchez, J. M. Benlloch and A. J. González.

   "Calibration of gamma ray impacts in monolithic-based detectors using Voronoi diagrams," IEEE Trans. Rad. Plasma Med. Sci. **4**, 350-360, 2019.

2. G. Cañizares, A. González-Montoro, **M. Freire**, E. Lamprou, J. Barrio, F. Sánchez, J. M. Benlloch, L. Hernández, L. Moliner, L. F. Vidal, I. Torres and A. J. González.
   "Pilot performance of a dedicated prostate PET suitable for diagnosis and biopsy guidance," EJNMMI Phys. **7**, 1-17, 2020.

3. J. Barrio, N. Cucarella, A. J. González, **M. Freire**, V. Ilisie and J. M. Benlloch.
   "Characterization of a high-aspect ratio detector with lateral sides readout for Compton PET." IEEE Trans. Rad. Plasma Med. Sci. **4**, 546-554, 2020.

4. **M. Freire**, G. Cañizares, S. Echegoyen, A. González-Montoro and A. J. González.
   “Reducing Calibration Time in PET Systems Based on Monolithic Crystals,” Frontiers in Medicine **8**, 734476, 2021.

5. **M. Freire**, A. González-Montoro, G. Cañizares, A. Rezaei, J. Nuyts, S. S. Berr, M. B. Williams, J. M. Benlloch and A. J. and González,
   “Experimental validation of a rodent PET scanner prototype based on a single LYSO crystal tube,” IEEE Trans. Rad. Plasma Med. Sci. **6**, 697-706, 2021.

6. **M. Freire**, S. Echegoyen, A. González-Montoro, F. Sánchez and A. J. González,
   “Performance evaluation of side-by-side optically coupled monolithic LYSO crystals,” Med. Phys. **49**, 5616-5626, 2022.

7. **M. Freire**, J. Barrio, N. Cucarella, C. Valladares, A. González-Montoro, C. de Alfonso, J. M. Benlloch and A. J. González.
   “Position estimation using neural networks in semi-monolithic PET detectors,” Phys. Med. Biol. **67**, 245011, 2022.

8. A. González-Montoro, J. Barbera, D. Sánchez, A. Mondéjar, **M. Freire**, K. Diaz, A. Lucero, S. Jiménez-Serrano, J. Álamo, C. Morera-Ballester, J. Barrio, N. Cucarella, V. Ilisie, L. Moliner, C. Valladares, A.J. González, J. Prior and J.M. Benlloch
   “A new brain dedicated PET scanner with 4D detector information,” Bio-Algorithms and Med-Sys. **18**, 107-119, 2022.

Conference Proceedings

1. E. Lamprou, A. González-Montoro, G. Cañizares, V. Ilisie, F. Sánchez, **M. Freire**, L. Hernández, L.F. Vidal, J. Barrio, A.J. González and J.M. Benlloch.
   “TOF-PET Detectors Based on ASIC Technology and Analog SiPMs,” IEEE NSS-MIC Conference Proceedings, 1-4, 2018.

2. **M. Freire**, A. González-Montoro, F. Sánchez, and A.J. González,
   “Calibration of PET Detectors Based on Monolithic Blocks Using Voronoi Diagrams,” IEEE NSS-MIC Conference Proceedings, 1-3, 2018.

3. A.J. González, A. González-Montoro, **M. Freire**, L. Vidal, L. Hernández, C. Correcher, R. Polo, A. Orero, G. Pastor, V. Carrilero and T. Greeb.

“Performance of a PET/MR Insert for Mice Based on Monolithic Crystals,” J. Nucl. Med. **61**, 2020.

4. **M. Freire**, A. González-Montoro, G. Cañizares, S.S. Berr, L.F. Vidal, L. Hernández and A.J. González.
   “Calibration Methodology of an Edgeless PET System Prototype,” IEEE NSS-MIC Conference Proceedings, 1-5, 2020.

5. J. Barrio, N. Cucarella, **M. Freire**, E. Lamprou, S. Aguilar, C. Valladares, V. Ilisie, J.M. Benlloch and A.J. González.
   “PET Detector based on a Semi-Monolithic Crystal with DOI and TOF Capabilities,” IEEE NSS-MIC Conference Proceedings, 1-3, 2020.

6. **M. Freire**, A. González-Montoro, G. Cañizarcs, S.S. Berr, L.F. Vidal, L. Hernández and A.J. González,
   “Calibration Methodology of an Edgeless PET System Prototype,” In 2020 IEEE NSS-MIC Conference Proceedings, 1-5, 2020.

7. E. Lamprou, C. Valladares, J. Barrio, N. Cucarella, S. Aguilar, G. Cañizares, **M. Freire**, S. Echegoyen, F. Sanchez, L.F. Vidal, L. Hernadez, A. Mascarell, J.M. Benlloch and A.J. González.
   “Towards 100 ps PET Detectors Suitable for High-Resolution Brain Mouse Imaging,” IEEE NSS-MIC Conference Proceedings, 1-3, 2020.

8. **M. Freire**, S. Echegoyen, L.F. Vidal, C. Valladares, A. González-Montoro, M. Vergara, J.F. Toledo, M.J. Rodríguez-Álvarez, F. Sánchez and A.J. González.
   “Using Neural Networks for Impact Position Estimation in a PET Prototype Based on Glued Monolithic Crystals,” IEEE NSS-MIC Conference Proceedings, 1-4, 2021.

9. J. Barrio, N. Cucarella, M. Freire, E. Lamprou, J.M. Benlloch and A.J. González.
   “Characterization of a PET Detector based on Semi-Monolithic Crystals,” IEEE NSS-MIC Conference Proceedings, 1-3, 2021.

10. **M. Freire**, G. Cañizares, A. González-Montoro, C. Correcher, L. Moliner, S.S Berr, M.B. Williams and A.J. González.
    “Addressing Light Distribution Truncation and 3D Impact Positioning in PET: Edgeless Approach.,” IEEE NSS-MIC Conference Proceedings, 1-3, 2021.

11. C. Valladares, E. Lamprou, A.J. González, J. Barrio, N. Cucarella, **M. Freire**, L.F. Vidal and J.M. Benlloch.
“Evaluation of Crystal Arrays for Accurate Positioning and Timing PET detectors,” IEEE NSS-MIC Conference Proceedings, 1-3, 2021.

12. G. Cañizares, J. Barrio, N. Cucarella, D. Sánchez, **M. Freire**, C. Valladares, A. González-Montoro, S. Jiménez-Serrano, A. Lucero, C. Morera, E. Lamprou, J. Barberá, L. F. Vidal, J. M. Benlloch and A. J. González.
“Pilot Results of Detectors Enhancing TOF and DOI Capabilities, Suitable for TB-PET,” IEEE NSS-MIC Conference Proceedings, 1-3, 2021.

Participation in conferences during the course of the PhD thesis

In the following a list of the main contributions to conferences by the PhD candidate is provided:

1. Conference. IEEE Nuclear Science Symposium (NSS) and Medical Imaging Conference (MIC)
   Place and year. Manchester. 2019
   Type of participation. Oral presentation accepted
   Title. " Pilot Results of an Edgeless Small Animal PET Insert"

2. Conference. IEEE Nuclear Science Symposium (NSS) and Medical Imaging Conference (MIC)
   Place and year. Manchester. 2020
   Type of participation. Oral presentation accepted
   Title. " Performance Evaluation of an Edgeless PET Insert for Small Animal Imaging"
   Award: Best Student Paper Award

3. Conference. Total Body PET Conference
   Place and year. Edinburgh. 2021. (Online)

Type of participation. Oral presentation accepted
Title. " Reducing Calibration Times in Total Body PET Designs Based on Monolithic Crystals"

4. Conference. Total Body PET Conference
   Place and year. Edinburgh. 2021. (Online)
   Type of participation. Oral presentation accepted
   Title. " Calibration Techniques for Monolithic Crystals Detectors Based on Neural Networks"

5. Conference. PSMR-9th Conference on PET/MR and SPECT/MR and Total Body PET Workshop
   Place and year. Elba (Italy). 2022
   Type of participation. Oral presentation accepted
   Title. " Performance evaluation of semi-monolithic detectors for TB-PET systems "
   Award: Best oral presentation

6. Conference. PSMR-9h Conference on PET/MR and SPECT/MR and Total Body PET Workshop
   Place and year. Elba (Italy). 2022
   Type of participation. Poster presentation accepted
   Title. "ScintoTube: An Edgeless preclinical PET insert"

7. Conference. IEEE Nuclear Science Symposium (NSS) and Medical Imaging Conference (MIC)
   Place and year. Japan. 2022 (Online)
   Type of participation. Oral presentation accepted
   Title. " Using Neural Networks for Impact Position Estimation in Glued Monolithic Crystals"

8. Conference. IEEE Nuclear Science Symposium (NSS) and Medical Imaging Conference (MIC)
   Place and year. Japan. 2022 (Online)
   Type of participation. Poster presentation accepted
   Title. " Neural Networks for Position Estimation in Monolithic Crystals: Comparison of Experimental and Simulated Training"

9. Conference. IEEE Nuclear Science Symposium (NSS) and Medical Imaging Conference (MIC)
   Place and year. Japan. 2022 (Online)
   Type of participation. Poster presentation accepted
   Title. " Addressing Light Distribution Truncation and 3D Impact Positioning in PET: Edgeless Approach"